Matched Template Signal Processing of Continuous Wave Laser for Ranging to Space Debris

Shasidran Raj

A thesis submitted for the degree of
Doctor of Philosophy
at the Australian National University

Submitted
19th August, 2019

We are not now that strength which in old days
Moved earth and heaven;
That which we are, we are;
One equal temper of heroic hearts,
Made weak by time and fate, but strong in will
To strive, to seek, to find, and not to yield.

-Ulysses by-
-Alfred, Lord Tennyson-

Declaration

This thesis is an account of research undertaken between October 2013 and December 2017 at the Centre for Gravitational Physics, Department of Quantum Science, in the Research School of Physics and Engineering at the Australian National University, Canberra, Australia.

Except where acknowledged in the customary manner, the material presented in this thesis is, to the best of my knowledge, original and has not be submitted in whole or part for a degree in any university.

Shasidran Raj
August 2019

Acknowledgements

This research was conducted by the Australian Research Council Centre of Excellence for Gravitational Wave Discovery (OzGrav) through project number CE170100004. The research was also supported under a student scholarship from the Space Environment Research Centre (SERC).

Working on this PhD has been one of the most difficult and fulfilling challenges of my life. I could not have achieved completing it without the support from my family, friends and colleagues.

I first want to thank all my PhD supervisors, Daniel, Rob, Sam and David for your guidance and patience.

I will forever be grateful to Daniel for taking the chance on me and allowing me to pursue my PhD. Thank you for your guidance, support and for always being patient with me.

Rob, I will always appreciate giving me your time and how you always let me figure the problems out for myself even though you knew the solution as soon as I walked in the door.

David, CGP and DQS would not be what it is if not for you. Thank you for creating a supporting, friendly and enjoyable work environment.

Sam, I will always treasure our friendship and thank you for always keeping me positive. The last 6 months of my PhD at ANU was the most fun I had when we get to go to the lab every day and solve all the problems with my experiment. I will always be grateful for the time you have taken to help me get over the finish line and the taking the time to read my thesis even when you were busy and after you moved to JPL. And I do miss our PARSA adventures.

I also want to thank all the other Graviteers at the Centre of Gravitational Physics during my PhD. Canberra was never dull with you guys. I especially want to thank Tarquin for always inviting me to your house for Christmas. Being far away from home during the festive period, it meant a lot to me to join your family and friends. And thank you for reading my thesis and giving me feedback when it was at it's worse. Thanh, I miss our hot chocolate chats. Thank you for always being honest with me and telling me what I needed to hear, not what I want to hear. I am glad I have a friend like you in my life. Georgia, I miss all out random adventures and thank you for always making me feel better when I am down. I also want thank Chatters, Paul, Lyle, James, Perry, Terry, Roland, Jarrod, David, Min Jet, Nutsinee, Silvie, Cathy, Danielle and the atom optics football group. I am sure I have missed people out and I am sorry for that. I also want to thank Laura for always helping me out with all the admin work and for buying me flapjacks every time you travelled from the UK.

I want to thank my friends in Ireland, Niamh, Pardis, MJ, Apoorva, Stuart, Donal, Marta and Daniele. Thank you for keeping me positive through my thesis writing stage. You guys make Ireland fun!!! Thank you to my CHIC office work friends Sam, Gourav and Enayet for your advice and support on my PhD. I also want to thank Manisha for encouraging me to pursue a PhD at ANU.

I would not be in a position to study a PhD without the love and support of my family. Mom, thank you for all the sacrifices you have made to give us a better life. I could not have asked for two better siblings. Both of you put your lives on hold to support me and paid for my university education. No words can ever describe the appreciations I have for what you both have done for me. Finally to my dad, I hope you are enjoying all your children's accomplishments with a bottle of beer in one hand. Cheers!!!!!

Abstract

The ever-increasing congestion in Earth's orbital space is a worrying environmental condition. The global community is reliant on various vital services provided by satellites orbiting the Earth. However, sharing these same orbits are pieces of space debris, including human-made objects, taking up valuable orbital space. As the congestion in Earth's orbit increases, there is a higher probability of a collision occurring between the various orbiting objects. Each collision generates more space debris and contributes to a potential cascade chain reaction where eventually Earth's orbit will be filled with space debris and satellites will no longer be safely launched into orbit. There are several proposed space debris removal methods in the literature, investigated with the aim of reducing the debris population. One promising method is using photon pressure from a ground-based continuous wave laser to gradually alter the orbit of a small piece of space debris.

This thesis investigates the development of a ranging method using the same continuous wave laser source used to manoeuvre the space debris. This approach would allow the continuous wave laser method to simultaneously manoeuvre and measure the change in position of the piece of space debris. The experiments presented in this thesis amplitude modulated a continuous wave laser with a pseudo-random noise (PRN) code and used a matched filter analysis approach to measure the position and change in position of a target.

The motion of the space debris causes a Doppler shift of the amplitude modulated code. The matched filter analysis generates a template PRN code where the properties of the template code can be altered to model the Doppler effect caused by a moving target space debris. The correlation between the template and amplitude modulated code indicates how similar the two codes are to each other. The parameter values of the altered template code with the highest correlation is an estimate of the time-varying delay of the reflected optical signal due to the space debris' motion.

The thesis investigated two detection schemes for potential space debris application. The first detection scheme is called the direct detection scheme where the optical intensity of the signal beam is directly measured. The experimental results showed that by taking advantage of the PRN code properties to integrate the signal for a more extended period, both signal detection and precision in estimating the time-varying delay was improved for low signal-to-noise ratio optical signals. The second detection method investigated in this thesis is called the coherent detection scheme. In this detection scheme, the optical signal, with the amplitude modulated PRN code, is interfered with a second brighter optical beam called a local oscillator. The interference aims to amplify the modulated signal and improve the signal-to-noise ratio of the optical signal for the matched filter analysis.

The proposed laser ranging and analysis methods models using a 1.8 m telescope aperture with a 10 kW transmitting laser power. The aim of the analysis is to estimate the time-varying delay of a piece of space debris between 1 cm and 10 cm in size to within 1 mm/s. The estimated time-varying delay can be used for orbit prediction to determine potential collisions and the effect of the manoeuvring effort. Assuming the received signal power from a piece of space debris is equal to 3.5 fW, to achieve 1 mm/s precision the integration time needed for the direct detection scheme is 83 hours while for the coherent detection scheme is 250 s.

The coherent detection scheme would be able to achieve the desired measurement precision within a flyover of the target debris. In addition, current space debris pulsed-laser ranging methods may not be able to operate during daylight hours due to the low signal-to-noise ratio of the reflected optical signal. For the coherent detection scheme, the optical signal can be amplified above the additive noise sources and potentially allow daylight operations. The bench-top experimental results in this thesis clearly showed the coherent detection scheme is superior to the direct detection scheme and potentially could overcome some of the challenges faced by current laser ranging methods for space debris ranging and maneuvering application.

Contents

List of Abbreviations

ADC	Analogue to Digital Converter
AM	Amplitude Modulation
AO	Adaptive Optics
APD	Avalanche Photo-Diode
BPN	Background Photon Noise
EOM	Electro-Optic Modulator
EOS	Electro Optic Systems
FFT	Fast Fourier Transform
FIFO	First In First Out
FMZ	Fibre Mach-Zehnder
FOV	Field of View
FPGA	Field Programmable Gate Array
FS	Fibre Stretcher
FWHM	Full Width Half Maximum
GEO	Geostationary Earth Orbit
GMT	Giant Magellan Telescope
HEO	Highly Elliptical Orbit
HPF	High Pass Filter
LEO	Low Earth Orbit
LIDAR	LIght Detection And Ranging
LO	Local Oscillator
LPF	Low Pass Filter
MEO	Medium Earth Orbit
MF	Matched Filter
ND	Neutral Density
NEP	Noise Equivalent Power
OD	Optical Density
PD	Photodetector
PRBS	Pseudo-Random Bit Stream
PRN	Pseudo-Random Noise
PSD	Power Spectral Density
RMS	Root Mean Square
SERC	Space Environmental Research Centre
SDLR	Space Debris Laser Ranging
SLR	Satellite Laser Ranging

SN	Shot Noise
TIRA	Tracking and Imaging Radar

List of Figures

List of Tables

Introduction

On the 4^{th} of October 1957 the Soviet Union launched Sputnik 1, the first human-made satellite to enter orbit around the Earth. Today there are approximately 1300 operational spacecraft orbiting our planet [1]. These satellites are used to provide many essential services back on Earth, including satellite communication, Global National Satellite System (GNSS), weather forecasting and disaster alerts. Scientific spacecraft, such as the Hubble telescope, have also been launched into Earth's orbit to study various celestial bodies and to peer back at the mysteries of the universe.

In order to satisfy the global community's desire for the various satellite services, the number of spacecraft in Earth's orbit has steadily increased. Earth's orbital space also contains orbiting space debris such as meteorites and human-made objects that no longer serve a useful purpose [2]. As the congestion in the limited available space in Earth's orbit increases, there is a higher likelihood of a collision between the different orbiting objects. Each collision increases both the number of space debris and the congestion in Earth's orbital space, further increasing the likelihood of future collisions [3]. The unwanted space debris in Earth's orbit must be removed to make room for active satellites.

1.1 Earth Orbital Space Debris

The most significant number of unwanted space debris in Earth's orbit are human-made. Human-made space debris size varies from large defunct satellites at the end of their mission's lives to small pieces of debris due to fragmentation, explosions or material ageing of the spacecraft. These orbital space debris share the same orbits as active satellites, taking up valuable space. The four main Earth orbital boundaries shared by both active satellites and space debris are shown in Figure 1.1. These orbits are:

1. Low Earth Orbit (LEO): 160 km to 2000 km above the Earth's surface.
2. Medium Earth Orbit (MEO): 2000 km to 35 786 km above the Earth's surface.
3. Geostationary Earth Orbit (GEO): beyond 35 786 km above the Earth's surface.
4. Highly Elliptical Orbit (HEO): orbit has low altitude perigee but high altitude apogee allowing for longer coverage by the spacecraft over the desired location.

Figure 1.2 shows the severity of the congestion of satellites and space debris in Earth's orbital space. Figure 1.2b also shows the formation of a ring of orbiting objects congested in the most valuable satellite positions for GEO.

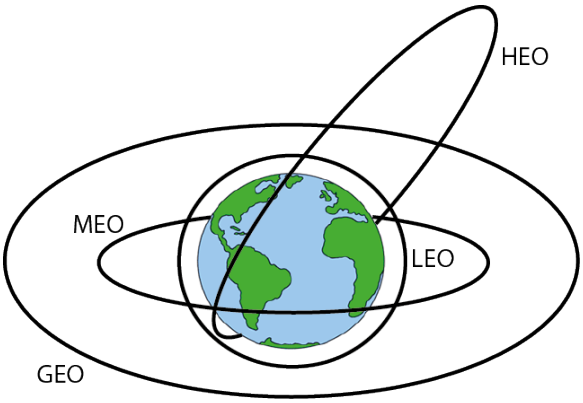

Figure 1.1: The four main orbit altitudes around the Earth used by active satellites.

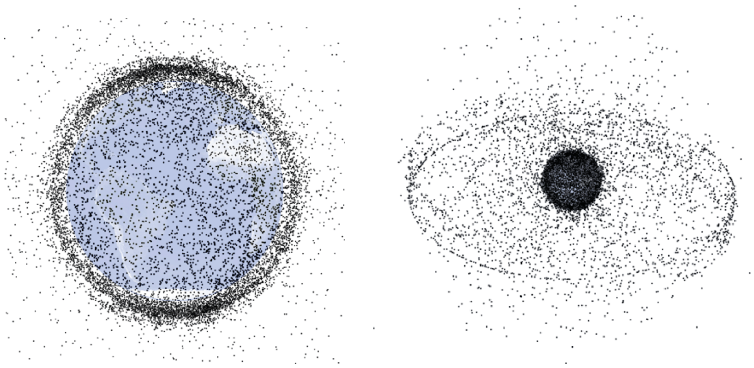

(a) Human-made objects occupying Low Earth Orbit.

(b) Human-made objects circling the Earth in the different orbits.

Figure 1.2: Each black dot in both images shows either a functioning satellite, an inactive satellite, or a piece of space debris orbiting the Earth. The diagram was retrieved from [4].

Figure 1.3 shows that the number of active spacecraft has been steadily increasing since the 1960's due to the increase in demand for satellite services. Figure 1.3 also shows an increase in the number of orbiting fragmentation debris, with two noticeable sudden jumps. The first spike in 2007 was caused by a Chinese anti-satellite missile test and the second spike in 2009 was an accidental collision between an active Iridium satellite and a defunct Cosmos satellite [5].

Collisions between orbiting objects would be catastrophic due to the high orbital velocities involved. Satellites can travel as fast as 7 km/s in LEO and space debris, depending on its mass and altitude, can circle the Earth with velocities as high as 15 km/s in LEO [7]. Metals struck by projectiles travelling at these velocities tend to behave like liquids [8], leaving a crater with a depth typically two to five times the diameter of the projectile [7]. Space debris as small as 1 cm in diameter can significantly damage active satellites.

The debris clouds generated by collisions similar to Iridium-Cosmos incident are of great concern for satellites operators and space agencies [4]. As more satellites enter the already congested orbits, there is a higher likelihood of similar collisions occurring in the future, with each collision producing similar spikes to those seen in Figure 1.3. For example, the Iridium-Cosmos incident created more than 1800 pieces of debris larger than 10 cm [9]. The resulting debris cloud covers a large area, increasing the probability of these pieces of debris colliding with other orbital objects. Future subsequent collisions could contribute to the rapid increase in the number of fragmented debris in orbit [3].

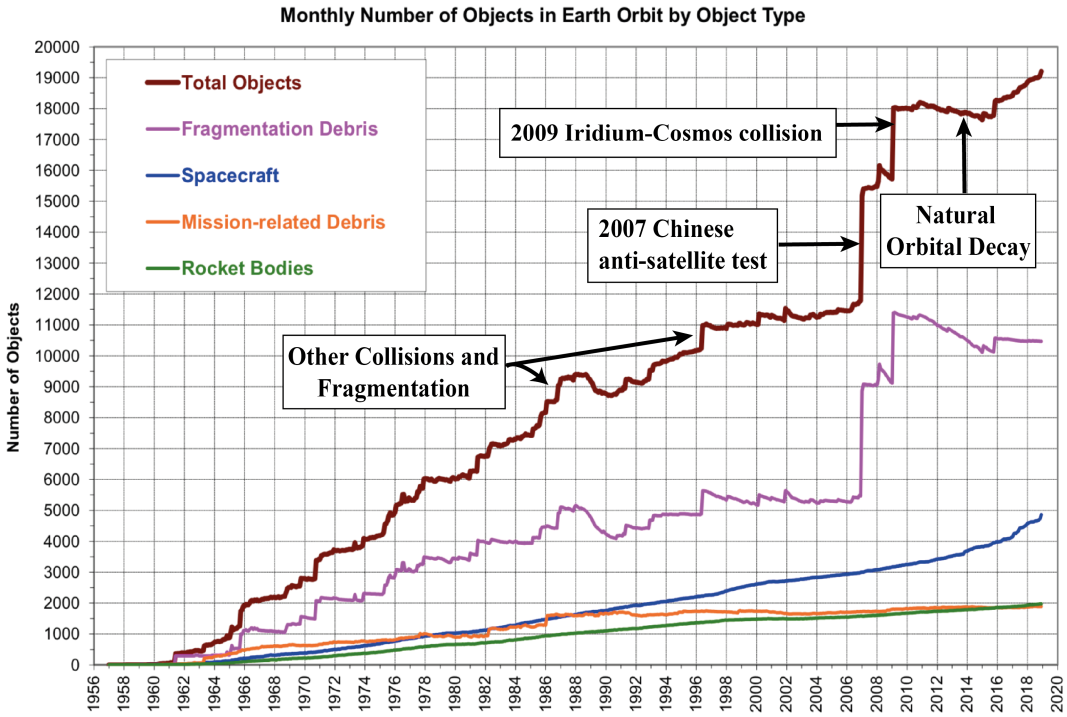

Figure 1.3: Population of objects in Earth orbit categorised by object type officially catalogued by the U.S. Space Surveillance Network. Data was retrieved from [6].

Active satellites can perform a collision avoidance manoeuvre if the piece of space debris is catalogued and precisely tracked. The Iridium-Cosmos incident suggests the current tracking system are not precise enough. Even though avoiding collisions between active satellites and space debris can reduce the rate of debris growth; currently, there is no solution to prevent space debris-on-space debris collisions. The number of debris generated from space debris-on-space debris collisions will exceed the reduction from the natural orbital decay [10, 11] leading to the formation of a debris belt [3].

LEO is the most congested orbit for both the number of active satellites and space debris. Most satellite operators prefer LEO to other orbits as it is much cheaper to reach. However, to provide complete global coverage, the satellite operator approximately needs between 25 to 40 satellites in orbit simultaneously [12]. The high number of orbiting objects in LEO increases the likelihood of collisions in this region, resulting in an unstable environment [13] with the predicted collision rate between catalogued debris in 2009 occurring at once every five years [9]. Without taking further actions to mitigate the growth of space debris, this rate is expected to increase.

Between June 2009 and May 2019, the number of orbital space debris has increased from 11,429 [14] to 14,432 [6] objects due to several fragmentation events. In 2019, the European Space Agency (ESA) has stated 11.6 non-deliberate fragmentation events are occurring every year, of which 2.4 are considered important contributing events [15]. Therefore LEO debris removal is the main focus of many debris removal techniques [16, 17].

1.2 Space Debris Removal

Many different debris removal concepts are being investigated to reduce the congestion in Earth's orbital space. Most of these studies involve using a spacecraft to rendezvous and

capture the space debris to either de-orbit or move the debris out of the most congested regions [18–21]. These methods are practical solutions to removing large debris objects such as defunct satellites and rocket bodies. However, over 80% of all catalogued objects in LEO are small pieces of debris, resulting from explosions or collisions [22]. These methods would be impractical to continually capture and remove space debris smaller than 10 cm [15] to a safer orbit. To accomplish this task, the entire process would be complex [11] and would require several spacecraft in operation simultaneously. Also, access to all the spacecraft for maintenance and upgrade is not feasible after launch into Earth's orbit.

One proposed collision avoidance method that would be more practical in de-orbiting smaller pieces of space debris is using ground-based high powered lasers. Using momentum transfer from the laser photons has been considered as alternative propulsion or to apply orbital changes of a spacecraft [23, 24]. Figure 1.4 illustrates the proposed debris manoeuvring concept [25]. The ground-based laser is used to apply photon pressure to alter a piece of debris' orbit to avoid collision with other orbiting objects and eventually move the debris out of the congested regions. High-intensity pulsed lasers have been considered to ablate the surface of the debris [26]. However, a high-intensity pulsed laser can be expensive, and the surface ablation could result in the object assuming a complicated orbit [27]. Instead, using constant momentum transfer from a continuous wave laser to change the debris orbit gradually is a better alternative for space debris manoeuvring application [11].

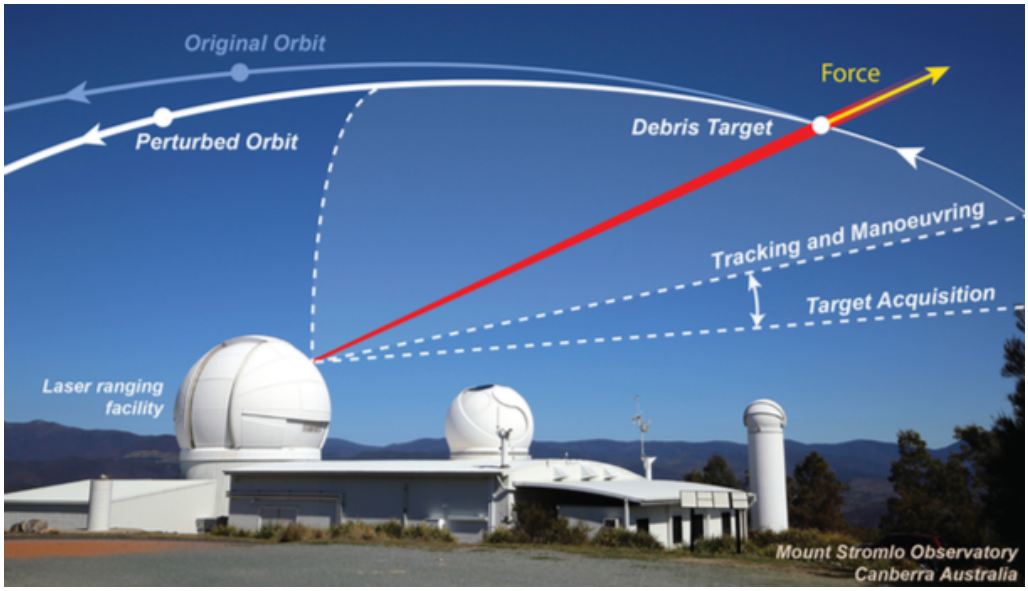

Figure 1.4: Remote orbital debris manoeuvring concept at the EOS Mount Stromlo facility. Image was photographed and designed by Lyle Roberts and presented in [25].

The Space Environmental Research Centre (SERC) aims to use the 1.8 m telescope at Mount Stromlo facility, shown in Figure 1.4, to demonstrate manoeuvring small space debris in LEO with a 10 kW continuous-wave laser [28]. The SERC facility routinely performs laser ranging of LEO debris [29] and a second 1.0 m telescope is used to track active satellites. A ground-based laser has several advantages compared to using multiple spacecraft in-orbit to remove space debris, such as more straightforward operation, access for maintenance, ease of upgrade [11] and can share infrastructure with current satellite [30–32] and space debris laser ranging ground stations. Potentially, a ground-based laser system could operate for a longer period than the mission life of an in-orbit spacecraft. Larger space debris objects such as defunct satellites are too heavy to be effectively perturbed using photon pressure from the proposed ground-based laser. However, as the technology matures, these larger pieces of debris may also be manoeuvred in the future.

1.3 Thesis Goals

SERC plans on demonstrating using a ground-based continuous wave laser as a viable solution to alter the orbits of small pieces of debris, for both collision avoidance and to reduce the debris population in LEO. To achieve this goal, several key challenges must be resolved when determining the position of the debris for the manoeuvring application:

1. Using a continuous wave laser to measure the position of the space debris
2. Improving the measurement precision of the space debris' change in position to better predict the space debris' orbit in relation to other orbiting objects
3. Reducing the impact of background photon and photodetector noise.

Most laser ranging facilities, including the Mount Stromlo telescopes, use a pulsed laser instead of a continuous wave laser to measure the range of both satellites and space debris. Without changing this approach, two different laser sources must be used to measure the range and manoeuvre the debris by either switching between sources or using two telescopes simultaneously. This thesis explores an alternative to measure both the position of space debris and apply radiation pressure using the same telescope with a continuous wave laser.

Precisely measuring the change in position of the space debris provides vital orbital information of the space debris for two purposes. The first reason is to provide a more accurate prediction of the space debris' orbit, as well as its interaction with other orbiting objects. Satellite operators can use this information to anticipate and react to potential collisions more effectively, and prevent collisions such as the Iridium-Cosmos collision in 2009. The second reason is to determine the effect of the photon pressure on altering the space debris' orbit and to predict the new future position of the space debris with other orbiting objects. SERC aims to measure the space debris' velocity to within 1 mm/s. This thesis introduces an experimental design to achieve the desired 1 mm/s velocity measurement precision.

The performance of an optical space debris ranging system depends on the signal-to-noise ratio of the acquired optical signal. Compared to an active satellite, space debris is considered a non-cooperative target with a higher scattering of the reflected optical signal resulting in a lower signal-to-noise ratio. Most space debris laser ranging, including the EOS telescope, is limited to short periods during dusk and dawn [33]. During the day, the higher background noise in the signal measurement makes signal detection more challenging. Night time operation is also challenging as it is more difficult to locate the space debris without solar illumination. Operating within the small period during dusk and dawn is a compromise between having sufficient lighting for the acquisition of the space debris and lower background noise to allow signal detection to measure the range of the space debris. This thesis explores two different detection methods to improve the signal-to-noise ratio and allow space debris ranging operations during the day.

1.4 Thesis Outline

Section 1.3 presented the three main goals investigated in this thesis. The first is developing a space debris laser ranging system to measure the position of the space debris using a continuous wave laser. The continuous wave laser is amplitude modulated using a pseudo-random noise (PRN) code to time-tag the outgoing laser light. Figure 1.5 illustrates the proposed ranging concept. The PRN code is used to measure the propagation delay τ of

the laser light. The propagation delay is used to measure the range of the target space debris. PRN codes have been used in radar ranging applications and as modulation on a continuous wave laser to determine propagation delays [34–37], including ranging to a satellite [38]. PRN codes have also been used to provide accurate pico-level measurements using lasers [39] for different applications.

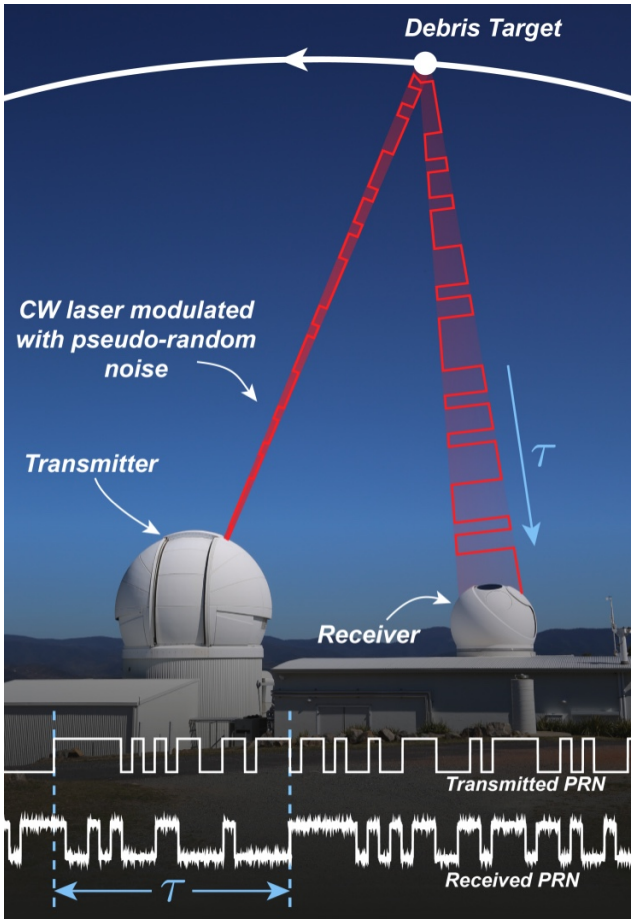

Figure 1.5: A continuous wave laser modulated with pseudo-random noise codes to measure the range between the telescope and space debris target. Image was photographed and designed by Lyle Roberts and presented in [40].

The second goal is measuring the change in position of the space debris. The space debris target has a time-varying delay and causes a Doppler shift of the PRN code modulated onto the continuous wave laser. A matched filter analysis approach, with parameter estimation, is used to measure the change in the PRN code properties due to the time-varying delay. The measurements are used to estimate the target debris' position and change in position due to its higher-order derivatives of motion. The matched filter parameter estimation approach is chosen since the parameters of the Doppler shifted PRN code is not known. The parameters are used to generate an altered version of the modulated code, called the template code, and correlated with the Doppler shifted code. The parameter values used to generate the template code with the most significant correlation with the Doppler shifted code provides the best estimate of the position and change in position of the space debris. Parameter estimation analysis is used in different applications including range measurement [41], optical communication links [42] and in determining the properties of the celestial bodies that generated gravitational waves [43].

The third goal is reducing the impact of background photon and photodetector noise. This

goal is achieved by investigating two different detection designs. The first detection method is called the direct detection scheme where the intensity of the reflected laser is directly measured by a photodetector, similar to current pulsed-laser ranging methods. The second detection scheme is called the coherent detection scheme where the reflected laser interferes with a second laser beam before signal detection by a photodetector. This approach is used to amplify the reflected laser signal above both photodetector and background photon noise sources, improving the signal-to-noise ratio and hence both the debris' change in position measurement precision.

Figure 1.6 shows the structural layout of the thesis.

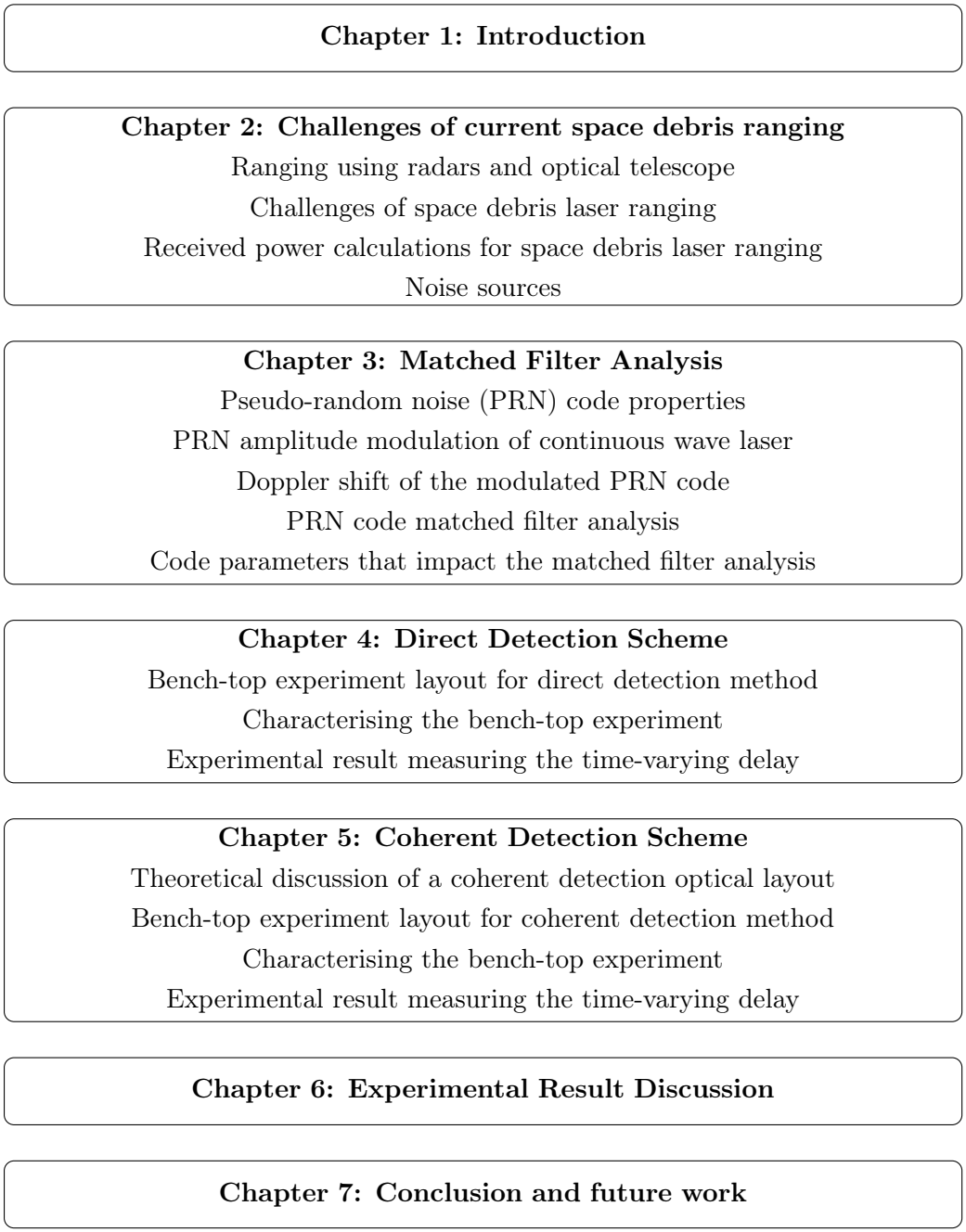

Figure 1.6: Thesis structure

Chapter 2 presents current space debris ranging using radars and an optical illuminating source. The chapter aims to show that the primary challenge of space debris ranging with

an optical source is the low signal-to-noise ratio of the optical signal, which limits the ranging precision. The chapter presents the different aspects of space debris ranging that affect the optical signal power reflected by the space debris and collected by an optical telescope. The chapter also presents the different noise sources present in the optical signal. Chapter 2 also discusses that the reflecting surface of a piece of space debris is a diffuse surface. A diffuse surface causes the reflected light to scatter in many random directions and could also add varying propagation path length to the different parts of the reflected beam. The result is reduced signal power of the optical signal and the electric field of each beam collected by the telescope may have a varying phase. Depending on the signal-to-noise ratio of the measured optical signal, most coherent detection method used for propagation delay measurement using phase modulation may not be applicable.

Chapter 3 presents the properties of m-sequence PRN codes used to amplitude modulate the continuous wave laser. The modulated optical signal is correlated with a local copy of the modulating code to measure the propagation delay of the light. The chapter also presents the time-varying delay aspects of space debris. The debris' high-velocity Doppler shifts the modulated PRN code and reduces the signal correlation output. The chapter discusses using a matched filter analysis with parameter estimation to measure the time-varying delay of the target from the Doppler shifted modulated PRN code. The matched filter analysis changes the template code properties to apply the same Doppler shift effects. The altered template code properties are used to determine the time-varying delay of the space debris. The chapter also presents the effect of both code properties and noise on the signal correlation.

Chapter 4 presents the optical bench-top experiment for the direct detection scheme. The chapter discusses how the experiment generates a Doppler shifted PRN code modelling reflection from a moving space debris target. The chapter discussed the amplitude modulation of the signal continuous wave laser, signal acquisition and matched filter analysis steps taken to measure the time-varying delay applied in the bench-top experiment. The chapter also discusses the experimental results for the direct detection scheme. The results demonstrate how the matched filter analysis can be used to measure the time-varying delay. The chapter also investigates the impact of a background photon noise source on the time-varying delay measurements.

Chapter 5 investigates adapting the optical bench-top experiment discussed in Chapter 4 for the coherent detection scheme. The chapter explains interfering the amplitude modulated PRN code signal with the second optical beam to improve the signal detection above additive noise sources that impact the direct detection scheme. The chapter then presents the method of recovering the PRN code and using the same matched filter analysis discussed in Chapter 4 to measure the time-varying delay. The bench-top experiment also introduces frequency noise into the signal path and using a second free-running laser source as the local oscillator to introduce $\frac{1}{f}$ laser frequency noise. The experiment aims to present improved results on the matched filter analysis performance of the coherent detection scheme compared to the direct detection scheme and unaffected by the added frequency noise. The chapter also presents simulated results showing the random phase effect from a diffuse surface does not impact the coherent detection scheme.

Chapter 6 discusses and compares the experimental results from Chapter 4 and 5 for the space debris ranging application. The results are used to calculate the required received signal power and integration time needed to measure of 1 mm/s change in the velocity parameter for a space debris target.

Chapter 7 concludes the discussion in the thesis and also presents future experiments to be carried out beyond the scope of this thesis.

1.5 Chapter Summary

Space debris is a growing environmental threat. Space debris collisions with active satellites and other debris will generate further debris at a rate that exceeds the natural orbital decay resulting in Earth's orbital space being inaccessible. In the absence of large-scale debris removal, altering a debris' orbit using photon pressure from a ground-based continuous wave laser is one option currently being investigated to prevent collisions in Earth's orbit. Such a system would take advantage of current laser ranging facilities used to range to both space debris and satellites.

Moving to a continuous wave laser requires a different approach to ranging to space debris. This thesis proposes using a PRN code modulation to time-tag the outgoing laser light and measures the time-varying delay of the laser light with a matched filter analysis. This method provides a measure of the higher-order derivatives of motion and can potentially achieve a change in velocity measurement of 1 mm/s.

Current Space Debris Ranging

There are several different ranging methods currently used to determine the Earth orbital properties of a piece of space debris. The two most common methods are using ground-based radars and optical illumination [33]. Figure 2.1 illustrates the concept to measure the range of a defunct satellite orbiting around the Earth in a mono-static or bi-static arrangement using either a radar antenna or an optical telescope at the ground stations.

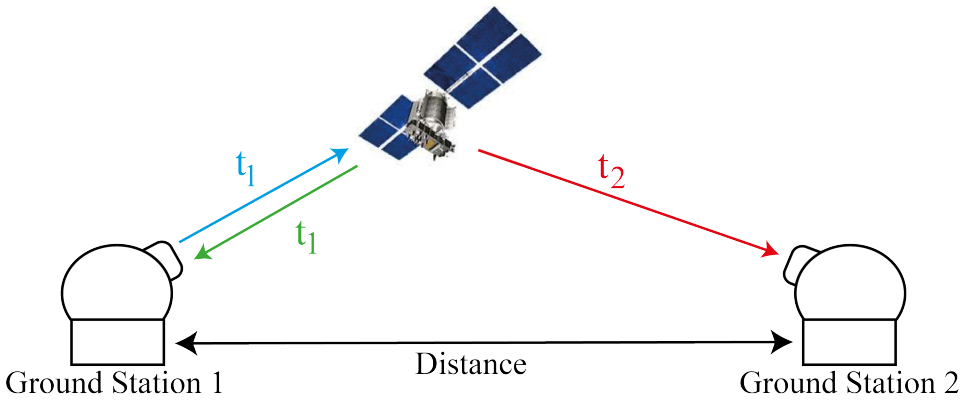

Figure 2.1: A space debris ranging concept where the ground station is used to represent either radar antennas or optical telescope. The range to the defunct satellite can be measured using a single ground station in a mono-static arrangement with a propagation delay of $2t_1$ or in a bi-static agreement using a second ground station with propagation delay $t_1 + t_2$.

Radar and optical ranging methods operate in a different wavelength of the electromagnetic spectrum. Radars use radio or microwaves which have a longer wavelength while optical illumination operates at a shorter wavelength than radars in the optical or near infra-red regions. Both methods have similar ranging concepts and are limited in their ranging capabilities by:

- Transmitted signal power.
- The cross-sectional area of the target.
- The effective collecting area of the telescope or antenna.
- Signal-to-noise ratio of the reflected signal and detection sensitivity.

2.1 Radar

RAdio Detection And Ranging (RADAR) was developed before and during the Second World War by several different nations as a means of detecting and providing early warnings of incoming enemy aircraft. Sir Robert Watson-Watt demonstrated the first successful practical radar system in 1935 [44]. Today, radars are used in many different range measurement applications outside the military [45].

Radars can be of a mono-static or bi-static arrangement, as illustrated in Figure 2.1. Radars use a radar dish or antenna to transmit pulses of radio waves or microwaves that then reflect off an object in their path. The reflected signals propagate in various directions. In a mono-static arrangement, a small amount of the reflected signal energy propagates back to the transmitting antenna. The distance between the radar dish and target is calculated by measuring the propagation delay $2t_1$ of the signal to and from the target. In a bi-static arrangement, a second antenna is used to collect the reflected signal energy. The measured propagation delay is $t_1 + t_2$. The distance between the two radar dishes must be known to calculate both t_1 and t_2. The measured propagation delay is used to calculate the position of the target. Multiple independent range measurements are obtained and together used to determine the change in the position of the target.

2.1.1 Space Debris Ranging using Radar

Radars were the earliest and are the most widely used method of detecting and ranging space debris in Earth's orbit [33]. Radars can provide all-weather, day and night operation [33, 46]. The longer wavelength of the radar signal has lower signal energy loss due to atmospheric scattering and absorption [47]. The Haystack Ultrawideband Satellite Imaging Radar (HUSIR) is capable of tracking space debris in the size range of 5 mm to 30 cm in LEO [48] and radars can identify and track a piece of space debris as small as 1 cm in GEO [49].

Most radar space debris ranging uses a mono-static arrangement since a bi-static arrangement can be more expensive and complex [50]. However, using multiple receiving dishes increases the active collecting area [51] of the reflected pulse and improves the measurement precision. For example, the FGAN Tracking and Imaging Radar (TIRA) uses a 34 m radar dish [52] to track and image space debris in a mono-static arrangement. In the mono-static configuration, the TIRA system is capable of detecting objects as small as 2 cm in size 1000 km away [53]. A second 100 m parabolic antenna located 21 km away is also used in a bi-static arrangement. In the bi-static configuration with both radar dishes used for data collection, the TIRA system can detect objects as small as 0.9 cm in size 1000 km away [53].

The field of view (FOV) of a radar system can vary. A wider FOV allows the radar system to cover a larger area simultaneously by spreading the energy of each pulse. This approach allows the radar system to identify and track new pieces of space debris, with several of these sensors used to create a detection net [49]. A narrower FOV provides improved ranging precision [54] by focusing more of the signal energy onto the target debris. However, the narrower FOV makes it more difficult for the radar system to locate a new space debris target.

The collected observation vectors are used to obtain the orbital parameters and the radar signature of the target. The radar signature can provide clues to the object's natural motion such as rotation and if the piece of space debris is tumbling [53]. Averaging the gathered information over several observed orbits improves the initial ranging precision [49].

2.2 Ranging using Optical Sources

LIght Detection And Ranging (LIDAR) is a method used to measure the distance of a target by illuminating with a pulse of light [55]. LIDAR systems were first used in meteorology applications to measure the motion of clouds [56] but have since been used for different applications including in autonomous cars [57]. LIDAR can provide several advantages compared to radar, such as high spatial resolution [58] and measure aerosols that radars cannot [59]. The outgoing laser used in a range finder application can be either a pulsed or a continuous wave laser modulated with a known signal [38, 60].

In some applications, the reflected optical signal coherently interferes with a second laser [61]. The result produces an interference pattern depending on the frequency and phase difference of the two laser beams. Since the transmitted laser and the second laser frequencies are both known, this method is used to measure the Doppler shift of the reflected laser beam due to the motion of the target [62]. A coherent LIDAR system is more sensitive to the Doppler shift caused by a moving target than a Doppler radar system due to the higher frequencies of the optical source [58, 63].

2.2.1 Current Space Debris Laser Ranging

There are currently two methods of obtaining the range of space debris using an optical telescope. One is called passive tracking where the Sun is the illuminating source and the second method is called active tracking where a light source such as a laser is projected onto the target [64]. This thesis focuses the discussion on the active tracking methods.

Figure 2.1 can be used to explain the space debris laser ranging (SDLR) concept for both a mono-static and bi-static arrangement. The ranging concept is very similar to the radar ranging concept, discussed in Section 2.1.1, and satellite laser ranging (SLR). Most SDLR and SLR systems use a pulse of energy from a laser source to illuminate the target. In the simplest form, the range of the target is determined by measuring the time of flight of the pulse from the transmission to the reception at the receiving optical telescope [65]. Further signal processing on the detected pulse can be performed to improve the accuracy of the measurement. This will be discussed more in Chapter 3. The pulse repetition rate of SLR systems is commonly around the kHz level [66, 67]. Sending multiple pulses at a higher pulse repetition rate for an entire tracking period, allows the change in the object's range to be more accurately measured and the orbital velocity of the object to be obtained. An SLR system with 100 kHz pulse repetition rate has also been successfully tested [68].

Modern pulsed laser ranging systems can achieve ranging precision of about 5 cm for space debris target with radar cross-sections between $2\,m^2$ and $12\,m^2$ [69]. The EOS Mount Stromlo facility uses a 100 W laser source and can track a piece of space debris as small as 10 cm in LEO [29] with an accuracy of 20 arc-seconds after averaging for 3 to 4 complete orbits [70].

Compared to using radars, optical sources have not been able to achieve the same level of performance in space debris ranging. This is because the SDLR system faces several challenges such as constraints on the optical telescope aperture, limited tracking periods at dusk and dawn and atmospheric effects. For example, both TIRA and HUSIR use a 34 m and 37 m antenna [48, 52] respectively for radar ranging of space debris while the EOS telescope is only 1.8 m. These challenges will be discussed further in Section 2.3.

2.3 Factors that Affect Received Optical Signal Power

The precision of the range measurements depends on the signal-to-noise ratio of the optical signal detected at the receiving telescope. The factors that affect the collected optical signal power are:

1. Divergence of the laser beam propagating the distance R to the target debris
2. The cross-sectional area of the space debris A_{SD}
3. Diffuse surface of the space debris
4. Telescope aperture used to calculate the area of the telescope A_T
5. Signal loss due to atmospheric effects

As discussed in Section 2.2 and presented in Figure 2.1, ranging using optical sources can be performed using either a mono-static or bi-static arrangement. There are several potential advantages of using a bi-static arrangement in an SDLR application such as improved target detection due to the geometric layout of the two telescopes [71]. Also, if both telescopes are used as a receiving telescope to gather the reflected light, a more precise range measurement of the target can be obtained. However, the EOS telescope, used as a model for the telescope design in this thesis, has a mono-static arrangement and is used as the focus of the discussions in this section.

2.3.1 Laser Beam Divergence

A laser is a coherent light source where the emitted beam is represented as a Gaussian function [72] and propagates a considerable distance without much beam divergence [73]. The low beam divergence allows more of the signal laser to be focused on the target, improving the signal-to-noise ratio. However, in a space debris application, there is signal loss due to beam divergence as the signal propagates the large distances R to the target.

Figure 2.2 illustrates a laser beam focused by a lens to a beam waist ω_0. The beam waist is the location along the propagation direction where the beam radius ω is minimum [74]. As the beam propagates over large distances, the beam starts to diverge, and the width of the beam expands, with a beam divergence angle of θ.

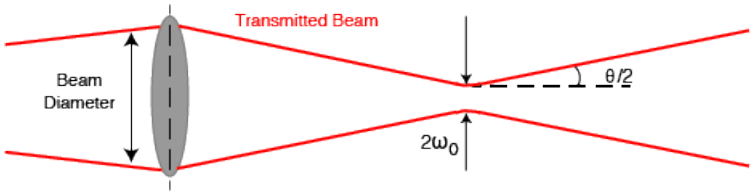

Figure 2.2: Gaussian laser beam with a beam divergence θ and a beam waist ω_0. The beam reflected by the mirror also diverges along the propagation path.

The diffraction-limited divergence angle θ can be calculated using Equation 2.1 where λ is the laser wavelength. Equation 2.1 shows that a laser beam with a broad beam waist ω_0 produces a smaller beam divergence angle θ. For laser ranging applications, the beam waist is at the output of the transmitting telescope and the beam waist is approximately equal to the radius r of the telescope aperture ($\omega_0 = r$). Therefore a large aperture size of the telescope is essential to form a laser beam with a broad beam waist ω_0.

$$\begin{aligned}\theta &= \frac{\lambda}{\pi\omega_0} \\ &= \frac{\lambda}{\pi r}\end{aligned} \tag{2.1}$$

As the laser beam propagates the distance R to the space debris position, the beam diverges. The increased diameter of the beam reduces the overlap between the beam area and the cross-sectional area of the space debris, reducing the reflected optical signal power. A large aperture telescope can output a broader beam waist and minimise the beam divergence. By using a larger telescope to produce a transmitted signal laser beam with a smaller beam divergence, more of the signal laser is reflected by the target debris resulting in an improved signal-to-noise ratio of the acquired signal.

2.3.2 Size of the Space Debris

The amount of laser light reflected by the space debris depends on the overlap between the space debris cross-sectional area A_{SD} and the area of the beam at the debris' position. The larger the overlap between the space debris cross-sectional area and the beam, the more optical signal power is reflected by the target debris, increasing the signal-to-noise ratio of the optical signal collected at the receiving telescope.

Pieces of space debris come in different shapes and sizes. For simplicity, most debris targets are treated as a circular object and categorised based on the diameter of the debris as shown in Table 2.1. The cross-sectional area A_{SD} is calculated from the categorised diameter of the piece of space debris. This categorisation of the space debris is also used to identify the ease of tracking the piece of space debris as well as how dangerous the debris would be to an active spacecraft.

Category	Object Diameter (cm)	Ease of Tracking	Potential Damage
1	>10	High	Catastrophic
2	10 to 1	Low precision	Sig. Damage
3	<1	Extremely Low	Moderate

Table 2.1: Categorising space debris based on diameter of the debris [75].

Category 1 contains large debris such as old defunct satellites and rocket bodies. If a piece of Category 1 debris were to collide with a satellite, the impact would destroy the spacecraft like the Iridium-Cosmos collision. However, this debris is large enough for current range measurement systems to identify and track with sufficient precision to produce a more detailed prediction of the debris' orbit. This information can then be used by satellite operators to determine the likelihood of collision with an active satellite and take precautionary steps if required.

Category 2 space debris are between 1 and 10 cm in diameter. Though most debris removal research focuses on the re-entering Category 1 space debris, Category 2 space debris are of most concern for satellite operators [76]. The size of the debris is still large enough to cause significant damage upon impact but the precision of the range measurement is low making orbit prediction and collision avoidance more challenging.

Category 3 space debris cannot be tracked easily due to the small size. The signal-to-noise ratio of the optical signal reflected by the space debris is inadequate to predict its orbits accurately. Most modern spacecraft have sufficient shielding [77] to protect vital spacecraft systems from an impact with a Category 3 debris. The disadvantage of using such shielding is the increase in weight and size of the satellites, making it more difficult to fit in launch vehicles and more expensive to launch the spacecraft. Also, Category 3 space debris can damage externally mounted equipment and unshielded portions of the spacecraft, leading mission degradation or reduced mission life [75].

A piece of space debris with the larger cross-sectional area has a higher overlap with the area of the laser beam at the debris' position resulting in more reflected optical signal power and improved ranging precision. The focus of this thesis will be on Category 2 space debris.

2.3.3 Diffuse Reflecting Surface of Space Debris

The discussion so far has treated space debris as an ideal reflecting surface. In reality, a piece of space debris would have a rough and complicated surface resulting in a diffuse reflection. The effect of a diffuse surface is illustrated in Figure 2.3 where the incident optical signal is scattered randomly in many different directions [78]. The scattered light from each individual scattering centre interferes with each other to produce a speckle pattern [78]. In some applications, these speckle patterns are used to characterise the reflecting surface [79]. However, this discussion is beyond the scope of this thesis and is not considered for a space debris application in this thesis.

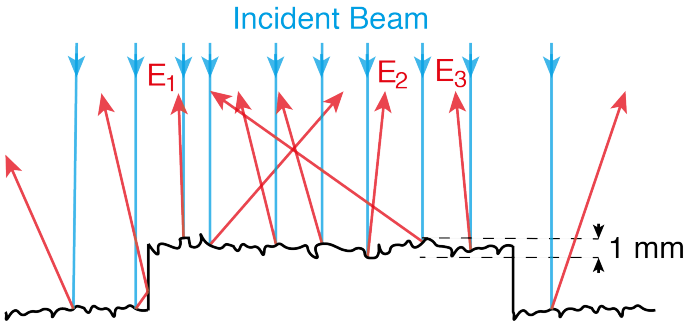

Figure 2.3: Illustration of the scattering effect of the incident optical signal of a diffuse surface. The blue lines represent the incident optical beam. The red lines represent the scattered reflected beam. E_1, E_2 and E_3 are the electric fields of three optical beams reflected back to the telescope.

Using Figure 2.3, a diffuse reflecting surface has two effects on the reflected optical signal:

1. Scattering the optical signal in many directions
2. Adds random phase to the reflected signal

As seen in Figure 2.3 the incident beam is reflected in various different directions. A smaller amount of the optical signal is reflected parallel to the incident beam. In a space debris ranging application, the reflected optical signal from a diffuse reflecting surface would have reduced signal-to-noise ratio.

The second effect of a diffuse surface is that each scattered signal has a different path length. Each k^{th} reflected signal can be represented as an electric field $E_k(t)$, as shown

in Equation 2.2, where A_k is the amplitude, f frequency and ϕ_k is the phase. The phase of the electric field ϕ_k depends on the propagating distance L_{Sig} of the optical signal ($\phi_k = \frac{2\pi f}{c} L_{Sig}$) [80].

$$E_k(t) = A_k e^{i(2\pi f t + \phi_k)} \tag{2.2}$$

Using Figure 2.3, the propagating distance L_{Sig} of each reflected optical signal is slightly different. For example E_2 has a propagating distance larger than 1 mm compared to E_1. Therefore each k^{th} electric field of the reflected optical signal has a different phase ϕ_k. The randomness of the phase of the optical signal reflected by the diffuse surface can be represented by a Gaussian distribution [78, 81].

Figure 2.4 is used to illustrate the impact of the diffuse surface on the magnitude of individual electric fields using Equation 2.2. For simplicity to show the statistics of the diffuse surface effects on the reflected electric field, A_k is generated using a Gaussian distribution where the mean is equal to 1 and standard deviation is equal to 0.2 while ϕ_k is also generated using a Gaussian distribution where the mean is equal to 0 and standard deviation is equal to 2π. The simulation is repeated for a million times to produce the histogram. The simulated result shows the magnitude of the electric fields varies following a Gaussian distribution with the mean equal to 1 and the standard deviation equal to 0.2.

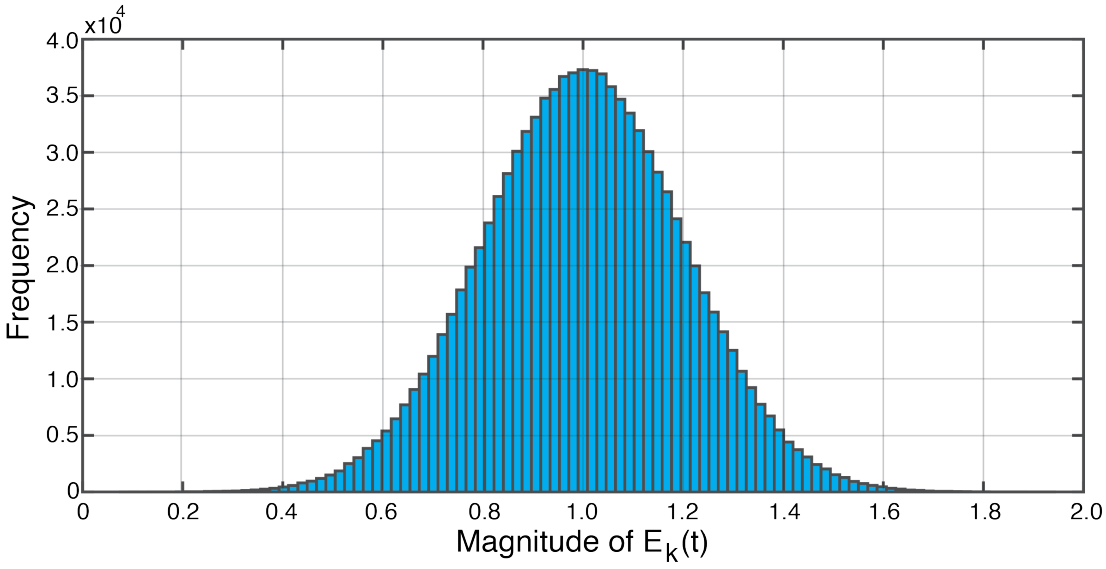

Figure 2.4: Histogram showing the Gaussian distribution of the electric field magnitude reflected from a diffuse target.

The electric field $E_{Sig}(t)$ of the optical signal collected at the receiving telescope is the complex sum of the different electric fields as shown in Equation 2.3 [79]. Equation 2.3 shows the amplitude of the electric field $E_{Sig}(t)$ depends on the amplitude of the different scattered signals collected by the telescope.

$$\begin{aligned} E_{Sig}(t) &= E_1(t) + E_2(t) + E_3(t) + ... E_N(t) \\ &= \sum_{k=1}^{N} A_k e^{i(2\pi f t + \phi_k)} \end{aligned} \tag{2.3}$$

Figure 2.5 illustrates the resultant electric field $E_{Sig}(t)$ after adding the different electric

fields from a diffuse target. Since the propagating path length of each electric field is different, the electric fields are not in phase. This causes the phase of the summed electric field $E_{Sig}(t)$ to behave in a random manner. The result is the amplitude of $E_{Sig}(t)$ is reduced.

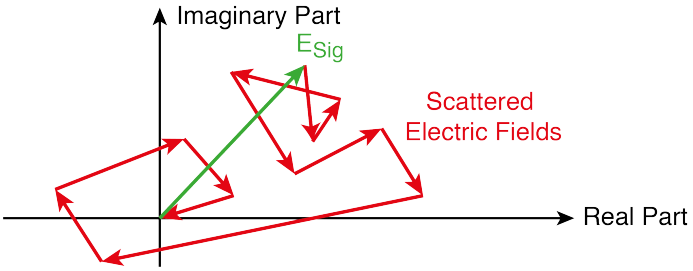

Figure 2.5: Impact of summing the scattered electric field from the diffuse surface. The scattered electric fields causes the phasor to behave in a random manner and reduce the amplitude.

Figure 2.6 illustrates a histogram to represent the summed electric fields using Equation 2.3. In the simulation, N is equal to 100 and the simulation is repeated a million times to identify the statistics. The histogram shows the magnitude of the summed electric fields $E_{Sig}(t)$ follows a Rayleigh distribution with the mean equal to 10. The result shows a change in the statistic of the magnitude of the summed electric field $E_{Sig}(t)$ from the individual reflected electric fields $E_k(t)$ due to the diffuse surface. In the case of an ideal reflecting surface, where the individual electric fields $E_k(t)$ are in phase with each other, the summed electric field $E_{Sig}(t)$ follows a Gaussian distribution with a mean equal to 100 ($N = 100$). The reduced mean of the summed electric field distribution in Figure 2.6 shows that the diffuse surface has reduced the overall magnitude of the electric field.

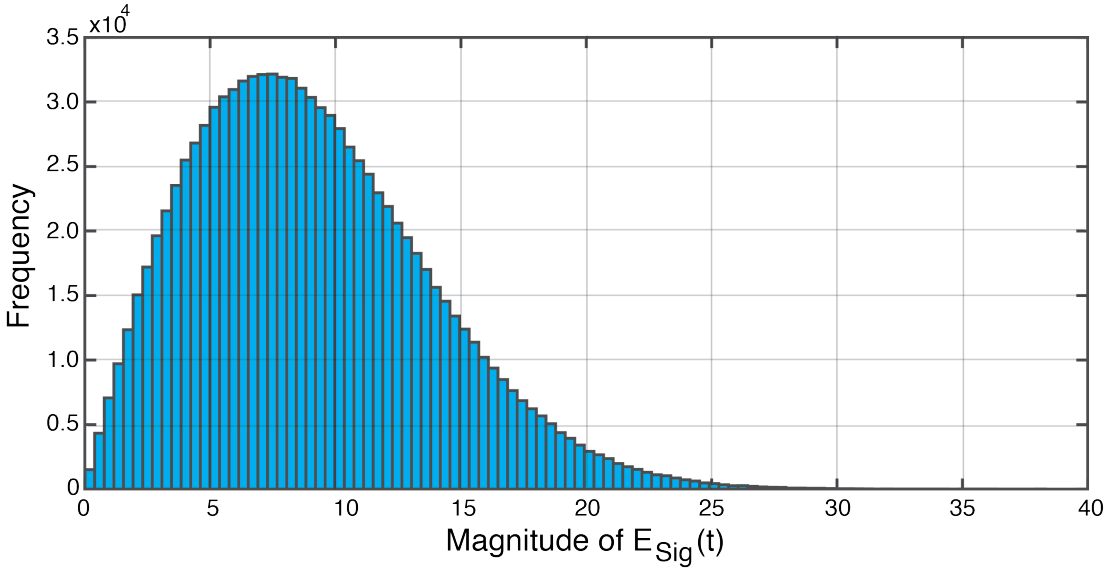

Figure 2.6: Histogram showing the Rayleigh distribution of the summed electric field magnitude reflected from a diffuse target.

For a direct detection method, such as the pulse laser ranging and the direct detection scheme discussed in Chapter 4, the phase of the laser is not measured. The small change in path length of the optical signal for a piece of space debris between 1 cm and 10 cm would not impact propagation delay measurement. However, the optical power of the received signal would be reduced due to the scattering effect of the diffuse surface.

A coherent detection method is sensitive to phase fluctuations of the optical signal [73]. In a coherent detection method, the optical signal beam interferes with a second beam at the receiving telescope. The result is an interference pattern called a beat note which depends on the frequency and phase difference, f_h and $\Delta\phi$ respectively, of the two interfering beams. Coherent detection methods are widely used to measure the velocity of a moving target [62] and by modulating the phase of the signal laser [25, 82] to measure the propagation distance of the signal beam. Statistically, as shown in Figure 2.6 for a diffuse surface, a beat note will always be present but the magnitude of the phasor sum is reduced. This also reduces the amplitude of the interference pattern. In a space debris application, the combination of a diffuse surface and a received signal with a low signal-to-noise ratio, a coherent detection and phase modulation method to measure the range may not be possible.

In summary, a space debris target with a diffuse reflection of the optical signal affects both the amplitude and phase of the reflected signal. The resulting signal loss affects both direct and coherent detection methods. Chapter 5 will discuss the approach for the coherent detection scheme to measure the propagation distance of the target space debris.

2.3.4 Telescope Aperture

The receiving telescope is used to collect the space debris reflected optical signal photons. The optical signal power collected by the telescope is directly related to the active collecting area A_T of the telescope. A telescope with a larger A_T collects more of the reflected optical signal. Equation 2.4 is used to calculate the A_T of the telescope with an aperture D.

$$A_T = \pi\Big(\frac{D}{2}\Big)^2 \tag{2.4}$$

Structural design and cost constraints typically prevent the building of telescope with a single large mirror. Larger modern astronomical optical telescopes, such as the Giant Magellan Telescope (GMT), may use lightweight segmented mirrors [83], where each mirror has an individual support structure, but when installed together act as a single mirror with a much larger aperture [84].

Another approach is linking multiple telescopes to emulate a larger aperture telescope. Since the laser beam is scattered off debris in various direction, a second telescope can be also be used in a bi-static arrangement to collect the tracking data as shown in Figure 2.1. One study was able to show a pulse laser signal reflected from a large defunct ENVISAT satellite was detected at a second optical telescope, approximately 300 km away [85]. When using the tracking data collected from both telescopes, the range measurement precision showed an improvement of an order of magnitude [85].

The telescope used at the Mount Stromlo facility has an aperture of 1.8 m [29] for space debris ranging and is used for all calculations related to the telescope design in this thesis.

2.3.5 Atmospheric Loss

Atmospheric effects on the propagating beam are:

1. Distorting the wavefront of the laser beam causing an increase in beam divergence.
2. Change in the polarisation of the laser beam [86].
3. Reducing the returning signal power through photon absorption and scattering.

The Point Spread Function (PSF) and the Fried Coherence length are two parameters that help describe the impact of atmospheric distortion for an optical system. The PSF describes the response of an imaging system to a point source or point object. For a telescope with an aperture D, the smallest angular resolution that can be observed is given by the telescope's PSF. As the optical signal passes through the atmosphere, the wavefront distortion increases the telescope's smallest observable angular resolution by a factor of D/r_0 [87]. r_0 is the Fried Coherence length which is a measure of the quality of the optical transmission through the atmosphere.

The refractive index of the atmosphere changes with a change in the atmospheric density. The net effect is a distortion of the phase of the laser, reducing the coherence of the propagating laser beam causing the laser beam to defocus and increase the beam divergence [88]. This results in a larger beam width at the telescope's location and less of the signal photons is collected. The phase distortion also acts as a noise source and can impact range measurements based on using the phase or frequency of the laser.

Atmospheric conditions are challenging to gauge since the effects can change rapidly depending on weather conditions. Adaptive optics (AO) can be used to reduce the wavefront distortion of the laser beam [89]. Installing an AO system to the optical telescope has been proposed for space debris ranging [11] and is being developed by SERC as part of their debris manoeuvring demonstration [28, 90]. A sodium laser guide star is used to form an artificial star [91] with the AO system used to measure the wavefront distortion of laser guide star. The wavefront measurement is then used to correct for the distort of the transmitted laser beam, as the beam travels through the atmosphere, allowing the laser beam to be focused on the target.

Atmospheric absorption and scattering of the laser photons also reduce the amount of power that returns to the telescope. Atmospheric absorption depends on the wavelength of the laser and the number of atmospheric molecules that can absorb the photons at the laser wavelength [92].

This thesis would not focus on the discussions related to the implementation of an A0 system to reduce the wavefront distortion while the signal loss from the atmospheric absorption and scattering is denoted as F.

2.3.6 Estimating the Reflected Signal Power

This section aims to derive an equation to calculate the optical power collected by the telescope. The same steps can be taken to calculate the collected signal for a radar ranging method. The initial discussions in this section will make two assumptions:

1. The target is a satellite
2. Beam divergence is diffraction-limited

Both the diffuse reflecting surface of a piece of space debris and atmospheric effects impact the optical power of the received signal but also vary greatly for different space debris targets and changing atmospheric conditions respectively. By making the initial assumptions, this section aims to present an equation to show how the fixed parameters in the ranging system impacts the received signal power. This equation is then updated to take into account signal loss due to the diffuse surface and atmospheric effects. Section 2.3.7 will discuss for the difference between a satellite and space debris targets between 1 cm and 10 cm.

Figure 2.7 illustrates the divergence of a laser beam transmitted in the direction of a satellite with a range of R. A_{SD} is the cross-sectional area of the satellite, and Ω_T is the solid angle of the laser beam. A solid angle is used to estimate the field of view covered by an object when observed from a particular point.

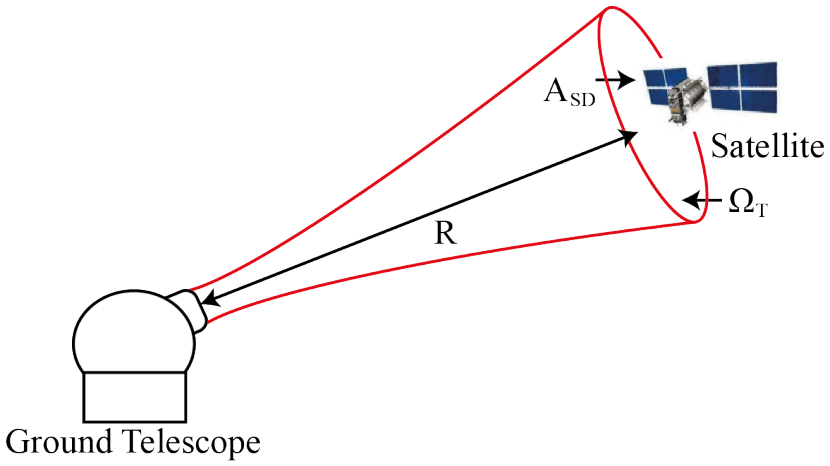

Figure 2.7: Illustration of a laser beam transmitted in the direction of a defunct satellite with range R and cross-sectional area of A_{SD}. Ω_T is the solid angle of the laser beam.

The solid angle gives the amount of outgoing laser power that reaches the target at a range of R. The solid angle of a diverging Gaussian beam from a telescope, as illustrated in Figure 2.7, is approximately the shape of a cone with beam divergence θ. The solid angle Ω_{cone} for a cone is calculated using Equation 2.5. The equation is simplified for small angles of θ ($\sin\theta \approx \theta$).

$$\begin{aligned} \Omega_{cone} &= 4\pi \sin^2\left(\frac{\theta}{2}\right) \\ &\approx \pi\theta^2 \end{aligned} \tag{2.5}$$

Using Equation 2.1, the diffraction-limited beam divergence angle θ is related to the radius of the telescope. Therefore replacing θ in Equation 2.5, the solid angle Ω_T of the transmitting laser beam from the telescope can be calculated by using Equation 2.6 where A_T is the active collecting area of the telescope.

$$\begin{aligned} \Omega_T &= \frac{\lambda^2}{\pi(D/2)^2} \\ &= \frac{\lambda^2}{A_T} \end{aligned} \tag{2.6}$$

The amount of light reflected back to the telescope depends on the portion of the light intensity that overlaps an area equal to the cross-sectional area of the target A_{SD}. If the transmitted power is P_T at a wavelength of λ, the reflected optical power P_{SD} is calculated with Equation 2.7.

$$\begin{aligned} P_{SD} &= P_T \frac{1}{\Omega_T} \frac{A_{SD}}{R^2} \\ &= P_T \frac{A_{SD} A_T}{\lambda^2 R^2} \end{aligned} \tag{2.7}$$

Assuming the reflected laser beam also has diffraction-limited beam divergence, Figure 2.8 shows the solid angle of the laser beam is also approximately a cone and can be used to calculate the signal power collected by the telescope. Equation 2.8 shows the reflected laser beam solid angle Ω_R calculated using the size of the target satellite D_{SD} to calculate the cross-sectional area of the target A_{SD}.

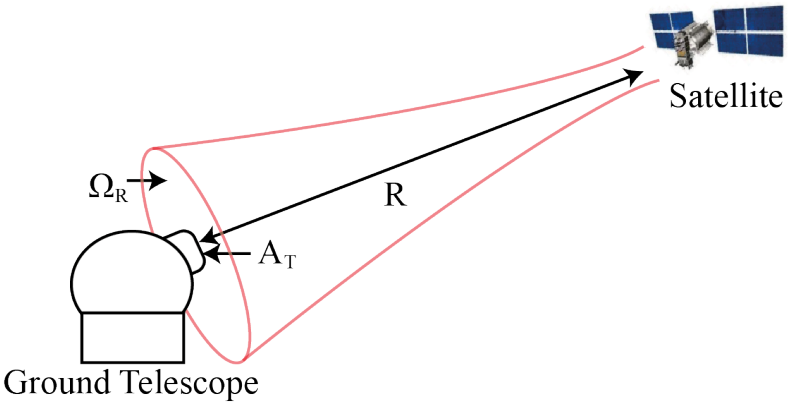

Figure 2.8: The reflected laser beam from the defunct satellite with range R has a solid angle of Ω_R. A_T is the effective collecting area of the telescope.

$$\begin{aligned} \Omega_R &= \frac{\lambda^2}{\pi(D_{SD}/2)^2} \\ &= \frac{\lambda^2}{A_{SD}} \end{aligned} \tag{2.8}$$

The amount of light collected by the telescope will depend on the portion of light, with the solid angle Ω_R at the range R, that overlaps with the area of the telescope A_T. With the reflected power of P_{SD} at wavelength λ, the amount of signal power collected at the telescope P_R can be calculated using Equation 2.9.

$$\begin{aligned} P_R &= P_{SD}\frac{1}{\Omega_R}\frac{A_T}{R^2} \\ &= P_T\frac{(A_{SD}A_T)^2}{(R\lambda)^4} \end{aligned} \tag{2.9}$$

Equation 2.9 shows how the relationship between the received signal power P_R with the laser wavelength λ, range of the target R, the target cross-sectional area A_{SD} and the active collecting area of the telescope A_T. Table 2.2 shows two examples, providing values for the various parameters, to calculate the received signal power P_R using Equation 2.9. For Example 1, a 10 cm target with a range of 1000 km results in 3 W received signal power P_R, using a 1.8 m telescope aperture and a 10 kW transmitted laser power P_T. In Example 2, only the target size is reduced to 1 cm and all other parameter values are fixed. The received signal power P_R is reduced to 300 μW. Table 2.2 shows that in the ideal conditions using Equation 2.9, taking into account the assumptions made, the signal-to-noise ratio for a small target can be low.

In reality, the actual received signal power P_R would be smaller than the values calculated in Table 2.2 for 1 cm and 10 cm target. By assuming a diffraction-limited beam divergence and a satellite as a target to derive Equation 2.9, the following conditions were not taken into account:

Parameters	E.g. 1 Values	E.g. 2 Values
Transmitted Power P_T	10 kW	10 kW
Laser Wavelength λ	1064 nm	1064 nm
Target Size	10 cm	1 cm
EOS Telescope Aperture D	1.8 m	1.8 m
Approx. Received Power P_R	3 W	300 μW

Table 2.2: Calculating P_R using Equation 2.9 for target size of 1 cm and 10 cm.

1. Increased beam divergence due to atmospheric wavefront distortion
2. Signal loss due to atmospheric absorption and scattering
3. Signal loss due to increase scattering from a target with a diffuse surface.

Equation 2.9 is updated and represented as Equation 2.10 in order to take into account the increased signal loss due to the above mention factors. F and β are parameters that aim approximate the signal loss from the atmospheric condition and from a small piece of space debris with a diffuse surface respectively. Since the signal passes through the atmosphere twice between the transmission and collection of the optical signal, F is squared in Equation 2.10.

$$P_R = P_T \frac{(A_T A_{SD})^2}{(R\lambda)^4} \frac{F^2}{\beta} \tag{2.10}$$

The main challenge is providing an approximate value for the F and β parameters to help calculate the received signal power P_R for a space debris target. F will vary depending on weather and atmospheric conditions which can change throughout the day. β depends on the size of the space debris, the nature of the diffuse surface and the reflecting material, with all three factors can vary for different targets.

2.3.7 Difference between Satellite and Space Debris Laser Ranging

Space debris laser ranging (SDLR) uses the same concept as satellite laser ranging (SLR). However, SLR measurements of the position of an LEO satellite, together with using onboard GPS, can be determined to between millimetre and centimetre level accuracy [93, 94]. The same level of performance cannot be achieved for space debris ranging.

All active satellites maintain a stable orbit [95]. A piece of space debris might not maintain a stable orbit, tumbling in space, and cause fluctuations in the reflected optical signal power.

Most active satellites have onboard retro-reflectors. A retro-reflector is a device that reflects light in the direction parallel to the incident beam. An onboard retro-reflector can increase the optical power of the signal beam reflected to the telescope [96]. The optical signal from a retro-reflector also dominates the reflected signal from diffuse surfaces of the satellite. This prevents the random phasor discussion in Section 2.3.3 and allows coherent systems

for range measurements [62]. Discussions presented by Lehr et al on using laser ranging on two satellites, with and without an onboard retro-reflector, showed an increase in the number of signal is approximately 10^8 for the satellite with an onboard retro-reflector [46].

The size and shape of the space debris also impact the reflected signal power. Due to collision or fragmentation events, the reflecting surface of a piece of space debris varies greatly. Optical reflectively of space debris is not known but considered comparable to microwave radar cross-section (RCS) [32, 97]. For comparison a stealth aircraft has an RCS of $0.1\,\mathrm{m}^2$ [98] and a retro-reflector as high as $20\,000\,\mathrm{m}^2$ [99]. Kirchner et al discussed several challenges of developing an SDLR system at the Graz SLR station [32]. The test carried out in Kirchner et al tracked space debris with RCS between $0.3\,\mathrm{m}^2$ and $15\,\mathrm{m}^2$ in a stable orbit at a target range between 600 km and 2500 km. The space debris system used 25 mJ/pulse, 10 ns pulse width and 1 kHz repetition rate laser source. With the help of an avalanche photodiode, approximately 4 photoelectrons/s was obtained during their tests.

The EOS SDLR system in Mount Stromlo uses a 4.5 J/pulse laser and 170 Hz repetition rate. The expected energy density on a target at a range of 800 km is equal to $0.08\,\mathrm{J/cm}^2$.

Due to the combination of these factors, a piece of space debris is considered a non-cooperative target. It is difficult to provide a sensible approximation of the received signal power for a space debris target as the reflected signal power from a piece of space debris varies greatly and can vary for different targets. For active satellites, with the help of retro-reflectors, the signal power is more consistent and higher than for a space debris target, resulting in better accuracy in the range measurement. For the discussion in Chapter 6, this thesis will try to approximate the parameter β to calculate the received signal power.

2.4 Noise Sources

Section 2.3 highlighted the factors that impact the optical signal collected by the receiving telescope. Using Equation 2.10 the upper bound optical power of LEO space debris would be low and the signal is exposed to various noise sources that degrade the signal-to-noise ratio and reduce the range measurement precision. The primary noise sources that affect the optical signal are:

1. Shot noise
2. Photodetector noise
3. Background photon noise
4. Analogue to Digital converter clock noise
5. Laser frequency and phase noise

Figure 2.9 shows the impact of the amplitude and clock noise sources on a pseudo-random noise (PRN) code amplitude modulated continuous wave laser. Amplitude noise sources such as shot noise, photodetector noise and background photon noise add amplitude fluctuations on the modulated signal. For low power optical signals, amplitude noise corrupts the modulated signal, making it difficult to distinguish the PRN code features and amplitude transitions. Clock-related noise will cause timing errors, adding to the uncertainty in the arrival time of the modulated code. These timing errors lead to the range and velocity measurement errors.

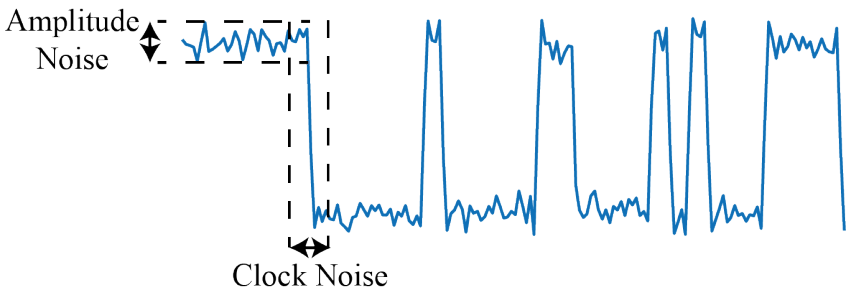

Figure 2.9: PRN code with amplitude noise distorting the optical signal detected and clock noise which affects the correct sampling of the detected PRN code.

Figure 2.9 does not show the effect of both laser frequency and phase-related noise. Both types of noise sources would not impact the direct detection methods since only the intensity of the signal laser is measured. However, a coherent detection method is sensitive to both frequency and phase-related noise. In the coherent system, the optical signal collected by the telescope interferes with a second laser called the local oscillator. The interference pattern is a sinusoidal function of time called the beat note with a frequency f_h and phase $\Delta\phi$. f_h is the difference in the laser frequency of the optical signal f_{Sig} and local oscillator f_{LO} ($f_h = f_{Sig} - f_{LO}$) while $\Delta\phi$ is the difference in the phase of the two interfering lasers ($\Delta\phi = \phi_{Sig} - \phi_{LO}$). Measuring the change in the beat note frequency f_h due to the Doppler shift of the signal laser frequency can be used to calculate the velocity of the target [62].

Figure 2.10 shows the effect of laser frequency noise on the beat note of an acquired interference pattern in the frequency domain. The beat note is obtained by interfering two free-running optical lasers and the intensity of the interference measured using a photodetector. Without frequency and phase noise, the expected beat note frequency would be a single harmonic at f_h. But due to the laser frequency noise, the peak of the beat note has drifted to a higher frequency and is broadened over a range of frequencies. This would lead to reduced accuracy in estimating the Doppler shift of the signal laser frequency in a coherent-lidar application to estimate the target's velocity. The two lasers can be frequency stabilised and phase-locked but this will be further discussed in Chapter 5.

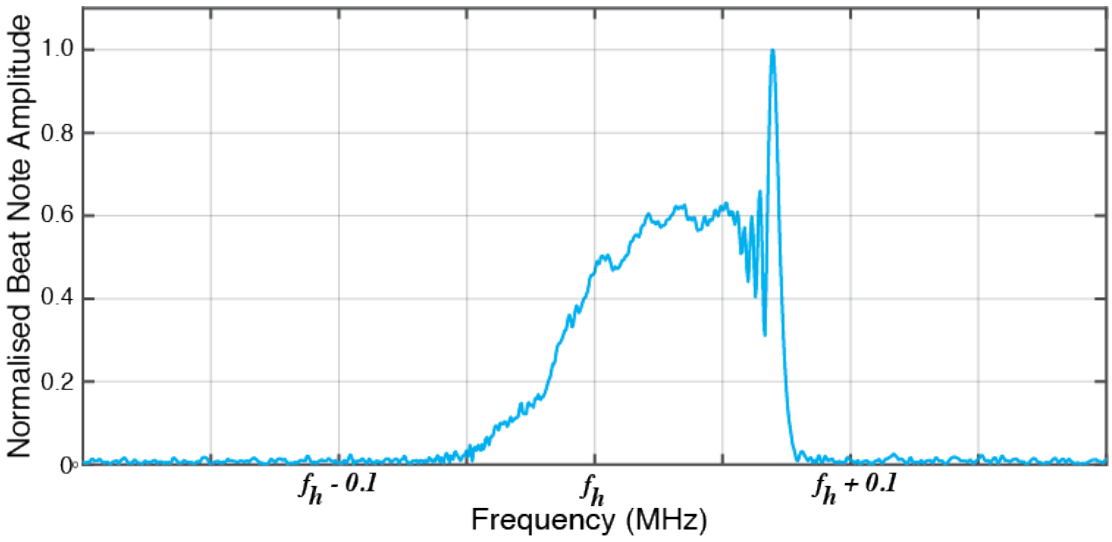

Figure 2.10: Effect of laser frequency noise on the beat note in a coherent detection method.

2.4.1 Shot Noise

Light is electromagnetic radiation made of up tiny packets of energy called photons [100]. The energy of each photon E depends on the wavelength λ of the light source as shown in Equation 2.11 where $\hbar$ is Plank's constant and c is the speed of light.

$$E = \frac{\hbar c}{\lambda} \tag{2.11}$$

The arrival of each photon is treated as a discrete independent event. The number of photons n arriving per measurement interval τ can be described using a *Poisson distribution* [101, 102]. Equation 2.12 calculates the optical power P of a light source by counting the average number of photons $\bar{n}$ arriving within a 1 second time interval.

$$P = \bar{n}E \tag{2.12}$$

Since the arrival follows a Poisson distribution, the standard deviation of the distribution is the measure of the fluctuations in the number photons arriving from one measurement interval of τ to another. The fluctuations in the number of photons arriving per second causes fluctuation in the optical power. This fluctuation is called *shot noise*. Shot noise is represented as σ_{SN} in Equation 2.13 where τ is equal to 1 second.

$$\sigma_{SN} = \sqrt{\bar{n}\tau E} \tag{2.13}$$

Equation 2.13 showed that shot noise is related to the optical power P of the signal. An increase in the optical signal power increases the shot noise. Figure 2.11 shows a simulation on how the shot noise of the optical source changes when the source is amplitude modulated with a sinusoidal signal. At the peak of the modulated signal, the uncertainty in the number of photons arriving is larger, and so the fluctuations in the optical power from shot noise would also is more substantial than at the troughs for the same interval of time.

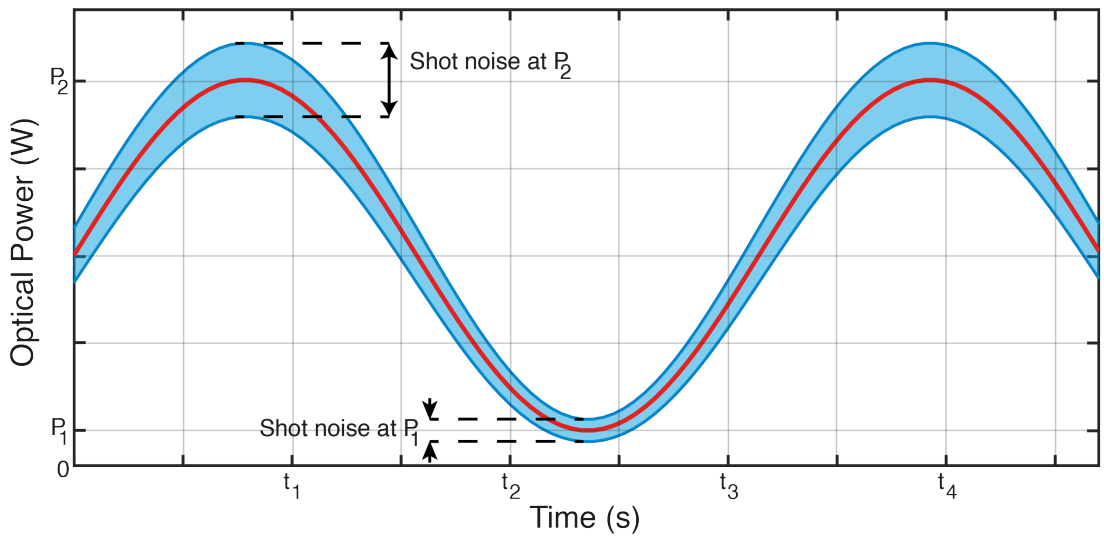

Figure 2.11: The red curve represents the mean optical power of the amplitude modulated laser source and the blue region indicates the amount of shot noise from the optical source.

Shot noise is a white noise source that is independent of frequency and is a property of the light source [103]. Both quantum noise and technical noise sources generate laser intensity

noise, but the lowest possible intensity noise level achievable is from shot noise [103]. Even though there are methods of reducing the intensity noise below the shot noise limit [103], for this thesis shot noise is the fundamental limit of the optical noise.

For the direct detection and coherent detection scheme discussed in this thesis for a space debris application, shot noise from the received optical signal would not be the dominant noise source. For the direct detection scheme, both photodetector and background photon noise would be larger. For the coherent detection scheme, the signal is amplified above the various additive amplitude noise and shot noise from the local oscillator laser is the dominant noise source.

2.4.2 Photodetector Noise

A photodetector is a device that is capable of measuring the intensity of the optical signal. When a photon arrives at the photodetector, the photon transfers its energy to the semiconductor in the photodetector, generating a photoelectron-hole pair [100] and flows like an electric current.

The photodetector also generates dark-current noise. Dark-current noise is the random generation of electron-hole pairs in the absence of light. Due to thermal effects, an electron can gain sufficient energy to generate an electron-hole pair. This electron-hole pair is indistinguishable from the photoelectron-hole pair. The dark current of a photodetector is reduced by cooling the environment that houses the detector. Also, the photodetector has additional noise sources from associated electronic circuits and amplifiers [100].

2.4.3 Background Photon Noise

Background photon noise is the dominant noise source for current space debris laser ranging methods [33] and limits daylight operations at Mount Stromlo [70]. Background photon noise is when the photodetector measures a photon associated with an external optical source unrelated to the signal. The telescope will also collect photons generated by sources in the surrounding environment including both starlight and sunlight. The largest background noise source in space debris ranging is the Sun. The spectrum of the solar radiation outside of the Earth's atmosphere is mostly between 200 nm and 2500 nm [104]. As the solar radiation passes through the Earth's atmosphere, the spectrum is altered due to absorption and scattering.

The continuous wave laser used in the bench-top experiment in this thesis is at 1064 nm. There is some loss of solar radiation in the near infra-red region due to water vapour and carbon dioxide molecules but a significant amount of the solar radiation at 1064 nm passes through the atmosphere [104]. The optical signal photons can become indistinguishable from the background photons for a low signal-to-noise ratio optical signal. Optical filters can be used to remove photons at the different wavelengths, but background noise within the wavelengths allowed by the optical filter reduces the signal-to-noise ratio.

2.4.4 ADC Sampling Timing Error

Clock-related noise is introduced into the measurement at two stages of the experiment. One is during the generation of the PRN code, and the other is the digitisation of the PRN code by the analogue to digital converter (ADC).

When digitising the signal, two different types of clock noise are present. The first causes a timing offset in the ADC sampling of the PRN code. This timing offset may also drift over time. In a bench-top experiment, the generation and digitisation of the PRN code are synchronised to a master clock. There is now a common clock timing error, and this prevents the independent drift of the clock frequency at each stage of the experiment.

The second clock noise is called timing jitter. The digitisation of an ADC is typically assumed to be periodic with a fixed time interval between the digitised samples. Due to the jitter of the ADC sampling time, the time interval between the samples varies and could lead to the incorrect digitisation of the PRN code. Due to the timing errors present in the digitised PRN code, the precision of the range measurement is reduced.

2.4.5 Laser Frequency Noise

Laser frequency noise is the random fluctuations of the instantaneous frequency or the random fluctuations in the linear evolution of the phase of the laser source [105, 106]. Laser frequency noise would not impact the direct detection methods but coherent detection methods are sensitive to fluctuations in the laser frequency and phase. If two unstabilised laser sources are used, one as the illuminating source and the second as the local oscillator, both would have the $\frac{1}{f}$ laser frequency noise [107]. The laser frequency noise from both sources introduces errors when measuring the beat note frequency f_h since the resulting beat note frequency when interfering the two laser beams broadens [108] and drifts over time. Laser frequency noise of a source can be stabilised and reduced by locking the output of the laser to an optical cavity [109, 110].

Heterodyne interferometry based measurements often require frequency stabilised lasers [111] or deriving both signal and local oscillator from the same source [73] to reduce the impact of laser frequency noise. Laser frequency stabilisation has been shown to achieve sub-Hz resolution using a frequency comb [112]. In space-based interferometer missions such as GRACE Follow-On and LISA, the laser stabilisation is designed to achieve $30\,\mathrm{Hz}/\sqrt{\mathrm{Hz}}$ [113] and $100\,\mathrm{Hz}/\sqrt{\mathrm{Hz}}$ [114] respectively. Chiodo et. al showed that the laser frequency of the source can be stabilised and tuned to track the Doppler shift of the reflected signal laser frequency in satellite ranging application using a coherent detection method [62].

2.5 Chapter Summary

Chapter 2 looked at the two most common methods of ranging space debris using radars and optical telescopes. Space debris is a non-cooperative target. The range measurement obtained from a piece of space debris is less precise than from an active satellite with retro-reflector. Space debris ranging is also affected by space debris size and range, laser beam divergence due to the vast propagation distances, telescope size and atmospheric condition. These factors impact the number of signal photons reflected and collected by the ranging system. The chapter also presented the different noise sources present in the signal laser beam that impact the delay measurement accuracy.

The diffuse surface of a piece of space debris causes scattering of the optical signal and varies the phase of the reflected signal's electric field. This reduces the amplitude of the electric field and may prevent using a coherent detection method for low signal-to-noise ratio scenarios.

Matched Filter Analysis

The discussions in Chapter 2 highlighted the challenges faced by current space debris laser ranging applications. The low signal-to-noise of the optical signal is the main limiting factor for poor ranging precision of the optical illumination method compared to radar. Low signal-to-noise ratio also prevents current space debris laser ranging operation during the daylight hours because of the increase in background photon noise. Further, a piece of space debris is a non-cooperative target with a diffuse reflecting surface. The diffuse surface increases the scattered reflection of the optical signal and varies the phase of each reflected signal's electric field. Both reduce the amplitude of the optical signal and may prevent using phase modulation methods to measure the propagation delay.

This chapter discusses amplitude modulating the continuous wave laser with pseudo-random noise (PRN) codes. By taking advantage of the code statistics [34], a more extended period than a single pulse of the acquired optical signal is used to improve signal detection and the range measurement precision. The different phase of the electric fields do not affect the amplitude modulation method as only the PRN code amplitude transitions of the optical signal are required for the range measurement, and the phase of the optical signal can be ignored. The amplitude modulated PRN code is shifted in time due to the propagation delay of the optical signal. The motion of the space debris also causes a Doppler shift of the PRN code properties. A matched filter analysis with parameter estimation is used to determine the position and change in position of the space debris. This method provides information on the space debris range, velocity and higher-order derivatives of motion. These estimated parameters can be used to determine the orbit of a piece of space debris and predict future collisions. The estimated parameters can also be used to determine the effectiveness of the manoeuvring laser on the debris' orbit.

3.1 Background on Matched Filters with Parameter Estimation

Matched filters have been used as a signal processing tool in many different fields for several different applications since the 1950s [115]. A matched filter can be used to look for the presence of the desired signal, called the *template*, in the measured time series by cross-correlating the template signal with the acquired signal [116]. Equation 3.1 shows the output $y[n]$ of the matched filtering process where $h[n]$ is the template and $x[n]$ is the acquired signal.

$$y[n] = \sum_{n=-\infty}^{\infty} x[n]h[n+k] \tag{3.1}$$

If the template $h[n]$ is present in the acquired signal $x[n]$, the output of the matched filter $y[n]$ will be typically much larger compared to when the template is absent, even if the acquired signal is corrupted with noise. The template has a high correlation with the acquired signal but has a weak correlation with the additive noise present in the signal.

The good cross-correlation property of matched filters is also used to determine the parameters of the acquired signal. In some cases, the properties of the transmitted signal have changed, resulting in poor correlation with the template. Parameter estimation techniques are used to adjust the properties of the template, and the cross-correlation output provides a measure of how similar the template is to the acquired signal. The template parameters that generated the most significant cross-correlation output provides the best estimate of the acquired signal's properties.

3.1.1 Example of Ranging Applications using Parameter Estimation

Matched filters with parameter estimation are commonly used in ranging applications. One example is the pulsed-compression matched filter used in pulse radar ranging applications [117]. A pulse-compression matched filter is used at the receiver with parameter estimation to improve signal detection of the reflected pulse and to improve the measurement resolution of the position of the target.

Figure 3.1a shows the transmitted pulse with pulse peak amplitude equal to A_1 V and a pulse width Ts. Figure 3.1a also shows that within the pulse, the radio signal is frequency modulated with a chirp signal to reduce the frequency linearly by B_1 Hz. Figure 3.1b shows the received pulse shifted in time by τ_D due to the propagation delay. The received pulse is shown to have a peak amplitude of A_2 V, pulse width Ts and modulation bandwidth B_1.

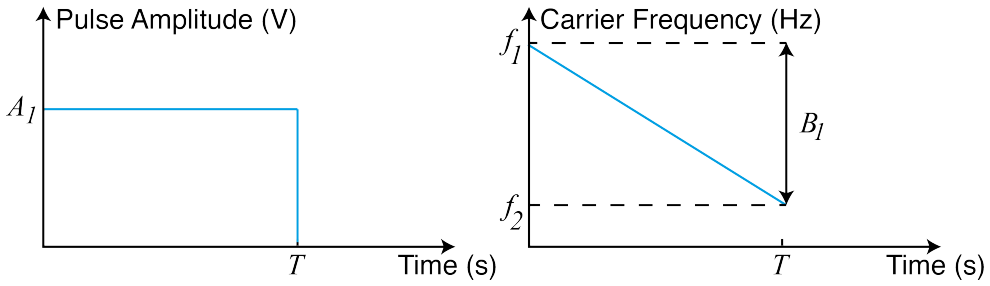

(a) Transmitted pulse with width T and a linear frequency sweep of the radio wave decreasing by B_1 Hz within the pulse.

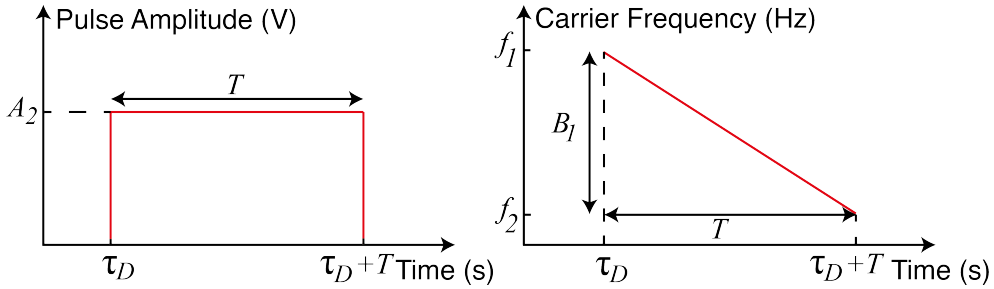

(b) The detected pulse at the receiver and frequency modulation of the radio wave are both shifted in time due to the propagation delay.

Figure 3.1: Comparing the transmitted pulse and the reflected pulse with a linear frequency sweep from a stationary target.

In an ideal case, the peak amplitude of target reflected pulse acquired at the receiver (A_2) has a good signal-to-noise ratio to provide accurate and precise measurement of the propagation delay τ_D. In some applications, A_2 is small and increasing A_1 to improve the signal-to-noise ratio of the acquired reflected pulse can be complex and difficult to achieve. A transmitted pulse with a wider pulse width has more energy per pulse and a pulse-compression matched filter can be used to improve both signal detection and measuring the propagation delay [118].

The acquired pulse is passed as one of two inputs for the pulsed-compression matched filter analysis. The second input is the template pulse with the same pulse width Ts and modulation bandwidth B_1Hz. The matched filter analysis carries out a cross-correlation of the two input pulses. Figure 3.2 shows the output of the matched filter analysis resembling a *sinc* function as the template parameter τ is altered. The peak of the *sinc* function scales with the amplitude A_2, the modulation bandwidth B_1 and the width T of the received pulse [118]. Figure 3.2 also shows that the width of the main peak of the *sinc* function is affected by the bandwidth B_1 [118]. Since $\frac{1}{B_1}$ s $\ll T$ s and A_2B_1T V $\gg A_2$ V, the width of the *sinc* function is smaller with a larger peak amplitude compared to the received pulse.

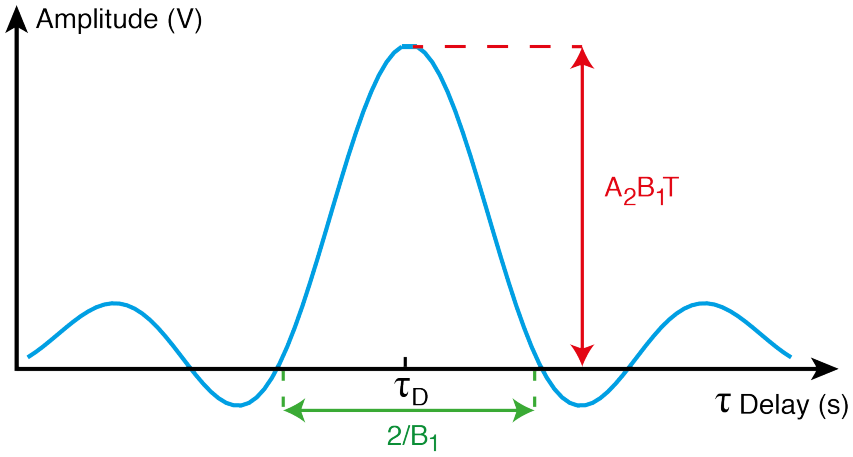

Figure 3.2: The cross-correlation output of a pulse-compression matched filter. The result is a sinc function with both the peak and width of the pulse affected by the frequency modulation B_1.

The largest cross-correlation amplitude, equal to A_2B_1T V, is produced when the time shift τ applied to the template pulse matches the propagation delay τ_D of the acquired pulse. The cross-correlation peak amplitude is used to estimate the propagation delay τ_D and hence the position of the target. Equation 3.2 shows that the range resolution δR depends on the width of compressed pulse [45, 118] where c is the speed of light.

$$\delta R = \frac{c}{2B_1} \tag{3.2}$$

If the target is in motion, the received signal pulse modulation bandwidth B_1 is altered to $B_{Doppler}$ ($B_1 \neq B_{Doppler}$) due to being Doppler shifted by the target's motion. The Doppler shift of the modulation bandwidth B_1 can be large enough where the acquired pulse does not correlate as well with the template pulse, reducing the cross-correlation peak amplitude.

Figure 3.3 shows three different cross-correlation results where the parameter value for the for modulation bandwidth of the template pulse B is altered and the initial propagation delay of the target is τ_D. For simplicity, only the chirp signal with the different B parameter value used to generate the template pulse is compared to the Doppler shifted chirp $B_{Doppler}$

of the acquired pulse are shown in Figure 3.3. These three different chirp signals are modulated onto the template pulse. As before the acquired pulse is cross-correlated with the template pulse to produce the cross-correlation output.

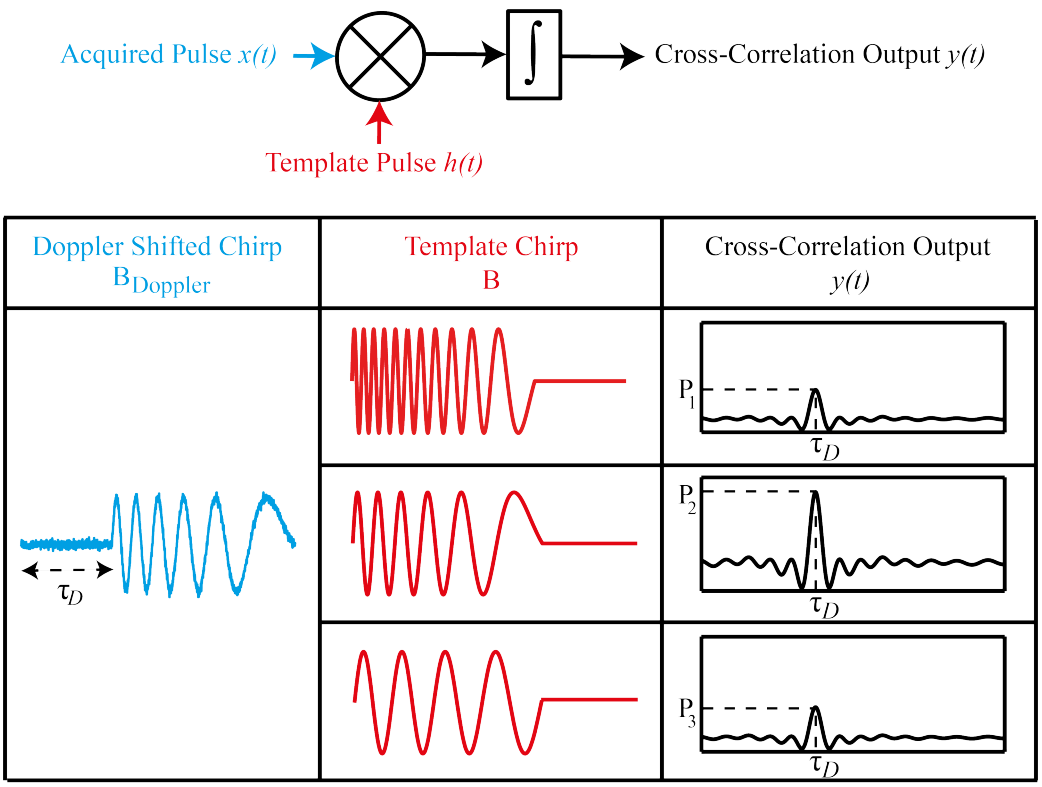

Figure 3.3: Matched filter concept where the delay and linear chirp frequency of the template chirp are altered before correlating with the signal. The peak value of the correlation is equal to P_2 when the template $h(t)$ is matched to the acquired signal $x(t)$.

For the first template in Figure 3.3, the input parameter value B used to generate the chirp for the template pulse is larger than the Doppler shifted chirp $B_{Doppler}$ for the acquired pulse ($B > B_{Doppler}$). Despite the mismatch, the two pulses are similar enough to produce a cross-correlation with a peak value of P_1. For the second template, the input parameter value B matches the Doppler shifted chirp signal ($B = B_{Doppler}$). The result is a larger cross-correlation output with a peak value of P_2. For the final template, the input parameter value B is smaller than the Doppler shifted chirp ($B < B_{Doppler}$). The result is a reduced cross-correlation output equal to P_3.

The pulse-compression matched filter example showed that two parameters, τ and B, of the transmitted signal, can be changed during the propagation of the signal. These changes reduce the cross-correlation output of the received signal with a copy of the originally transmitted signal. Using a parameter estimation approach to alter the same two parameters for the copy of the transmitted signal, the cross-correlation output can be used to estimate received signal's τ and B parameter value. These two values can then be used in estimating the position and change in position of the target.

Another type of parameter estimation matched filter is the correlation of two m-sequence PRN codes [119]. This method is widely used in continuous wave radar [120] and lidar [34] ranging applications. This method is discussed in more detail in Section 3.2. Other examples of the use of parameter estimation matched filters are in gravitational wave detection [121, 122].

3.2 Pseudo-Random Noise Sequences

Pseudo-Random Noise (PRN) codes are widely used in both radar [120] and lidar [34] applications to measure the range of a target. A PRN code is a deterministic and periodic binary sequence [123]. Within the sequence period, the bit pattern is random, but the sequence pattern repeats itself indefinitely [123].

One such PRN code sequence is called the maximal length sequence, also known as m-sequence [123]. Figure 3.4 shows a 4-bit m-sequence PRN code. The properties of an m-sequence PRN code are:

1. Code length L is $2^n - 1$ chips for an n-bit linear feedback shift register code generator
2. Output sequence of 1's and 0's are deterministic
3. Contains $2^{(n-1)}$ 1's and $2^{(n-1)} - 1$ 0's
4. An all-zero state in the shift register will remain latched with constant zero output.
5. When a shifted sequence is modulo-2 added to an identical unshifted sequence, it generates the same sequence with a different shift
6. Has good auto-correlation.

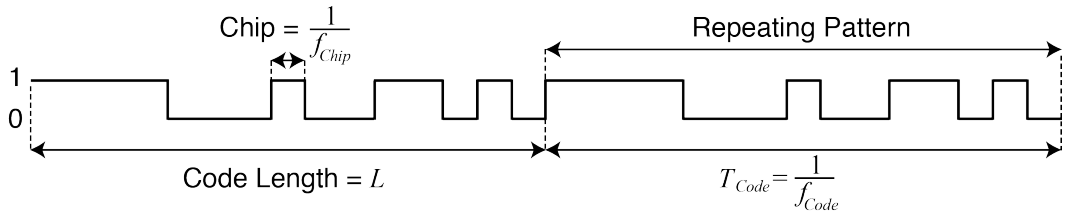

Figure 3.4: A 4-bit m-sequence PRN code. The code length of a 4-bit code is 15 chips where each chip is $\frac{1}{f_{Chip}}$ seconds. The m-sequence pattern will repeat at the end of the code length.

The chip frequency f_{Chip} determines the rate at which the PRN code generator creates a new output. This time interval is called a *chip*. The code repetition frequency f_{Code} is the rate at which the sequence repeats itself. As shown in Equation 3.3, the code repetition frequency f_{Code} of the sequence depends on the chip frequency f_{Chip} and the code length L of the sequence ($L = 2^n - 1$).

$$f_{Code} = \frac{f_{Chip}}{2^n - 1} \tag{3.3}$$

3.2.1 Generation of a PRN Sequence

An m-sequence PRN code is generated using a linear feedback shift register [124]. Figure 3.5 shows a 4-bit linear feedback shift register. The shift register can be described by the polynomial expression $x^4 + x^3 + 1$ indicating that bits from position x_3 and x_2 of the 4-bit shift register are the XOR operation inputs. The output of the XOR operation is fed back to the shift register in position x_0 while the bits in the registers are shifted by one position. The bit that was previously in position x_3 moves out of the register as the output of the PRN code generator. Only using certain positions of the shift register, as inputs to the XOR operations, will generate an m-sequence [123].

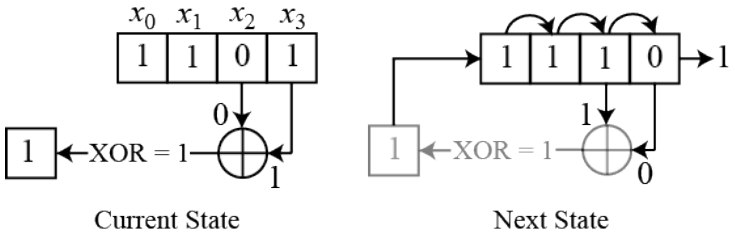

Figure 3.5: A 4-bit linear feedback shift register for generating an m-sequence PRN code.

The PRN code generation cycle is repeated and the time taken for the generator to output a new value depends on the chip frequency. The sequence in the shift register is unique at every cycle resulting in the PRN code output to appear random [123, 125]. However, the sequence will repeat itself every period resulting in a repeating pattern.

3.2.2 Spectra of a PRN Sequence

Figure 3.6 shows the normalised power spectrum of the 4-bit m-sequence PRN code. The frequency response of the PRN code has a $sinc^2 f$ envelope [123], spread over a broad range of frequencies. The nulls in the spectrum occur at integer multiples of the chip frequency. The spacing between the frequency lines is dependent on the code repetition rate (f_{Code} Hz). A longer PRN code sequence will reduce the frequency spacing between the PRN code harmonics.

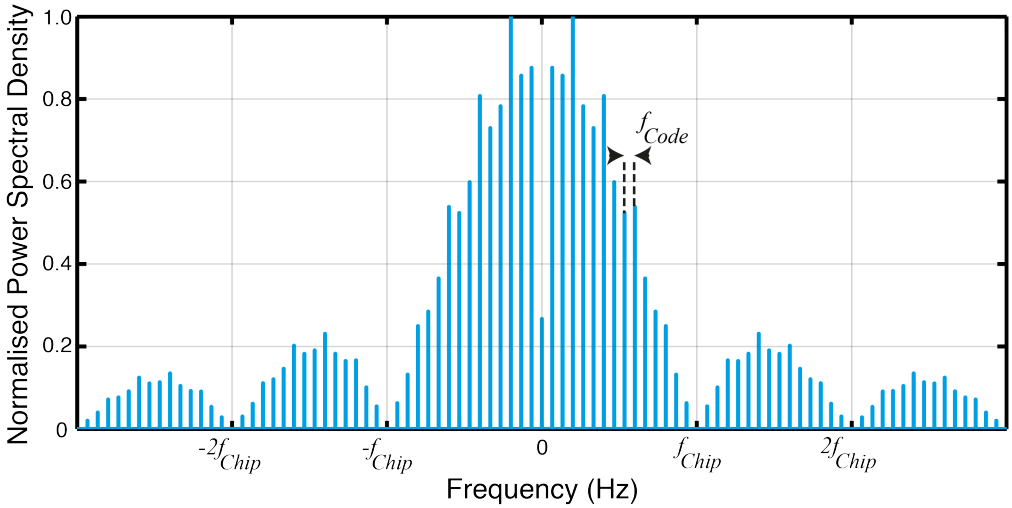

Figure 3.6: A PRN code spectra with a $sinc^2 f$ envelope and the nulls of the envelope occurring at integer multiples of the chip frequency f_{Chip}.

3.2.3 Applications of PRN Codes

PRN code sequences are used in many different fields and applications to take advantage of the sequence's spread-spectrum properties highlighted in Figure 3.6. For example, an analogue noise source with white Gaussian characteristics can be built using a large PRN sequence generator. PRN code sequences can also be used to modulate a carrier frequency. The spectrum of the code will spread the signal over a broader range of frequencies [126], scrambling the data and preventing jamming or interference at a specific frequency. M-

sequence PRN codes have good auto-correlation properties and are widely used in ranging applications with a parameter estimation matched filter. Two m-sequence PRN codes are also used in the generation of Gold Codes [127]. Gold codes generated from one GPS satellite has poor cross-correlation with Gold codes from another satellite [128]. This property of Gold codes allows GPS operators to broadcast from multiple satellites in the same frequency range.

3.2.4 Correlation of PRN Codes

Most PRN code sequences have either good auto-correlation or cross-correlation properties. Correlation is the measure of how similar two PRN code sequences are to each other [125]. Auto-correlation is the correlation of PRN code with a delayed copy while cross-correlation is the correlation of two different PRN codes. The auto-correlation of two identical m-sequence PRN codes is sensitive to time-shifts applied to one of the PRN code. The amplitude of the correlation output can be used to measure the time-shift of a delayed PRN code.

Equation 3.4, shows the correlation output $R[m]_{xy}$ of two identical m-sequences $x(n)$ and $y(n)$ with code length L as a function of the differential delay m. For simplicity, $x(n)$ is considered a binary signal with amplitude transitions between 1 and 0 for the discussion in this section only. $y(n)$ is the template code with the amplitude transitions between 1 and -1. In the correlation, the two codes are first multiplied together. If the amplitude of the n^{th} chip for both $x(n)$ and $y(n)$ is equal to 1, the two chips are in agreement, and the output of the multiplication is equal to 1. If $x(n)$ is equal to 1 and $y(n)$ is equal to -1, the output is equal to -1. If $x(n)$ is equal to 0, the output of the multiplication is equal to 0. The correlation then counts the number of chips in agreement by summing the multiplication of the two PRN codes for the length L of the sequence. The process is repeated for every m^{th} chip shift applied to the template code $y(n)$ to produce $R[m]_{xy}$.

$$R[m]_{xy} = \sum_{n=0}^{L-1} x(n)y(n+m) \tag{3.4}$$

When the two sequences are aligned with each other, the output of the correlation is approximately equal to $\frac{L}{2}$ since half of the $x(n)$ sequence is equal to 0. This is also known as the group delay of an Finite Impulse Response (FIR) filter. When the two sequences are not aligned, the correlation output is approximately equal to 0. Therefore the delay of the PRN code $x(n)$ can be determined using the correlation output $R[m]_{xy}$. Section 3.2.5 discusses using a PRN code to estimate the propagation delay of the outgoing laser light in a ranging application.

3.2.5 PRN Code Amplitude Modulation of the Continuous Wave Laser

PRN codes can be modulated onto the amplitude [34] or the phase [82] of the laser to measure the propagation delay. However, the discussion in Section 2.3.3 showed that phase modulation may not suitable for space debris ranging application due to the diffuse reflecting surface of a piece of space debris. The addition of the scattered electric fields with varying phase would degrade the amplitude of the beat note. In a low signal-to-noise ratio application such as space debris ranging, the accuracy and precision of the range measurement using phase modulation of the laser may not be applicable. Hence the amplitude modulation method is considered for space debris applications.

PRN codes have been used to amplitude modulate a continuous wave radar signal [129] and continuous wave laser in lidar [130, 131] for ranging applications. Equation 3.5 shows the transmitted output power of a continuous wave laser $s(t)$, with the optical power of the laser P, amplitude modulated with the PRN code $C(t)$. The PRN code sequence is represented as n number of rectangular-shaped pulses, represented as *rect* function, with a width equal to T_{Chip} [34]. a_n is used to represent the binary value of the n^{th} bit of the sequence, either equal to 1 or 0.

$$\begin{aligned} s(t) &= P.C(t) \\ &= P(a_n rect(t - nT_{Chip})) \end{aligned} \tag{3.5}$$

From Equation 3.5 the output power of the continuous wave laser is turned on and off by the PRN code sequence. If the binary value a_n is equal to 1, the output power is equal to P. If the binary value a_n is equal to 0, the output power is also equal to 0. The output power of the laser in the time series will show a PRN code sequence transitioning between P and 0.

Equation 3.6 shows the acquired signal $y(t)$ using a photodetector. In the equation, $y(t)$ is the delayed version of the transmitted signal $s(t)$ due to the propagation delay τ and α is the conversion of the power of the delayed optical signal $s(t - \tau)$ to the output voltage amplitude by the photodetector. $b(t)$ is the background noise present in the detected optical signal.

$$y(t) = \alpha(s(t - \tau) + b(t)) \tag{3.6}$$

Figure 3.7 shows the correlation output between the acquired optical signal $y(t)$ and the template code for sequence length equal to t_i seconds. As the delay of the template code is shifted to τ, the two codes are aligned. Hence the correlation output changes to the maximum value of $\frac{\alpha}{2}\sum_{n=1}^{t_i f_{Chip}} P$. This value is denoted as A_{max} in Figure 3.7.

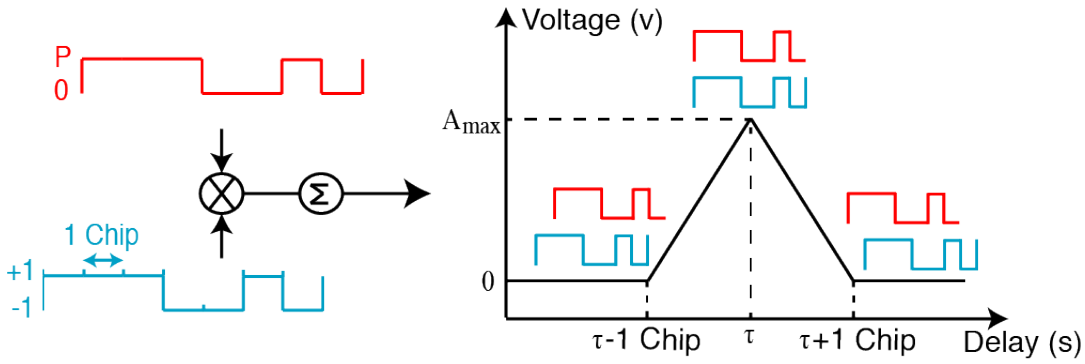

Figure 3.7: The auto-correlation process to find the propagation delay of a PRN code reflected by a simulated target

The peak amplitude of the signal correlation is dependent on the acquired signal's optical power P and the integration time t_i. If the detected signal has a low signal-to-noise ratio, increasing the integration time t_i results in a larger A_{max} value. The background noise $b(t)$ present in the acquired signal is also present in the signal correlation but has poor correlation with the template code. The integrated noise causes fluctuations in the correlation output but increases by $\sqrt{t_i}$ for increasing integration time t_i while the desired

signal increases proportional to t_i. Therefore the improvement in signal detection and the precision in measuring τ using the correlation method improves by $\sqrt{t_i}$.

The ambiguity range $R_{Ambiguity}$ depends on the distance light travels within the time taken to generate a complete PRN code sequence of L chips. Equation 3.7 is used to calculate the ambiguity range of a L chip length PRN code ($L = 2^n - 1$).

$$R_{Ambiguity} = c\Big(\frac{2^n - 1}{f_{Chip}}\Big)\ m \tag{3.7}$$

Figure 3.8 shows a signal correlation at τ delay and a second signal correlation output at the delay of $\tau + \frac{L}{f_{Chip}}$. Since the PRN code pattern is periodic, if $\tau + \frac{L}{f_{Chip}}$ delay is applied to the template code, the PRN codes are once again aligned, and so the correlation output produces a second signal correlation peak. If the propagation distance to the target is larger than the ambiguity range $c\tau >> R_{Ambiguity}$, the absolute range of the target cannot be measured. A PRN code range measurement method can have a larger $R_{Ambiguity}$ by either using a longer PRN code sequence or reducing the chip frequency f_{Chip}.

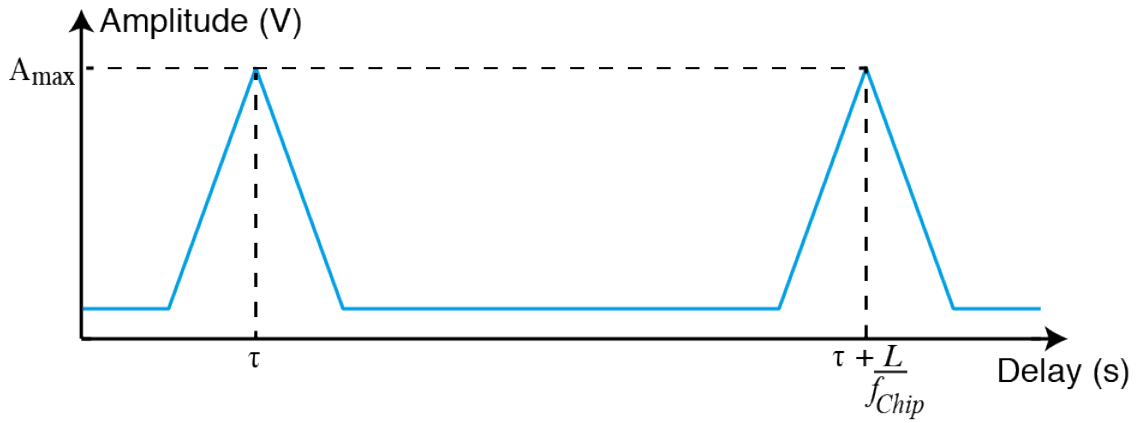

Figure 3.8: The ambiguity range of the PRN code depends on the code length L. At $\tau + L$ delay a second correlation peak is generated.

Time of flight measurement using a continuous wave laser amplitude modulated with PRN codes can provide improved accuracy and high unambiguous estimation of the parameter τ, by controlling the chip frequency and code length of the sequence. The PRN modulation method can also provide improved signal detection and ranging precision compared to pulse ranging methods [34, 38] due to the extended integration time t_i being larger than the pulse width T.

3.3 Doppler Shift of the Amplitude Modulated Optical Signal

Section 3.2.5 discussed a method to determine the position of a piece of space debris using a continuous wave laser. The outgoing laser light is amplitude modulated with an m-sequence PRN code, and the acquired signal is correlated with a template code to measure the parameter for the propagation delay τ. However, a piece of space debris in Earth's orbit is not a stationary target. Some space debris in LEO can travel as fast as 15 km/s [7]. Due to the target debris's motion, the propagation delay of the reflected PRN code changes as a function of time. This results in the Doppler shift of the modulated PRN code statistics.

3.3.1 Background on Earth Orbital Mechanics

The Doppler shift applied to the reflected optical signal is directly related to the orbital motion of the target space debris. This orbital motion can be approximated using Kepler's Laws of Planetary motion. Figure 3.9 illustrates the elliptical orbits of two planets, at different distances, from the Sun as described by Kepler's Laws of Planetary motion [132].

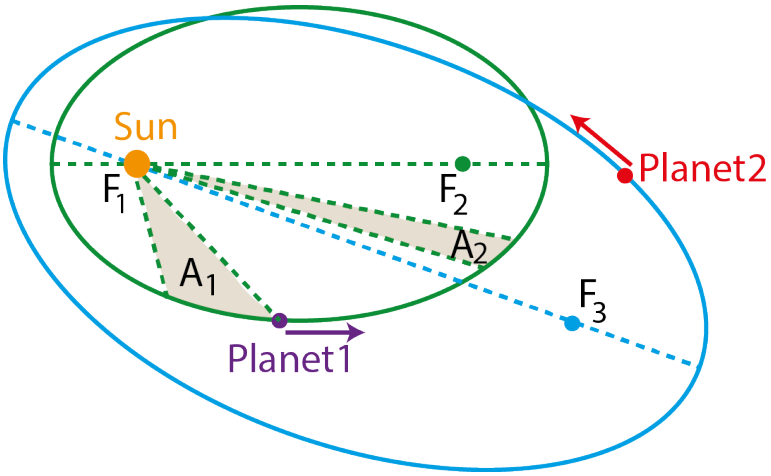

Figure 3.9: Illustration of Kepler's three laws with two planetary orbits.

1. Law 1: The orbit of a planet is an ellipse with the Sun at one of the 2 foci (F_1 and F_2 for planet 1).

2. Law 2: A line segment joining the planet and Sun sweeps equal areas during equal intervals of time (A_1=A_2).

3. Law 3: The square of the orbital period of a planet is proportional to the cube of the semi-major axis of its orbit.

The same three Kepler's Laws can also be used to describe the elliptical orbit of a piece of space debris about the centre of the Earth. Equation 3.8 shows the three main orbital properties of the orbiting space debris. These properties are the total distance of a complete orbit d_{orbit}, orbital velocity v_{orbit} and orbital period T_{orbit}. R_S is the altitude of the space debris from the surface of the Earth, R_E and M_E is the radius and mass of the Earth respectively, and G is the gravitational constant. R_E, M_E and G are constants in the orbital equations. Hence the orbital parameters are dependent on the altitude of the space debris R_S. For space debris orbiting the Earth in LEO, due to a smaller value of R_S, the debris has a larger orbital velocity v_{orbit} and shorter orbital period T_{orbit} than a similarly sized space debris in GEO.

$$\begin{aligned} D_{orbit} &= 2\pi(R_S + R_E) \\ v_{orbit} &= \sqrt{\frac{2GM_E}{(R_S + R_E)}} \\ T_{orbit} &= 2\pi\sqrt{\frac{(R_S + R_E)^3}{GM_E}} \end{aligned} \tag{3.8}$$

The ground station used to transmit and collect the optical signal is located on the Earth's surface. Therefore the point of reference must be changed from the centre of the Earth. The relationship to alter the reference point is illustrated in Figure 3.10. B is the location of the ground station on the Earth's surface, and A is the location of the orbiting space debris. θ is the angle of the space debris at position A from the centre of the Earth using the reference illustrated in Figure 3.10.

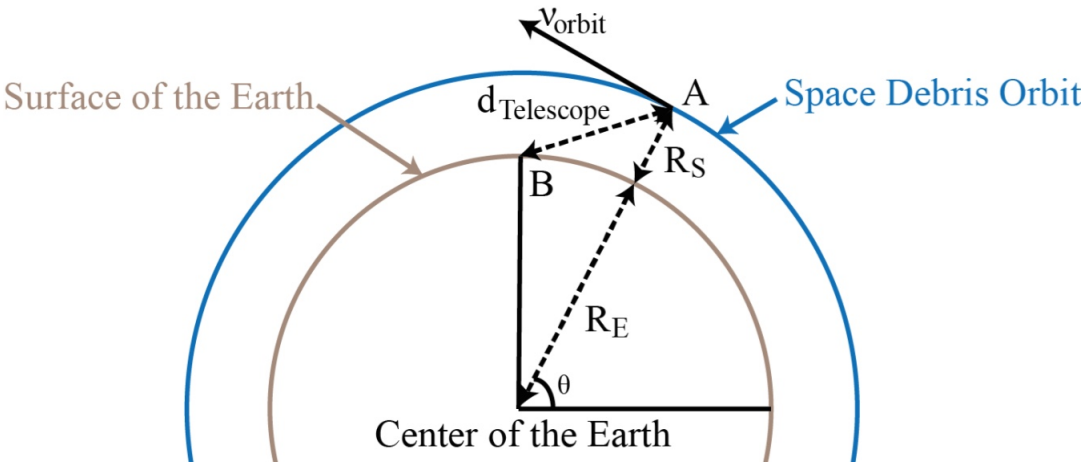

Figure 3.10: Geometry of a space debris orbiting around the Earth in reference to both the center of the Earth and the telescope on the Earth's surface at position B. $d_{Telescope}$ is the distance of the debris from the telescope.

From the telescope's point of view, the space debris appears to have different properties to that described by Kepler's Laws. The scenario that produces the most significant Doppler shift of the optical signal is when the LEO space debris travels directly overhead the telescope with a zenith angle equal to 0°. Using this assumption and that the telescope is able to track the space debris from horizon to horizon, Equation 3.9 is used to calculate the distance $d(t)_{Telescope}$ between the telescope and the space debris. As the angle θ varies with time, the distance $d_{Telescope}$ also changes.

$$d(t)_{Telescope} = \sqrt{[(R_E + R_S)\cos(\theta(t))]^2 + [(R_E + R_S)\sin(\theta(t)) - R_E]^2} \tag{3.9}$$

Figure 3.11 shows $d(t)_{Telescope}$ calculated for a piece of space debris observed by the ground telescope using Equation 3.9 for an altitude R_S equal to 500 km. This is the minimum altitude space debris the EOS telescope can track due to the slew rate of the telescope. For space debris at a lower altitude, the EOS telescope is unable to track the debris during its observational pass of the telescope. Figure 3.11 shows that $d(t)_{Telescope}$ is time-varying. Even though the space debris has a constant orbital velocity v_{orbit}, from the telescope's reference on the Earth's surface, the space debris has higher-order derivatives of motion such as acceleration and jerk.

The orbital properties presented in Figure 3.11 assumes the space debris has a stable circular orbit. In reality, the orbital velocity v_{orbit} is not constant and has an acceleration term [133]. The piece of space debris could have an unstable and complicated orbit and various external factors such as atmospheric conditions [134] could also alter the orbital properties. The observing telescope also has a relative velocity due to the rotation of the Earth. The time-varying distance of the space debris may be more complicated than presented in Figure 3.11.

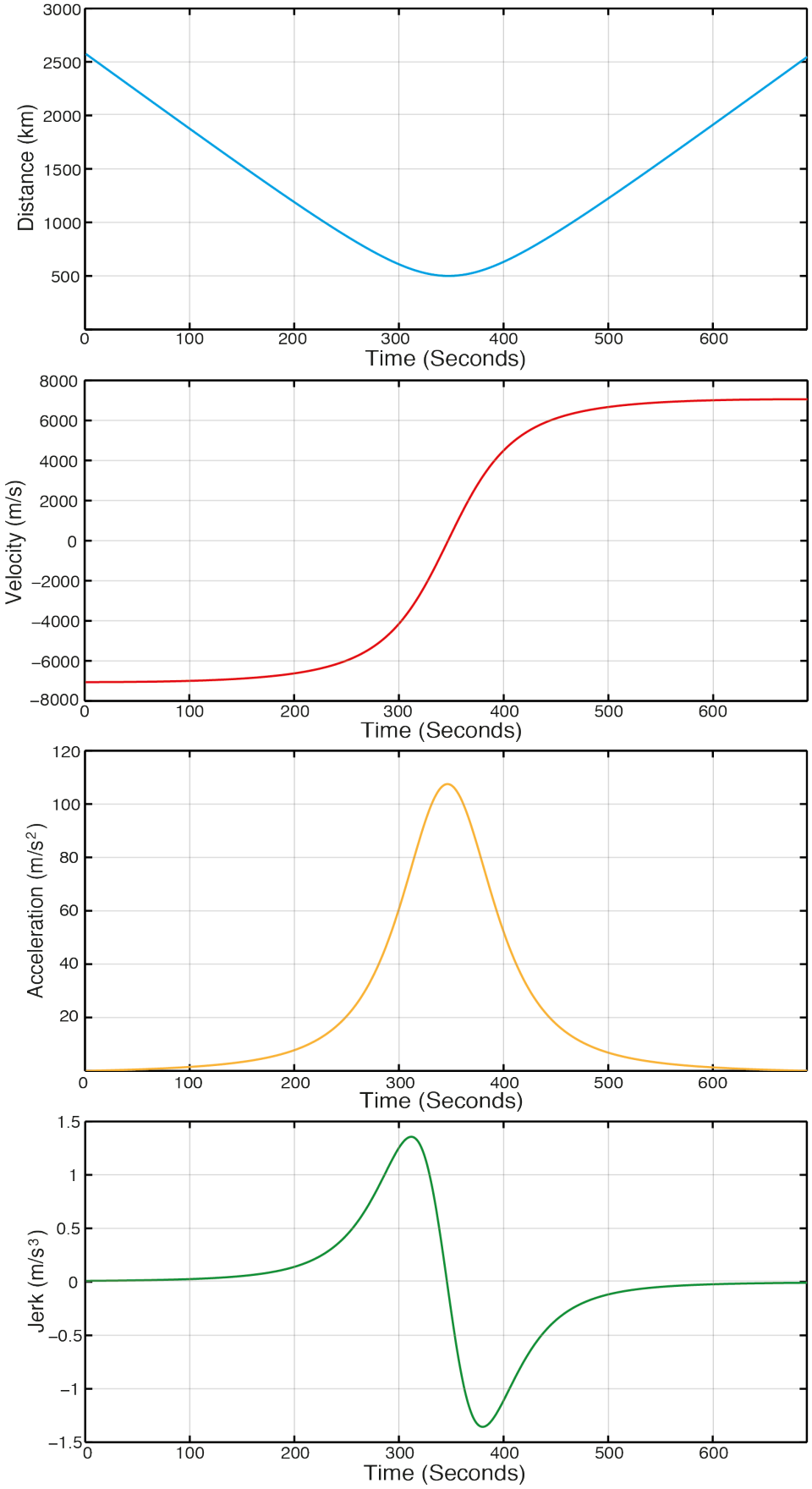

Figure 3.11: Derivatives of displacement of a satellite in reference to the optical telescope for a circular orbit with altitude of 500 km.

3.3.2 Doppler Shift of the Laser Frequency

The space debris' time-varying distance causes a Doppler shift of the optical signal laser frequency. A piece of space debris at an altitude of 500 km in LEO can cause a Doppler shift of the laser frequency by as much as ±8 GHz.

The Doppler shift of the optical signal laser frequency is ignored for the direct detection scheme in Chapter 4 since the laser frequency is not measured during signal detection and the Doppler shifted laser frequency does not impact the amplitude modulated PRN code.

For the coherent detection scheme in Chapter 5, used to amplify the amplitude modulated PRN code optical signal, the Doppler shift would change the beat note frequency and impact the amplitude modulated PRN code on the beat note. Satellite ranging applications of a coherent system overcome this challenge by either using a large bandwidth photodetector or by frequency tuning the local oscillator frequency using the known orbital information of the target debris to keep the beat note frequency within the photodetector bandwidth [62]. Many applications use frequency stabilised lasers with wide tuning ranges [62, 114, 135] in satellite ranging and other fields. A similar approach can be used to prevent the beat note frequency from being shifted beyond the bandwidth of the photodetector and lose the amplitude modulated PRN code. However, as discussed in Section 2.3.3, there are additional challenges in a space debris application that need to be considered in an attempt to measure the Doppler shift of the laser frequency.

3.3.3 Doppler Shift of the Modulated PRN Code

The space debris' time-varying distance observed from the telescope location causes the Doppler shift of the amplitude modulated PRN code collected by the telescope. Spacetime diagrams are used to explain the Doppler effect on the amplitude modulated PRN code as it provides the relationships of positions and time as measured in a coordinate system [136]. For simplicity, the two spacetime diagrams in Figure 3.12 explain the time-varying delay on single pulses of light transmitted at equal intervals of time. Each chip of a PRN code is represented as single pulses with the time interval of each chip also fixed. Therefore the spacetime diagram results are used to present the effect on the reflected pulses of the PRN code sequence by a target moving at a constant velocity equal to v m/s.

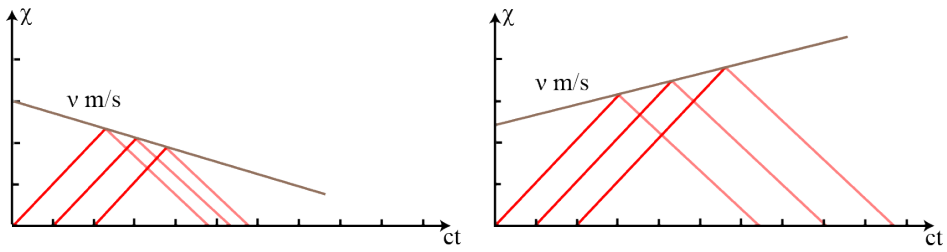

(a) Spacetime diagram showing the compression of the transmitted pulses.

(b) Spacetime diagram showing the stretching of the transmitted pulses

Figure 3.12: Spacetime diagram comparing affects on the arrival of pulses transmitted at equal intervals due to the change in propagation delay between the reflecting target and the observer.

In Figure 3.12a the target is moving towards the observing telescope with a constant velocity v m/s. As the distance between the target and the telescope reduces, so does the propagation delay of each subsequent pulse reducing the time interval between the arriving pulses. As the time width of each chip is reduced, the chip frequency of the amplitude

modulated PRN code collected at the telescope has increased. The acquired signal PRN code appears compressed compared to the original code.

In Figure 3.12b the target is moving away from the telescope with a constant velocity v m/s. As the distance between the target and the telescope increases, so does the propagation delay of each subsequent pulse increasing the time interval between the arriving pulses. As the time width of each chip is increased, the chip frequency of the amplitude modulated PRN code collected at the telescope has decreased. The acquired signal PRN code appears stretched compared to the original code.

Figure 3.13 compares the compressed and stretched code due to the Doppler shift of the chip frequency with the template PRN code. Even if the start of the PRN codes sequences is aligned to the original position of the space debris target, due to the time-varying delay, the Doppler shifted PRN code sequences move out of alignment with the template code.

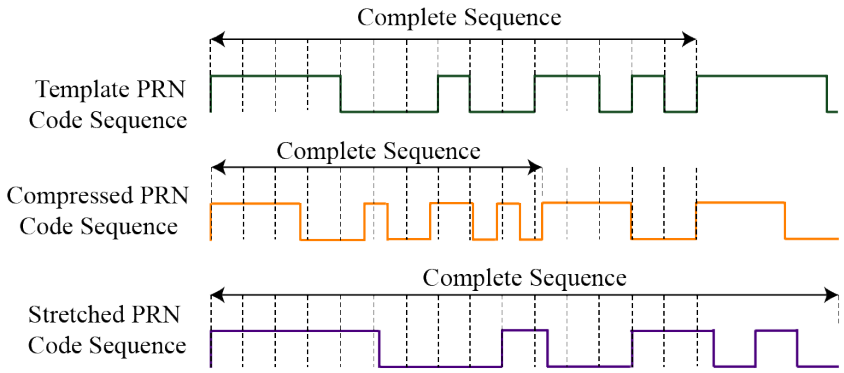

Figure 3.13: Comparing the original transmitted PRN code with a compressed and a stretched version of the code when the reflecting target has a constant velocity.

Figure 3.14 compares the impact on the reflected PRN code if the target has an acceleration term. Figure 3.11 shows that the space debris is observed to have an acceleration term which changes the rate of compression or stretching on the acquired PRN code at the receiver unlike in Figure 3.13 where the rate is constant. If either a longer PRN code or for larger integration time is chosen for the analysis, the acceleration term can reduce the signal correlation. This is further discussed in Section 4.1.9 for the bench-top experiment.

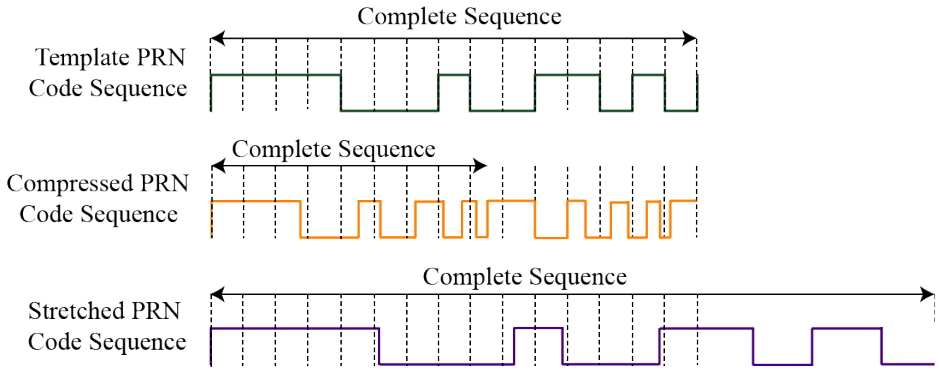

Figure 3.14: Comparing the original transmitted PRN code with a compressed and a stretched version of the code when the reflecting target has a constant acceleration.

3.3.4 Correlation with a Doppler Shifted PRN Code

As the space debris position changes with time, the propagation delay τ of the optical signal also varies with time. This time-varying delay causes a Doppler shift of the amplitude modulated PRN code's chip frequency. The PRN code from the acquired optical signal is no longer an identical sequence to the template code resulting in weaker correlation output.

The time-varying delay of τ can be estimated by measuring the τ for subsequent signal correlations. Assuming the simulation can collect the reflected signal from the moving target at 7 km/s for 1 s and the analysis divides the acquired signal into 4 consecutive segments. Each segment is used to estimate the parameter τ. Figure 3.15, shows the correlation output of the four consecutive segments where the integration time t_i is equal to 0.25 s. If the target is stationary, the τ parameter measurement is equal to τ_1 for each consecutive signal. However, for a moving target, the signal correlation is shifted in time resulting in a time-varying τ parameter measurement from τ_1 to τ_4 for the 4 consecutive signals. Estimating the time-varying delay τ using consecutive signal correlation is possible if the acquired signal has a high enough signal-to-noise ratio for signal detection.

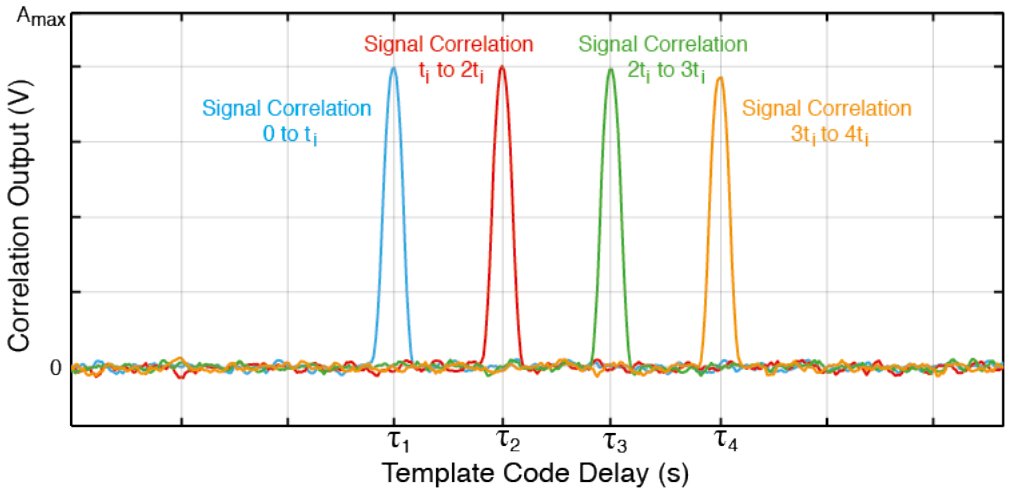

Figure 3.15: Comparing four consecutive simulated signal correlations where the detected signal is reflected from a target moving with velocity of 3000 km/s away from the telescope. The integration time is equal to 0.25 s.

Figure 3.16 compares, in simulation, the signal correlation from a signal reflected by a stationary target, to the signal correlation where the PRN code is a Doppler shifted by a target travelling at 7 km/s. Since less of the Doppler shifted PRN matches the template code, the signal correlation is reduced as seen in Figure 3.16.

Another observation of the two signal correlations in Figure 3.16 is that the signal correlation from the Doppler shifted acquired signal is broader than the 2 chip width than observed with the acquired signal without Doppler effect. The misalignment between the Doppler shifted PRN code and the template code due to the time-varying delay causes the signal correlation to spread into the surrounding delays. This spreading effect would be more significant for larger Doppler shifts of the acquired signal resulting in a smaller correlation peak output.

The simulated results in this section show that the time-varying delay of a target can be measured from consecutive signal correlations using the PRN code correlation method. This approach is similar to measuring the time-varying delay for consecutive pulses in the pulse laser ranging method. Amplitude Modulating the continuous wave laser would

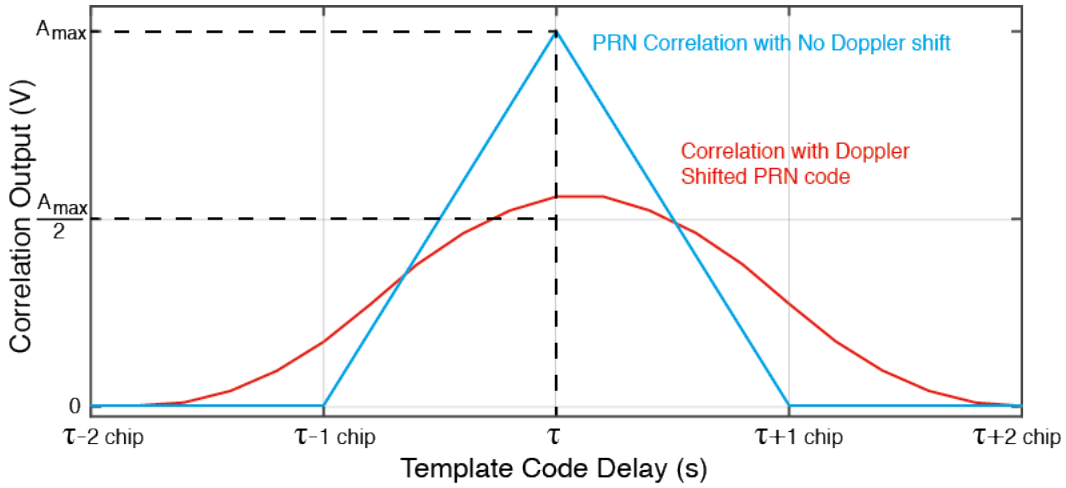

Figure 3.16: Simulation comparing the signal correlation for target moving with a constant velocity equal 7 km/s and a stationary target. The initial propagation delay of light between transmission and reception is τ.

provide an improvement in signal detection and range measurement precision due to a longer integration time than a single pulse. However, the result in Figure 3.16 shows that the correlation output is not ideal as the time-varying delay within the chosen integration time for the analysis causes a reduction in the signal correlation. This result can make signal detection more challenging for low signal-to-noise ratio optical signals.

3.4 Parameter Estimation to Measure the Time-Varying Delay

Section 3.3 showed that the position of the space debris is time-varying with higher derivatives of motion resulting in a Doppler shifted modulated PRN code. The discussions also showed the signal correlation is reduced due to the time-varying delay of the target debris. Using parameter estimation to apply the Doppler effect on the template code allows the matched filter analysis to:

1. Maximise the signal correlation improving low signal-to-noise ratio signal detection.
2. Estimate the time-varying delay parameters to provide a more accurate and precise measurement of the target's motion

3.4.1 Modelling the Time-Varying Delay of a Target

A model of the time-varying delay is used to apply the Doppler effect and adjust the template code. This model is referred to as the *Delay model*. Equation 3.10, together with Figure 3.17, shows the Delay model used to calculate the time-varying delay $\tau(t)$ of the optical signal between the telescope and the target. The time-varying delay can be described using the Taylor series. Equation 3.10 shows the calculation of the time-varying delay up to the first three terms of the Taylor series. d_0 is the initial distance between the target and the telescope, v_0 is the initial velocity of the target and a_0 is the initial acceleration of the target at time $t = 0$. Together the distance $d(t)$ changes with time depending on the term d_0, v_0 and a_0.

$$\begin{aligned}\tau(t) &= \frac{d(t)}{c} \\ &\simeq \frac{1}{c}\Big(d_0 + v_0 t + \frac{a_0 t^2}{2}\Big)\end{aligned} \tag{3.10}$$

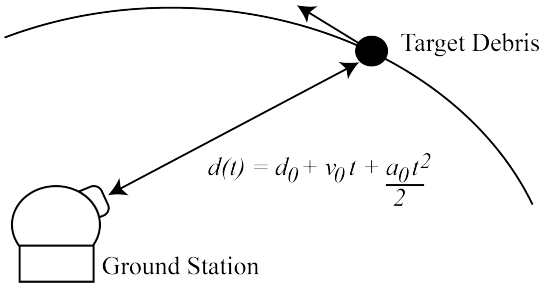

Figure 3.17: Illustration of change in the distance $d(t)$ between the ground telescope and target debris depending on the space debris' observable parameters d_0,v_0 and a_0.

Equation 3.11 shows the template code $x(t)$ generated by inserting the Delay model from Equation 3.10 to delay the PRN code $C(t)$.

$$x(t) = C(t - \tau(t)) \tag{3.11}$$

For a stationary target where both v_0 and a_0 are equal to zero ($v_0 = a_0 = 0$), $d(t) = d_0$ for all values of t. For a target moving with a constant velocity ($a_0 = 0$), the sign of the velocity parameter determines the direction of the target's motion. A positive velocity value causes $d(t)$ to increase with time, indicating that the target is moving away from the telescope. The template code $x(t)$ is a stretched version of the original code $C(t)$. A negative velocity value causes $d(t)$ to decrease with time, indicating that the target is moving towards the telescope. The template code $x(t)$ is a compressed version of the original code $C(t)$. Adding the acceleration term changes the rate at which the PRN code is compressed or stretched.

In a space debris application, the parameter values of d_0, v_0 and a_0 are not known. To estimate these parameter values, a parameter bank, with a range of possible values, is generated for each parameter. The different parameter values are used to generate the altered template code and produce a correlation. Section 3.4.2 and Section 3.4.3 show the impact of changing each parameter value on the template code and Section 3.4.4 shows the impact on the signal correlation output.

3.4.2 Estimating the d_0 Parameter Using Template Banks

Figure 3.18 shows a two-dimensional grid representing the template bank for the parameters d_0 and v_0. In Figure 3.18 only the parameter value for d_0 is changed and v_0 is fixed and equal to v_{SD}, the velocity of the target. Figure 3.18 shows three points on the grid with different d_0 values and compares the generated template code to the acquired optical signal.

As d_0 in Figure 3.18 is changed, the template code is shifted in time. The second template code example in Figure 3.18 is aligned to the acquired optical signal, unlike the first and third template codes where the time shift is smaller and larger than the propagation delay of the optical signal respectively. The second example would generate a larger signal correlation than the surrounding d_0 parameter values.

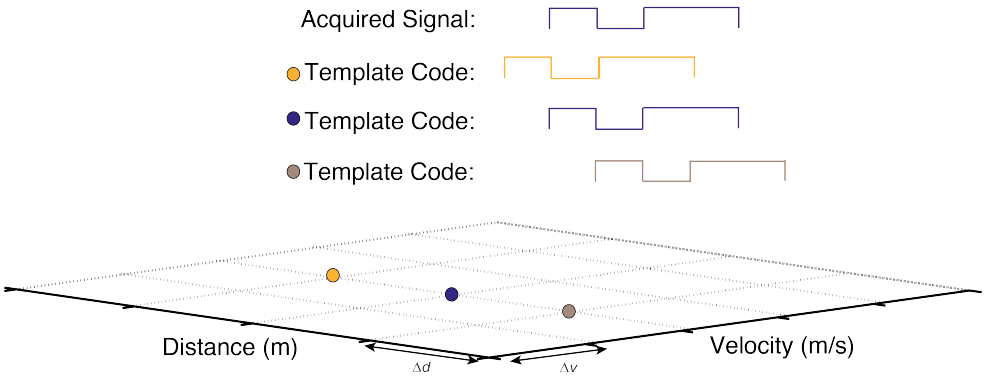

Figure 3.18: Matched template for both the distance and velocity parameters. Only the input value for the distance parameter is changed. The template code will be aligned to the acquired signal when the distance parameter value matches the target's distance.

3.4.3 Estimating the v_0 Parameter Using Template Banks

Figure 3.19 shows the same two-dimensional grid in Figure 3.18, but the three points on the grid show a change in the velocity parameter v_0. The distance parameter d_0 is fixed and equal to d_{SD}, the initial propagation distance to the target. Figure 3.19 also shows the impact of changing the v_0 parameter on the generated template code in comparison to the acquired optical signal.

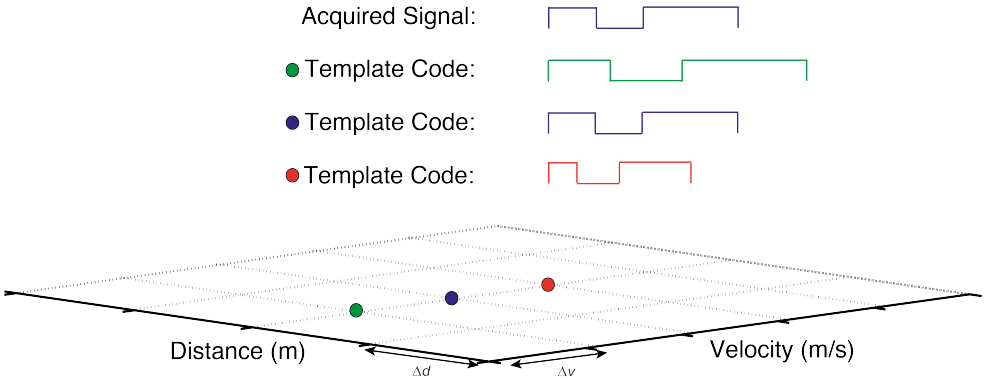

Figure 3.19: Matched template for both the distance and velocity parameters. The distance parameter input value is constant and only the velocity parameter value is changed. The template code remains aligned to the acquired signal for the chosen sequence length when the velocity parameter value matches the target's velocity.

By changing the input value v_0, a different time-varying delay is applied to the template code. The second template code example in Figure 3.19 is aligned with the optical signal. However, the first appears to be more stretched while the third template code appears to be more compressed compared to the optical signal resulting in both codes moving out of alignment with the acquired signal. The second template code would produce a more significant signal correlation of the three examples for the velocity parameter.

3.4.4 Cross-Correlation of Optical Signal with the Template Code

Figure 3.20 shows the signal correlation between the optical signal and the template codes by varying the d_0 and v_0 parameter values. The output of the signal correlation indicates the similarity of the template code parameter values to the parameters of the Doppler shifted PRN code modulated onto the optical signal. The template code parameter values that generated the most substantial signal correlation would likely present the optimal values for d_0 and v_0 that best matched the optical signal.

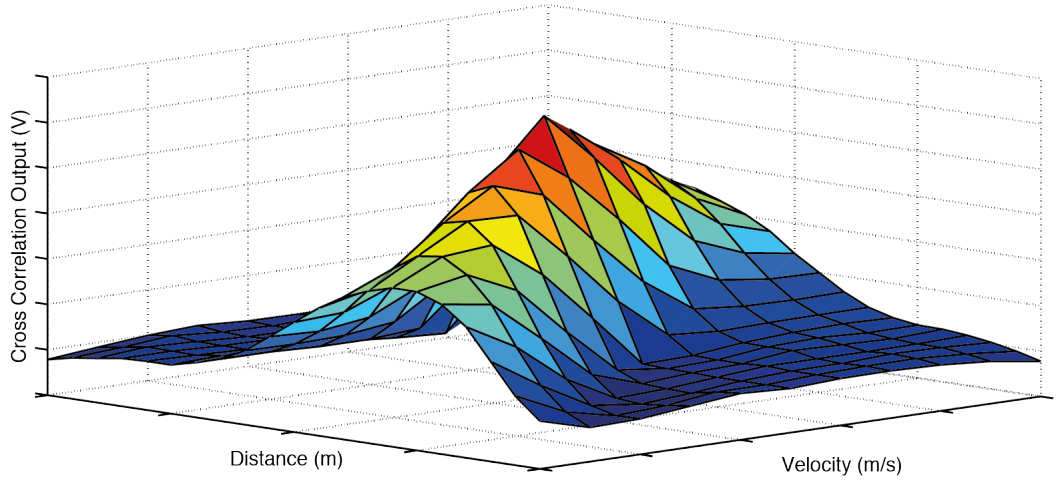

Figure 3.20: Cross-correlation between the return signal and template code for the input parameters d_0 and v_0.

Both the template spacing and noise in the correlation would impact the correct estimation of the optimal parameter values. If the optimal values are between the template points, the matched filter analysis cannot obtain the maximum signal correlation, and the optimal values are not measured. The smaller the template spacing the closer the matched filter analysis can identify the optimal values, but this also increases the computational requirement. Fluctuations in the signal correlation due to noise can cause errors in the correlation peak position and introduce errors in estimating the parameter values. An interpolation of the signal correlation or applying a fit that matches the shape of the signal correlation may provide a better estimate of the optimal parameter values and will be discussed further in Chapter 4.

3.4.5 Adding More Parameter Template Banks to the Delay Model

In practice, the higher-order effects will be included as needed in the analysis to maximise the signal correlation and improve estimating the time-varying delay parameters. The same approach introduced in Section 3.4.2 and 3.4.3 can be used with higher derivatives of motion from the Taylor series, such as the acceleration term a_0. Another parameter template bank can be added to account for the parameter. However, due to the limitation of the computational resources for the bench-top experiment, discussed in Chapter 4, these higher-order derivatives are not included in the analysis. The discussion in Section 3.5 will focus on the distance and velocity parameters. The bench-top experiment limitations are discussed in Chapter 4.

3.5 Factors That Impact the Matched Filter Analysis

The parameter estimation matched filter analysis presented in Section 3.4 is the proposed method to adjust the template code parameters and match the template code to the Doppler shifted acquired signal. Matching the template parameter values to the acquired signal improves signal detection and estimates the time-varying delay parameters to produce more precise information on the space debris' orbit. The parameter values used as inputs to the Delay model that generated the most significant signal correlation is the best estimate of the acquired signal time-varying delay.

The time-varying delay measurement accuracy and precision for the parameter estimation matched filter analysis depend on the slope of the signal correlation and the noise present in the correlation. The determinants that impact the signal correlation are:

1. Bandwidth effects
2. Chip frequency
3. Integration time
4. Amplitude noise

3.5.1 Bandwidth Effects

Up until this section, the chip frequency, f_{Chip}, of the PRN code generator is assumed to be equal to the analogue to digital (ADC) sampling frequency, $f_{Sampling}$. For the simulation of the matched filter analysis in this section, the chip frequency can be changed independently of the ADC sampling frequency. The ADC sampling frequency is equal to 1.5 GHz to match the bench-top experiment and the chip frequency is equal to 75 MHz. For the discussions in this section, both the ADC sampling frequency and the chip frequency can be altered.

The ADC sampling frequency sets the maximum bandwidth limit of the simulation. *Nyquist-Shannon sampling theorem* states that when digitising a continuous-time signal, the sampling frequency must be more than twice the bandwidth of the digitised signal [137]. In the bench-top experiment, discussed in Chapter 4 and 5, the bandwidth of the digitised signal is limited by the photodetector. The photodetector bandwidth is equal to 125 MHz [138] and the PRN code chip frequency is 75 MHz. The ADC chosen to digitised the signal is fixed at 1.5 GHz. Therefore the criteria set by the Nyquist-Shannon sampling theorem is satisfied.

For simplicity of the discussion, the ratio between the ADC sampling frequency and the chip frequency ($\frac{f_{Sampling}}{f_{Chip}}$) is called the *oversampling ratio*. This oversampling ratio must be larger than 2. Section 3.5.2 further discusses the impact of changing the chip frequency, and hence the oversampling ratio, on the matched filter analysis estimate of the delay and velocity parameters.

Other bandwidth effects come from the limited bandwidth of electronic devices used to generate, modulate and detect the optical signals. The bandwidth of these components limits the measurable chip frequency in the optical experiment. These limited bandwidths also affect the digitised PRN code. Figure 3.21 shows two simulated results comparing a digitised PRN code, that has a peak to peak amplitude equal to A, with the same PRN code passed through a high pass filter in Figure 3.21a with a cut-off frequency equal to 10 kHz and a low pass filter in Figure 3.21b with a cut-off frequency equal to 125 MHz.

These frequencies were chosen to match the photodetector used in the optical bench-top experiment in Chapter 4.

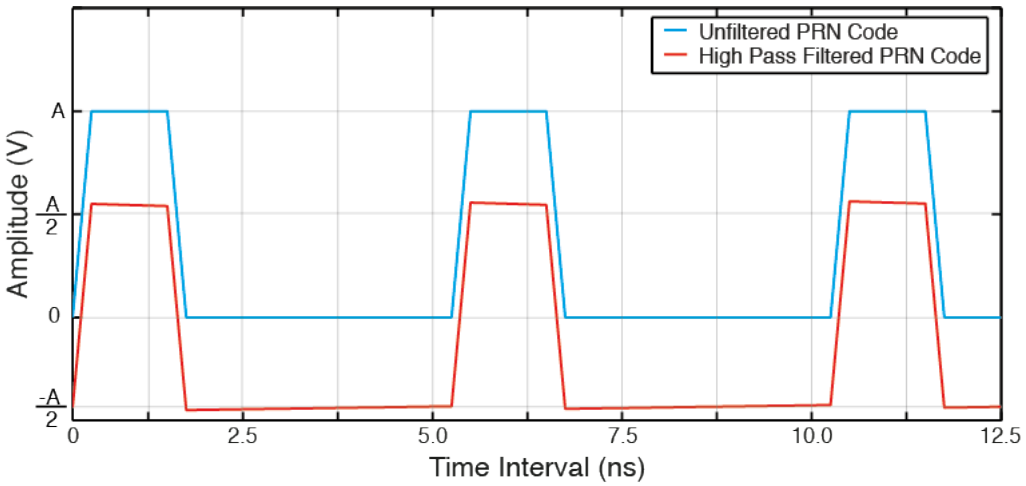

(a) Effect of 10 kHz high pass filtering (HPF) on the PRN code.

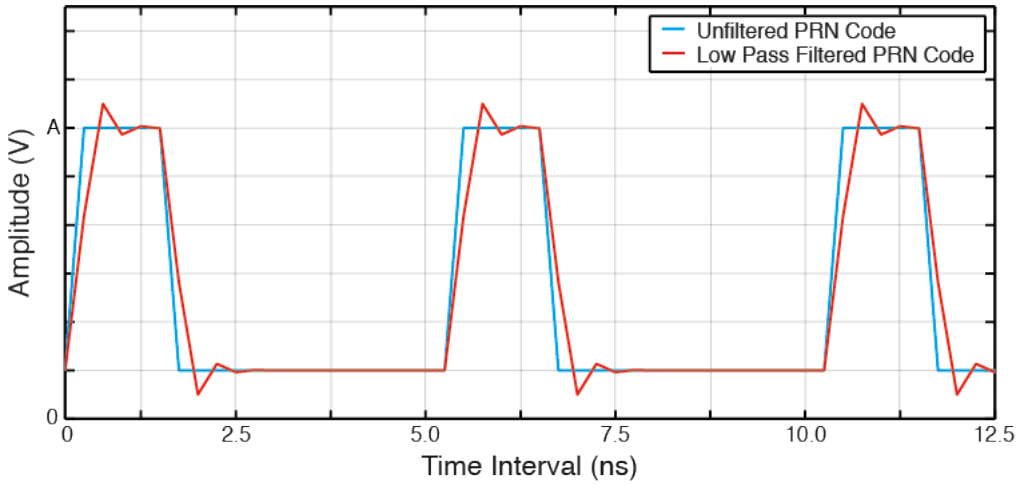

(b) Effect of 125 MHz low pass filtering (LPF) on the PRN code.

Figure 3.21: Simulating bandwidth affects on a PRN code sequence.

The unfiltered digitised PRN code in both Figure 3.21a and Figure 3.21b has transition between 0 and A and has a DC offset equal to $\frac{A}{2}$. The high pass filter in Figure 3.21a removes the DC offset of the signal, but the peak to peak amplitude of the code transitions is still instantaneous and equal to A.

The low pass filter in Figure 3.21b no longer outputs a PRN code with instantaneous transitions but has rounded edges. The unfiltered PRN code spectra is a $sinc^2$ function in the frequency domain with PRN code harmonics up until the maximum bandwidth limit set by the ADC sampling frequency. The low pass filter removes the higher frequency harmonics above 125 MHz. The loss of the higher frequency components results in a more rounded feature at the transition points with some low pass filter ripple effects. The peak to peak amplitude is equal to A with a DC offset of $\frac{A}{2}$. The loss of these higher frequency harmonics will produce a slightly smaller signal correlation than the unfiltered PRN code. If the chip frequency is larger than the cut-off frequency (125 MHz), the PRN code is filtered out; hence a 75 MHz chip frequency is chosen for the simulation.

The matched filter analysis also applies a second low pass filter to the digitised PRN code

before correlating the acquired signal with the template code. The low pass filter has a cut-off frequency equal to 375 MHz to reduce the data rate of the acquired PRN code without introducing aliasing. This step is done to overcome the limited computational resources available in the data acquisition and allowing for the acquisition of a longer sequence signal. The other alternative is using an ADC with a smaller sampling frequency, reducing the maximum bandwidth limit of the digitisation of the PRN code. Figure 3.22 shows the signal correlation, using the distance d_0 parameter template when the ADC sampling frequency is reduced from 1.5 GHz to 375 MHz compared to when the PRN code is digitised at 1.5 GHz and then low pass filtered to 375 MHz. No further bandwidth effects, such as from the photodetector, was added in the simulation.

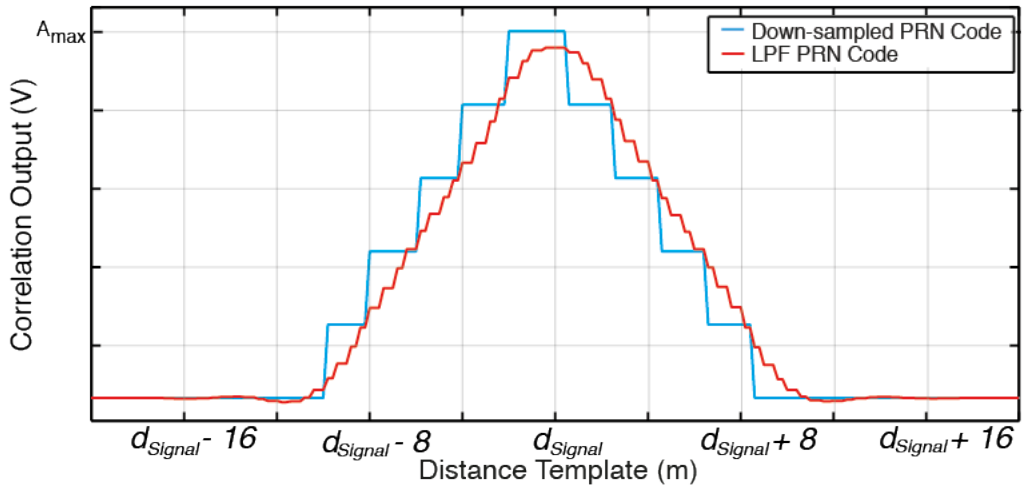

Figure 3.22: Comparing the cross-correlation when the sampling frequency is reduced from 1.5 GHz to 375 MHz to when the code is digitised at 1.5 GHz and then low pass filtered to 375 MHz.

Both signal correlations in Figure 3.22 show horizontal steps. However, the low pass filtered PRN code correlation has smaller width horizontal steps than the PRN code digitised at 375 MHz, for the same template spacing used in the analysis. The low pass filtered PRN code has retained the higher digitised sampling frequency information. In the simulated scenario, the accuracy of the matched filter analysis is reduced by going to a smaller sampling frequency than reducing the data rate by low pass filtering the digitised signal.

As discussed earlier, the low passed filtered PRN code correlation has a slightly smaller signal correlation peak than the unfiltered PRN code correlation. This is again due to the low pass filter filtering out the PRN code harmonics above 375 MHz.

In summary, different bandwidth effects must be considered in the matched filter analysis for the bench-top experiment. A higher sampling frequency is desirable to generate a PRN code with higher chip frequency, as will be discussed in Section 3.5.2, but electronic components in the experiment such as the photodetector also apply bandwidth limits on the digitised PRN code and impact the signal correlation. If the computational resources limit the data acquisition, rather than reducing the ADC sampling frequency, the digitised PRN code can be low pass filtered before the matched filter analysis.

3.5.2 Chip Frequency f_{Chip}

Chip frequency f_{Chip} is the rate at which the PRN code generator outputs a new binary value and determines the width of each chip ($\frac{1}{f_{Chip}}$ s). The chip frequency also affects the slope of the signal correlation when varying the parameters d_0 and v_0. In the presence

of noise, a steeper signal correlation slope results in a more precise estimate of the two parameters. The Full Width Half Maximum (FWHM) of the signal correlation slope is used to measure the steepness of the correlation slope for varying chip frequencies.

Figure 3.23 compares the signal correlation when varying only the distance d_0 parameter when using three different chip frequency to generate the signal and template codes. The integration time chosen for the matched filter analysis is equal to 1 ms. The simulated distance of the target is equal to d_{Signal}. The target is stationary with a velocity equal to 0 m/s. The sampling frequency of the ADC is equal to 1.5 GHz.

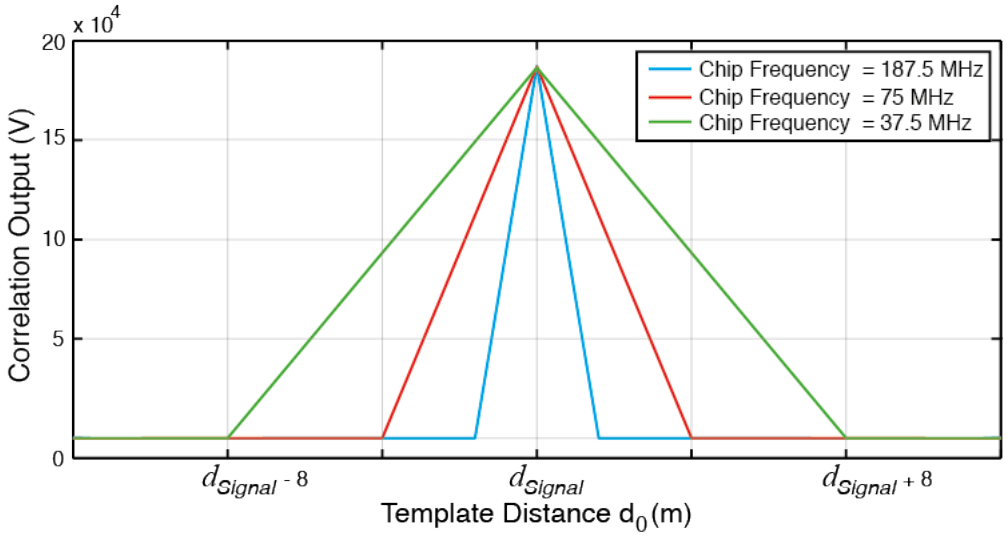

Figure 3.23: Comparing the signal correlation for different chip frequencies for varying delay d_0 parameter values.

From Figure 3.23, the FWHM of the signal correlation increases as the chip frequency is reduced. Equation 3.12 is used to calculate the FWHM of the signal correlation along the distance parameter d_0. The FWHM is equal to the distance the optical signal travels within 1 chip interval ($\frac{1}{f_{Chip}}$) at the speed of light c. The result shows that a higher chip frequency produces a signal correlation with a steeper slope when varying the distance parameter d_0.

$$FWHM_{Distance} = \frac{c}{f_{Chip}} \tag{3.12}$$

Figure 3.24 compares the signal correlation when varying only the velocity v_0 parameter when using the three different chip frequencies. As in Figure 3.23, the integration time chosen for the matched filter analysis is equal to 1 ms and the sampling frequency of the ADC is equal to 1.5 GHz. The initial position of the target in the simulation is equal to d_{Signal} but the target has a velocity equal to 10 km/s.

From Figure 3.24, the FWHM of the signal correlation increases as the chip frequency is reduced. Equation 3.13 is used to calculate the FWHM of the signal correlation along the velocity parameter v_0. The FWHM is a function of integration time t_i but in this section t_i is fixed to 1 ms.

$$FWHM_{Velocity} = 2\left[\frac{c}{t_i}\frac{1}{f_{Chip}}\right] \tag{3.13}$$

The conclusion of the simulated results in this section is a higher chip frequency produces

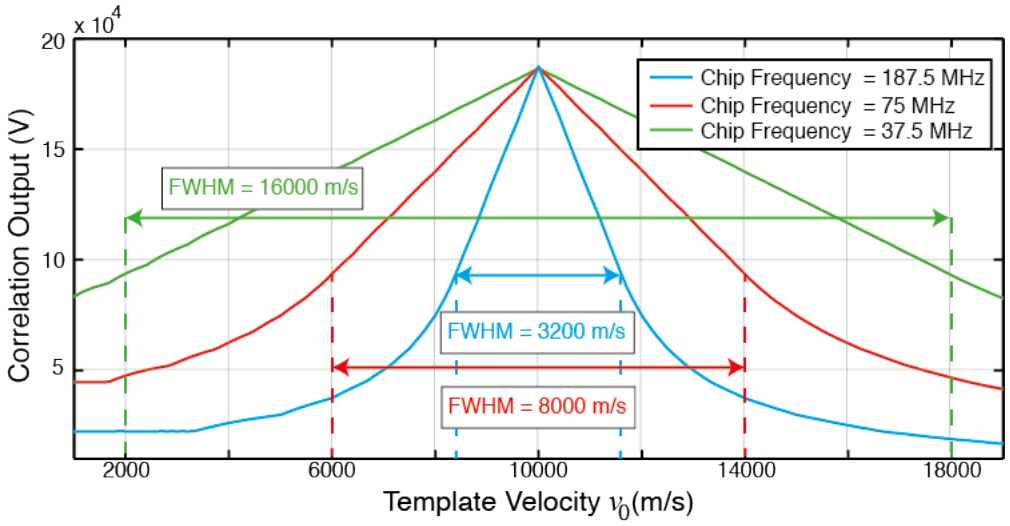

Figure 3.24: Comparing the signal correlation for different chip frequencies for varying velocity v_0 parameter values. The Full Width Half Maximum (FWHM) of the signal correlation is also shown.

a steeper signal correlation when varying both the distance d_0 and velocity v_0 parameters. It is crucial that the chip frequency must be at most half the ADC sampling frequency to satisfy the *Nyquist-Shannon sampling theorem*. However, in a bench-top experiment, bandwidth limitations from the electronic components may require the chip frequency to be smaller than half the ADC sampling frequency.

3.5.3 Integration Time t_i

Section 3.2.5 presented that the peak output value of the signal correlation increased linearly with the received signal power P_{Sig} and integration time t_i. For low signal-to-noise ratio optical signals, the integration time can be increased to improve both signal detection and the precision in estimating the d_0 parameter. Section 3.5.2 also showed that the FWHM of the signal correlation is also affected by the integration time when varying the velocity parameter v_0. Therefore increasing the integration should also reduce the FWHM.

Figure 3.25 compares the signal correlation for two integration times of 1 ms and 10 ms. The chip frequency of the simulation is equal 75 MHz and the ADC sampling frequency is equal to 1.5 GHz. The initial position of the target in the simulation is equal to d_{Signal} but the target has a velocity equal to 10 km/s. Figure 3.25a shows the signal correlation amplitude has increased from approximately 18×10^4 V to 18×10^5 V, increased by an order of magnitude. Figure 3.25b shows that the FWHM of the correlation peak has reduced from 8000 km/s to 800 km/s, reduced by an order of magnitude.

The results in Figure 3.25 confirm that the integration time is proportionally related to the maximum output amplitude of the signal correlation and inversely proportional to the FWHM. Both affect the steepness of the signal correlation. Therefore the precision of the estimated v_0 is expected to be related to square of the integration time t_i (t_i^2) while the precision in estimating d_0 with integration time is t_i.

The advantage of increasing the integration time is improved precision in the parameter estimate and if the smaller chip frequency had to be used in the bench-top experiment

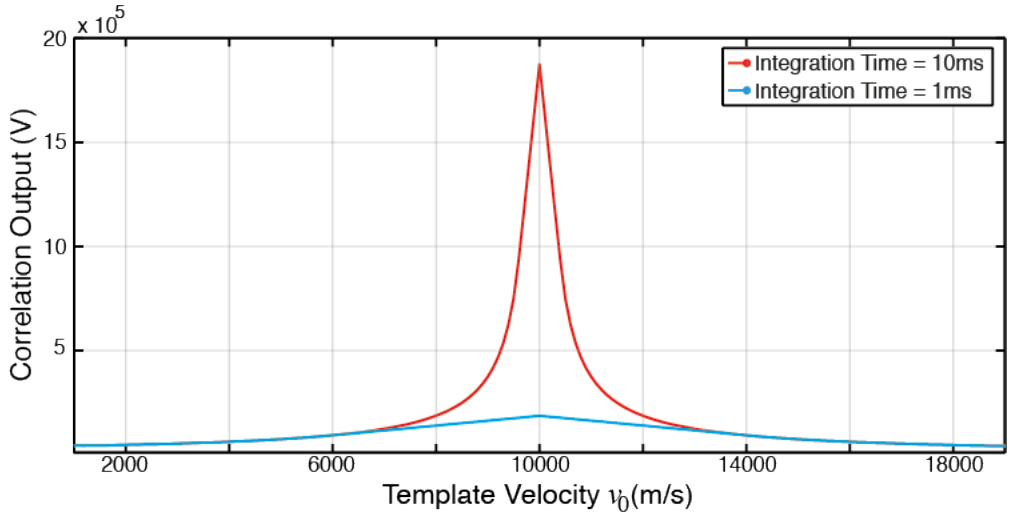

(a) Comparing the Signal Correlation for 1 ms and 10 ms integration times.

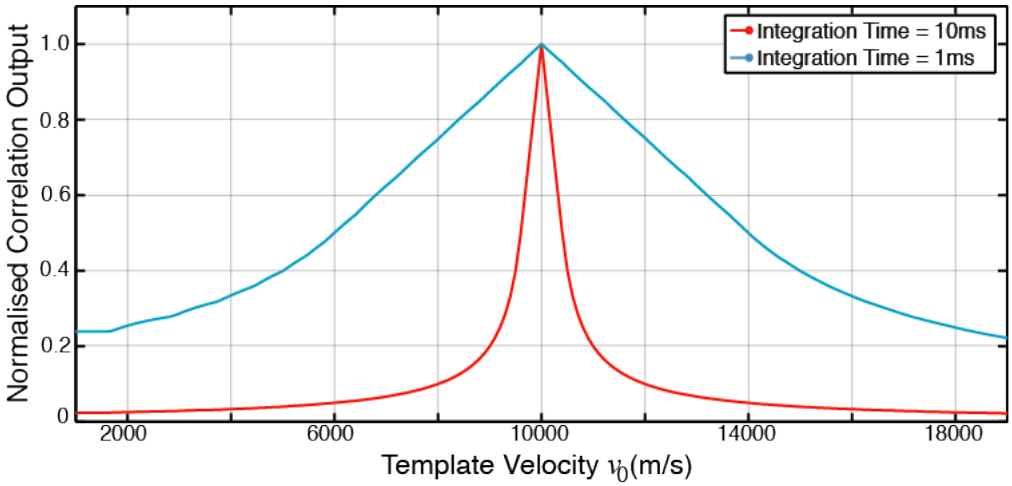

(b) Comparing the normalised signal correlation for 1 ms and 10 ms integration times.

Figure 3.25: Signal correlation using only a velocity template bank to vary v_0. The distance parameter value d_0 is fixed to d_{Signal}.

due to bandwidth limitations, a steeper correlation slope can be produced to improve the precision of estimating the time-varying delay. The disadvantage is the increased time taken to complete the analysis and may require additional computational resources.

3.5.4 Noise on the Signal Correlation

This section investigates the impact of both amplitude noise and clock noise in simulation on the signal correlation. Equation 3.14 shows the detected signal $y(t)$ where $C(t)$ is the PRN code sequence with both amplitude noise δA from the photodetector and clock noise δt added during acquisition of the signal. The simulation ignores the impact of laser frequency noise since the direct detection scheme does not measure the laser frequency.

$$y(t) = \alpha P.C(t - \delta t_{Clock}) + \delta A_{PD} \tag{3.14}$$

Figure 3.26 compares the signal correlation of a simulated signal both with and without

amplitude and clock noise. The photodetector noise added in the simulation is equal to 250 nW matching the noise floor of the photodetector used in the bench-top experiment. The timing jitter due to clock noise has a root mean square (RMS) of 1 ps. The clock noise is matched to the ADC used in the bench-top experiment. The impact of the timing jitter on the signal correlation in the simulation was much smaller than the impact of the amplitude noise from the photodetector. Therefore the amplitude noise from the photodetector is the dominant noise source in the signal correlation.

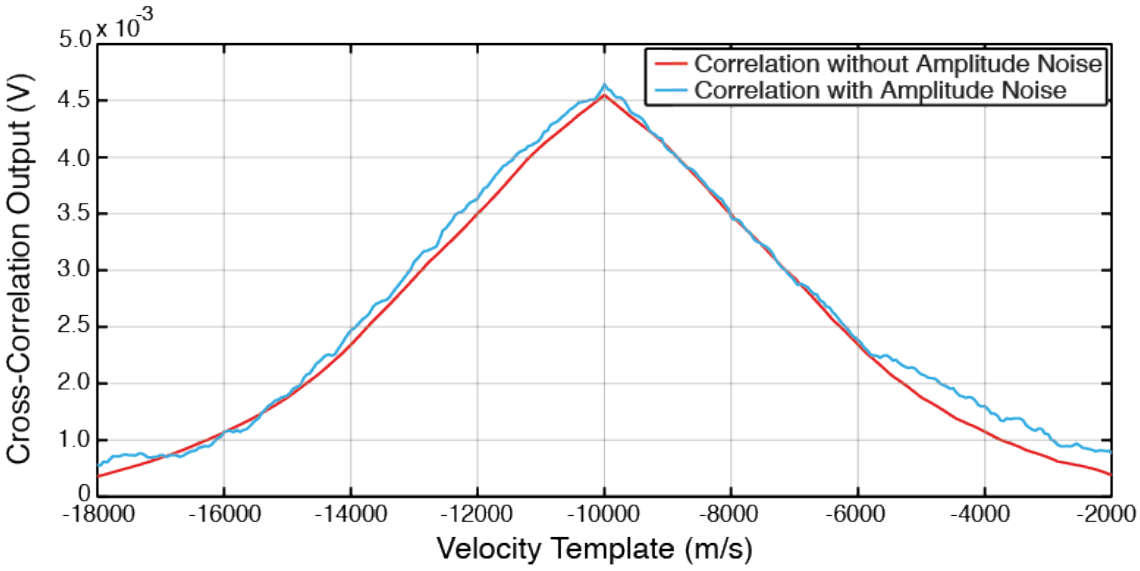

Figure 3.26: Comparing the cross-correlation of a simulated signal with amplitude noise and a simulated signal without amplitude noise with a template code.

Figure 3.26 shows that amplitude noise causes fluctuations in the signal correlation output. If the analysis searches for the maximum amplitude, the noise on the signal correlation will introduce an error in the measurement. However, despite the fluctuations due to amplitude noise, the signal correlation has the same shape as the signal correlation output without amplitude noise. An interpolation of the signal correlation would give a better estimate of the parameters in the presence of noise.

Equation 3.15 shows how the simulated amplitude noise impacts the correlation between the simulated signal and template PRN codes. σ_{Corr} is the noise in the signal correlation and σ_{PD} is the RMS of the noise source added to the simulated signal. Amplitude noise in the received signal will add incoherently in the correlation. The RMS of the fluctuation on the correlation depends on the amplitude of the noise sources added to the signal and the integration time t_i.

$$\sigma_{Corr} = \sigma_{PD}.\sqrt{t_i} \tag{3.15}$$

Equation 3.15 shows the noise added in the correlation is influenced by t_i but is not affected by the PRN code properties. Increasing the integration time t_i will increase the peak correlation output resulting in a steeper correlation slope and improve the parameter estimate. But increasing the value of t_i will also increase the noise fluctuations on the correlation by $\sqrt{t_i}$.

3.6 Chapter Summary

The discussion in Chapter 3 presented using a matched filter analysis with parameter estimation to estimate the different parameters of the target's time-varying delay with the chapter discussions focused on the distance and velocity parameters. Matched filters have been used in several applications to measure unknown parameters of a modulated signal including in range measurement applications. The signal correlation provides a measure of the similarity between the signal and the template. The template that produced the highest signal correlation most likely has the same PRN code parameters as the signal.

The chapter also discusses the PRN code properties such as the chip frequency and integration time, as well as bandwidth effects, that can impact the range and time-varying delay measurement.

Direct Detection Scheme

This chapter presents the bench-top experimental layout and results for the direct detection scheme. The bench-top experiment generates an m-sequence pseudo-random noise (PRN) code and amplitude modulates the sequence onto the continuous wave laser. The chip frequency of the modulated PRN code is altered to model the Doppler effect from a moving reflecting target. The Doppler shifted acquired signal is passed through the matched filter analysis to estimate the time-varying delay applied onto the continuous wave laser. Table 4.1 shows the chosen PRN code properties and bench-top experiment parameters. Section 4.1 discusses and justifies the values selected for the experiment.

Parameters	Parameter Values
ADC sampling frequency $f_{sampling}$	1.5 GHz
PRN chip frequency f_{chip}	75 MHz
PRN code length L	32 767 chips
PRN code period $Tcode$	0.44 ms
Matched filter analysis frequency f_{MF}	375 MHz
Laser wavelength λ	1064 nm
Photodetector NEP	22.5 pW/$\sqrt{\text{Hz}}$
Photodetector bandwidth	125 MHz
Background Photon Noise Source	120 μW
Max. Integration time	0.1 s

Table 4.1: Table summarising the parameters chosen for the optical bench-top experiment.

4.1 Experimental Layout

The bench-top experiment aims to simulate the time-varying delay of the amplitude modulated PRN code when used in space debris ranging applications. Setting up an optical bench-top experiment that modelled a moving space debris target was achieved by breaking the problem up into a smaller number of tasks:

1. Generate a Doppler shifted PRN code sequence

2. Amplitude modulate the continuous wave laser with the PRN code
3. Add different noise sources that limit current space debris ranging
4. Measure the PRN modulated optical signal at different optical powers
5. Estimate the time-varying delay using the matched filter analysis
6. Collect statistics on the precision in estimating the time-varying delay
7. Characterise how integration time t_i and received signal power P_{Sig} impacts the precision of the measurement.

4.1.1 Pseudo-Random Noise Code Generation

The first step in the bench-top experiment is generating a Doppler shifted PRN code sequence. A Keysight N4970A Pseudo-Random Bit Stream (PRBS) generator [139] is used to generate an m-sequence PRN code. The PRBS can generate a PRN code with a chip frequency between 50 MHz and 12.5 GHz. Figure 4.1 shows an external clock frequency (f_{PRBS}) is supplied to the PRBS device to control the chip frequency (f_{Chip}) of the PRN code sequence. This approach of changing the chip frequency of the PRBS output allows the bench-top experiment to emulate the Doppler shift of the PRN code caused by a space debris target.

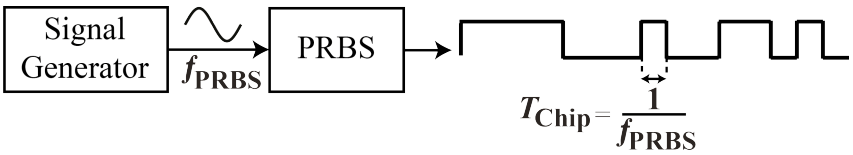

Figure 4.1: Block diagram of the PRN code generation from the PRBS where the chip frequency f_{chip} is supplied from a signal generator.

Figure 4.2 shows the power spectrum density of the PRN code sequence with a 75 MHz chip frequency. The spectrum shows a $sinc^2$ function, with the first null occurring at 75 MHz. This chip frequency was used in the experiment as the unaltered chip frequency, without Doppler shift. The chip frequency was chosen as it is well within the photodetector bandwidth (125 MHz) and the analogue to digital converter (ADC) sampling frequency (1.5 GHz) is an integer multiple of the chip frequency.

Figure 4.2 also shows two unexpected harmonics at 75 MHz and 150 MHz. These harmonics are generated by the PRBS generator when generating the PRN code but are not a property of the PRN code as both harmonics were not observed in the simulated PRN code spectra presented in Figure 3.6 and when generating the PRN code on an FPGA module. The harmonics are observed to always occur at the nulls of the spectra even when changing either the chip frequency or code length of the PRN code. The harmonics would not impact the matched filter analysis as the spectrum of the template code will have nulls close to these frequencies, significantly reducing the amplitude of the harmonics, and the remaining magnitude of these harmonics is spread into multiple frequencies when correlated with the template code.

Table 4.2 shows the different sequence lengths generated by the PRBS. As discussed in Section 3.2.5, both the code length and chip frequency affects the ambiguity range. Ideally, the ambiguity range is larger than the maximum propagation distance of the optical signal, which for an LEO space debris target is up to 5500 km. In practice, the 23-bit PRN code

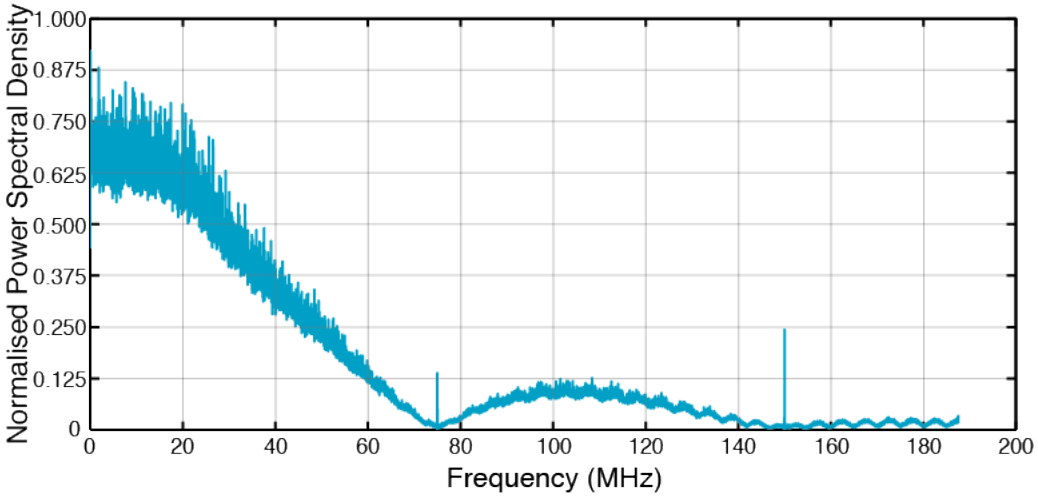

Figure 4.2: Frequency Spectrum of a 15-bit PRN code generated by the PRBS and recorded using the ADC. The acquisition stage is discussed in more detail in Section 4.1.8.

with 75 MHz chip frequency is suitable for space debris ranging, with a code repetition rate of approximately 0.11 s and ambiguity range of 33 000 km, but due to the limited computational resources available for the experiment that allows maximum acquisition time of 0.1 s the 15-bit PRN code was chosen. The code repetition rate of a 15-bit PRN code with a 75 MHz chip frequency is approximately 0.4 ms. The ambiguity range of the modulated optical signal is equal to 130 km. This decision would not affect the experimental results but if used in a space debris application, the absolute range of the debris cannot be measured.

Code Length L	Polynomial	f_{code} @ $f_{chip} = 10$GHz
$2^7 - 1$	$x^7 + x^6 + 1$	78.7MHz
$2^{10} - 1$	$x^{10} + x^7 + 1$	9.78MHz
$2^{15} - 1$	$x^{15} + x^{14} + 1$	305kHz
$2^{23} - 1$	$x^{23} + x^{18} + 1$	1.19kHz
$2^{31} - 1$	$x^{31} + x^{28} + 1$	4.67Hz

Table 4.2: Keysight N4970A PRBS code pattern properties. [139]

The proposed system would generate a Doppler shifted PRN code with the aim of amplitude modulating onto the continuous wave laser. The modulated optical signal acquired by the ADC would contain the Doppler shifted code, and the matched filter analysis is used to measure the Doppler shift applied at the PRN code generation stage of the experiment.

The main limitation of this proposed method is its inability to synchronise the start of the PRN code with the signal acquisition, introducing a delay called L_{Code} that is different for two different acquired signals with amplitude modulated PRN codes from the bench-top experiment. The delay estimate for each acquired signal would be different even though the propagation distance within the bench-top experiment is the same. The optical layout of the bench-top experiment aims to solve this challenge and remove the effect of L_{Code}.

4.1.2 Fibre Mach-Zehnder Interferometer

The Doppler shifted PRN code is amplitude modulated onto the output of the continuous wave laser using a Fibre Mach-Zehnder interferometer. Figure 4.3 shows the optical layout of the bench-top experiment. The optical source is a 1064 nm wavelength laser with a maximum output intensity of approximately 200 mW. The output of the laser is passed through a beam splitter to control the input optical power entering the Fibre Mach-Zehnder interferometer to protect the components used in the interferometer from high optical intensities. The second output from the beam splitter is blocked in Figure 4.3 but will be used as the local oscillator for the coherent detection scheme discussed in Chapter 5.

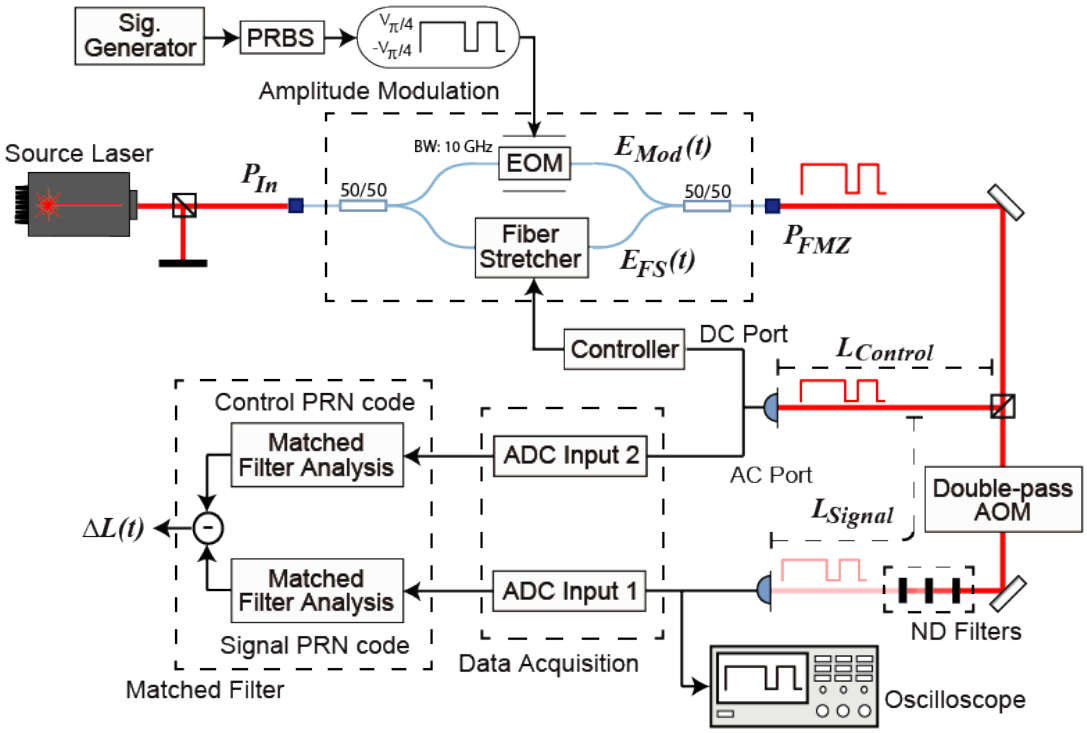

Figure 4.3: Optical layout of the direct detection scheme bench-top experiment. The continuous wave laser is amplitude modulated with PRN codes using a Fibre Mach-Zehnder and used to measure the both the L_{Signal} and $L_{Control}$ propagation distances.

The Fibre Mach-Zehnder interferometer was built using off-the-shelf Electro-optic modulator (EOM) and fibre stretcher, and connected using fibre splitters, as shown in Figure 4.3. In the Fibre Mach-Zehnder interferometer, the input optical power is split equally into two arms using a 1×2 fibre splitter. Equation 4.1 shows the electric field of the two arms from the fibre splitter. The electric field equations contain amplitude, frequency and phase information on the optical signal for each arm. The first path is called the *phase modulation arm* represented by the electric field $E_{Mod}(t)$ where an EOM is used to phase modulate the laser with the PRN code (ϕ_{PRN}). The second path is called the *fibre stretcher arm* containing a fibre stretcher with the electric field $E_{FS}(t)$. The fibre stretcher is used to control the optical path length of the fibre stretcher arm.

$$\begin{aligned} E_{Mod}(t) &= E_{Mod} e^{i(2\pi f_{Laser} t + \phi_{Mod} + \phi_{PRN})} \\ E_{FS}(t) &= E_{FS} e^{i(2\pi f_{Laser} t + \phi_{FS})} \end{aligned} \tag{4.1}$$

In Equation 4.1 $\phi_{Mod} = \frac{2\pi f_{Laser}}{c} L_{Mod}$ and $\phi_{FS} = \frac{2\pi f_{Laser}}{c} L_{FS}$. Changing the path length

L_{Mod} and L_{FS} alters the phase of the optical beam in the phase modulation and fibre stretcher arm respectively.

An Electro-Optic Modulator (EOM) is used to phase modulation the PRN code onto the phase modulation arm. In an EOM, the laser beam propagates through a crystal where the refractive index of the crystal is changed by applying an electric field [140]. The change in the refractive index causes a change in the phase delay of the propagating laser beam and hence a phase shift of the output laser beam. The voltage supply needed to apply a π phase shift to the input laser beam is called V_π. In the experiment, a Photline EOM (NIR-MPX-LN-10) is used with 10 GHz bandwidth and V_π value equal to 5.5 V [141].

The fibre stretcher in the fibre stretcher arm contains a piezoelectric element [142] whereby applying an input voltage causes mechanical stress in the material, resulting in small path length changes in L_{FS} [143]. The path length change depends on the input voltage, and the fibre stretcher can apply path length changes within the optical laser wavelength (1064 nm). An alternative approach is using a Modulator Bias Controller to lock the operating point of the Photline EOM to ensure a stable operation over time and environmental conditions. However this equipment was not available during the experiment.

Figure 4.3 also shows a double-pass AOM optical configuration in the signal path. The double-pass AOM can be used to introduce additional frequency noise into the optical signal. This will be discussed further in Section 5.2.4 for the coherent detection scheme.

4.1.3 Output Signal of the Fibre Mach-Zehnder Interferometer

The two arms of the Fibre Mach-Zehnder interferometer are recombined using a 2x1 fibre coupler. The two arms electric fields interfere with each other, and the output optical signal of the Fibre Mach-Zehnder P_{FMZ} is shown in equation 4.2. The resulting interference pattern depends on the phase difference $\phi_{\Delta L}$ of the two arms [144], which is equal to $\phi_{Mod} - \phi_{FS}$, and the PRN code phase modulation ϕ_{PRN}.

$$P_{FMZ}(t) = \frac{P_{In}}{2} + \frac{P_{In}}{2}\cos(\phi_{\Delta L} + \phi_{PRN}(t)) \tag{4.2}$$

Using Equation 4.2, Figure 4.4 shows the change in the output optical power P_{FMZ} as the phase difference $\phi_{\Delta L}$ of the two path lengths is changed. Assuming $\phi_{\Delta L}$ can be controlled and set to a fixed phase offset equal to $\frac{3\pi}{2}$, phase modulating the PRN code onto the phase modulation arm can produce the desired amplitude modulated PRN code.

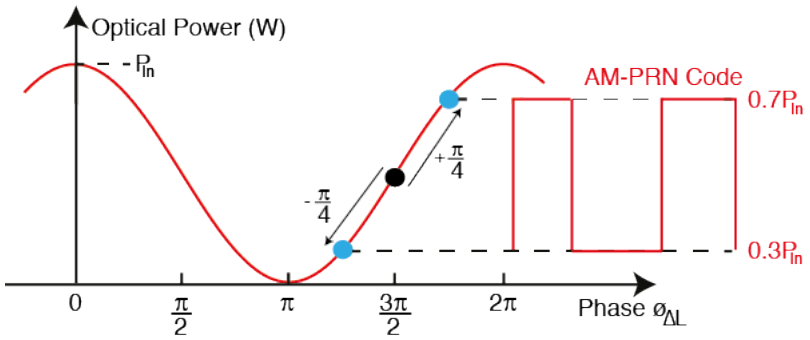

Figure 4.4: Illustration of the interference of two laser beams as a function of the difference in the phase of the two laser beams. The phase difference $\phi_{\Delta L}$ is equal to $\frac{3\pi}{2}$ and a $\pm\frac{\pi}{4}$ phase modulation is added using ϕ_{PRN}.

The desired phase difference is achieved by controlling the input voltage to the optical fibre stretcher in the fibre stretcher arm to change L_{FS} so that $\phi_{\Delta L}$ is equal to $\frac{3\pi}{2}$. As shown in Figure 4.4 a $\pm\frac{\pi}{4}$ phase modulation was chosen since the change in the output optical power is approximately linear between $\frac{7\pi}{4}$ and $\frac{5\pi}{4}$. Together with Figure 4.4, Equation 4.3 shows the impact of the phase modulation on the Fibre Mach-Zehnder interferometer output intensity.

$$P_{FMZ}(t) = \begin{cases} \frac{P_{In}}{2} + \frac{P_{In}}{2}\cos\left(\frac{3\pi}{2} + \phi_{PRN}\right) \approx 0.7P_{In}, & \text{if } \phi_{PRN} = \frac{\pi}{4} \\ \frac{P_{In}}{2} + \frac{P_{In}}{2}\cos\left(\frac{3\pi}{2} - \phi_{PRN}\right) \approx 0.3P_{In}, & \text{if } \phi_{PRN} = -\frac{\pi}{4} \end{cases} \tag{4.3}$$

If the modulating PRN code has a binary value of 1, a $\frac{\pi}{4}$ phase modulation is applied to the beam in the phase modulation arm and shifts the phase to $\frac{7\pi}{4}$. The output interference amplitude is equal to $0.7P_{In}$. If the modulating PRN code has a binary value of 0, a $-\frac{\pi}{4}$ phase modulation is applied to the beam and shifts the phase to $\frac{5\pi}{4}$ producing an output amplitude of $0.3P_{In}$. As the phase of the interference pattern changes due to the PRN phase modulation, so does the output intensity of the Fibre Mach-Zehnder interferometer, resulting in the amplitude modulation of the continuous wave laser.

Figure 4.4 assumes that the phase difference $\phi_{\Delta L}$ is fixed to $\frac{3\pi}{2}$. In the bench-top experiment, the optical fibre path length of each arm changes independently due to temperature fluctuations and vibrations [145]. These path length changes cause fluctuations in the optical power when the two paths interfere. The second use of the fibre stretcher in the bench-top experiment is to maintain the desired $\frac{3\pi}{2}$ phase offset.

The control layout using the fibre stretcher is shown in Figure 4.5. The low-frequency fibre fluctuation is obtained from the DC port of the control path photodetector, between 0 Hz to 50 kHz. The 50 kHz bandwidth of the DC port must be larger than the bandwidth of the controller presented in Figure 4.5. The controller uses an integrator in the adder/subtractor to maintain the desired path length difference of the two arms. Some of the amplitude modulated PRN code harmonics are present in the DC port but these harmonics did not disrupt the locking process during the time taken to complete the experiment.

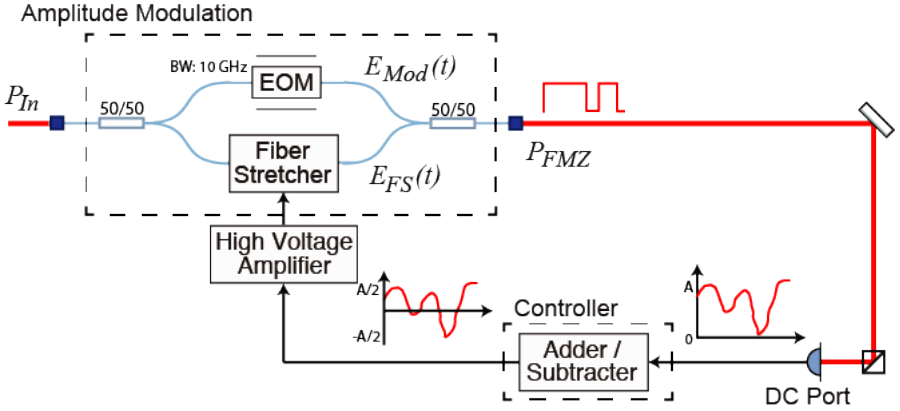

Figure 4.5: Illustration of the fibre fluctuation captured from the control arm photodetector and passed through the adder/subtracter. The output of the adder/subtracter is an error signal after passed through a high-voltage amplifier is fed back to the fibre stretcher.

As shown in Figure 4.5, due to the fibre fluctuations, the optical power will randomly fluctuate between the maximum and minimum intensity. The optical intensity measured from the DC port is passed through an adder/subtracter. The adder/subtracter is used as an integrator and to apply an offset in the path length of the fibre stretcher arm. By

shifting the fluctuations of the DC output to half the fringe height, a $\frac{3\pi}{2}$ phase difference is achieved. The output of the adder/subtracter is the error signal. This error signal is first passed through a high-voltage amplifier before used as input to the fibre stretcher.

If there is no fluctuation in the optical intensity, the output of the error signal is equal to 0, and the $\frac{3\pi}{2}$ phase difference is maintained. However, if there is an optical fluctuation, the non-zero error signal causes the fibre stretcher to change the path length of the fibre stretcher arm to maintain $\frac{3\pi}{2}$ phase difference. The sign of the error signal is used to either shorten or increase the path length of the arm. The control layout was able to remove large optical fibre fluctuations in the bench-top experiment. The residual optical intensity fluctuation is considered as optical intensity noise in the bench-top experiment.

In the ideal case, a π modulation depth would be applied to have a full intensity modulation of the laser between P_{In} and 0. However, the current control layout, could not apply the full intensity modulation for two reasons:

1. Fluctuations in the π phase modulation depth due to fluctuations in the PRN code amplitude from the output of the PRBS
2. Fluctuations in the phase difference $\phi_{\Delta L}$

Both these can cause intensity fluctuations. This translates to a PRN code with varying amplitude modulation depth. Instead the bench-top experiment focuses on the more linear section of the cosine term between $\frac{7\pi}{4}$ and $\frac{5\pi}{4}$ phase difference shown in Figure 4.4.

The matched filter analysis takes into account the modulation depth used in the bench-top experiment and uses the change in the optical power of the amplitude modulated PRN code as the received signal power P_{Sig} for the results in Section 4.2 and Section 4.3.

4.1.4 Using Different Propagating Path Lengths

The PRN amplitude modulated continuous wave laser, from the output of the Fibre Mach-Zehnder, is split into two separate paths:

1. *Control path* - used to measure the optical intensity fluctuations for the fibre stretcher control layout and to measure $L_{Control}$ path length
2. *Signal path* - used to measure L_{Signal} path length

The start of the PRN code generation from the PRBS is not synchronised with the data acquisition which means each time the PRN code is collected at either the control path or signal path photodetector, the PRN code delay L_{Code} is different, influencing the individual path length measurement. The control path length measured using the PRN code is the sum of the PRN code delay L_{Code} and physical path length $L_{Control}$ on the bench-top experiment while the signal path length measured using the PRN code is the sum of the PRN code delay L_{Code} and physical path length L_{Signal}. Since the PRN code delay L_{Code} is the same in both path lengths, calculating the path length difference ΔL removes the L_{Code}. Equation 4.4 shows the calculation of ΔL from the two PRN code path length measurements.

$$\begin{aligned} \Delta L &= (L_{Code} + L_{Signal}) - (L_{Code} + L_{Control}) \\ &= L_{Signal} - L_{Control} \end{aligned} \tag{4.4}$$

On the bench-top experiment the physical path length measured for L_{Signal} is equal to 2.75 m and for $L_{Control}$ is equal to 0.675 m. Therefore the physical path length difference ΔL is 2.075 m.

4.1.5 Attenuating The Optical Signal Power

In the signal path, the laser beam is attenuated using a combination of neutral density (ND) filters to reduce the optical signal power to test the matched filter analysis for varying received signal powers. In equation 4.5, I_O is the incident intensity, I is the intensity after the filter, and OD is the optical density of the neutral density filter.

$$\frac{I}{I_O} = 10^{-OD} \tag{4.5}$$

Table 4.3 lists the ND filters, with the calibrated OD measurements, used in the bench-top experiment. The calibration was performed by passing a 27.5 mW optical signal through each of the ND filters and measuring the attenuated optical power. The results in Table 4.3 shows that the specified value of OD is not equal to the calibrated measurement of the ND filter attenuation. Hence, the calibrated measurement of each ND filter is used when calculating the optical power attenuation in the bench-top experiment.

OD Value	Output Power I_O	Calibrated ND Measurement
0.2	20.1 mW	0.16
0.5	9 mW	0.49
1.0	2.63 mW	1.02
2.0	0.257 mW	2.03
3.0	20.23 μW	3.13

Table 4.3: Calibrated ND filters used in the optical experiment with $I = 27.5$ mW.

4.1.6 Photodetector

Two Newport 1811 free-space photodetectors are used to detect the amplitude modulated optical signal in both the control path and signal path of the bench-top experiment. The photodetector splits the measured optical intensity into two frequency bandwidths. The DC port produces signals between DC and 50 kHz. This port is used to measure small fluctuations in the optical intensity from the Fibre Mach-Zehnder interferometer. The AC port produces signals between 25 kHz and 125 MHz. This port contains the higher frequency information of the optical signal including the amplitude modulated PRN code. Due to the limited bandwidth of the photodetector, the PRN code obtained from the AC port is equivalent to passing the signal through both a high pass filter and low pass filter.

The AC output uses a transimpedance gain equal to 40 000 V/A [138]. Together with the responsivity of the photodetector, equal to 0.70 A/W at 1064 nm [138], the conversion from optical power in watts to the output voltage is equal to 28 000 V/W. In the bench-top experiment, as presented in Figure 4.3, the output of the AC port of the signal path photodetector is split into two outputs using an RF splitter. One output of the splitter is first passed through a 2 dB attenuator before an analogue to digital converter (ADC)

is used to digitise the signal. The attenuator is used to attenuate back reflections of the signal within the coaxial cable and reduce the amplitude of a false signal correlation due to the back reflections. The second output of the splitter is monitored on an oscilloscope to confirm the presence of the amplitude modulated PRN code before the ND filters are inserted in the signal path.

In the absence of a background photon noise source, photodetector noise is the dominant noise source in the bench-top experiment for the direct detection scheme. The minimum noise equivalent power (NEP) of the photodetector is 22.5 pW/$\sqrt{\text{Hz}}$ between 10 MHz and 200 MHz [138]. Equation 4.6 explains the relationship between the root mean square (RMS) of the photodetector noise σ_{PD} in Watts with the bandwidth B and NEP of the photodetector. The bandwidth B of the photodetector is equal to 125 MHz. Therefore the calculated σ_{PD} is approximately equal to 2.5×10^{-7} W.

$$\sigma_{PD} = NEP\sqrt{B} \tag{4.6}$$

Figure 4.6 shows the measured noise floor σ_{PD} of the Newport 1811 photodetector used as the signal path photodetector in the bench-top experiment measured using a spectrum analyser compared with the calculated noise floor using equation 4.6, taking into account the conversion rate and attenuation of the photodetector signal by the spectrum analyser. The measured photodetector noise from the spectrum analyser is shown to be slightly smaller at 75 MHz than the calculated photodetector noise.

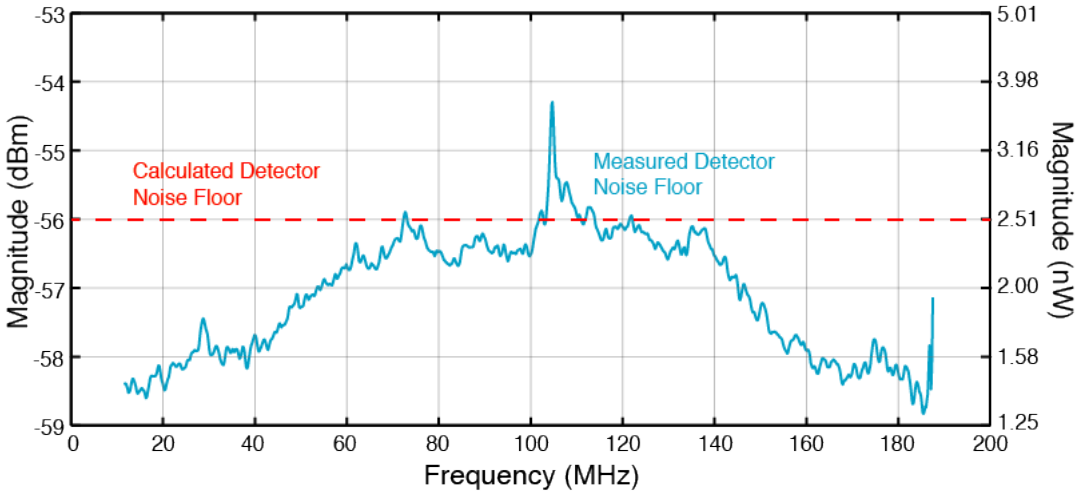

Figure 4.6: Comparing the measured noise floor of the Newport 1811 photodetector using a spectrum analyser to the calculated noise floor of the detector. The calculated noise floor takes into account the 20 dB attenuation of the signal by the spectrum analyser.

4.1.7 Background Photon Noise Source

Background photon noise is the most significant noise source for current pulsed laser ranging systems and could prevent operations during the day [33, 70]. Hart et al. discussed that the daytime sky surface brightness is typically between 4 and 5 magnitudes/arcsec^2 [146]. For the EOS telescope, where the experiment was carried out, this corresponds to 5×10^5 photons/ms/arcsec^2 [146]. Assuming the EOS telescope at Mount Stromlo collects the same amount of background photons and has 1 arcsec telescope resolution, the background source power is approximately equal to 90 pW.

For the bench-top experiment, the background source must be above the Newport 1811 photodetector noise floor to investigate the matched filter analysis performance when the dominant noise source is background photon noise. To achieve this the background noise source optical power must be more than the 90 pW.

Figure 4.7 shows the addition of a halogen lamp to the bench-top experiment to act as a background photon noise source. The halogen lamp is an incoherent light source with a broadband emission in the visible and near infra-red spectral regions (400 to 2200 nm). The optical output power is approximately 50 mW. A beam splitter is used to combine the background photon noise with the optical signal before the photodetector.

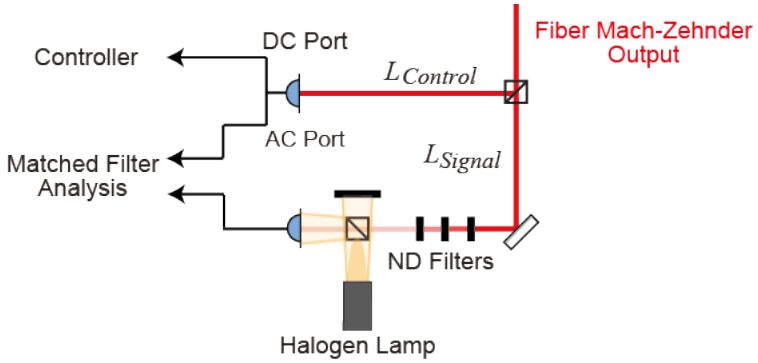

Figure 4.7: Optical layout similar to Figure 5.4 but with a Halogen lamp added to the experiment to add background photon noise to the acquired signal.

Figure 4.8 compares the frequency spectrum of the photodetector noise to the background photon noise produced by the halogen lamp. The lamp increased the noise floor of the spectrum by approximately 1.25 dB at the PRN code chip frequency ($f_{Chip} = 75$ MHz). Since the halogen lamp is an incoherent light source, the output beam has a large beam divergence. No further increase in the background photon noise was possible as the saturation limit of the photodetector was reached at 120 μW [138].

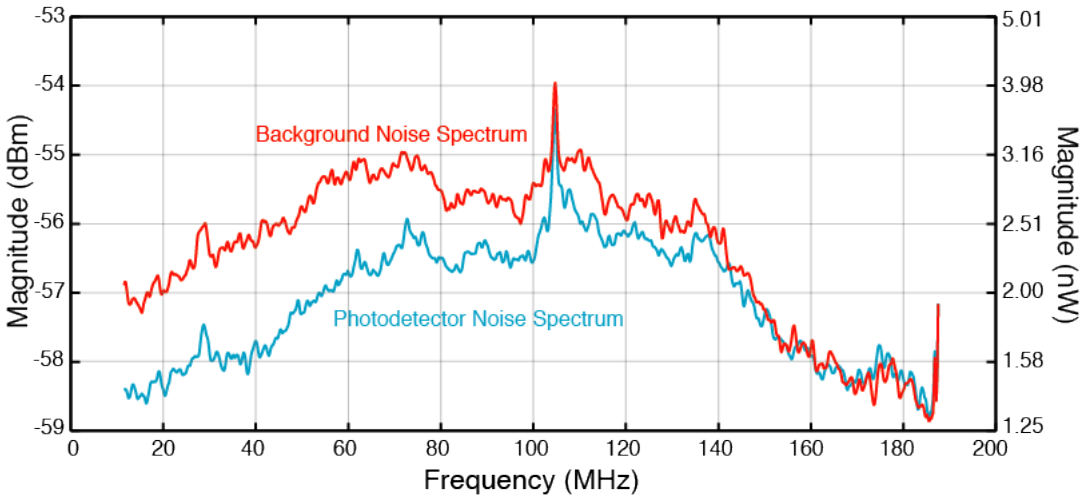

Figure 4.8: Comparing the noise floor of the 1811 photodetector to the addition of background photons from the halogen lamp in the signal path.

Using the increase in the noise floor in Figure 4.8, the background photon noise source is the dominant noise source in the experiment with an approximate power of 120 μW. This background photon noise source is much larger than the expected 90 pW background noise source calculated for the EOS telescope.

4.1.8 Data Acquisition

Section 4.1.2 to Section 4.1.7 discussed the bench-top experimental layout where the Doppler shifted PRN code from the PRBS generator, discussed in Section 4.1.1, is amplitude modulated onto the continuous wave laser. The optical signal is measured using a photodetector. This section discusses the digitisation of the photodetector output by an analogue to digital converter (ADC) to be used in the matched filter analysis.

Figure 4.9 illustrates the data acquisition of a photodetector measurement from both the signal and control paths and the data transfer of the acquired signal to a host computer for the matched filter analysis.

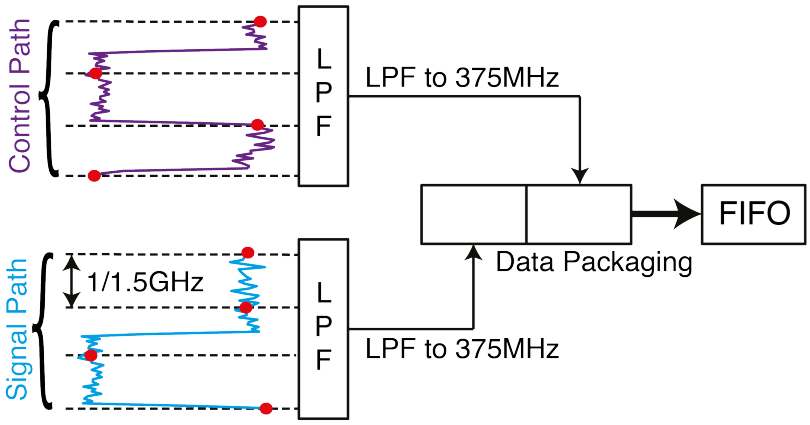

Figure 4.9: The red dots identify the points the two signals are digitised by the ADC. The digitised signal from the photodetector is decimated using a low pass filter (LPF) to the desired data rate before packing and passing through a FIFO for saving on the host computer.

The optical signals measured at both the signal and control path photodetectors are digitised using a NI-5771 analogue to digital converter. The NI-5771 ADC has two analogue input ports called AI0 and AI1. AI0 is used to digitise the optical signal from the signal path photodetector, and AI1 is used to digitise the optical signal from the control path photodetector. Both analogue input ports can digitise the incoming photodetector measurement at 1.5 GHz [147]. The digitised signal is converted to an integer value, which we refer to as a *count*, with the conversion rate of 5 mV/count. However, due to the ADC design, the control path measurement is digitised at AI1 approximately 0.33 ns after the signal path measurement is digitised at AI0. This timing offset adds a fixed path length bias of 0.1 m when measuring the path length difference of ΔL. Therefore the calculated ΔL of the two path lengths in the bench-top experiment using the PRN code measurement is expected to be equal to 2.175 m.

A National Instruments 7966r FlexRio FPGA is used to low pass filter the 1.5 GHz digitised signal to 375 MHz and transfer the data to a host computer for matched filter analysis. The FPGA onboard First In First Out (FIFO) memory is used to store the digitised signals while the data is transferred to the host computer. The rate at which data is read out of the FIFO is slower than the rate the data is stored in the FIFO. Eventually, the FIFO is filled, and no more ADC digitised data can be acquired. This is the main purpose of reducing the data rate of the digitised signal and allow for longer acquisition time. With the onboard FPGA memory of 256 MB [148] and reduced data rate of 375 MHz, the maximum acquisition time for the signal path is 0.1 s and 0.44 ms for the control path. Since the optical signal from the control path is not attenuated, a lower data acquisition time is sufficient to measure $L_{Control}$ accurately.

4.1.9 Matched Filter Analysis Procedure

The preceding sections up until this point of Chapter 4 presented and discussed the bench-top experiment. The Doppler shifted PRN code is generated using a PRBS generator to model a moving space debris target with a velocity of v_{SD}. The PRN code is modulated onto the output optical beam of a continuous wave laser source using a Fibre Mach-Zehnder interferometer. The output of the interferometer is split into the signal path and control path. The optical signal in each path is acquired using two photodetectors and digitised using an analogue to digital converter. This section presents the matched filter analysis procedure used to analyse the acquired signals to estimate the propagation distance of both paths and the time-varying delay applied in the bench-top experiment.

Section 3.4. discussed the parameter estimation, with simulated results, to measure both the position and change in position of a reflecting target. Equation 3.10, referred to as the Delay model, is used to calculate the time-varying delay. In the Delay model, the parameter d_0 is used to determine the initial position of the target, v_0 is the target's initial velocity and a_0 is the target's initial acceleration. The calculated time-varying delay is applied to the template code, and the correlation with the signal indicates how well the input values for the three parameters match the optical signal's time-varying delay.

The same approach is used for the bench-top experiment to determine both the path lengths L_{Signal} and $L_{Control}$ and the time-varying delay used to Doppler shift the modulating PRN code chip frequency. The matched filter analysis is performed in post-processing using MATLAB. Figure 4.10 shows the layout of the matched filter analysis procedure used for the acquired signal from the signal path to determine L_{Sig} and the time-varying delay applied in the bench-top experiment.

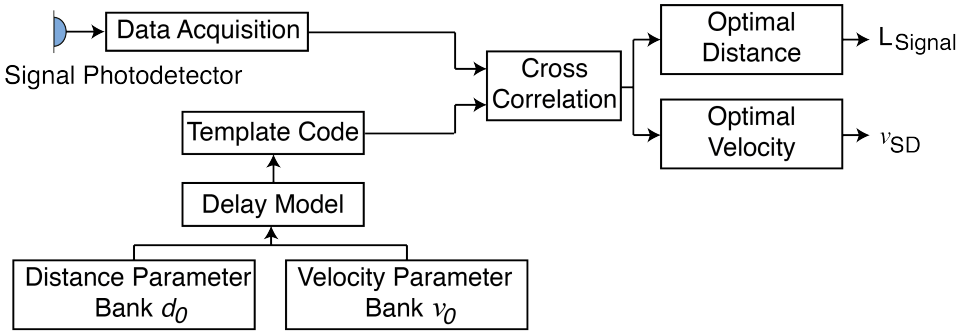

Figure 4.10: Block diagram of the signal acquired from the photodetector and correlated with the template code. In this example, the matched filter analysis aims to estimate the distance and the time-varying delay of a target due to the target's velocity v_{SD}.

A parameter bank containing a range of possible input values is produced for two of the Delay model's parameters d_0 and v_0. The calculated time-varying delay from these two parameter values is used to generate the altered template code. The template code is generated at a time interval equal to 1.5 GHz and is then low pass filtered to 375 MHz to match the template code generation with the acquisition of the signal. The template code is correlated with the acquired signal from the bench-top experiment, and the parameter values that create the most significant correlation output is the matched filter estimate of the two parameters. In Figure 4.10, d_0 estimates L_{Signal} and v_0 estimates the simulated space debris velocity v_{SD}. The acceleration term a_0 is equal to zero since the bench-top experiment only used a constant v_{SD} to Doppler shift the modulating PRN code. The same analytical steps are taken to estimate $L_{Control}$.

For 1 ms integration time, generating one template code and correlating with a digitised sig-

nal takes approximately 3 s of computational time, increasing for higher integration times. The total matched filter analysis time also depends on the total number of templates used in the analysis. The most straightforward analysis approach is a *brute-force* method which generates a broad range parameter bank for each parameter with a small spacing between the values. The disadvantage is that this method is time-consuming and computationally intensive because of the large number of templates used for the analysis. Approaches used for other different applications handling a large number of templates can be utilised for the matched filter analysis [121].

Figure 4.11 shows the analysis approach chosen for the bench-top experiment. Since the parameter values used in the test are known, the parameter bank for the distance and velocity parameters can have a smaller range of values around the optimal value of each parameter. The parameter estimation also utilised multiple matched filter analysis steps where for each subsequent step the range of the parameter bank and the spacing between the parameter values is smaller than the previous analysis step. This approach reduced the analysis time and computational requirements compared to the brute-force approach.

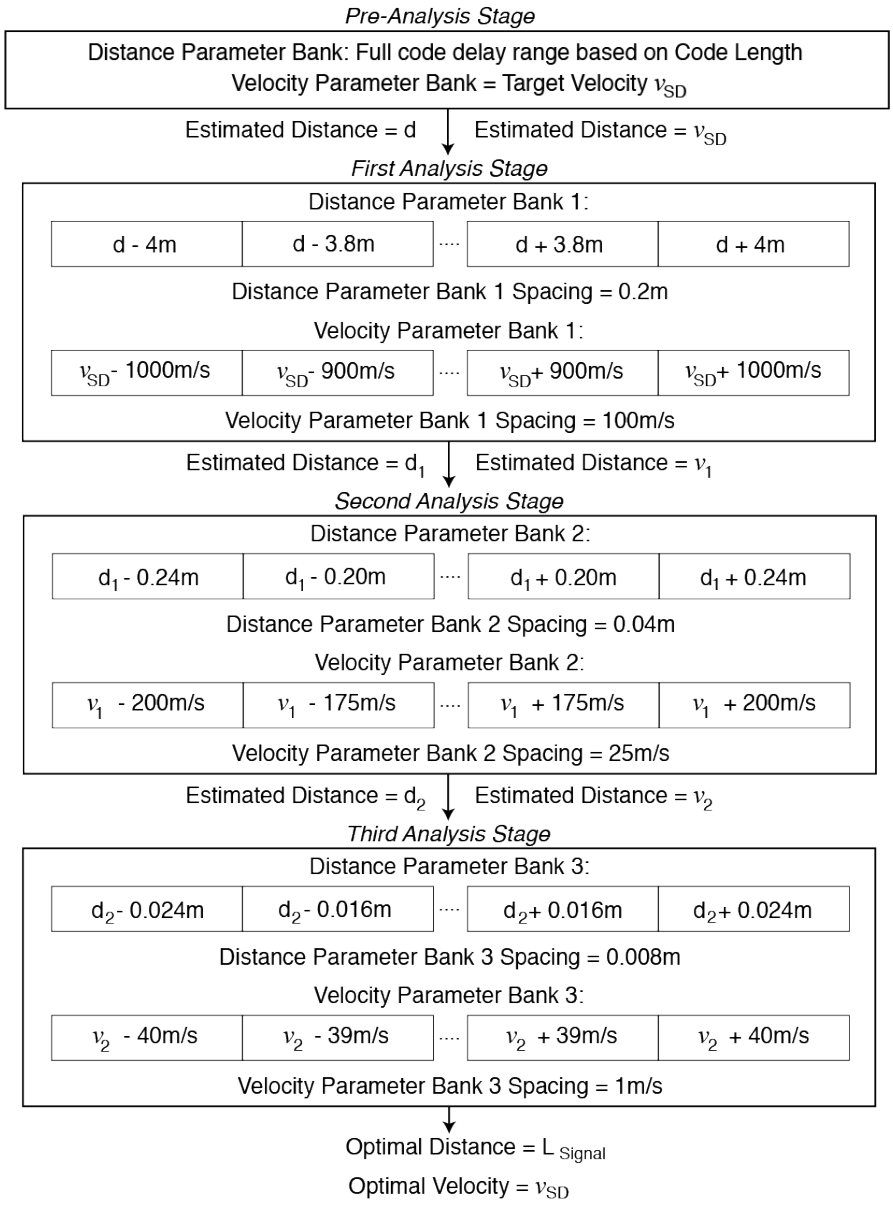

Figure 4.11: Block diagram of the template layout approach used for the matched filter analysis.

At the start of the matched filter analysis shown in Figure 4.11 the acquired signal is passed through the *Pre-analysis stage*. Due to L_{Code}, the propagation distance of the acquired PRN code is not known, and changes for different acquired signals as the PRBS output is not synchronised with the data acquisition. The analysis must be done for all time-shifts of the PRN code. To reduce the computational time, the pre-analysis stage sets the input velocity parameter v_0 to equal v_{SD} used to Doppler shift the modulating PRN code. The pre-analysis stage also multiplies the template code with the acquired signal in the frequency domain. This analysis step is only focused on finding the propagation distance $L_{Signal} + L_{Code}$ for the signal path and $L_{Control} + L_{Code}$ for the control path. Once the propagation delay is determined to within a chip, equivalent to 4 m, the estimated distance parameter value, referred to as d, is passed to the *First analysis stage*.

In the *First analysis stage*, the distance parameter bank contains a range of parameter values over 8 m, using the estimate of $L_{Code} + L_{Signal}$ from the pre-analysis stage, with d as the central value, and with a parameter spacing of 0.2 m. The range for the velocity parameter bank is 2000 m/s with v_{SD} the central value, and a parameter spacing of 100 m/s. The parameter values with the most significant correlation with the acquired signal can be used as an estimate of the parameter values d_1 and v_1, but due to the low signal-to-noise ratio of the acquired signal, this result is less accurate. A cubic interpolation on MATLAB [149] is used to apply a fit onto the signal correlation measurements to better estimate the parameters values that produced the most significant correlation output.

The estimated parameter values (d_1 and v_1) are used as the central values for the *Second analysis stage*. The range of parameter values and the spacing is reduced compared to the previous stage. The correlation output is again passed through a cubic interpolation to estimate the parameter. This process is repeated for the *Third analysis stage*, as well as subsequent matched filter analysis stages if needed. The end of the analysis gives an estimate of the optimal distance L_{Signal} and velocity parameter v_{SD} values for the signal path. The same analysis steps are repeated for the control path.

For each matched filter analysis stage in Figure 4.11 only the distance and velocity parameter values are estimated. The experiment ignores higher-order derivatives of motion since the impact of the time-varying delay from these terms for a space debris target is indeterminant for the integration times used in the analysis. For example, a space debris target in a circular orbit at an altitude of 500 km has a maximum acceleration term equal to 110 m/s^2. Within 10 ms, the change in distance of the target due to a_0 term is equal to 5.5 mm. This change in distance is too small for the PRN code method to measure for a 10 ms matched filter analysis integration time. The minimum integration time required for the PRN code method to measure the change in distance is expected to be equal to 60 ms. This integration time could not be performed for the three different parameters due to the limited computational resources available for the matched filter analysis.

Using only distance and velocity parameters with different parameter stages, the matched filter analysis generated approximately a hundred templates, and for 1 ms integration time it would take roughly 300 s to complete the analysis. When the integration time is increased to 10 ms, the total analysis time took roughly 1 hour. In practice, the density of the parameter bank can be altered to reduce computational time depending on the signal-to-noise ratio of the acquired signal. In the absence of noise, a fairly sparse parameter bank can be used as the correlation function is smooth. However, as the signal-to-noise ratio is reduced, the parameter bank should be increased.

In summary, the matched filter analysis estimates both the propagation distance, $L_{Signal} + L_{Code}$ for the signal path and $L_{Control} + L_{Code}$ for the control path, and the model velocity v_{SD} used to Doppler shift the modulating PRN code.

4.2 Characterising the Bench-Top Experiment

Before Doppler shifting the modulating PRN code and using the matched filter analysis to measure the time-varying delay applied in the bench-top experiment, this section aims to characterise the bench-top experiment and identify any artefacts. The characterisation is categorised into two situations:

1. Blocking the optical signal in the signal path and acquiring the photodetector measurement for matched filter analysis
2. Generating and acquiring an unshifted PRN code with 75 MHz chip frequency

The acquired signal amplitude is converted back into *Volts* from the ADC *counts* using the ADC conversion rate presented in Section 4.1.8. Therefore acquired signal and the signal correlation obtained from the matched filter analysis is presented as Volts.

4.2.1 Acquisition of the Blocked Signal Path

With the optical signal blocked, the time series of the photodetector measured signal should only show the dominant photodetector noise. If this signal is passed through the matched filter analysis, using only the distance parameter bank d_0, the output is the correlation between the noise and template PRN code. This correlation output would fluctuate for varying d_0 values, due to the noise, but no signal correlation should be observed.

Figure 4.12 shows the correlation between the blocked signal and the template code. The integration time used in the analysis is equal to 1 ms. Figure 4.12 shows that for most d_0 parameter values, the correlation output between photodetector noise and template code, for the 1 ms integration time, fluctuates between ± 1.5 V. The correlation output units depend on the digitised photodetector output voltage and the integration time.

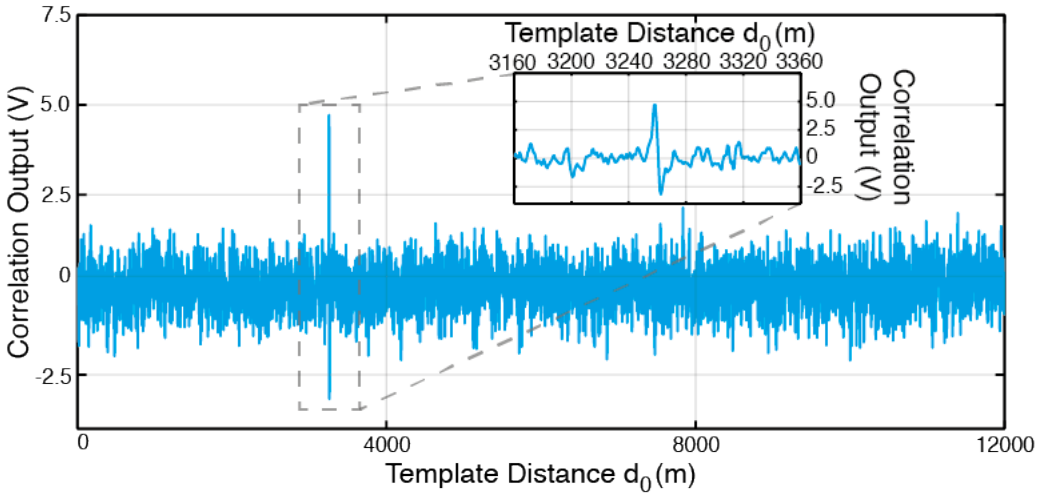

Figure 4.12: Correlation between the template code and the signal from a blocked photodetector shows a spurious correlation, between 3240 m and 3280 m, due to electronic cross-talk.

Figure 4.12 also shows an unexpected spike at d_0 approximately equal to 3260 m. This spike is identified as a spurious correlation between the template code and a PRN code pick-up by the coaxial cable connecting the photodetector AC port to the ADC AI0 input. When the PRBS generator is turned off, and the blocked signal is passed through the

matched filter analysis, the spike observed in Figure 4.12 is not present. The presence of the false correlation with the template PRN code could cause false detection of low signal-to-noise ratio optical signals and produce incorrect path length measurements if not properly taken into account.

The PRBS generator and amplifiers used in the bench-top experiment were moved away from the photodetector output cable to minimise the pick-up. To further reduce the impact of the false signal correlation, the control path delay is used as a delay reference in the matched filter analysis. The false correlation with a similar amplitude is observed in the control path correlation, but since the control signal always has a high signal-to-noise ratio, it is easier to distinguish the two different correlations. The distance separation between the control correlation and false correlation is fixed at 56 m while the signal correlation is expected to be within 2.2 m of the control correlation. Hence, the matched filter analysis excludes all signal correlations from the signal path with a delay larger than 40 m from the peak of the control correlation.

4.2.2 Modulating PRN Code with 75 MHz Chip Frequency

Figure 4.13 shows the first 1 μs of the acquired signal from the signal path photodetector. The time series in Figure 4.13 shows the amplitude transitions of the modulated PRN code is 190 $\mathrm{mV_{pk-pk}}$, after passing through the photodetector high pass filter. Converting the measured PRN code in Figure 4.13 to the corresponding optical power, the optical signal in the bench-top experiment transitions approximately between 21.5 μW and 0 μW. This transition of the optical signal is referred to as the *received signal power* P_{Sig} and in Figure 4.13 the P_{Sig} of the acquired signal is equal to 21.5 μW.

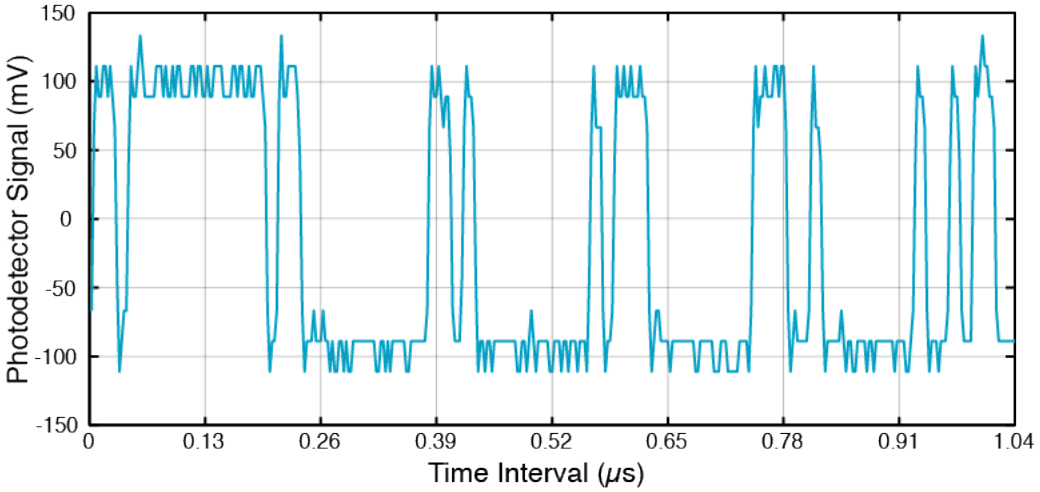

Figure 4.13: Time series of the Fibre Mach-Zehnder output acquired by the ADC.

Figure 4.14 shows the frequency spectrum of the acquired signal from the signal path photodetector. The power spectrum resembles a $sinc^2$ function similar to the PRN code spectrum shown in Figure 4.2, the power spectrum of the PRBS output. In Figure 4.14, the first null of the spectrum occurs at 75 MHz and the second null is at approximately 150 MHz, the second harmonic of the PRN code. Frequency components above 125 MHz in Figure 4.14 have a lower amplitude due to the bandwidth limitation of the photodetector filtering out the higher frequency in the spectrum.

Figure 4.14 shows the same two frequency harmonics, one at 75 MHz and the second at 150 MHz, that were observed in Figure 4.2. As discussed in Section 4.1.1, neither

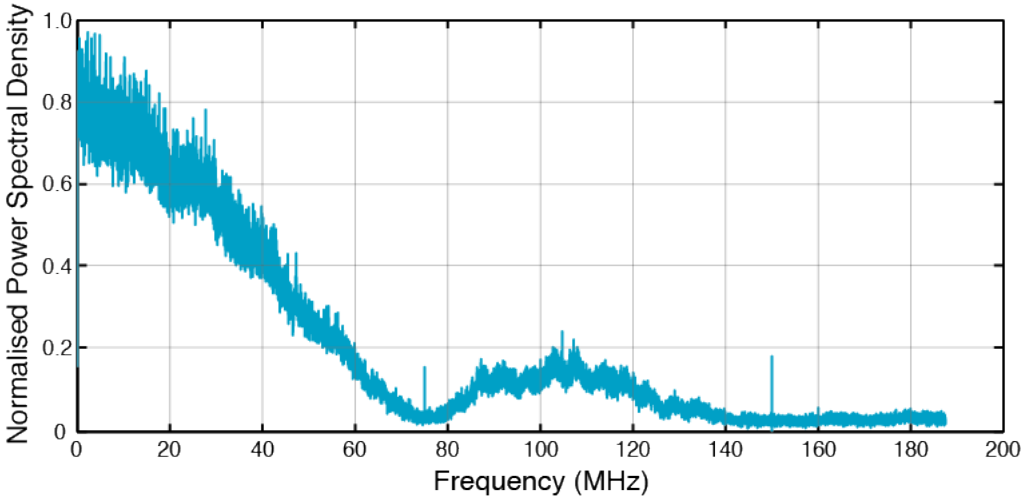

Figure 4.14: Power Spectral Density of the Fiber Mach-Zehnder output acquired by the ADC. The spectrum shows a $sinc^2$ function with nulls at 75 MHz and 150 MHz.

frequency harmonics would impact the path length and time-varying delay measurement when correlating the acquired signal with the template code. Figure 4.14 also shows radio frequency (RF) interference present in the spectrum around 100 MHz that where also observed in Figure 4.6.

4.2.3 Measuring the Signal and Control Path Length

As in Section 4.2.2, the chip frequency is equal to 75 MHz, modelling a static target. The two signals from the signal and control path are passed through the matched filter analysis to measure both L_{Signal} and $L_{Control}$ path lengths. The two path length measurements are used to calculate the path length difference ΔL ($\Delta L = L_{Signal} - L_{Control}$). In the matched filter analysis for this section, only the distance parameter d_0 value is changed while the velocity parameter v_0 is fixed and equal to 0 m/s.

Figure 4.15 shows the normalised signal and control correlation as a function of the delay parameter d_0. The optical signal power of the signal path is equal to 775 nW, and the optical signal power of the control path is equal to 50 μW. Since the two paths have different optical signal powers, by normalising the two correlations where the peak correlation value is equal to 1, the signal and control correlations are more easily compared in Figure 4.15.

It is immediately clear from Figure 4.15 that the signal and control correlation have peaks at different template distance d_0 values. Table 4.4 compares both the PRN code measurement and physical measurement on the bench-top experiment for both path lengths. Table 4.4 also shows the path length difference ΔL of the two measurement methods.

	L_{Signal}	$L_{Control}$	ΔL
Physical Measurement	2.75 m	0.68 m − 0.10 m	2.17 m ± 0.03 m
PRN Correlation Measurement	115.1 m	113.0 m	2.1 m ± 0.2 m

Table 4.4: Table comparing the L_{Signal} and $L_{Control}$ path length measured on the optical table and using the PRN codes for 775 nW received signal power.

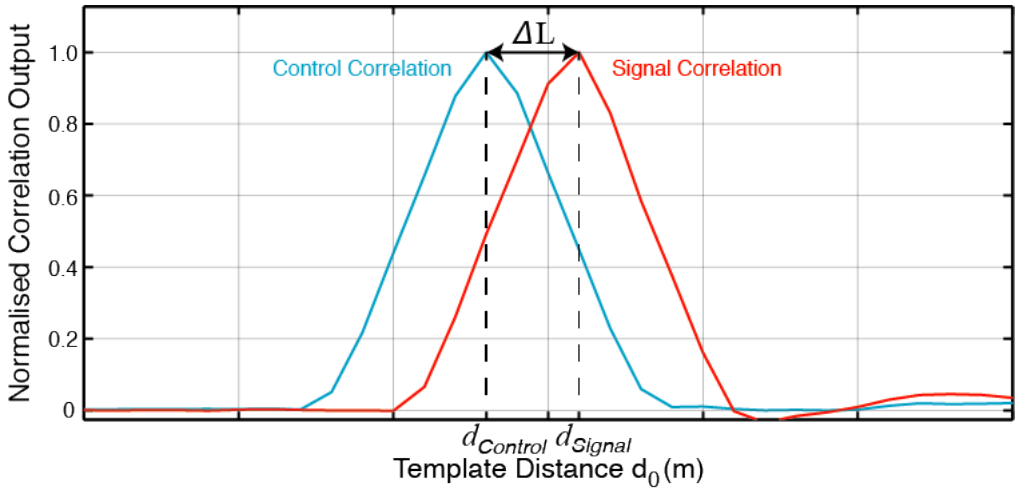

Figure 4.15: Normalised correlation of the PRN code acquired from the control and signal photodetectors as a function of the input value for the distance parameter d_0.

The physical distance measured for L_{Signal} and $L_{Control}$ are 2.75 m and 0.68 m respectively. The difference in the path lengths ΔL is equal to 2.07 m. Table 4.4 shows that the control path physical measurement is reduced by 0.1 m. This step was taken to take into account the fixed time offset added by the ADC when digitising the two path's optical signals. As discussed in Section 4.1.8, this distance bias is equal to 0.1 m. Hence, the ΔL shown in Table 4.4 for the physical measurement methods is equal to 2.17 m.

For the PRN code method, the matched filter analysis was performed for a 1 ms integration time. L_{Signal} and $L_{Control}$ are 115.11 m and 113.00 m respectively. Since both path length PRN code measurements are influenced by L_{Code}, as discussed in Section 4.1.4, the path length measurement is different from the physical measurement. However, ΔL of the PRN code method is equal to 2.11 m. The ΔL calculated by both methods is similar.

Table 4.4 also shows the accuracy of both the physical and PRN code measurement methods. For the PRN code method, the accuracy is equal to 0.2 m. This accuracy limit can be explained using both Figure 4.16 and Figure 3.22, where the signal correlations are generated using an acquired signal from the bench-top and in simulation respectively. In both Figures, when using a template spacing equal to 0.3 m the signal correlation has a smooth correlation slope. This is not the case when the template spacing is equal to 0.2 m, where horizontal steps are present in the correlation output. Using a smaller template spacing than 0.2 m would not improve the accuracy of the distance parameter estimate.

Section 3.5.1 discusses in more detail on the signal correlation seen in Figure 4.16. In the simulation presented in Section 3.5.1, the limiting bandwidth in the simulation is the ADC sampling frequency. Despite the photodetector in the bench-top experiment having a smaller bandwidth, the PRN code in Figure 4.13 has sharp transitions in the time series between the two amplitude values, similar to the PRN code generated in simulation. Within the ADC sampling time interval, the optical signal would have travelled a distance of 0.2 m. The change in the optical signal distance within the ADC sampling time matches the accuracy of the matched filter analysis observed in the bench-top experiment. Figure 3.22 also shows horizontal steps with a width equal to 0.2 m when the simulated signal is digitised by the 1.5 GHz ADC sampling frequency and is passed through the matched filter analysis. The experimental results match the simulation in Section 3.5.1, but further tests could not be carried out as the ADC sampling frequency in the experiment is fixed. However, Figure 3.22 did show that changing the ADC sampling frequency in simulation

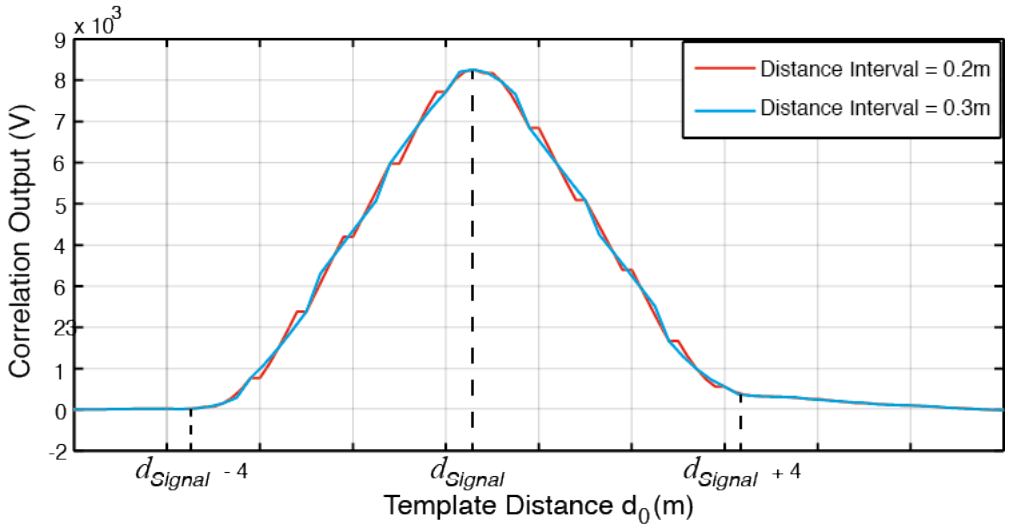

Figure 4.16: Comparing the correlation of the PRN code when using 0.2 m and 0.3 m parameter spacing for the delay parameter.

altered the width of the horizontal steps.

The second observation from Figure 4.15 is a small ripple at the tail of the signal correlation, from $d_{Signal} + 4$ m onwards due to bandwidth effects on the PRN code translated into the signal correlation. The same ripple effect is also present in the control correlation. The control correlation amplitude is larger than the signal correlation and when normalising the control correlation the effect is not visible in Figure 4.15. In Figure 3.22, where the signal path optical beam is generated in simulation, the acquired signal is passed through a low pass filter the side of the signal correlation has similar ripples but the unfiltered acquired signal has no ripples. The simulated analysis used the MATLAB built-in *decimate* function which uses a finite impulse response type low pass filter [150].

4.2.4 Impact of Integration time

One of the main benefits of using a PRN code sequence in a ranging application is utilising the PRN code statistics for a longer integration period of the matched filter analysis to improve signal detection and ranging precision. This benefit is advantageous for low signal-to-noise ratio optical signals such as in a space debris application. To test the impact of integration time on both the signal detection and path length measurements, a weak optical signal from the signal path is acquired and passed through the matched filter analysis for different integration times. The ΔL calculations are then compared.

Figure 4.17 shows two signal correlations, as a function of the distance parameter d_0, where the signal path optical power is attenuated to 520 pW. In Figure 4.17a the integration time for the matched filter analysis is 1 ms and for Figure 4.17b the integration time is increased to 20 ms. In both Figure 4.17a and Figure 4.17b, the signal correlation output is referenced from $d_{Control}$ as $d_{Control}$ is accurately measured, since the control path signal correlation has high optical signal power (50 μW), and the signal path correlation is expected to be approximately 2.175 m away from $d_{Control}$. The cubic interpolation is then applied on both the signal correlation in Figure 4.17 to determine the peak of the correlations and estimate signal path length d_{Signal}.

Figure 4.17a does not show a distinctive signal correlation. Only the false correlation,

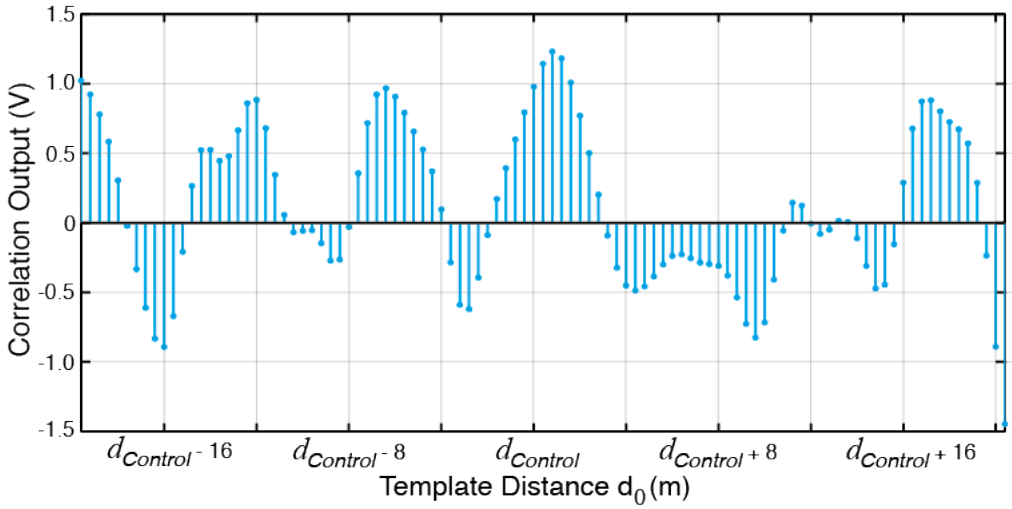

(a) Signal correlation for 1 ms integration time.

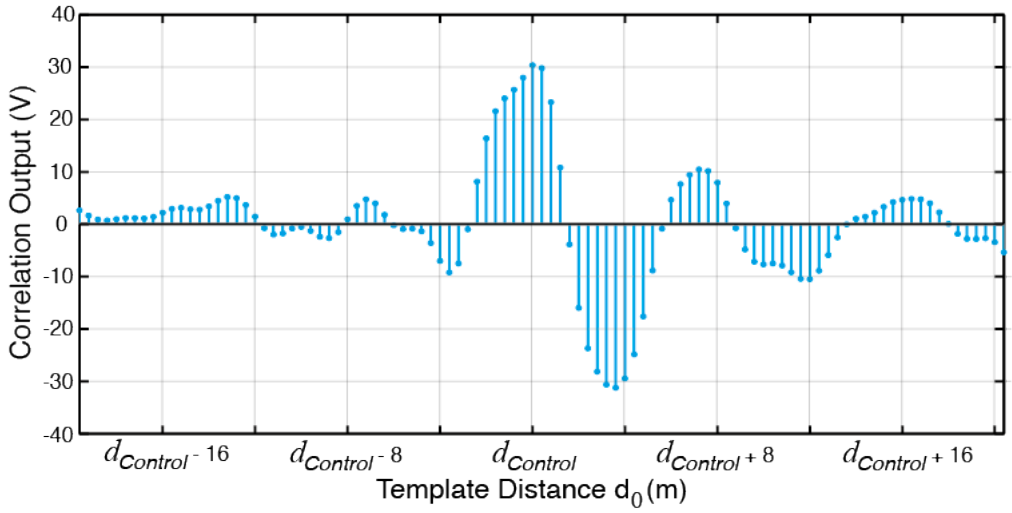

(b) Signal correlation for 20 ms integration time.

Figure 4.17: Signal correlation of the acquired PRN code with 520 pW received signal power.

discussed in Section 4.2.1, is visible at a d_0 value equal to $d_{Signal} - 54\,\text{m}$. As discussed in Section 4.2.1, this false correlation is ignored during the matched filter analysis. Since there is no signal correlation, the matched filter analysis cannot provide a path length measurement. If the peak value of the correlation output is used, the ΔL calculation is equal to $-14.68\,\text{m}$ confirming using the correlation peak method to measure the path length is not accurate for low signal-to-noise ratio ranging applications. The results show that if the optical signal is 520 pW, then for the direct detection scheme a 1 ms integration time is not sufficient for signal detection and path length measurement.

In Figure 4.17b, the integration time is increased to 20 ms. Compared to Figure 4.17a, the signal correlation output amplitude in Figure 4.17b has increased due to the larger integration time. A signal correlation is visible above the surrounding correlated noise. Using the cubic interpolation on the signal correlation, ΔL is equal to 2.96 m. The error in the measurement from the expected ΔL shown in Table 4.4 is equal to 0.785 m. Despite the poor accuracy in the path length measurement, increasing the integration time has improved signal detection.

Figure 4.17b also shows that at a slightly larger time shift from the signal correlation,

the correlation output reduces to approximately −30 V. This negative excursion with ripple effects for subsequent time shifts is due to the bandwidth effects present in the acquired signal. The negative excursion is also observed in both Figure 4.12, for the spurious correlation, and Figure 4.15, indicating bandwidth effects on the PRN code. Since this negative excursion is due to bandwidth effects on the PRN code, the excursion also increased for increasing integration times.

This section has proven that both signal detection and estimating the d_0 parameter using the matched filter analysis is improved by using a longer integration time. Section 4.3 will discuss estimating the velocity v_0 parameter for weak signals.

4.3 Measuring the Doppler Shift of the Amplitude Modulated PRN Code

In Section 4.2, the chip frequency of the modulating PRN code was fixed at 75 MHz to model a stationary target. The experimental results showed that the matched filter analysis was able to accurately estimate the difference in the signal and control path lengths ΔL. The experimental results also showed that the matched filter analysis signal detection and parameter estimation is improved with higher integration times.

In this section, the modulating PRN code's chip frequency in the bench-top experiment is increased by 1750 Hz to model the optical signal reflecting from a space debris target with a constant velocity v_{SD} equal to −7 km/s and moving towards the telescope. As discussed in Section 4.1.1, in the bench-top experiment the optical signal is not reflected by a moving target but the modulating PRN code frequency is altered to model the impact of the time-varying delay. The signal and control arm have the same path length as presented in Table 4.4 but both have a Doppler shifted PRN code amplitude modulated on the optical beams. The resulting time-delaying effect must be taken into account to estimate both L_{Signal} and $L_{Control}$.

The experimental results first presented in this section aim to show the impact of the time-varying delay on the matched filter analysis estimate of the d_0 parameter if the velocity parameter is not taken into account. The matched filter analysis then used both the distance d_0 and velocity v_0 parameters to estimate both the path lengths, and hence calculate ΔL, and the velocity of the model space debris target.

4.3.1 Impact of the Time-Varying Delay on the Signal Correlation

Assuming the matched filter analysis does not take into account the velocity parameter v_0, subsequent signal correlations would produce different signal path length measurements. This is shown in Figure 4.18 using 4 subsequent signal correlations each with an integration time t_i equal to the period of the PRN code sequence L s ($L = 0.44$ ms).

As expected, the subsequent signal correlation peaks are produced at different d_0 parameter values due to the time-varying delay of the modulating PRN code. The peak of the first signal correlation (0 s to L_1s) occurs at a d_0 equal to 79 998.3 m. The peak of the second signal correlation (L_1s to L_2s) occurs at a d_0 equal to 79 995.2 m. The reduction in the distance measurement indicates a target was moving closer to the telescope. The difference in the distance measurement is equal to 3.1 m. Since v_{SD} is equals to −7 km/s, within 0.44 ms the target would have moved closer by 3.08 m, closely matching the time-varying delay measurement using the first and second signal correlations in Figure 4.18.

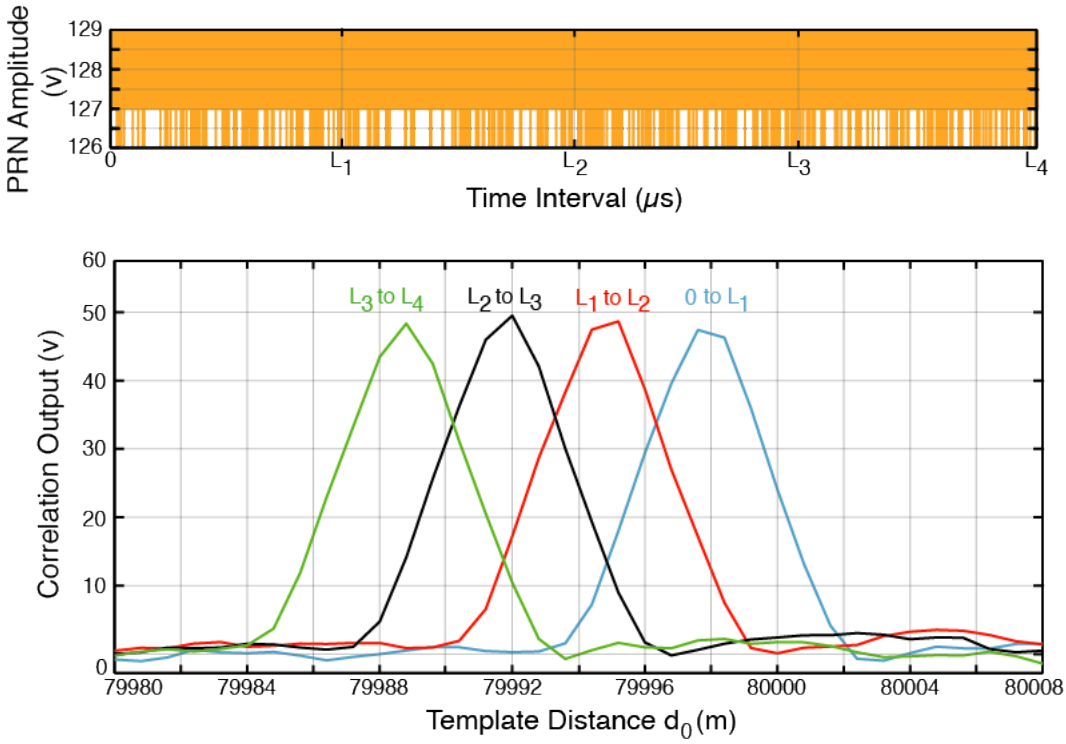

Figure 4.18: The acquired PRN code between time 0 and time L_4 is divided into four segments. Each segment is 0.44 ms long and passed through the matched filter analysis with the delay parameter. The velocity parameter is set to 0 m/s for only this analysis. The four subsequent signal correlation outputs present the impact of the time-varying delay on the signal correlations as the correlation peaks of each signal correlation occur at different d_0.

The result in Figure 4.18 shows that the time-varying delay of the target can be approximated by estimating the distance d_0 parameter of subsequent signal correlations. However, Figure 4.19 illustrates the effect of the time-varying delay on the shape and amplitude of the signal correlation indicating this method would not provide an accurate and precise estimation of the target's time-varying delay required for space debris ranging and manoeuvring applications. One of the signal correlations in Figure 4.19 is produced by setting the input velocity parameter v_0 value to equal to 0 m/s. The second signal correlation sets the v_0 parameter value to equal -7 km/s, to match the model target's velocity v_{SD} used to Doppler shift the modulating PRN code.

Comparing the two different signal correlations, when v_0 is equal to 0 m/s, the signal correlation is wider and has a smaller peak amplitude value compared to when v_0 is equal to -7 km/s. The time-varying delay within the integration time causes parts of the PRN code in the acquired signal to have a different delay from the template code with v_0 equal to 0 m/s. The acquired code is slightly misaligned from the template code, reducing the signal correlation and spreading the correlation into the surrounding d_0 values. Hence, signal detection can be more challenging for low signal-to-noise ratio optical signals, and there would be a larger error in estimating d_0, which would also translate into a larger error in determining the time-varying delay. The width of the signal correlation is also wider when using a larger integration time, further reducing the signal correlation. The results in Figure 4.19 match the simulated result presented in Figure 3.16. Section 3.3.3 and Section 3.3.4 provide a more detail explanation on how the time-varying delay alters the signal correlation.

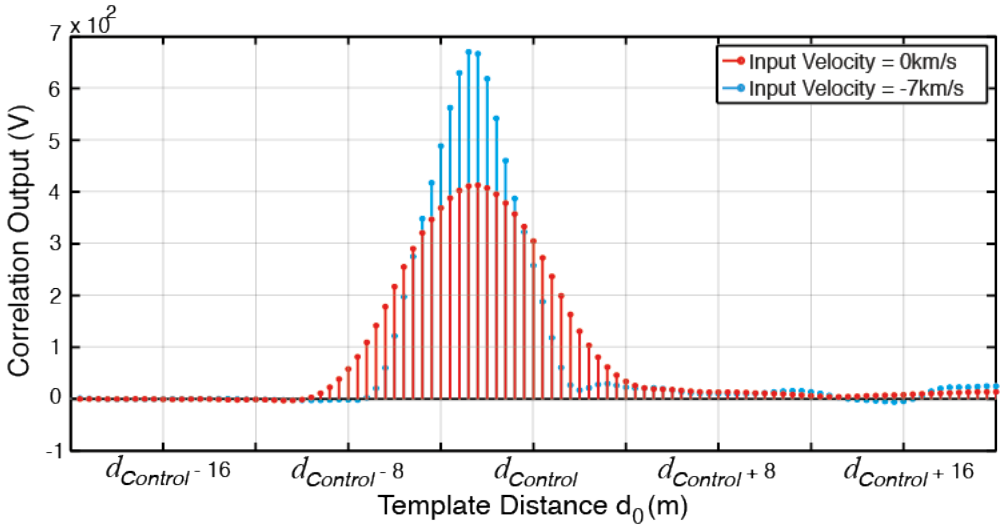

Figure 4.19: Comparing the signal correlation for a 1 ms integration time where the matched filter analysis input velocity parameter value is changed to generate the template code. For the red correlation v_0 is 0 m/s and the the blue correlation v_0 is -7000 m/s.

The result in Figure 4.19 indicates that using the change in d_0 of subsequent signal correlations to determine the time-varying delay would not provide an accurate and precise estimation of the target's time-varying delay required for space debris ranging and manoeuvring applications. Larger integration times discussed previously in Section 4.2.4 to improve both signal detection and parameter estimation also would not be possible. Hence a better approach is using the parameter estimation of the matched filter analysis to estimate the time-varying delay. By altering the template code, the matched filter analysis can maximise signal detection and provide a more precise estimate of the target's motion. The parameter estimation is also improved with increasing integration time since the template code is aligned to the acquired signal PRN code for the length of the integration time.

4.3.2 Impact of Varying v_0 Parameter on the Signal Correlation

Section 4.2.3 presented measuring both the signal and control path lengths when the chip frequency is equal to 75 MHz. The calculated difference in the path lengths ΔL is equal to 2.11 m. In Section 4.3.1, the modulating PRN code is Doppler shifted with the discussion showing the impact on the signal correlation and the requirement to better estimate the time-varying delay. This section uses the ΔL calculation using the PRN code from Table 4.4 as a fixed input value to d_0 ($d_0 = 2.11$ m) and varies v_0 to demonstrate the impact of the velocity parameter on the signal correlation. As in Section 4.3.1, the PRN code is Doppler shifted modelling a target moving with a velocity equal to -7000 m/s.

Figure 4.20 provides two different representations of the same signal correlations for a 1 ms and 10 ms integration time. Comparing the two correlations in Figure 4.20a shows that increasing the integration time has increased the correlation peak value by an order of magnitude from 685 V to 6850 V. Figure 4.20b presents the normalised version of the same signal correlations in Figure 4.20a where the maximum correlation value is equal to 1. Comparing the two correlations shows that increasing the integration time has reduced the Full Width Half Maximum (FWHM) of the signal correlation by an order of magnitude. For the 1 ms, the FWHM of the correlation is 8000 m/s (from $-11\,000$ m/s to -3000 m/s). For 10 ms, the FWHM of the signal correlation is 800 m/s (from -7400 m/s to -6600 m/s).

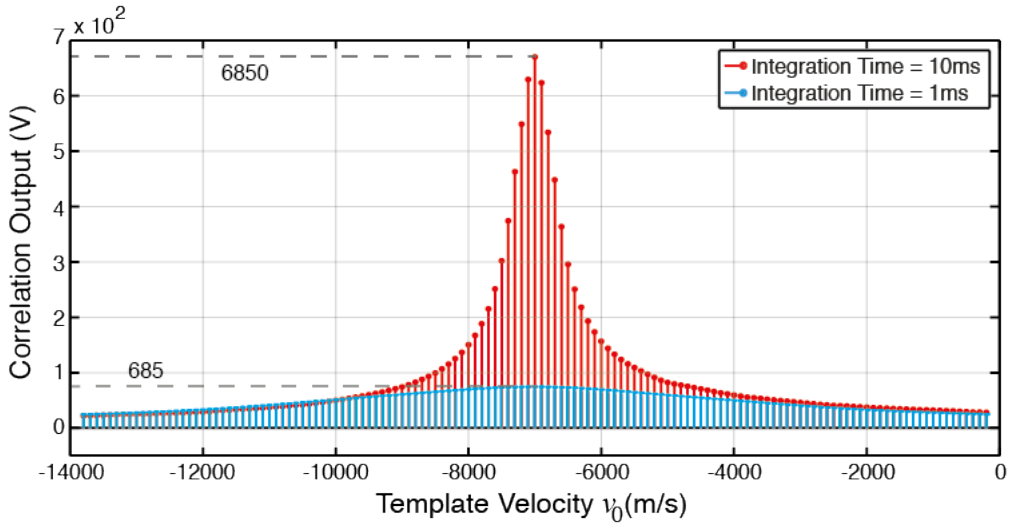

(a) Comparing the signal correlation

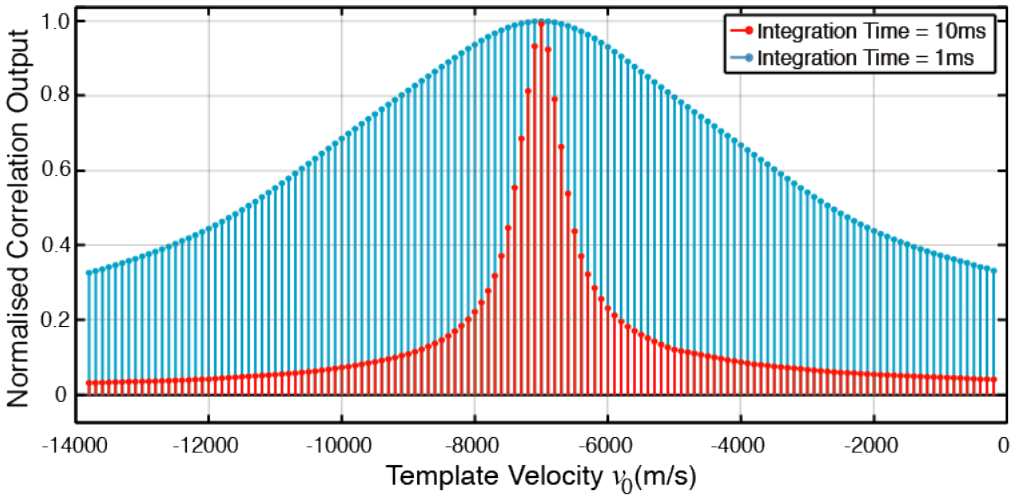

(b) Comparing the normalised signal correlation

Figure 4.20: Signal correlation using only a velocity parameter bank to vary v_0 for both 1 ms and 10 ms integration time. The distance parameter value d_0 is fixed to $L_{Control} + 2.11$ m.

The results in Figure 4.20 shows that the amplitude of the signal correlation scales proportionally while the signal correlation width scales inversely proportionally with integration time. Increasing the integration time allows the matched filter analysis to better estimate the time-varying delay of the PRN code since the signal correlation has a steeper slope. The combination of a larger correlation peak and smaller FWHM, the relationship between the integration time t_i and the precision of estimating v_0 parameter is expected to be t_i^2. However, increasing the integration time also increases the noise present in the signal correlation by $\sqrt{t_i}$. Therefore the overall improvement in the precision of the matched filter estimation of v_0 is expected to be $t_i^{1.5}$.

To measure the impact of integration time on the precision of estimating the time-varying delay requires analysis of more acquired signals. This analysis is carried out and presented in Section 4.3.4 and Section 4.3.5. However, by adding an interpolation on both the signal correlations in Figure 4.20a, when the integration time is 1 ms v_0 is estimated as -7025.5 m/s and when the integration time is 10 ms v_0 is estimated as -7002 m/s. The analysis has shown an improvement in estimating v_0 for larger integration times.

4.3.3 Signal Correlation Varying Both d_0 and v_0 Parameters

Figure 4.21 presents a contour plot of the 2-dimensional signal correlation where both the distance d_0 and velocity v_0 parameters are varied during the matched filter analysis. The integration time chosen for the analysis is 1 ms.

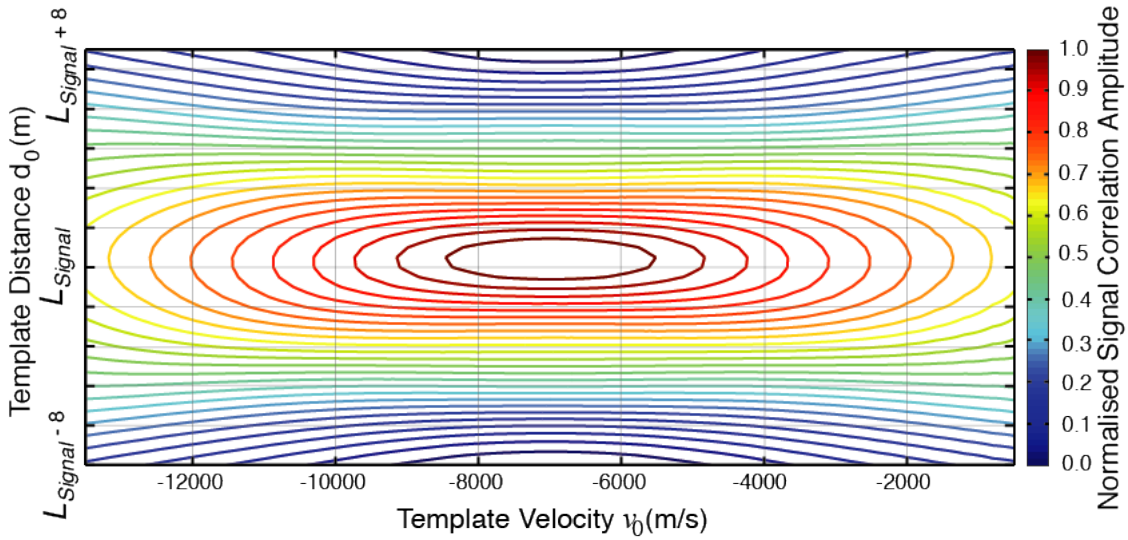

Figure 4.21: Contour plot showing the signal correlation after the First analysis Stage shown in Figure 4.11 where both the distance and velocity parameters are changed using a parameter bank for each parameter.

The contour plot in Figure 4.21 shows that as the parameter values of both d_0 and v_0 change closer to the optimal values used in the bench-top experiment, the signal correlation peak increases. The FWHM of the signal correlation along the distance d_0 parameter is 4 m since the width is related to the chip frequency while the FWHM along the velocity v_0 parameter is equal to 8000 m/s and is dependent on the integration time used in the analysis.

An interpolation of the signal correlation in Figure 4.21 is used to estimate the d_0 and v_0 parameters. d_0 parameter estimate is used to calculate ΔL which is equal to 2.08 m and v_0 is estimated to equal -7022 m/s. Both measurements are close to the expected values with the estimation of d_0 within the 0.2 m accuracy.

For all future sections, the matched filter analysis will estimate both d_0 and v_0 using the interpolation of the signal correlation.

4.3.4 Precision of the Matched Filter Analysis

Up until Section 4.3.3, both the d_0 and v_0 parameters were varied separately to investigate the impact of each parameter on the signal correlation. Section 4.3.2 showed the change in the signal correlation output due to varying the v_0 parameter is used to estimate the target velocity v_{SD} used to Doppler shift the modulating PRN code. Even though this section focuses on the precision of the matched filter analysis in estimating v_{SD}, the analysis varied both d_0 and v_0 parameters.

Figure 4.22 illustrates the steps taken to determine the precision of the matched filter analysis in estimating v_{SD}. First, a total of 25 signals at the same received optical power P_{Sig} are acquired from the bench-top experiment. Before the matched filter analysis every acquired signal, each 0.1 s long, is first divided into segments. The time length of each

segment depends on the integration time t_i chosen for the matched filter analysis. For example, if a 1 ms integration time is chosen, the acquired signal is divided into a 100 1 ms long segments. Five of these segments are chosen at random and passed through the matched filter analysis. This step was taken to identify the variation in estimating target velocity v_{SD} using different sections of the same acquired signal.

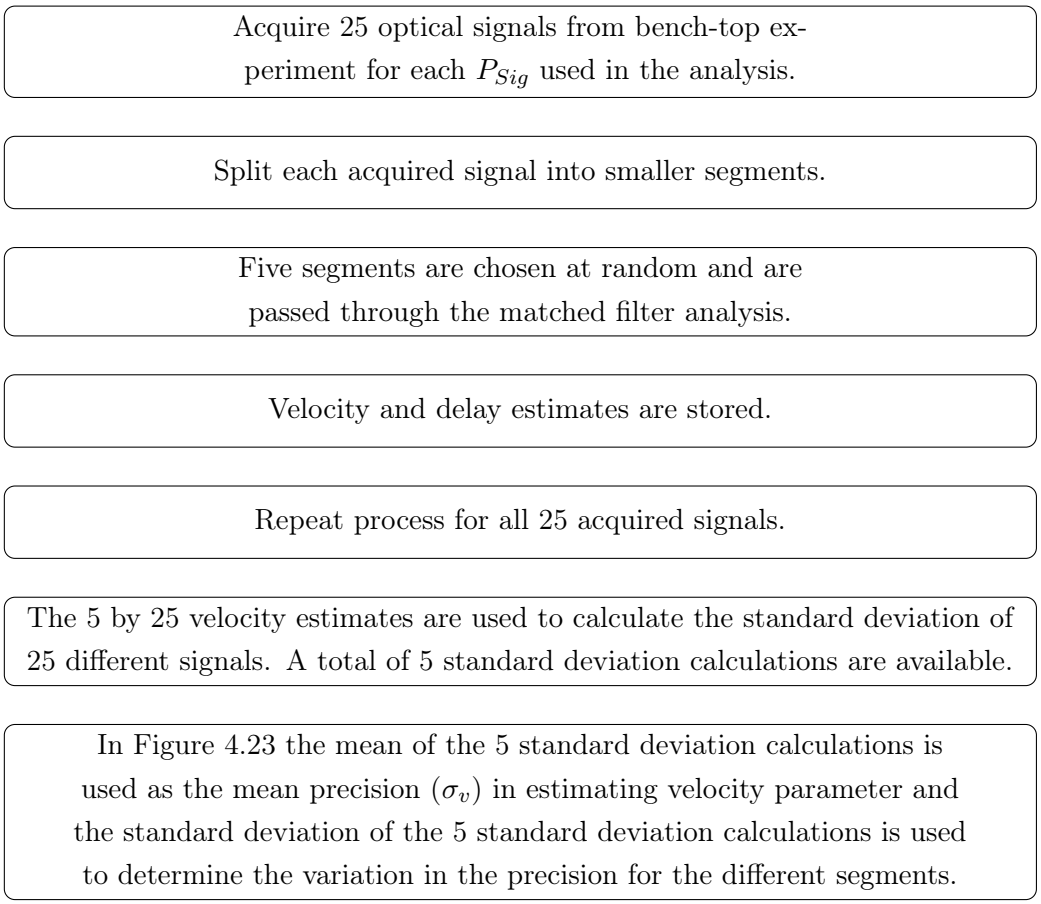

Figure 4.22: Flowchart describing how the precision of the matched filter analysis is determined.

The matched filter analysis provides 5 estimates for each acquired signal and the process is repeated for 25 acquired signals. In total there are 125 estimates of v_{SD} stored in a 25 by 5 matrix for every P_{Sig} and t_i. The main reason the matched filter analysis is repeated for the same acquired signal is that initial results for the matched filter analysis showed that different portions of the same acquired signal produced a different estimated value of the velocity parameter v_{SD}. This highlighted there is a variance in the velocity estimate within the same acquired signal that must be taken into account.

The standard deviation (1σ) of the v_{SD} estimates using the 25 different acquired signals gives the precision of the bench-top experiment in estimating v_{SD} using the matched filter analysis. This step of the analysis is repeated for the 5 different segments resulting in a total of 5 different precision measurements of the v_{SD} estimate. The 5 different precision measurements are not the same. Therefore these 5 precision measurements are used to find the mean precision (σ_v) in estimating v_{SD} for the received signal power P_{Sig} and integration time t_i chosen for the analysis. The standard deviation of the 5 different precision measurements is used to determine how the precision measurement varies for different segments of the same 25 signals. The same steps are repeated for different P_{Sig} and t_i, providing information on how the precision of the matched filter's estimate of v_{SD} varies with the two experimental parameters.

The mean precision of the v_{SD} estimate is expected to change inversely proportionally with P_{Sig} and change by $t_i^{-1.5}$ with t_i. Changing the received signal power P_{Sig} and integration time t_i impacts the slope of the signal correlation. A higher signal power linearly increases the peak of the signal correlation. Section 4.3.2 discusses more on the integration time relationship with the correlation slope. The steeper the slope, the more precise (smaller σ_v) the velocity measurement is over the noise added onto the signal correlation.

To recap, the mean precision σ_v for the direct detection scheme is expected to have the relationship:

- P_{Sig}^{-1} with received signal power P_{Sig}
- $t_i^{-1.5}$ with the integration time t_i

Figure 4.23 presents the precision of the matched filter analysis in estimating v_{SD} as a function of received signal power P_{Sig}. The analysis is carried out using the same acquired signals for three different integration times. The mean precision is represented as a solid dot while the variation (1σ) in both the precision measurement and received signal power are represented as a shaded region around the mean. The variation in the optical signal power is due to fluctuations in the Fibre Mach-Zehnder. Figure 4.23 also shows a straight line, in the logarithmic scale, fitted to the mean precision for the three integration times. Each line has a slope fixed to -1 since the precision is inversely proportional to P_{Sig}.

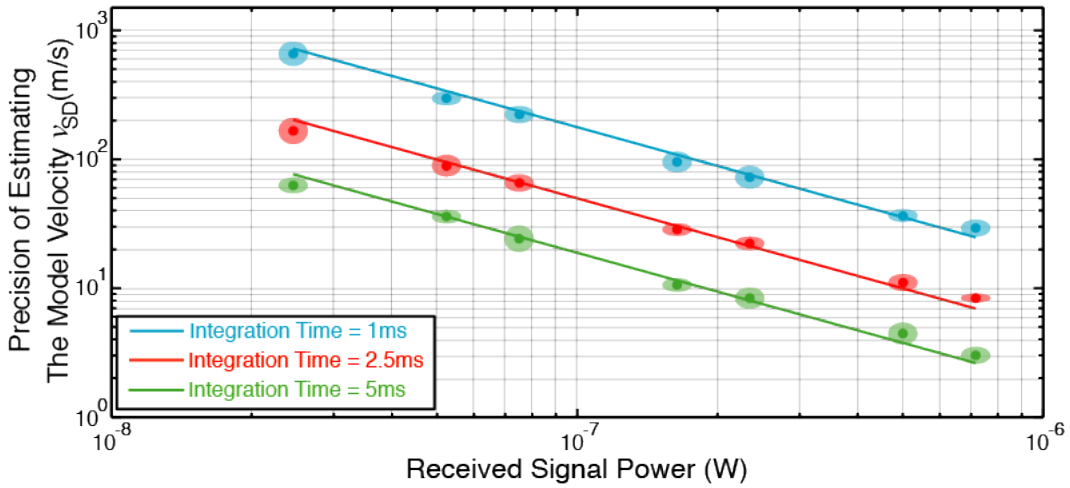

Figure 4.23: Precision of estimating v_{SD} as a function of received signal power. The solid dots in the plot represents the mean precision of the velocity measurement while the shaded region around the mean represents the variation in the precision for different segments of the same 25 signals. The line is fitted to the mean of the precision and has a slope of -1.

The result in Figure 4.23 shows that the mean precision of the matched filter analysis matches closely, within the variations of the precision and signal power, with the fitted line. This result confirms that the mean precision of the matched filter analysis is inversely proportional to P_{Sig} for the direct detection scheme.

Figure 4.24 presents the the matched filter analysis error in estimating v_{SD} as a function the integration time t_i. The analysis was repeated for four different received signal powers P_{Sig}. As in Figure 4.23, the precision of the matched filter analysis has variations, and a line is fitted to the mean of the precision. The slope of the line is -1.5 to test if the mean precision of the matched filter analysis follows the expected relationship of $t_i^{-1.5}$ with the

integration time. The results show that the line passes through the measured data points, within the variations, confirming the mean precision changes by $t_i^{-1.5}$.

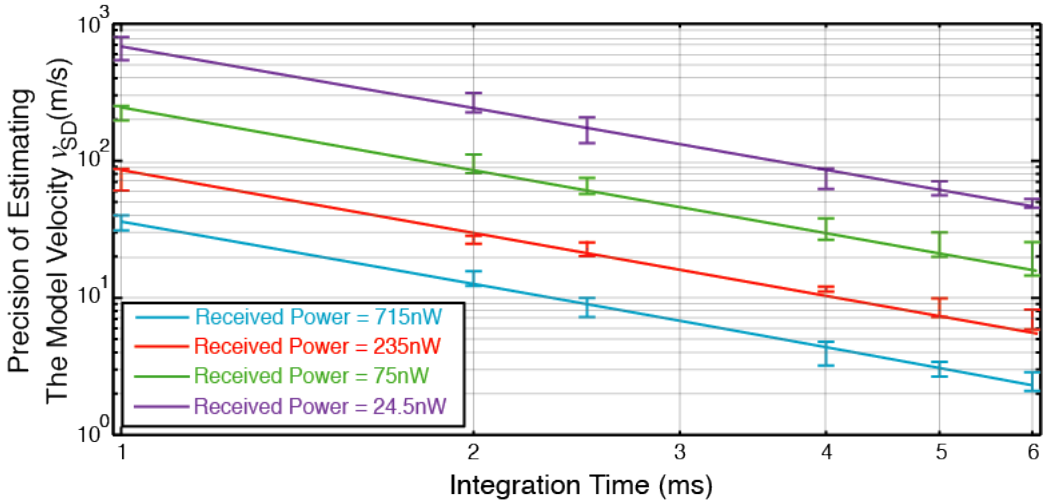

Figure 4.24: Precision of estimating v_{SD} for varying integration times. The trend line has a $t_i^{-1.5}$ relationship with the integration time t_i for each received signal power.

One observation from Figure 4.23 and Figure 4.24 is the variations in the precision measurements are different for different P_{Sig} and t_i. Using only 5 segments of the acquired signal contributes to this variation, but a larger number of segments cannot be used, particularly for larger integration times, due to the increased analysis time and the limited acquisition resources that limit the total acquired signal to 0.1 s. The 5 segments were considered sufficient to confirm, based on the results in Figure 4.23 and Figure 4.24, that the mean precision of the matched filter analysis in estimating the velocity parameter follows the expected relationship with both P_{Sig} and t_i.

The relationship between the precision of the matched filter analysis to estimate v_{SD} can be represented as an equation using the results from both Figure 4.23 and Figure 4.24 by picking the mean precision σ_v from the experimental results for a given received signal power P_{Sig} and integration time t_i. In Equation 4.7 the mean precision of 224.35 m/s was chosen for 75 nW received signal power and 1 ms integration time. Equation 4.7 is used in Chapter 6 to determine the precision of the matched filter analysis of the direct detection scheme in estimating a target's velocity for varying received signal power and integration time. This is a part of the discussion for implementing the direct detection scheme for a space debris ranging application.

$$\sigma_v \; m/s = 224.35\,\text{m/s}\left(\frac{75\,\text{nW}}{P_{Sig}\;W}\right)\left(\frac{1\,\text{ms}}{t_i\;s}\right)^{1.5} \tag{4.7}$$

4.3.5 Precision of the Matched Filter Analysis with Background Photon Noise

Section 4.1.7 considered the addition of an incoherent light source into the bench-top experiment as a background noise source. The background photon noise source added in the experiment is much larger than the background noise expected in space debris ranging application but is only approximately 1.25 dB larger than the photodetector noise, making background noise the dominant noise source in the bench-top experiment.

Background photon noise would reduce the signal-to-noise ratio of the optical signal measured at the photodetector. However, since the acquired signal is correlated with the template for a longer period than a single pulse, the mean precision of estimating v_{SD} would not change for the slight increase in the noise floor of the experiment. The main purpose of the test is to confirm that the matched filter analysis has the same relationship between P_{Sig} and t_i when background photon noise is the dominant noise. This result is shown in Figure 4.25 when comparing the v_{SD} estimate with the background photon noise to the result in Figure 4.23. The two results in Figure 4.25 overlap each other and have the same relationship between the P_{Sig} and t_i with the mean precision σ_v.

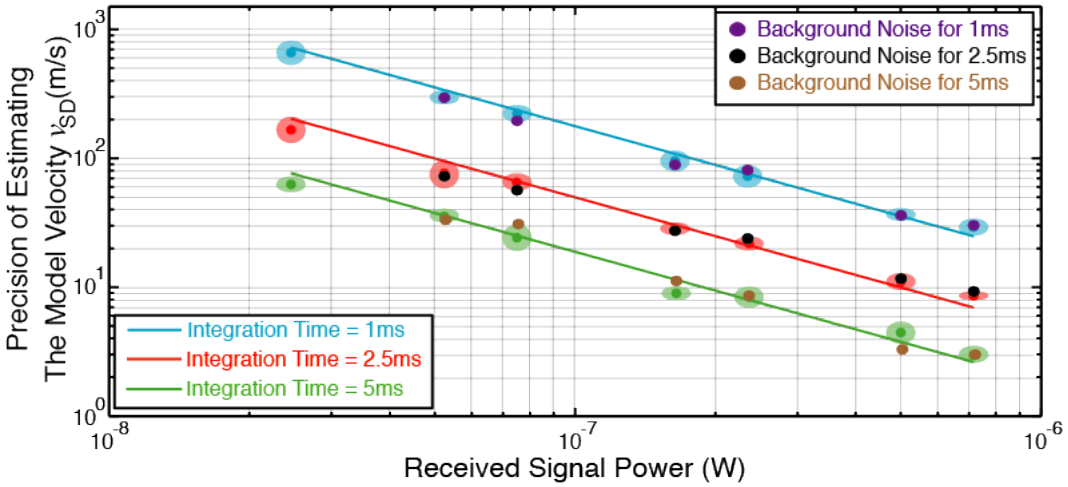

Figure 4.25: Comparing the precision in the velocity measurement when 120 μW background photon noise is added in the bench-top experiment from the halogen lamp to the precision of the velocity measured in Section 4.3.4 from Figure 4.23.

For the direct detection scheme, if background photon noise is the dominant noise source, increasing the integration time improves both signal detection and precision of estimating v_{SD}. Another alternative is amplifying the optical signal to enhance the signal-to-noise ratio. This concept is the basis for the coherent detection scheme discussed in Chapter 5.

4.3.6 Estimating both d_0 and v_0 Parameters for Different v_{SD}

The matched filter analysis method is capable of estimating the two path lengths, L_{Signal} and $L_{Control}$, and calculating the path length difference ΔL. The matched filter analysis also showed the capability of estimating the time-varying delay of a model target travelling at a constant velocity of v_{SD} equal to -7 km/s. The precision of the v_0 measurement was shown to be inversely proportional to the received signal power P_{Sig} and the relationship with the integration time t_i is $t_i^{-1.5}$. The final test for the matched filter analysis is estimating both ΔL and the time-varying delay for different v_{SD} values.

As in Section 4.3.4, a total of 25 different acquired signals are obtained from the bench-top experiment. However, for each acquired signal, a different target velocity v_{SD} is used to apply the Doppler shift of the modulating PRN code. The 25 different values of v_{SD} were chosen randomly within the range of $\pm 10\,000$ m/s. This range of velocity aims to test the matched filter's capability to estimate a target's velocity when the target is moving towards and away from the telescope. The acquired signal is passed through the matched filter analysis to estimate both input parameters d_0 and v_0. The d_0 estimate for the control path gives $L_{Control}$ and d_0 for the signal path is L_{Signal}. v_0 gives the matched filter

estimate of v_{SD}. Since v_{SD} has a large range the result is presented as v_{err}, the difference between the estimated velocity v_0 with the velocity v_{SD} used to Doppler shift the PRN code ($v_{err} = v_{SD} - v_0$). Figure 4.26 shows a scatter plot of the matched filter analysis estimate of ΔL and v_{err} for all 25 acquired signals.

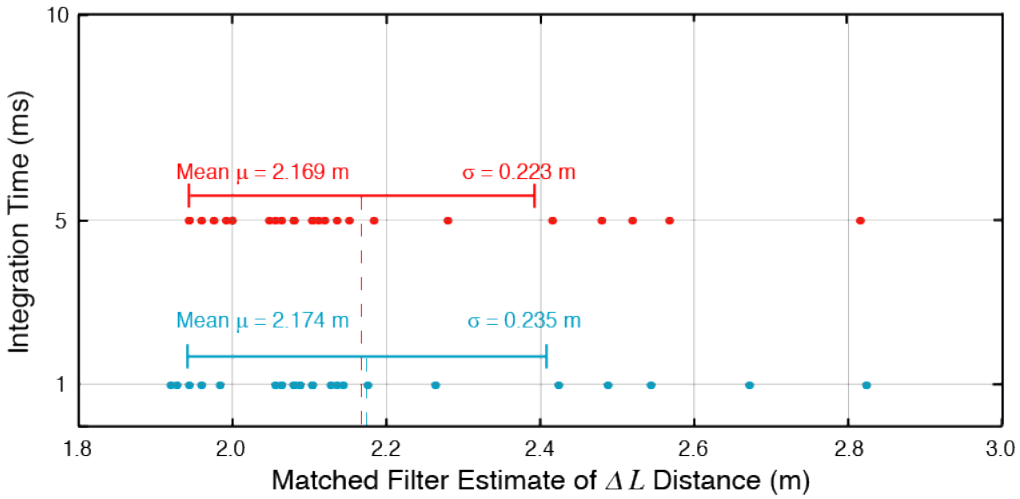

(a) Scatter plot showing the estimate of ΔL. The true value of the path length difference ΔL is equal to 2.175 m. The result of the plot aims to show that the matched filter analysis can correctly estimate ΔL and is independent of v_{SD} used to Doppler shift the PRN code chip frequency.

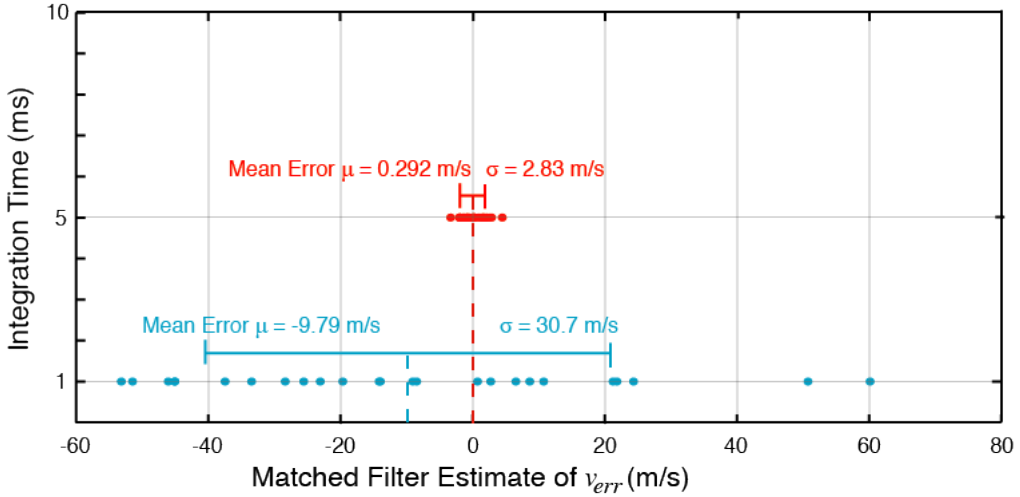

(b) Scatter plot showing the error in estimating the velocity. v_{err} is the difference between estimated velocity parameter v_0 and velocity value v_{SD} used to Doppler shift the modulating PRN code. The true value of v_{err} is equal to 0 m/s. The result of the plot aims to show that the matched filter analysis can correctly estimate the values of v_{SD} used to Doppler shift the PRN code chip frequency.

Figure 4.26: Scatter plot showing the 25 estimates path length difference ΔL and velocity v_{err} for 1 ms and 5 ms integration times. The blue dots represent the matched filter analysis results using 1 ms integration time and the red dots for using using 5 ms integration time.

Figure 4.26a shows the individual ΔL estimates for each of acquired signal using both 1 ms and 5 ms integration time. For 1 ms integration time, the mean of the measurement is equal to 2.174 m, approximately equal to the expected ΔL of 2.175 m in the bench-top experiment. The standard deviation is equal to 0.235 m, close to the limit of the analysis

path length estimate of 0.2 m. For 5 ms integration time, mean of the measurement equal to 2.169 m but there is a slight improvement in the standard deviation which is equal to 0.223 m as some of the outlying results from the 1 ms integration time have moved closer to 2.17 m.

Figure 4.26b shows the difference in the velocity estimate v_{err} for each of the acquired signals for 1 ms and 5 ms integration time. For 1 ms the mean and standard deviation of v_{err} is equal to -9.79 m/s and 30.70 m/s respectively. Since the standard deviation of the measurement indicates the precision of the velocity measurement, the result can be compared to Figure 4.23 where v_{SD} is equal to -7 km/s for all 25 acquired signals. Both standard deviations of the matched filter analysis are similar. For the 5 ms the mean and standard deviation of v_{err} has improved and are equal to 0.292 m/s and 2.83 m/s respectively. The standard deviation also closely matches the precision of the matched filter analysis in Figure 4.23.

The results in Figure 4.26 show that the matched filter analysis can estimate the time-varying delay of a target with any velocity expected from a space debris target. The precision of the position and change in the position of the estimates match the results observed in previous sections.

4.4 Chapter Summary

The chapter presented the bench-top experiment with the aims of amplitude modulating the continuous wave laser with a Doppler shifted version of the PRN code and acquiring the signal estimating the path length and time-varying delay using a matched filter analysis approach. The amplitude modulation was achieved using a Fibre Mach-Zehnder where the modulating PRN code's chip frequency can be changed in the experiment to apply the Doppler shift of the PRN code. The chapter also discussed the data acquisition stage and the matched filter analysis layout stage to estimate distance and velocity parameters. A hierarchical matched filter analysis approach was shown to be faster and more computationally efficient.

The experimental results indicated that the matched filter analysis can estimate both distance and velocity parameters applied to the bench-top experiment. Section 4.2.3 presented measurements of both the signal and control paths using the matched filter analysis when the PRN code chip frequency is unaltered. The two measurements are used to calculate ΔL, the difference in the two paths. The section also showed that the bench-top experiment accuracy to measure ΔL is limited to 0.2 m.

Section 4.3 presented the impact of Doppler shifting the modulating PRN code chip frequency and matched filter analysis estimating the velocity parameter. The experimental results showed that the precision of the matched filter analysis is inversely proportional to the received signal power P_{Sig} and is $t_i^{-1.5}$ to the integration time t_i. Hence for low signal-to-noise ratio optical signals, even when background photon noise is the dominant noise source, the precision of the velocity estimate can be improved by increasing the integration time.

Coherent Detection Scheme

Chapter 4 presented the bench-top experiment and matched filter analysis results for the direct detection scheme. The examinations showed that the signal-to-noise ratio of the received optical signal influences the accuracy and precision in estimating the time-varying delay parameters d_0 and v_0. Chapter 5 builds on the results from the direct detection scheme by investigating a method to optically amplify the received optical signal to increase the signal-to-noise ratio and improve both the accuracy and precision in estimating these parameters. This method is referred to as the coherent detection scheme.

In the coherent detection scheme, the optical signal in the signal path interferes with a second optical beam at the same wavelength ($\lambda = 1064\,\text{nm}$). This second laser beam is called the *local oscillator*. Controlling the optical power of the local oscillator influences the signal-to-noise ratio of the resulting interference with the optical signal. The examination of the coherent detection scheme shows that the amplitude modulated optical signal is amplified and improves the signal detection. Hence, the accuracy and precision of the matched filter analysis estimate of both d_0 and v_0 parameters are better compared to the results from the direct detection scheme.

5.1 Coherent Detection Theory

5.1.1 Background on the Coherent Detection Scheme

The simplest description of a coherent detection method is the measurement of the interference of two electromagnetic waves, with the application of the detection method in both the radio [151] and optical spectrum [152]. Since the thesis focuses on using optical signals, the coherent detection concept is discussed using optical sources. Figure 5.1 shows two continuous wave laser sources where the optical beams have interfered with each other. One of the laser beams is called the *signal* and the second beam is called the *local oscillator*. The optical beam from each laser source can be represented as an electric field containing information on the optical beam's energy E, frequency f and phase ϕ. In equation 5.1, $E_{Sig}(t)$ and $E_{LO}(t)$ is the electric field for the signal and local oscillator beams respectively.

$$\begin{aligned} E_{Sig}(t) &= E_{Sig}e^{i(2\pi f_{Sig}t+\phi_{Sig})} \\ E_{LO}(t) &= E_{LO}e^{i(2\pi f_{LO}t+\phi_{LO})} \end{aligned} \tag{5.1}$$

The phase of each optical beam is related to the propagating path length [80]. Therefore $\phi_{Sig} = \frac{2\pi f_{Sig}}{c} L_{Sig}$ and $\phi_{LO} = \frac{2\pi f_{LO}}{c} L_{LO}$.

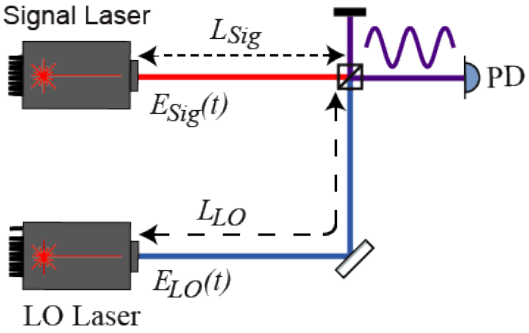

Figure 5.1: Interference of two continuous wave laser sources with electric field $E_{Sig}(t)$ and $E_{LO}(t)$.

The output of the beam splitter after the interference of the signal and local oscillator laser sources in Figure 5.1 produces two interfered optical beams. One of these beams is measured using a photodetector and represented by equation 5.2 as $A_{PD}(t)$. α in equation 5.2 is the conversion of the measured optical signal in watts to the photodetector output in Volts.

$$A_{PD}(t) = \frac{\alpha}{2}\Big[\underbrace{P_{Sig} + P_{LO}}_{\text{DC Term}} + \underbrace{2\sqrt{P_{Sig}P_{LO}}\ \cos(2\pi f_h t + \phi_{\Delta L})}_{\text{Beat Note}}\Big] \tag{5.2}$$

The measured interference pattern $A_{PD}(t)$ is split into the DC term and a *cosine* function called the beat note. The DC term is ignored and is usually filtered out. The beat note's frequency f_h and phase $\phi_{\Delta L}$ is the frequency and phase difference of the two interfering electric fields. Hence, f_h is equal to $f_{Sig} - f_{LO}$ and $\Delta\phi$ is equal to $\phi_{Sig} - \phi_{LO}$.

If the beat note frequency f_h is non-zero, the interference pattern is called a *heterodyne beat note* and this indicates that the two optical laser sources have different frequencies. If f_h is equal to zero then the interference is called a *homodyne beat note*. Measuring the frequency difference f_h can indicate if the signal frequency was shifted [153] during the signal propagation. The phase difference can be used to estimate the difference in the propagating path length $(L_{Sig} - L_{LO})$. The amplitude of the beat note scales with the square root of the product between the signal and local oscillator optical powers. Increasing the optical power of one of the two beams increases the amplitude of the measured beat note.

The optical layout in Figure 5.1 used one of the two interfered beams. If a second photodetector is used to measure the second interfered beam, this layout is called a balanced heterodyne or homodyne configuration [154]. This type of configuration can be used to measure the difference between the two photodetector measured signals and suppress the common noise in the layout [155].

5.1.2 Examples of Coherent Detection Applications

There are several different applications of a coherent system taking advantage of the information contained in the beat note. A direct detection method only measures the intensity of an optical signal but as seen in equation 5.2, the optical power, frequency and phase of the optical signal is present in the measured beat note. Assuming the frequency and phase of the local oscillator is known, the frequency and phase of the optical signal can be determined from the beat note. And for a low signal-to-noise ratio optical signal, the local

oscillator optical power can be increased to improve signal detection.

Measuring the phase of the beat note can be used to track the path length difference of an interferometer [156, 157] or phase modulating the signal laser to measure the propagation distance of the optical signal for ranging applications [25, 82] and optical communications [158]. Other applications of coherent systems are also used in spectroscopy applications [159] and atmospheric studies [160].

A coherent system is used in LIDAR applications to resolve small Doppler shifts of the optical signal laser frequency [152] to provide accurate tracking of a target's motion such as in satellite tracking [62] and weather forecasting [61]. LIDAR systems also use the coherent detection method to amplify the weak reflected signals [152] for improved signal detection. This application of the coherent system is of most interest for this thesis.

5.1.3 Signal-to-Noise Ratio in a Coherent Detection System

The chief factors that impact the signal-to-noise ratio in a coherent detection configuration for space debris ranging are:

1. Photodetector noise
2. Shot noise
3. Laser frequency noise
4. Diffuse surface of the target

Section 2.4 provides a more detail discussion of the noise sources and Section 2.3.3 on the diffuse surface for a piece of space debris. This section provides a brief discussion on how these factors impact a coherent detection configuration presented in Figure 5.1.

Both shot noise and photodetector noise add amplitude noise on the measured beat note. The photodetector is used to measure the interference pattern of the beat note. In the process dark current and electronic noise is introduced to the measured amplitude. Equation 5.3 is used to calculate the Newport 1811 photodetector noise σ_{PD} where NEP is the noise equivalent power of the photodetector, and B is the detector bandwidth [138].

$$\sigma_{PD} = NEP\sqrt{B} \tag{5.3}$$

Shot noise is a property of the light and depends on the optical power of both the signal beam and local oscillator beam [100, 103]. In most coherent detection applications, the local oscillator beam optical power is much higher than the signal beam optical power. Therefore shot noise from the local oscillator beam is more substantial than shot noise from the signal beam. Equation 5.4 is used to calculate shot noise σ_{SN} from the local oscillator where $\hbar$ is Planck's constant, c is the speed of light and λ is the wavelength of the local oscillator [100, 103]. Together, $\frac{\hbar c}{\lambda}$ is the energy of a photon at λ wavelength and is denoted as E_λ. P_{LO} is the optical power of the local oscillator beam.

$$\begin{aligned} \sigma_{SN} &= \sqrt{P_{LO}\left(\frac{\lambda}{\hbar c}\right)} \\ &= \sqrt{\frac{P_{LO}}{E_\lambda}} \end{aligned} \tag{5.4}$$

In a direct detection system, photodetector noise σ_{PD} is often the dominant amplitude noise source. However, in a coherent detection system, the local oscillator optical power is increased to amplify the measured amplitude of the beat note $\sqrt{P_{Sig}P_{LO}}$ in the presence of the photodetector noise σ_{PD}. The local oscillator optical power can be large enough where the local oscillator's shot noise σ_{SN} is larger than the photodetector noise σ_{PD} and is the dominant amplitude noise source. When this happens, the signal-to-noise ratio is fundamentally limited by the shot noise [152]. Equation 5.5 describes the signal-to-noise ratio of a shot noise limited system [100] where B is the bandwidth of the photodetector.

$$\begin{aligned} \frac{S}{N} &= \frac{2P_{Sig}P_{LO}}{2eP_{LO}B} \\ &= \frac{P_{Sig}}{eB} \end{aligned} \tag{5.5}$$

From equation 5.5, any further increase in the local oscillator optical power P_{LO} would not increase the signal-to-noise ratio of the measured beat note for a shot noise limited system. The signal-to-noise ratio can only be improved by increasing the optical power of the signal beam P_{Sig}. An amplitude-squeezed local oscillator beam can be used to reduce the shot noise limit [161], but this is beyond the scope of this thesis. It is also important to note that there are situations where a shot noise limited detection cannot be achieved if the photodetector is saturated and limits the local oscillator optical power [162].

Both laser frequency and phase noise cause fluctuations in the frequency f_h and $\phi_{\Delta L}$ measurement of the beat note. Both laser sources in Figure 5.1 are free-running lasers, and each has a $\frac{1}{f}$ laser frequency noise independent of each other. The two laser frequencies also drift over time independently of each other. When the two optical beams have interfered the beat note frequency f_h broadens in the frequency domain and drifts over time. This reduces the accuracy and precision of measuring f_h and hence affects determining the frequency of the signal beam f_{Sig}. The $\frac{1}{f}$ laser frequency noise of a laser source can be stabilised [109, 110], reducing the laser frequency noise. The independent drift of the two laser sources can be avoided by phase-locking the two lasers using a phase-locked loop [163]. One laser will be the master laser source and the second is laser acts as a slave and has the same laser frequency as the master laser.

A piece of space debris is a non-cooperative target with a diffuse reflecting surface. The result is the reflected signal is scattered in many directions and adds a random path length to each scattered reflected signal. Section 2.3.3 discusses in more detail the effects of a diffuse reflecting surface including for a coherent detection method. Since path length is related to the phase [80], the diffuse surface will impact a coherent system where the heterodyne beat note [62] and phase modulation methods [25, 82, 156], used to measure the time of flight. However, for an amplitude modulated system the small random change in the optical signal's path length does not change the propagation delay of each individual chip of the PRN code. The PRN code statistics remain unaffected. Hence, the coherent detection scheme focuses on interfering the amplitude modulated signal with a bright local oscillator.

5.1.4 Coherent Detection of Amplitude Modulated PRN Code

Building on the theoretical coherent detection layout presented in Figure 5.1, Figure 5.2 shows the theoretical optical layout where the output of the signal laser is first amplitude modulated with the PRN code sequence. The signal beam has a total propagation path

length L_{Sig} equal to $L_a + 2L_\tau + L_b$. L_τ is the range of the reflecting target. The amplitude modulated signal beam interferes with the local oscillator and the beat note is measured using a photodetector. Another addition in Figure 5.2 from Figure 5.1 is that the two laser sources are frequency stabilised using a phase-locked loop. The signal laser is the master laser source, and the local oscillator is the slave laser source.

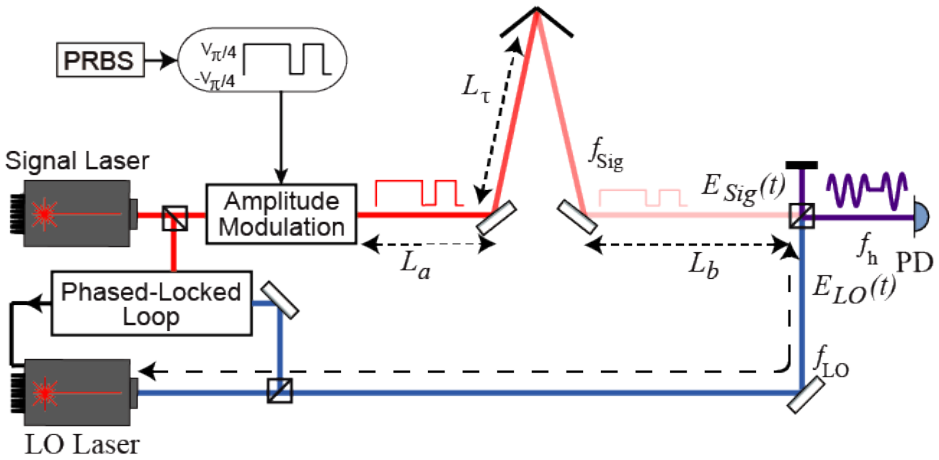

Figure 5.2: Optical layout where the signal laser is amplitude modulated with the PRN codes and propagates a distance of L_{Sig} before interfering with the LO laser.

Equation 5.6 is used to describe the signal $E_{Sig}(t)$ and local oscillator $E_{LO}(t)$ electric fields. $\phi_{Sig} = \frac{2\pi f_{Sig}}{c} L_{Sig}$ and $\phi_{LO} = \frac{2\pi f_{LO}}{c} L_{LO}$ while τ_{Sig} is the propagation delay of the signal beam and is equal to $\frac{L_{Sig}}{c}$. $C(t - \tau_{Sig})$ is the delayed version of the modulated PRN code.

$$\begin{aligned} E_{Sig}(t) &= C(t - \tau_{Sig}) E_{Sig} e^{i(2\pi f_{sig} t + \phi_{Sig})} \\ E_{LO}(t) &= E_{LO} e^{i(2\pi f_{LO} t + \phi_{LO})} \end{aligned} \tag{5.6}$$

When the two electric fields, $E_{Sig}(t)$ and $E_{LO}(t)$, are interfered with each other, the measured optical beat note at the photodetector $A_{PD}(t)$ is described in equation 5.7 where f_h is equal to $f_{Sig} - f_{LO}$ and $\phi_{\Delta L}$ is equal to $\phi_{Sig} - \phi_{LO}$.

$$A_{PD}(t) = \frac{\alpha}{2}\Big[\underbrace{C(t - \tau_{Sig}) P_{Sig} + P_{LO}}_{\text{DC Term}} + \underbrace{2\sqrt{C(t - \tau_{Sig}) P_{Sig} P_{LO}}\ \cos(2\pi f_h t + \phi_{\Delta L})}_{\text{Beat Note}}\Big] \tag{5.7}$$

Assuming the DC term is filtered out by the photodetector, the measured beat note is a cosine function that changes depending on the frequency difference f_h and phase difference $\phi_{\Delta L}$ of the signal and local oscillator beams. As in Section 5.1.1, the amplitude of the beat note scaled with the square root of the signal and local oscillator optical power. However, the delayed version of the amplitude modulated PRN code is encoded onto the amplitude of the beat note. Therefore by interfering the amplitude modulated signal with the local oscillator, the PRN encoded beat note can be amplified above the different amplitude noise source present in the bench-top experiment to a shot-noise limited detection.

5.1.5 Spectra of the PRN Code Amplitude Modulated Beat Note

Equation 5.7 is used in the simulation to generate an amplitude modulated PRN code beat note. f_h is equal to 70 MHz and $\phi_{\Delta L}$ is equal to 0 radians. The chip frequency f_{Chip} of the PRN code is equal to 75 MHz. τ_{Sig} is also equal to 1 s. For simplicity, the simulation assumed a shot noise limited configuration and neither frequency nor phase noise was added. Equation 5.8 shows the output of the simulated beat note when the PRN code has a binary value of 1 and 0.

$$A_{PD}(t) = \begin{cases} \sqrt{P_{Sig}P_{LO}}\ \cos(2\pi f_h t + \phi_{\Delta L}) & \text{if } C(t-\tau_{Sig}) = 1 \\ 0 & \text{if } C(t-\tau_{Sig}) = 0 \end{cases} \tag{5.8}$$

Figure 5.3 illustrates the frequency spectra of the simulated heterodyne beat note. The heterodyne beat note is observed at f_h equal to 70 MHz and a $sinc^2$ function is also seen centred around f_h. The first null of the $sinc^2$ function is at 145 MHz which is equal to $f_h + f_{Chip}$. The result shows that the PRN code harmonics are modulated onto the heterodyne beat note in the frequency spectrum. Approximately half the beat note power in power spectral density is spread over multiple frequencies as PRN code harmonics and the other half is observed as the heterodyne beat note at f_h. This is because half the PRN code sequence has a binary value of 1 and produces a beat note with amplitude $\sqrt{P_{Sig}P_{LO}}$ while the other half has a binary value of 0 and produces a beat amplitude equal to 0.

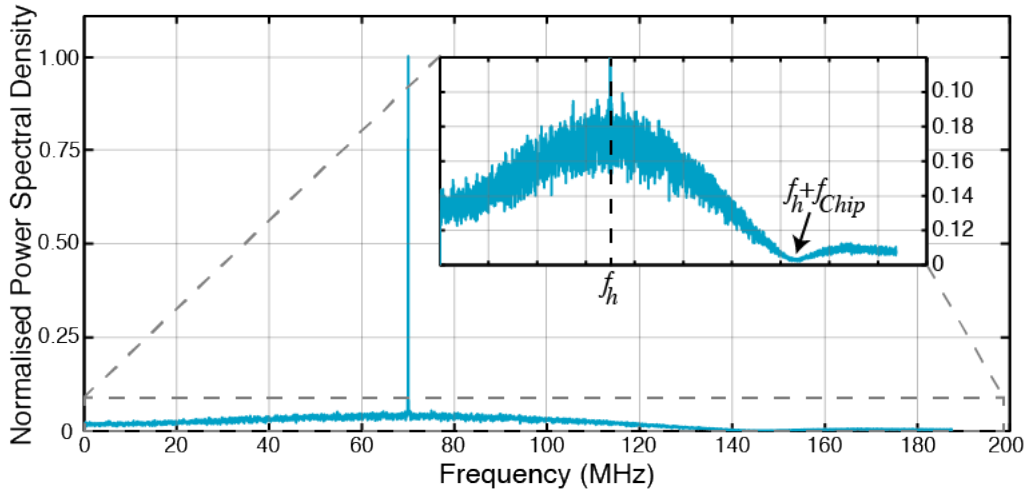

Figure 5.3: Power Spectral Density of the simulated heterodyne beat note where the amplitude modulated PRN code signal is coherently mixed with the local oscillator.

Figure 5.4 shows, in simulation, the power spectrum of the PRN encoded heterodyne beat note together with the different amplitude noise sources that limit the signal-to-noise ratio of a direct detection method. In the simulation, the photodetector noise is equal to 1 pW, and the background photon noise source P_{BPN} is equal to 100 pW. The optical signal P_{Sig} is equal to 10 pW and the local oscillator P_{LO} is equal to 1 μW. As seen in Figure 5.4, even though the optical signal has lower received power than the background photon noise source ($P_{Sig} < P_{BPN}$), the local oscillator has amplified the beat note above the background photon noise to a shot noise limited detection. The null of the PRN code harmonic from 145 MHz is the shot noise level from the local oscillator. Hence, shot noise is the dominant noise source in the simulated optical system.

As discussed in Section 5.1.3 and presented in equation 5.5, for shot noise limited detection,

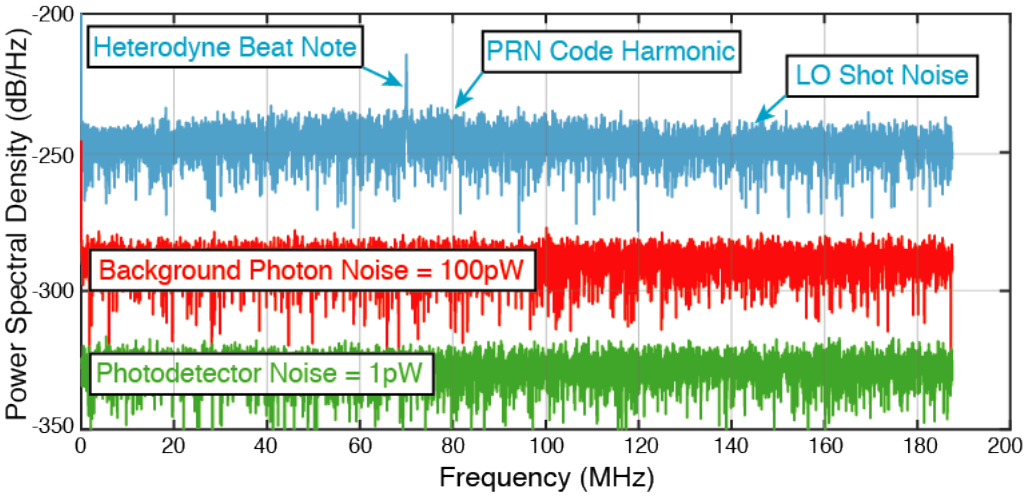

Figure 5.4: Frequency spectrum showing the amplitude modulated PRN code heterodyne beat note amplified above the various noise sources.

increasing the local oscillator optical power P_{LO} does not result in improved signal-to-noise ratio. Equation 5.5 can be updated to equation 5.9 taking into account the amplitude modulated PRN code signal beam. Any further increase in the signal-to-noise ratio can only be achieved by increasing the signal optical power P_{Sig}.

$$\begin{aligned} \frac{S}{N} &= \frac{2C(t-\tau_{Sig})P_{Sig}P_{LO}}{2eP_{LO}B} \\ &= \frac{C(t-\tau_{Sig})P_{Sig}}{eB} \end{aligned} \tag{5.9}$$

Amplifying the signal using a local oscillator in a coherent detection could be advantageous for weak signal detection, improving the ranging accuracy and precision for a space debris application. By mixing with a bright local oscillator, a coherent detection scheme can be less susceptible to additive amplitude noise sources such as background photon noise and photodetector noise. The coherent detection scheme might allow space debris daylight operation and provide a more precise estimation of the time-varying delay without requiring the large integration times of the direct detection scheme.

5.1.6 Recovering the Amplitude Modulated PRN code from the Beat Note

Figure 5.5 shows the post-signal processing used to recover the amplitude modulated PRN code from the measured heterodyne beat note. The signal processing method used is called the *In-phase and Quadrature phase demodulation* ($I^2 + Q^2$) where the acquired beat note is mixed with an in-phase ($I = \sin(2\pi f_{IQ} + \phi_{IQ})$) and quadrature phase ($Q = \cos(2\pi f_{IQ} + \phi_{IQ})$) component [164]. The $I^2 + Q^2$ demodulation method is widely used in several different applications, such as in a phase-locked loop [165] and optical communications [166], to measure the amplitude and phase of an unknown signal. This section presents the mathematical output of each step of the $I^2 + Q^2$ demodulation to recover the amplitude modulated PRN code for the matched filter analysis. For simplicity, the discussions in this section will first ignore both amplitude and phase noise. The impact of a diffuse reflecting surface is introduced in Section 5.1.7.

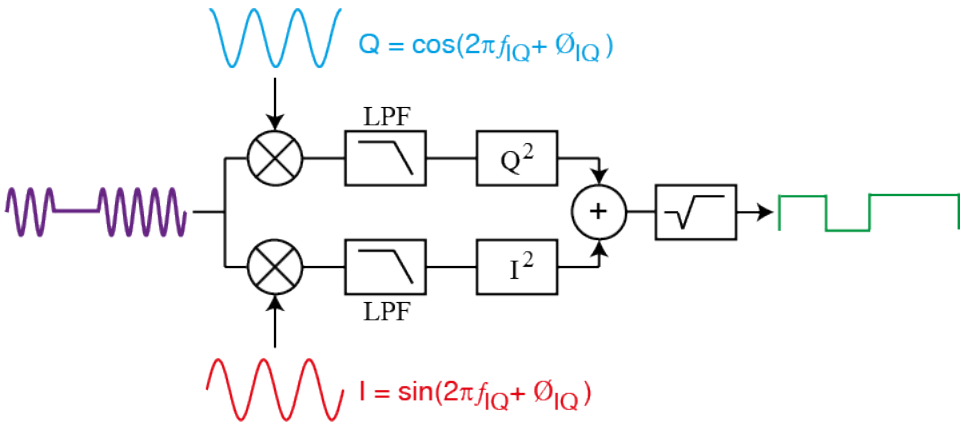

Figure 5.5: Block diagram of the I^2+Q^2 demodulation steps to recover the amplitude modulated PRN code from the heterodyne beat note.

Figure 5.6 shows the phasor diagram presenting the relationship of an unknown signal with amplitude A and phase ϕ, with the I and Q components. The I and Q components are orthogonal to each other with a phase offset equal to $\frac{\pi}{2}$ radians. By mixing the unknown signal with the two orthogonal components, the amplitude A and the phase ϕ of the unknown signal can be calculated using Pythagoras theorem and Trigonometric functions.

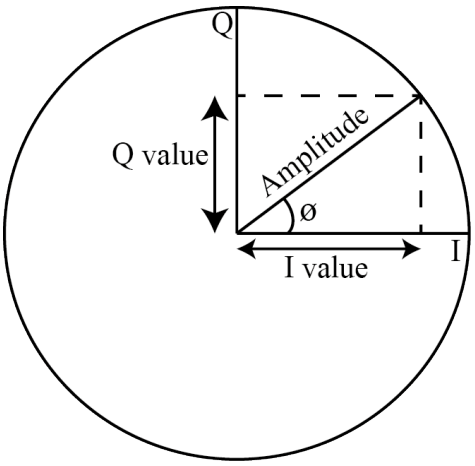

Figure 5.6: Phasor diagram showing the I and Q components have a $\frac{\pi}{2}$ phase difference. The I and Q components can be used to find the amplitude and phase of an unknown sinusoidal function.

Equation 5.10 and equation 5.11 present the output of mixing the I and Q components respectively with the acquired beat note $s(t) = A(t)\cos(2\pi f_h t + \phi_{\Delta L}(t))$.

$$I_{Output} = A(t)\cos(2\pi f_h t + \phi_{\Delta L}(t))\sin(2\pi f_{IQ} t + \phi_{IQ}) \tag{5.10}$$

$$Q_{Output} = A(t)\cos(2\pi f_h t + \phi_{\Delta L}(t))\cos(2\pi f_{IQ} t + \phi_{IQ}) \tag{5.11}$$

Using the trigonometric identities shown in equation 5.12 and equation 5.13, equation 5.10 and equation 5.11 can be rewritten into equation 5.14 and equation 5.15 respectively. To simplify the number of terms in equation 5.14 and equation 5.15, ϕ_{IQ} is equal to 0 radian.

$$2\cos\alpha\cos\beta = \cos(\alpha-\beta) + \cos(\alpha+\beta) \tag{5.12}$$

$$2\sin\alpha\cos\beta = \sin(\alpha-\beta)+\sin(\alpha+\beta) \tag{5.13}$$

$$I_{Output} = \frac{A(t)}{2}\Big[\sin(2\pi(f_h - f_{IQ})t + \phi_{\Delta L}(t)) + \sin(2\pi(f_h + f_{IQ})t + \phi_{\Delta L}(t))\Big] \tag{5.14}$$

$$Q_{Output} = \frac{A(t)}{2}\Big[\cos(2\pi(f_h - f_{IQ})t + \phi_{\Delta L}(t)) + \cos(2\pi(f_h + f_{IQ})t + \phi_{\Delta L}(t))\Big] \tag{5.15}$$

Both the I_{Output} and Q_{Output} comprise two terms, the difference in the phase and frequency between the beat note and the I and Q components, and the sum of the phase and frequency of the beat note with the I and Q components. Since ϕ_{IQ} is equal to 0 radian, the two terms are referred to as the *difference frequency term* and *sum frequency term* respectively.

The sum frequency term is removed by passing both I_{Output} and Q_{Output} through a low pass filter. Figure 5.7 shows the simulated results of passing the I_{Output} and Q_{Output} through a low pass filter in the frequency domain. In the simulation the PRN code chip frequency is equal to 75 MHz while both f_h and f_{IQ} are equal to 70 MHz. The sum frequency term $(f_h + f_{IQ})$ of both I_{Output} and Q_{Output} is equal to 140 MHz. The cut-off frequency chosen for the low pass filter is equal to 125 MHz, to match the bandwidth limitation applied to the acquired signal by the Newport 1811 photodetector used in the bench-top experiment. In the simulation, the low pass filter attenuates the sum frequency term at 140 MHz by approximately -50 dB. Figure 5.7 shows a significant reduction in the power spectrum for frequencies above 125 MHz due to the high attenuation of the low pass filter. Even though the PRN code is modulated onto the amplitude of the signal beam, if the sum frequency term is not filtered out, unwanted harmonic terms will be present in the recovered signal.

Assuming $f_h = f_{IQ}$, the filtered output of I_{Output} and Q_{Output} is presented in equation 5.16 and 5.17 respectively.

$$I_{Filtered} = \frac{A(t)}{2}\Big[\sin(\phi_{\Delta L}(t))\Big] \tag{5.16}$$

$$Q_{Filtered} = \frac{A(t)}{2}\Big[\cos(\phi_{\Delta L}(t))\Big] \tag{5.17}$$

Both equation 5.16 and equation 5.17 contain information on both the amplitude $A(t)$ and phase $\phi_{\Delta L}(t)$ of the measured beat note. *Pythagoras theorem* is used to measure the amplitude $A(t)$ using the following steps shown in equation 5.18:

$$\begin{aligned} A_{IQ} &= 2\sqrt{I^2_{Filtered} + Q^2_{Filtered}} \\ &= A(t)\sqrt{\sin^2(\phi_{\Delta L}(t)) + \cos^2(\phi_{\Delta L}(t))} \\ &= 2\alpha\sqrt{C(t-\tau_{Sig})}\sqrt{P_{LO}P_{Sig}} \end{aligned} \tag{5.18}$$

Using Pythagorean identities, $\sin^2\phi_{\Delta L}(t)^2 + \cos^2\phi_{\Delta L}(t) = 1$, the output of A_{IQ} is equal to $A(t)$. In equation 5.7, the amplitude of the beat note $A(t)$ is equal to $\alpha\sqrt{C(t-\tau_{Sig})P_{Sig}P_{LO}}$. Hence, the result of using the Pythagoras theorem contains the delayed version of the amplitude modulated PRN code $C(t-\tau_{Sig})$, scaled by $\sqrt{P_{Sig}P_{LO}}$.

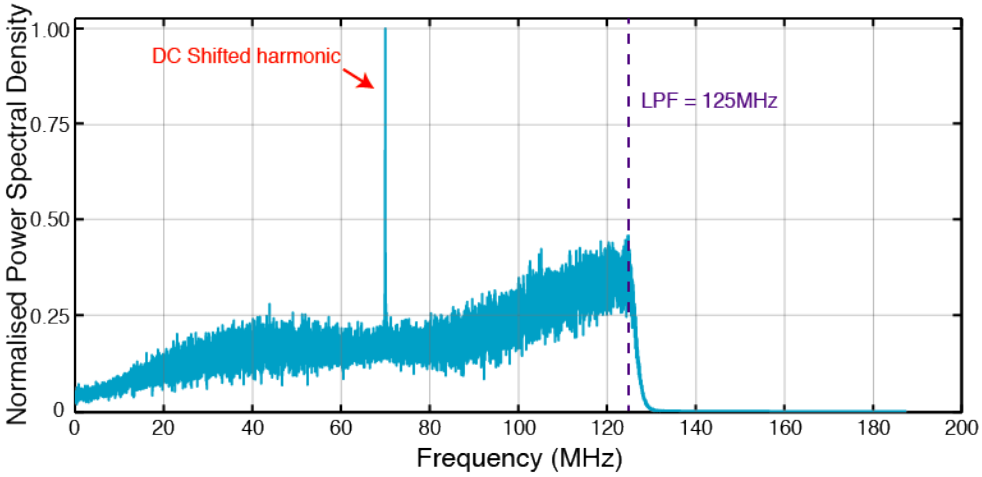

(a) Frequency spectrum of the Q filtered output.

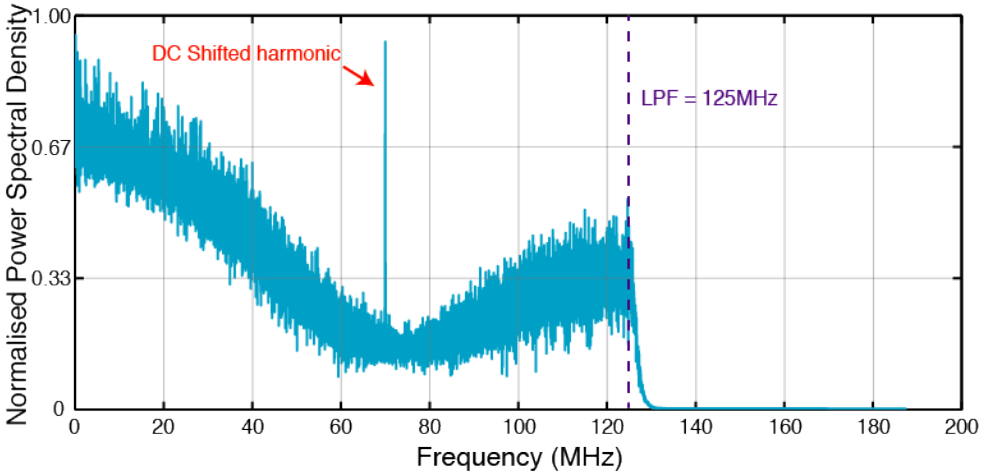

(b) Frequency spectrum of the I filtered output.

Figure 5.7: Simulated frequency spectrum of both the I and Q filtered output using 125 MHz low pass filter.

Figure 5.8 shows a simulation of the frequency spectrum of the recovered PRN code from the $I^2 + Q^2$ demodulation using the same beat note properties in Figure 5.7. The power spectral density shows the presence of a $sinc^2$ function with the null of the PRN code at 75 MHz. However, the PRN code harmonics above 125 MHz have been filtered out by the low pass filter used in the $I^2 + Q^2$ demodulation.

The phase difference $\phi_{\Delta L}(t)$ is calculated using the trigonometric functions shown in equation 5.19. The calculated phase $\phi_{\Delta L}(t)$ contains information of the signal beam's path length L_{Sig}, but as discussed in previous sections, laser frequency noise and the diffuse surface effects on the signal beam's phase would affect any information gathered from the phase of the beat note. Therefore the signal processing of the I^2+Q^2 demodulation ignores the phase measurement step in equation 5.19.

$$\begin{aligned} \phi_{\Delta L}(t) &= atan\left(\frac{\sin(\phi_{\Delta L}(t)}{\cos(\phi_{\Delta L}(t)}\right) \\ &= \frac{2\pi f_{Sig}}{c} L_{Sig} - \frac{2\pi f_{LO}}{c} L_{LO} \end{aligned} \tag{5.19}$$

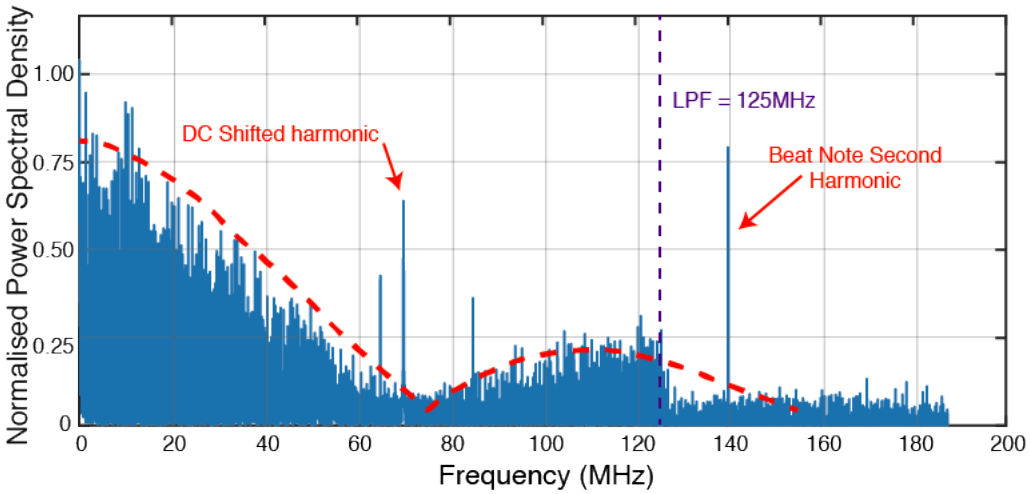

Figure 5.8: Simulated frequency spectrum of the interference pattern after passing through an $I^2 + Q^2$ demodulation. The red dotted line is the fit of a PRN code $sinc^2$ function. The frequency spectrum resembles the PRN code spectrum with the first null occurring at 75 MHz.

5.1.7 Simulated Analysis of the $I^2 + Q^2$ Demodulation for a Diffuse Surface

Equation 5.18 shows that the amplitude of the recovered PRN code $A(t)$ does not contain any information on the beat note frequency or phase. In theory, neither frequency noise nor the randomised phase effect are present in the recovered PRN code. Therefore both would not impact estimating the time-varying delay of the optical signal. This section demonstrates this in simulation for a diffuse reflecting surface and Section 5.4.3 and Section 5.4.4 will present experimental results for frequency-related noise.

Figure 5.9 compares two simulated signal correlation outputs, as a function of the distance parameter d_0. This simulation looked to determine if the random phase effect, discussed in Section 2.3.3, would impact the signal correlation for a coherent detection scheme. The scattering effect for a diffuse surface was not introduced in the simulation. However, in a real application of the coherent detection scheme, the received signal power would be reduced due to the scattering effect. The simulation also introduces both shot noise and photodetector noise to the received optical signal.

For one of the correlations, the signal beam is modelled to be reflected by a surface without the random phase effect. In this case, each reflected electric field has the same propagation path length L_{Sig} and hence the same phase. For the other signal correlation, the reflecting surface is modelled to be a complex surface that introduces the random phase effect. A random path length with a root mean square (RMS) of 0.5 μm following a Gaussian distribution is added to each reflected electric field. Therefore each reflected electric field has a varying phase. Both signals are passed through the $I^2 + Q^2$ demodulation and the matched filter analysis to estimate the signal beam's propagating path length L_{Sig}.

The result in Figure 5.9 first showed that the $I^2 + Q^2$ demodulation was able to recover the amplitude modulated PRN code and the matched filter analysis generated a signal correlation for both reflecting surfaces. Figure 5.9 also showed that both the two normalised signal correlations overlap each other. The simulated result confirms the discussions that apart the reduction in optical power from the scattering effect, the coherent detection scheme with the matched filter analysis is not affected by the random phase effect from a diffuse surface.

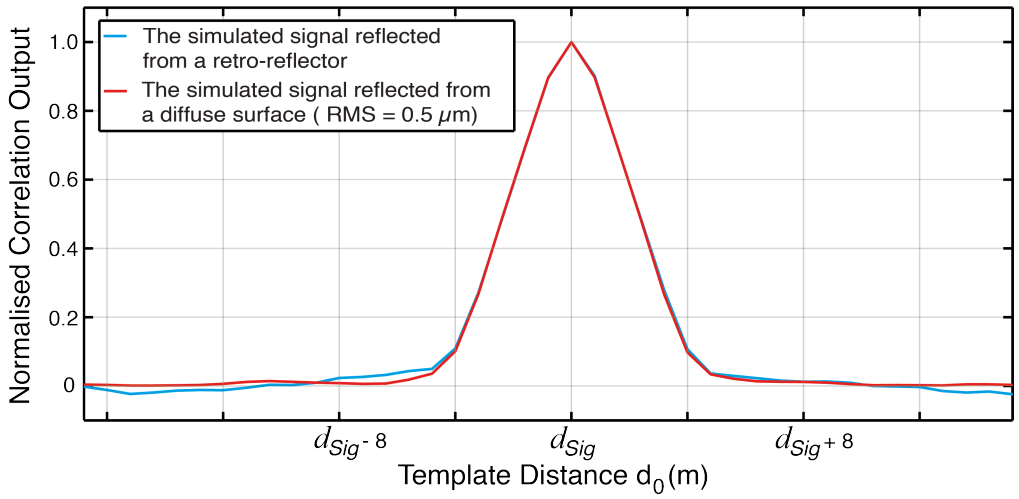

Figure 5.9: Comparing simulation of two normalised signal correlation where one signal is reflected by a retro-reflector and the second signal is reflected by a diffuse surface.

5.2 Experimental Layout

Table 5.1 shows the chosen PRN code properties and bench-top experiment parameters for the coherent detection scheme. Section 5.2 discusses and justifies the values selected for the experiment.

The bench-top experiment aims to simulate the time-varying delay of a piece of space debris and demonstrate a coherent detection scheme to amplify the signal and improve the matched filter estimate of the time-varying delay. The bench-top experiment used to model a moving space debris target and a coherent detection scheme was achieved by breaking the problem up into a smaller number of tasks:

1. Doppler shift the PRN code sequence using the PRBS generator.
2. Use the Fibre Mach-Zehnder interferometer to amplitude modulate the continuous wave laser.
3. Attenuate the optical power of the signal beam in the signal path.
4. Interfere the signal path beam with a local oscillator beam.
5. Estimate the time-varying delay parameters d_0 and v_0.
6. Collect statistics of the precision of estimating the time-varying delay.
7. Characterise how integration time t_i and received signal power P_{Sig} impacts the precision of the measurement.
8. Introduce laser frequency noise.
9. Identify if laser frequency noise has an impact on the precision of the matched filter estimate for the coherent detection scheme.

Parameters	Parameter Values
ADC sampling frequency $f_{sampling}$	1.5 GHz
PRN chip frequency f_{chip}	75 MHz
PRN code length L	32 767 chips
PRN code period $Tcode$	0.44 ms
Clock frequency f_{MF}	375 MHz
Laser wavelength λ	1064 nm
Photodetector NEP	22.5 pW/$\sqrt{\text{Hz}}$
Photodetector bandwidth	125 MHz
Signal single pass freq shift (changeable)	80 MHz
LO freq shift	90 MHz
Heterodyne beat note f_h (changeable)	70 MHz
Max. Integration time	0.1 s

Table 5.1: Table summarising the parameters chosen for the optical experiment.

5.2.1 PRN Code Generation and Amplitude Modulating the Continuous Wave Laser

Figure 5.10 shows the optical layout of the bench-top experiment used to evaluate the coherent detection scheme. The bench-top experiment for the coherent detection scheme builds on the experimental layout discussed in Section 4.1 for the direct detection scheme.

The PRBS generator discussed in Section 4.1.1 is used to generate a 15-bit PRN code (code length $L = 32767$ chips) with a chip frequency equal to 75 MHz. The chip frequency can be Doppler shifted to model the time-varying delay of a moving space debris target by changing the PRBS clock frequency.

The PRN code is then amplitude modulated onto the continuous wave laser using the Fibre Mach-Zehnder interferometer discussed in Section 4.1.2 and Section 4.1.3. The input beam optical power into the Fibre Mach-Zehnder is split equally using a 2x1 fibre splitter into two arms called the *Phase modulation arm* and the *Fibre stretcher arm*. The PRN code is phase modulated onto the phase modulation arm, and the optical fibre stretcher is used to control the fibre path length difference of the two arms to optimise the PRN code amplitude modulation. Equation 5.20 presents the electric fields $E_{Mod}(t)$ and $E_{FS}(t)$ of the phase modulation and fibre stretcher arm respectively.

$$\begin{aligned} E_{Mod}(t) &= E_{Mod}e^{i(2\pi f_{Laser}t+\phi_{Mod}+\phi_{PRN})} \\ E_{FS}(t) &= E_{FS}e^{i(2\pi f_{Laser}t+\phi_{FS})} \end{aligned} \tag{5.20}$$

The optical beams of the two arms are interfered using a 1×2 fibre coupler, and the output of the Fibre Mach-Zehnder interferometer $P_{FMZ}(t)$ is presented in equation 5.21 where $\phi_{\Delta L}$ is equal to $\phi_{Mod}-\phi_{FS}$. By controlling $\phi_{\Delta L}$ using the fibre stretcher, phase modulating the

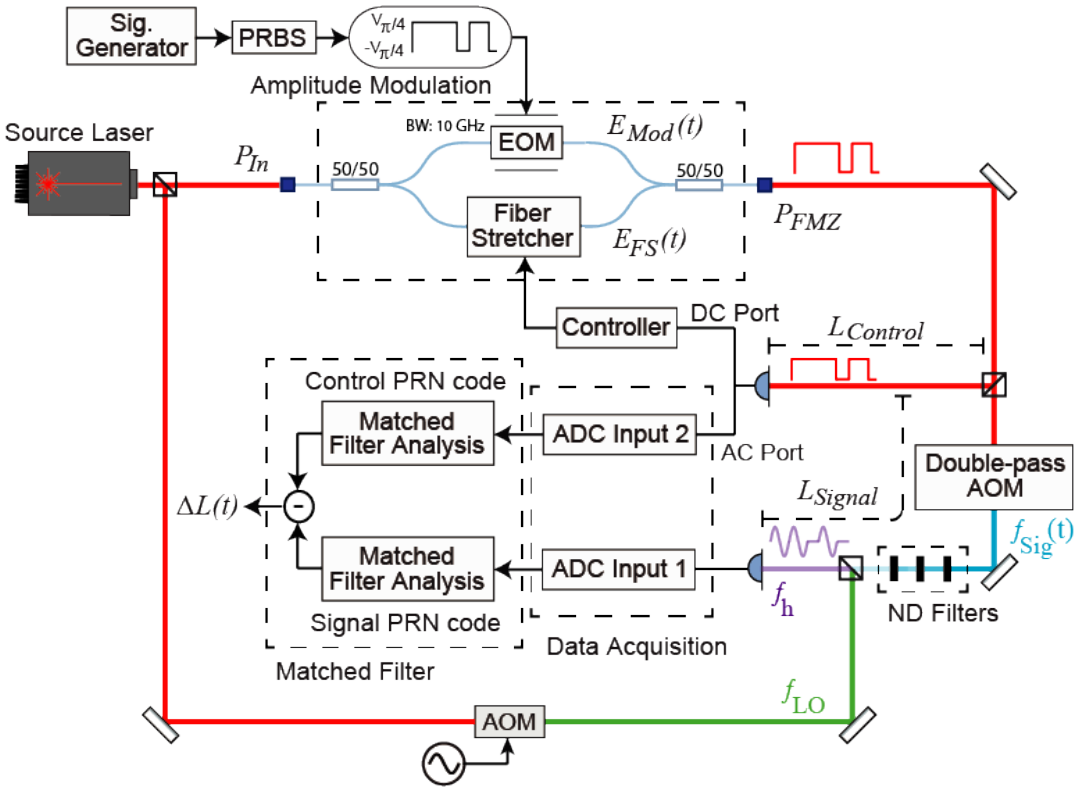

Figure 5.10: Optical layout to evaluate the coherent detection scheme where the amplitude modulated PRN code signal is interfered with the local oscillator prior to detection at the photodetector.

PRN in the Fibre Mach Zehnder interferometer results in an amplitude modulated PRN code optical signal at the output of the Fibre Mach Zehnder interferometer.

$$P_{FMZ}(t) = \frac{1}{2}\Big[P_{Mod} + P_{FS} + 2\sqrt{P_{Mod}P_{FS}}\cos(\phi_{\Delta L} + \phi_{PRN})\Big] \tag{5.21}$$

The output of the Fibre Mach-Zehnder is split into two paths as discussed in Section 4.1.4. One path is the *control path* with path length $L_{Control}$ equal to 0.675 m. The second path is the *signal path* to mimic the return path of the optical signal with path length L_{Signal} equal to 2.75 m. The path length difference ΔL ($L_{Signal} - L_{Control}$) is equal to 2.075 m.

The signal path optical signal is passed through a double-pass AOM configuration. This configuration is used to frequency shift the signal laser beam frequency to f_{Sig} using an acousto-optic modulator (AOM). An AOM is a device used to control the power, frequency and spatial direction of the laser beam [167] by using Bragg diffraction to scatter the propagating light [168]. Section 5.2.4 will provide more details on how this beam frequency shift was achieved.

The frequency-shifted optical signal is then attenuated using neutral density filters. The calibrated filter values are presented in Table 4.3 in Section 4.1.5. The attenuated signal then was interfered with the local oscillator.

5.2.2 Interference With the Local Oscillator

For the direct detection scheme, presented in Figure 4.3, the output of the laser source is split to control the optical intensity entering the Fibre Mach-Zehnder interferometer to

prevent damaging the components. Most of the output laser power is dumped. For the coherent detection scheme presented in Figure 5.10, this path of the laser output is used as the local oscillator beam. The main advantage of using the same laser source as both the amplitude modulated signal and as the local oscillator source is the beat note has a stable relative phase and frequency [152] to test the matched filter analysis of the coherent detection scheme.

The output of the laser source used as the local oscillator beam is first passed through an acousto optic modulator (AOM) to frequency shift the local oscillator laser frequency f_{LO} by 90 MHz. Equation 5.22 shows the electric field of the local oscillator beam where ϕ_{LO} is equal to $\frac{2\pi f_{LO}}{c} L_{LO}$.

$$E_{LO}(t) = E_{LO} e^{i(2\pi f_{LO} t + \phi_{LO})} \tag{5.22}$$

The frequency-shifted local oscillator beam then interferes with the signal path optical beam. Since the output of the Fibre Mach Zehnder interferometer is the interference of two electric fields, presented in equation 5.20, the beat note is the interference of three electric fields, $E_{Mod}(t)$, $E_{FS}(t)$ and $E_{LO}(t)$. The output optical intensity $P_{PD}(t)$ of the interference of the three electric fields is presented in equation 5.23.

$$\begin{aligned} P_{PD}(t) = \frac{1}{2}\Big[& \underbrace{P_{Mod} + P_{FS} + P_{LO}}_{\text{DC Term}} \\ & + \underbrace{P_{FMZ}(t)}_{\text{1st Beat Note Term}} \\ & + \underbrace{2\sqrt{P_{Mod} P_{LO}} \cos(2\pi f_h t + (\phi_{Mod} + \phi_{Sig} - \phi_{LO}) + \phi_{PRN}(t))}_{\text{2nd Beat Note Term}} \\ & + \underbrace{2\sqrt{P_{FS} P_{LO}} \cos(2\pi f_h t + (\phi_{FS} + \phi_{Sig} - \phi_{LO}))}_{\text{3rd Beat Note Term}} \Big] \end{aligned} \tag{5.23}$$

The DC term in equation 5.23 is obtained from the DC port of the Newport 1811 photodetector. The three higher frequency beat note terms, including shot noise, are obtained from the AC port of the photodetector. Only the signal from the AC port of the photodetector is digitised by the analogue to digital converter (ADC).

The 1st beat note term is equal to $P_{FMZ(t)}$ in equation 5.21, the interference between the phase modulation and fibre stretcher arm in the Fibre Mach Zehnder interferometer resulting in an amplitude modulated PRN code.

The 2nd beat note term is the beat note with the phase modulated PRN code $\phi_{PRN}(t)$. As in the 1st beat note term, $\phi_{PRN}(t)$ affects the output of the *cosine* function. The phase-modulated PRN code causes the beat note to be spread over a large frequency range resulting in a $sinc^2$ function in the frequency domain centred around f_h and the nulls occur at $f_h - f_{Chip}$ and $f_h + f_{Chip}$.

The 3rd beat note term does not contain any PRN code information. Therefore in the frequency domain, the 3rd beat note contributes only a heterodyne beat note at f_h.

The sum of the 2nd and 3rd beat note produces the amplitude modulated PRN code spectrum observed in the simulation in Figure 5.3. Both these terms are amplified by the local oscillator optical power P_{LO}, unlike the 1st beat note term. For example, if both P_{Mod} and P_{FS} are equal to 1 nW and P_{LO} is equal to 10 μW, the output power of the

1st beat note term is equal to 1 nW while the output power of the 2nd and 3rd beat note term are both equal to 100 nW. Therefore in a coherent detection scheme where a bright local oscillator interferes with a weak signal ($P_{Sig} < P_{LO}$), the 1st beat note term is much smaller than the 2nd and 3rd term. Hence, the impact of the 1st beat note term is ignored.

5.2.3 Shot Noise Limited Detection

In Figure 5.11 the local oscillator optical power was increased to achieve a shot noise limited detection where the shot noise from the local oscillator is larger than the Newport 1811 photodetector noise floor. In Figure 5.11 the optical signal beam is blocked, therefore no heterodyne beat note is observed at 70 MHz. The local oscillator optical power was measured at 115 μW. The result in Figure 5.11 shows that the shot noise from the local oscillator has increased the noise floor by approximately 1.1 dB at 70 MHz above the photodetector noise. The saturation limit of the Newport 1811 photodetector under continuous wave operation is roughly 120 μW [138]. The local oscillator optical power is close to the saturation limit, and several harmonics were observed when the local oscillator optical power was further increased. Hence the maximum optical power of the local oscillator was set to 115 μW.

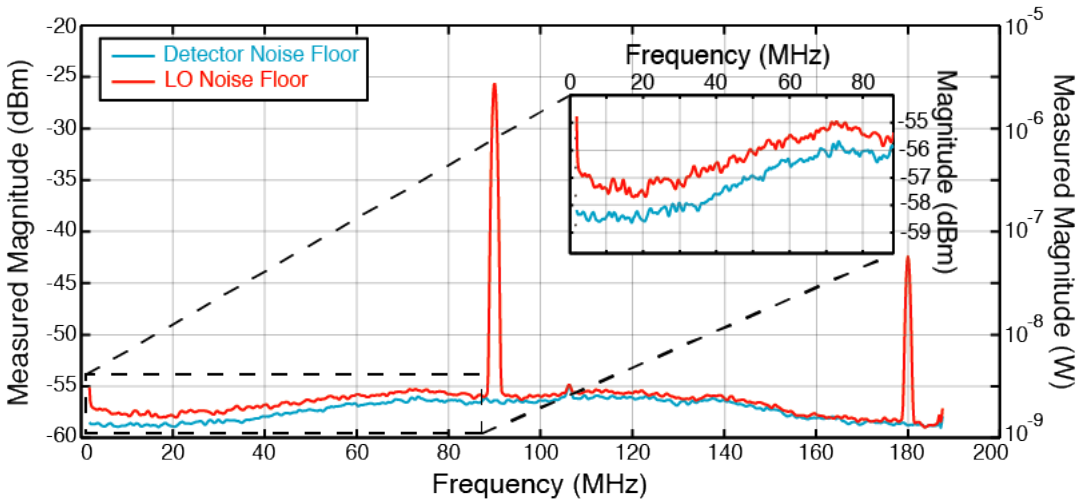

Figure 5.11: Comparing the noise floor of the Newport 1811 photodetector used in the signal path with the shot noise from the local oscillator used to amplify the signal.

The shot noise in Figure 5.11 is not the expected white noise for all frequencies because of bandwidth effects from the photodetector. These bandwidth effects were different for a second Newport 1811 photodetector.

Figure 5.11 also shows two harmonics in the frequency spectrum, one at 90 MHz and another at 180 MHz with an approximate magnitude of −26 dBm and −42 dBm respectively. The AOM used to frequency shift the local oscillator causes the 90 MHz harmonic and the 180 MHz is it's second harmonic. These harmonics are due to interference between the unshifted and shifted light at the output of the AOM. The magnitude of the harmonic changes with changing the alignment of the beam into the AOM but this also affects the power of the optical beam at the output of the AOM.

The 90 MHz and the 180 MHz harmonics would be present in the frequency spectrum of the recovered PRN code. When the recovered PRN code is correlated with the template code in the matched filter analysis, both harmonics are spread over a broad bandwidth [126] and would not impact the time-varying delay estimate.

5.2.4 Adding Random Frequency to Heterodyne Beat Note

Coherent detection methods are sensitive to both frequency and phase noise. In most cases, the laser sources are frequency stabilised [111] or derived from the same source to have a stable phase. However, in a space debris application, other factors such as propagating through the atmosphere can introduce additional frequency noise into the signal beam.

The discussion in Section 5.1.6 presented that the recovered PRN code from the beat note does not contain phase and frequency information and hence is not affected by frequency noise. In this section, a large random frequency is added to the optical signal frequency in the signal path to confirm the theoretical discussion in Section 5.1.6.

As discussed in Section 5.2.1, an AOM is placed in the signal path. By controlling the frequency of the sinusoidal signal f_{RF}, the AOM can frequency shift the optical signal frequency to f_{Sig} before the optical signal is attenuated and interfered with the local oscillator beam. If the input sinusoidal signal f_{RF} has an additional random frequency term δf, then the frequency shift of the optical signal ($f_{Sig} \pm \delta f$) is also randomised.

The disadvantage of frequency shifting the signal path optical beam using an AOM is the AOM output beam's spatial direction θ_D also changes with the change in the sinusoidal frequency f_{RF} as described in equation 5.24. λ is the wavelength of the laser source, and v is the acoustic velocity propagating through the crystal in the AOM. The steering of the signal path beam by the AOM reduces the overlap efficiency with the local oscillator and introduces amplitude fluctuations in the beat note.

$$\theta_D = \frac{\lambda f_{RF}}{v} \tag{5.24}$$

To avoid amplitude fluctuations in the beat note, the signal path beam uses a double-pass AOM configuration shown in Figure 5.12. The output of the Fibre Mach-Zehnder interferometer is split into the control and signal paths using a polarising beam splitter. The signal path beam is passed through the AOM for the first time. Figure 5.12 shows two of the output beams from the AOM. One is called the *zero order* beam which is the unshifted output beam and is ignored. The second is called the *first order* beam where the sinusoidal frequency f_{RF} shifts the optical signal's frequency by f_{RF} and steers the beam. Using an optical lens and reflecting mirror, this beam is reflected along the propagation path back into the AOM where the beam is frequency shifted by f_{RF} a second time. As before there are two output beams, the second *zero order* output has a frequency shift of f_{RF} and is ignored. The second *first order* output beam has a frequency shift of $2f_{RF}$ and propagates along the path of the input beam to the double-pass AOM configuration. The double-pass input and output beams are separated at the beam splitter at the output of the Fibre Mach-Zehnder interferometer.

The use of the double-pass AOM configuration allows the freedom of changing f_{RF} without impacting the beam's deflection angle at the output of the double-pass AOM configuration [169]. The signal path optical beam's signal frequency f_{Sig} is equal to $2f_{RF}$. The AOM used in the signal path has a centre frequency of 80 MHz with a bandwidth of ±15 MHz. When double-passed the signal laser frequency can be shifted between 130 MHz and 190 MHz. This frequency range is beyond the Newport 1811 detector bandwidth. However, the local oscillator beam is also frequency shifted. The AOM in the local oscillator path has a centre frequency of 90 MHz with a bandwidth of ±15 MHz. With the frequency shift applied to the local oscillator fixed to 90 MHz, f_h can be shifted between 40 MHz and 100 MHz. The beat note frequency range is now within the photodetector bandwidth.

Figure 5.13 shows the beat note amplitude measured at the signal path photodetector

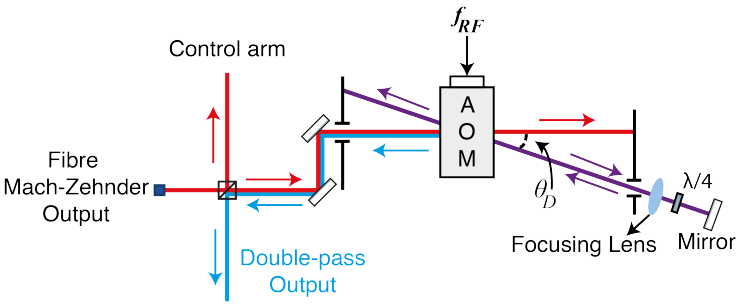

Figure 5.12: Double-pass AOM configuration of the signal path optical beam. The output of the Fibre Mach-Zehnder interferometer is passed through the double-pass AOM configuration and the signal path beam is frequency shifted by $f_{Sig} = 2f_{RF}$.

when the beat note frequency f_h is changed by changing f_{Sig}. The measured beat note amplitude has a 3 dB drop at f_h approximately equal to 55 MHz and at 82 MHz. This frequency range is used as the usable bandwidth of changing f_h.

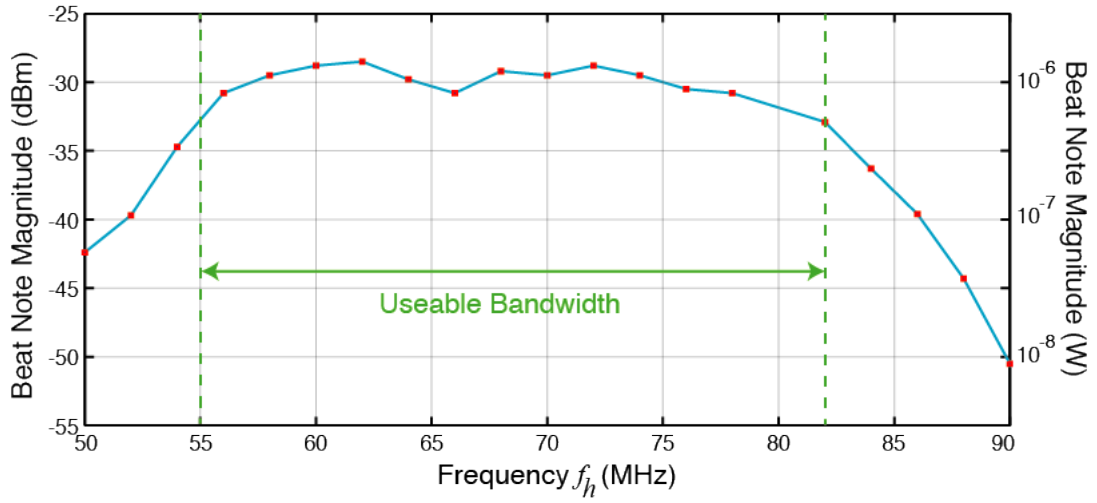

Figure 5.13: Measured bandwidth of the double pass AOM configuration in the bench-top experiment.

With the double-pass AOM configuration, the signal path beam can have a random frequency modulation $f_{Sig}(t)$. The frequency noise introduced in a space debris application is not known and could vary depending on atmospheric conditions and the reflecting target. Therefore the bench-top experiment tests the matched filter analysis capability of measuring the time-varying delay by randomising the frequency f_{REF} using a Gaussian distribution with an RMS of 5 MHz, utilising the available bandwidth of the double-pass AOM configuration shown in Figure 5.13.

Figure 5.14 compares two signals collected from the bench-top experiment in the frequency domain. One signal is where the signal beam is frequency shifted by the AOM ($f_{Sig} = 160$ MHz) and the resulting beat note frequency f_h is equal to 70 MHz which is visible in the frequency spectrum. The second signal is when the random frequency with an RMS of 5 MHz is added into the signal path laser ($f_{Sig} \pm \delta f = 160$ MHz $\pm$ 5 MHz). The random signal δf is generated using the signal generator and follows a Gaussian distribution. By adding the random frequency shift, the beat note is spread over 5 MHz bandwidth. The amplitude of the beat note at f_h is reduced and is no longer visible above the shot noise in the frequency spectrum.

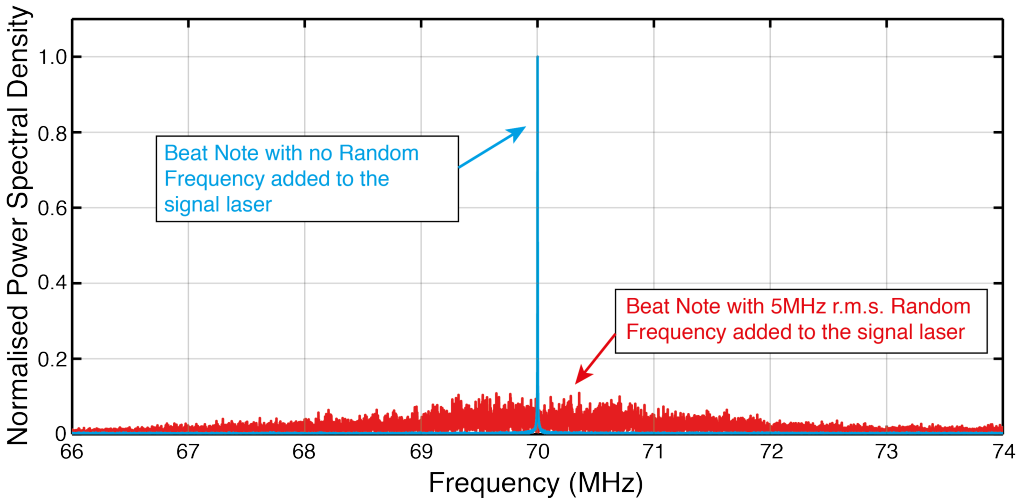

Figure 5.14: Comparing the acquired heterodyne beat note in the frequency domain for two conditions. For the blue signal, the optical signal is frequency shifted by f_{Sig}. The red signal is the optical signal is frequency shifted by $f_{Sig} \pm \delta f$ where δf is a random frequency with an RMS equal to when a 5 MHz following a Gaussian distribution.

5.2.5 Introducing $\frac{1}{f}$ Laser Frequency Noise

In a real space debris application, a coherent detection scheme would use two separate laser sources for the signal beam and local oscillator beam. However, reducing the laser frequency noise of each source is at odds with sweeping the frequency of the laser source. Frequency sweeping the laser source could be critical in a space debris application of a coherent system. As discussed in Section 3.3.2, the space debris reflected optical signal laser frequency is Doppler shifted. Hence both the beat note frequency f_h, and the PRN code harmonics centred at f_h are also Doppler shifted. Frequency sweeping the local oscillator laser source allows the experiment to mitigate the effect of the Doppler shift.

Since the recovered PRN code is not affected by the laser frequency noise, the ideal case is using two free-running laser sources and frequency sweeping the local oscillator. Despite the $\frac{1}{f}$ laser frequency noise broadening the heterodyne beat note, the PRN code harmonics are recovered from the amplitude of the beat note and provide the same precision in estimating the time-varying delay as using the same laser source with a stable frequency.

Figure 5.15 shows the two different optical layouts to investigate the impact of $\frac{1}{f}$ laser frequency noise. The second laser source used in the experiment is a fibre-coupled laser source. To introduce the laser into the experiment, the interference and detection stage of the experiment had to be altered. Hence, to compare the matched filter analysis one optical layout shown in Figure 5.15a had both the signal and local oscillator beam from the same laser source launched into and interfered in fibre. A fibre coupled Newport 1811 photodetector is used to measure the beat note. The second optical layout in Figure 5.15b replaced the local oscillator with the second fibre-coupled laser source.

The two laser sources are not stabilised or phase-locked to each other. Since the two laser sources are not phase-locked, the heterodyne beat note frequency drifted over time and eventually was observed to move beyond the bandwidth of the photodetector used in the experiment. At the start of each data acquisition, for particular optical signal power P_{Sig}, the frequency of the local oscillator is changed so that the heterodyne beat note is equal to 70 MHz and allowed to drift freely. All the experimental data for a P_{Sig} optical signal power were acquired before the heterodyne beat note drifted out of the photodetector

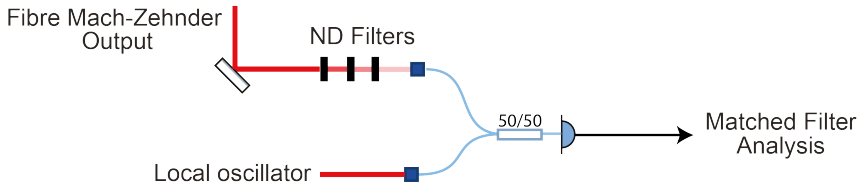

(a) Signal laser is interfered in fibre with the local oscillator from the same laser source.

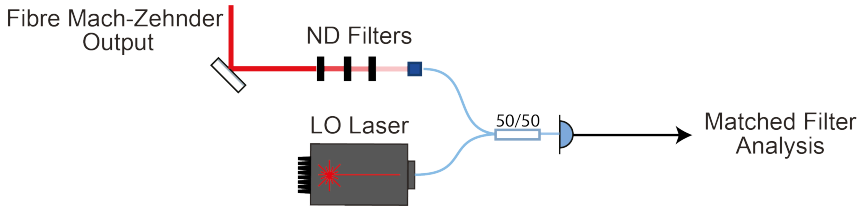

(b) Signal laser is interfered in fibre with the local oscillator from a second laser source.

Figure 5.15: Optical layout illustrating the bench-top experiment used to investigate the impact of $\frac{1}{f}$ laser frequency noise on the time-varying delay measurement.

bandwidth. Therefore each acquired signal has a broaden heterodyne beat note with peak amplitude at a different frequency in the frequency domain.

5.2.6 Data Acquisition and Matched Filter Analysis Procedure

The beat note measured from the photodetector is digitised using the ADC and passed onto the host computer. Section 4.1.8 provides a more detail description of the data acquisition stage. The data acquisition from the signal path undergoes the I^2+Q^2 demodulation before the matched filter analysis. The control path signal beam does not interfere with the local oscillator beam and does not require the $I^2 + Q^2$ demodulation step as the acquired data is the PRN amplitude modulated optical signal. The matched filter analysis procedure is presented in Section 4.1.9 where a matched filter analysis aims to estimate both L_{Signal} and $L_{Control}$ as the two path lengths in the bench-top as well as estimate the target velocity v_{SD} used to Doppler shift the PRN code chip frequency.

5.3 Characterising the Bench-Top Experiment

Before using the coherent detection scheme together with the matched filter analysis to estimate both d_0 and v_0 parameters of the time-varying delay, this section aims to characterise the bench-top experiments and compare with the simulated results in Section 5.1. The characterisation involved the following steps:

1. Generating an unshifted PRN code with 75 MHz chip frequency.
2. Interfering the amplitude modulated signal with the local oscillator with a beat note frequency f_h equal to 70 MHz.
3. Using the $I^2 + Q^2$ demodulation to recover the PRN code. $I^2 + Q^2$ demodulation refers to the demodulation of the signal at the heterogeneous frequency with sine and cosine. $I^2 + Q^2$ demodulation would provide the amplitude of the beat note.

5.3.1 Acquisition of the Beat Note

Figure 5.16 shows the first 1 μs of the measured signal when the signal path beam has interfered with the local oscillator. The time series shows that the beat note amplitude varies between two levels due to the amplitude modulated PRN code. Figure 5.16 also shows a PRN code fit applied to the acquired beat note, and matches the amplitude transitions of the acquired signal, taking into account the propagation delay.

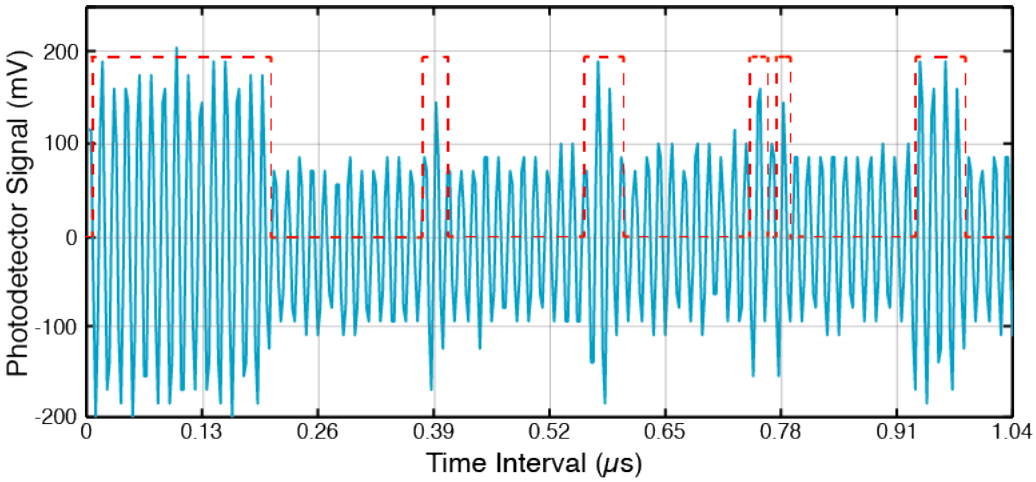

Figure 5.16: Time series of the heterodyne beat note acquired by the ADC when the signal laser interferes with the local oscillator laser. The dotted line shows a PRN code fit on the measured signal.

Figure 5.17 shows the power spectrum of the acquired signal. The spectrum shows a large amplitude beat note at 70 MHz. When focusing closer around the beat note, from 60 MHz to 160 MHz, the spectrum closely resembles the $sinc^2$ function fit applied to the spectrum with the expected null of the PRN encoded beat note at 145 MHz. The Newport 1811 photodetector has a bandwidth of 125 MHz. Therefore all higher PRN code harmonics are low pass filtered and not visible in the frequency spectrum.

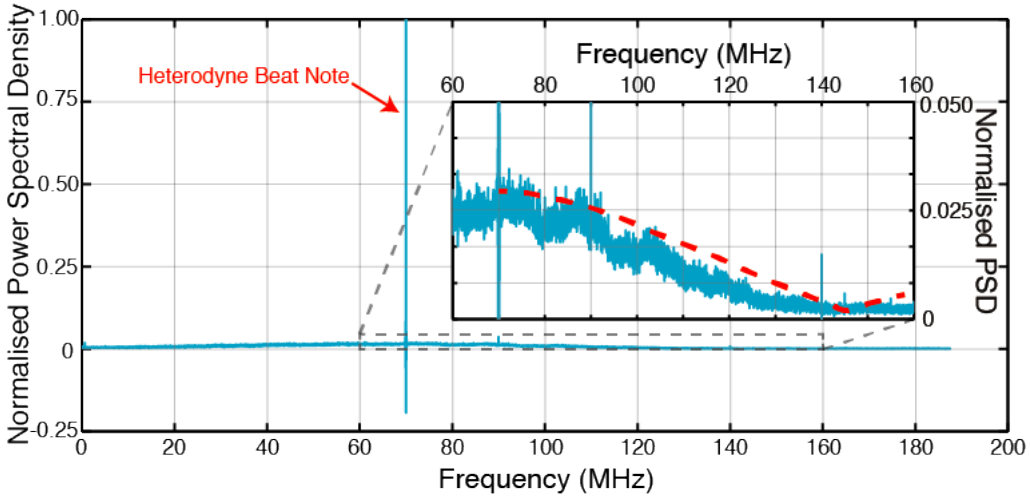

Figure 5.17: Power spectrum of the interference pattern acquired by the ADC. The red dotted line shows the expected $sinc^2$ function of a PRN code around the beat note with a null at 145 MHz.

5.3.2 $I^2 + Q^2$ Demodulation of the Acquired Beat Note

Figure 5.18 shows the first 1 μs of the recovered PRN code from the acquired beat note presented in Figure 5.16 using the $I^2 + Q^2$ demodulation. In the time series in Figure 5.18 the recovered PRN code also matches the fitted PRN code.

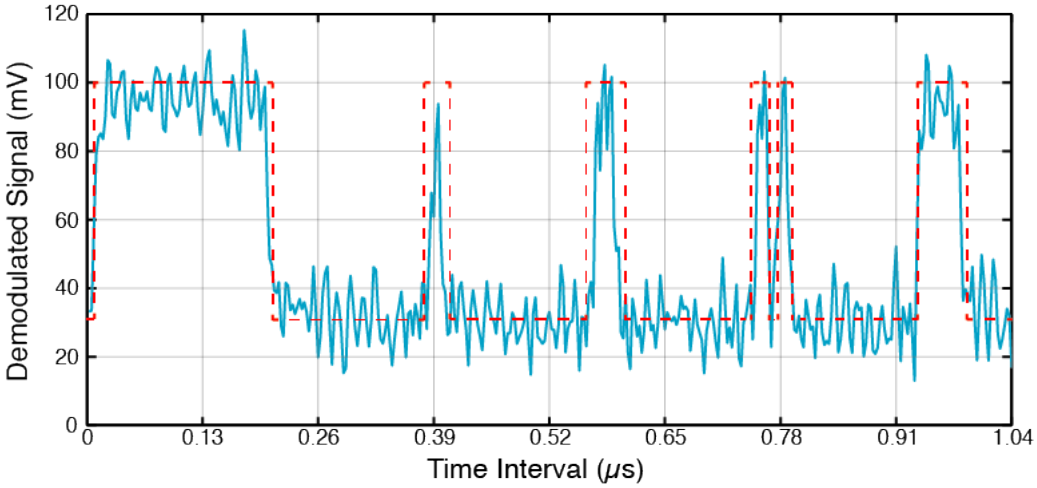

Figure 5.18: Time series of the $I^2 + Q^2$ demodulation output to recover the amplitude modulated PRN code.

Figure 5.19 shows the power spectrum of the recovered PRN code. The power spectrum resembles the expected $sinc^2$ function of a PRN code with the first null occurring at approximately 75 MHz. Figure 5.19 also shows a sudden drop in the signal amplitude for frequencies above 125 MHz due to the low pass filter used in the $I^2 + Q^2$ demodulation to filter out the $I^2 + Q^2$ sum frequency component. This low pass filter also filters out the PRN code harmonics above 125 MHz. An aggressive filter is used in the demodulation stage to remove the sum frequency component. The disadvantage is the loss of the higher frequency code harmonics which causes a reduction in the signal correlation. This thesis does not investigate the impact of varying the $I^2 + Q^2$ demodulation stage low pass filter properties.

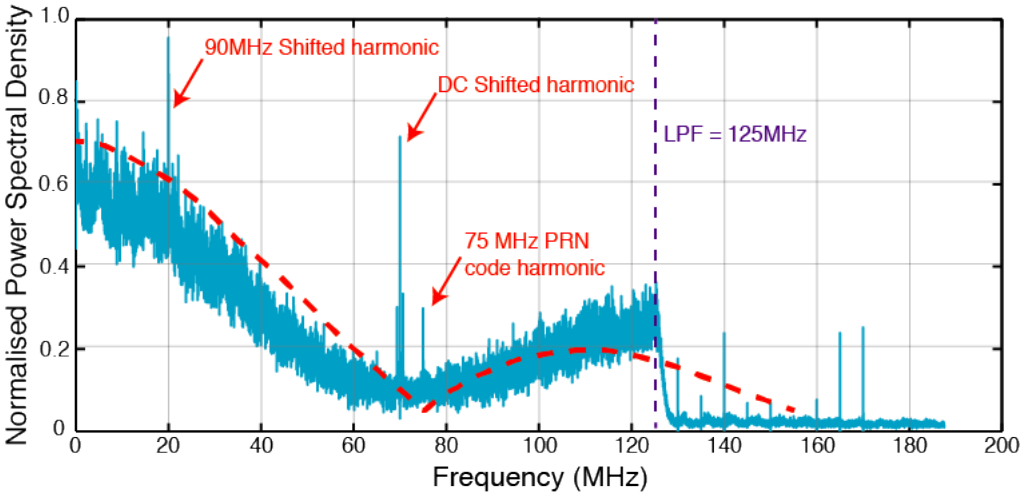

Figure 5.19: Power spectrum of the recovered PRN code. The red dotted spectrum is the simulated PRN code showing the $sinc^2$ function with nulls at 75 MHz.

The frequency spectrum also shows a harmonic at approximately 70 MHz which is a small amount of the DC term of the acquired beat note shifted to 70 MHz when mixed with the I and Q components. Another harmonic is observed at 20 MHz which is the 90 MHz harmonic from the local oscillator AOM observed in Figure 5.11 shifted when mixed with the I and Q components. The 75 MHz harmonic from the PRBS generator is also present in the spectrum. These harmonics will not impact the matched filter analysis since the energy of the harmonics is spread over a broad frequency range when correlated with the template code.

The results from Figure 5.18 and Figure 5.19 show that the amplitude modulated PRN code encoded onto the beat note from the bench-top experiment has been successfully recovered using the $I^2 + Q^2$ demodulation with coherent detection.

5.3.3 Measuring the Signal and Control Path Length

With a chip frequency equal to 75 MHz, modelling a static target ($v_{SD} = 0$ m/s), the recovered PRN code and control path signal are passed through the matched filter analysis to measure both L_{Signal} and $L_{Control}$ path lengths. The two path length measurements are used to calculate the path length difference ΔL ($\Delta L = L_{Signal} - L_{Control}$). In the matched filter analysis for this section, only the distance parameter d_0 value is changed while the velocity parameter v_0 is fixed and equal to 0 m/s.

Figure 5.20 shows the normalised signal and control correlation as a function of the delay parameter d_0. The optical signal power of the signal path is equal to 20 nW, the local oscillator optical power is equal to 115 μW and the optical signal power of the control path is equal to 50 μW. Since the two paths have different optical signal powers, by normalising the two correlations where the peak correlation value is equal to 1, the signal and control correlations are more easily compared in Figure 5.20.

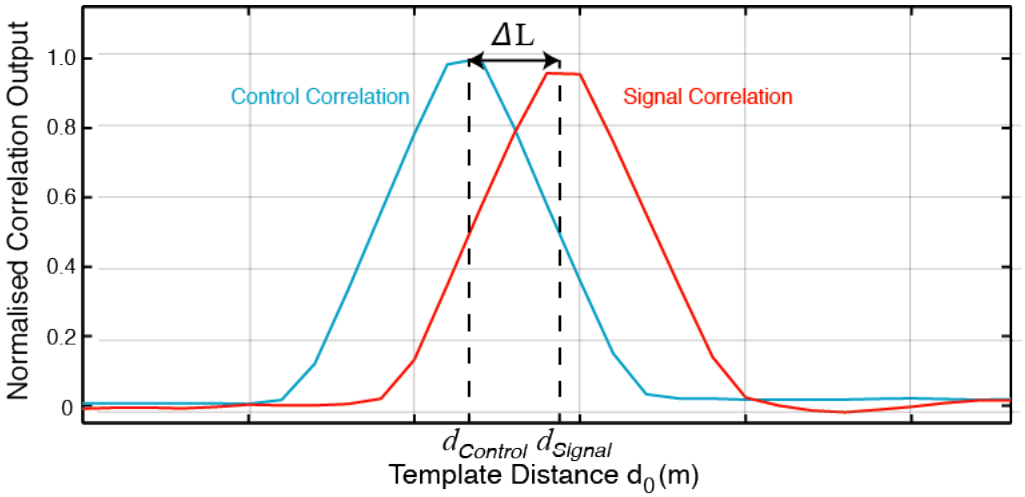

Figure 5.20: Normalised correlation of the PRN code acquired from the control and signal photodetectors as function of the input value for the distance parameter d_0.

Table 5.2 compares the measurement of the two path lengths on the optical table for both the coherent and direct detection schemes for a received signal power equal to 20 nW. For both detection schemes, the physical path length of L_{Signal} is equal to 2.75 m and $L_{Control}$ is equal to 0.68 m. The path length difference ΔL measured on the optical table is equal to 2.07 m. Due to the interleaved process, as discussed in Section 4.1.8, a fixed time offset is added by the ADC when digitising the two path length signals, adding a distance bias

of 0.1 m to the path length. Hence the expected ΔL calculation is equal to 2.17 m.

	L_{Signal}	$L_{Control}$	ΔL
Optical Table	2.75 m	0.68 m − 0.10 m	2.17 m ± 0.03 m
Direct Detection	9052.9 m	9050.4 m	2.5 m ± 0.2 m
Coherent Detection	59 699.4 m	59 697.2 m	2.2 m ± 0.2 m

Table 5.2: Table comparing the L_{Signal} and $L_{Control}$ path lengths measured for both the coherent and direct detection scheme.

The matched filter analyses for both detection schemes in Table 5.2 were performed for a 1 ms integration time. Comparing the different ΔL results in Table 5.2, the coherent detection scheme produced a more accurate ΔL measurement ($\Delta L = 2.22$ m) than the direct detection scheme ($\Delta L = 2.50$ m). The result is explained by Figure 5.21 which compares the signal correlation of both detection schemes. The coherent detection scheme produced a much larger signal correlation, clearly visible above the noise, due to the increased signal-to-noise ratio from interfering with the bright local oscillator. In the direct detection scheme, the signal correlation is slightly above the correlated noise.

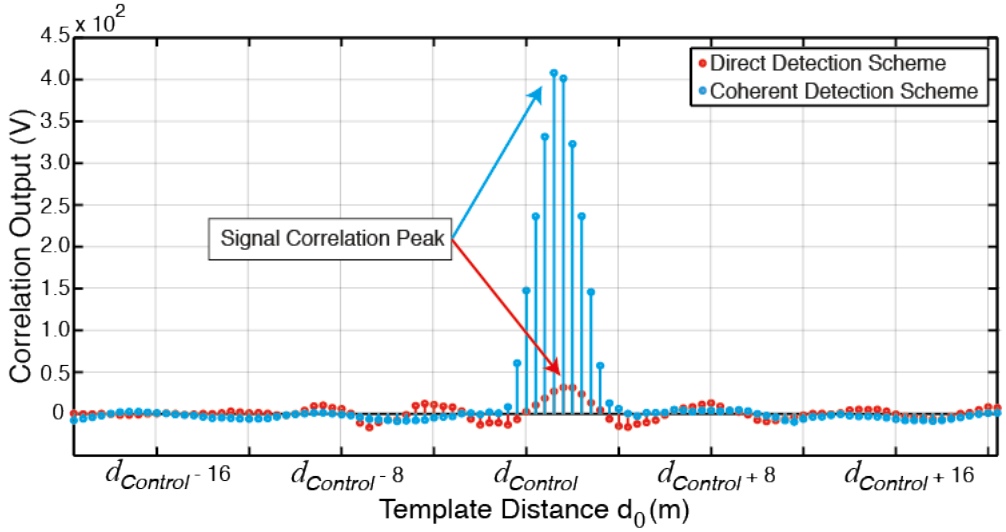

Figure 5.21: Cross-correlation comparing both detection schemes for 20 nW received signal power and a 1 ms integration time.

Table 5.2 also shows that the expected accuracy achievable for both the direct detection and coherent detection scheme is equal to ±0.2 m, even though the signal in the coherent detection scheme is amplified by the local oscillator. Figure 5.22 shows the correlation output when the matched filter analysis template spacing for the d_0 parameter is varied. The same result observed in Figure 5.22 is also observed in Figure 4.16 for the direct detection scheme. When the d_0 template spacing is equal to 0.2 m, horizontal steps are observed in the correlation output. This limits the accuracy of estimating the distance parameter d_0 to ±0.2 m. The accuracy of the matched filter analyses in estimating the d_0 parameter is discussed in more detail in Section 4.2.3 for the direct detection scheme. However, the coherent detection scheme can produce a more precise path length measurement to within ±0.2 m for lower signal laser powers than the direct detection scheme.

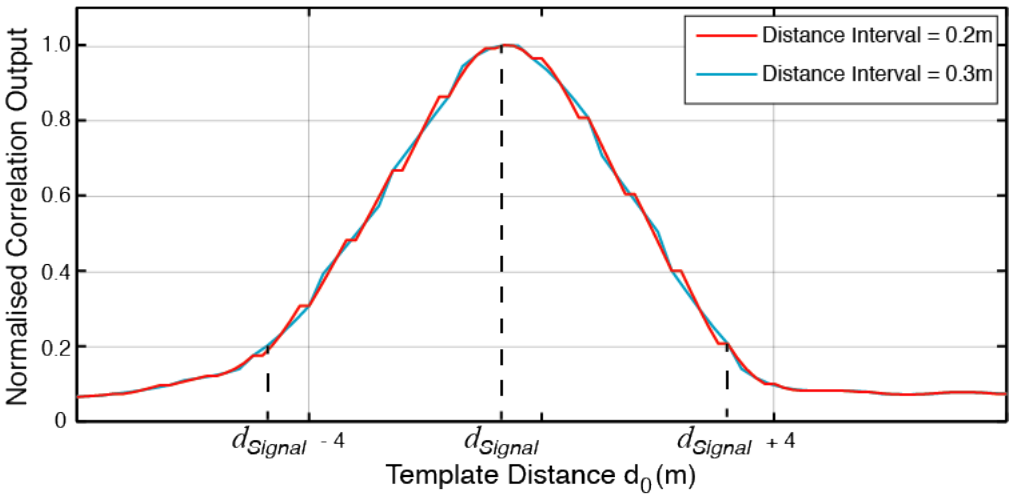

Figure 5.22: Comparing the correlation of the PRN code when using 0.2 m and 0.3 m parameter spacing for the delay d_0 parameter.

The result in Table 5.2 and Figure 5.21 supports the discussion that the signal is amplified when interfered with a bright local oscillator and improves the accuracy of the matched filter analysis's estimate of the signal path length. The coherent detection scheme can provide a path length measurement for signals weaker than 20 nW for 1 ms integration time. For example at a received signal power of 520 pW and 1 ms integration time, a power level and integration time that did not produce a signal correlation for the direct detection scheme as seen in Figure 4.17, but the coherent detection scheme produced a ΔL equal to 2.31 m.

In conclusion, the discussion in this section has shown the amplitude of the signal correlation is increased when the optical signal is amplified with a bright local oscillator in the coherent detection scheme compared to the direct detection scheme. The increase in the signal correlation amplitude results in improved signal detection and precision in estimating the path length difference ΔL of the bench-top experiment.

5.4 Measuring the Doppler Shift of the Amplitude Modulated PRN Code

In Section 5.3, the chip frequency of the modulating PRN code was fixed at 75 MHz. In this section, the modulating PRN code's chip frequency is increased by 1750 Hz to model the optical signal reflecting from a space debris target with a constant speed equal to 7 km/s and moving towards the telescope. The matched filter analysis aimed to estimate both the distance d_0 and velocity v_0 template parameters. The expected value for ΔL is equal to 2.175 m and the expected value for v_0 is equal to -7000 m/s.

5.4.1 Estimating both d_0 and v_0 parameters

Figure 5.23 presents a contour plot of the 2-dimensional signal correlation where both distance d_0 and velocity v_0 parameters are varied during the matched filter analysis with the recovered PRN code from the beat note. The received signal power P_{Sig} is equal to 20 nW and the integration time t_i is equal to 1 ms.

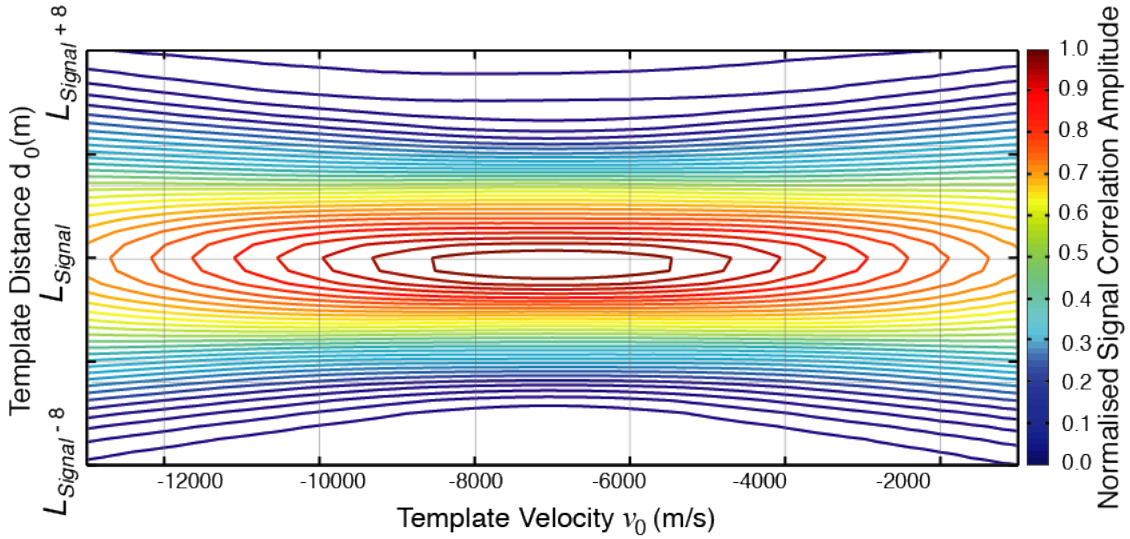

Figure 5.23: Contour plot showing the signal correlation as both the distance and velocity parameters are changed using a parameter bank for each parameter.

The contour plot in Figure 5.23 shows that as the parameter values for d_0 and v_0 are closer to the optimal values of L_{Signal} and v_{SD}, the output of the signal correlation increases. The Full-Width Half Maximum (FWHM) of the signal correlation along the d_0 parameter is 4 m, related to the chip frequency f_{Chip}, and for the v_0 parameter is 8000 m/s, related to the integration time chosen in the analysis. Both results match the matched filter analysis result for the direct detection scheme in Section 3.5.2. Section 4.3.1 and Section 4.3.2 give a more detailed explanation on the FWHM of the signal correlation for both parameters.

Using the same interpolation on the signal correlation as in the direct detection scheme to estimate both d_0 and v_0, the resulting ΔL estimate is equal to 2.21 m and the v_0 estimate is equal to -7016 m/s. Both measurements are close to the expected parameter values with ΔL within the 0.2 m accuracy of estimating d_0. In comparison, at the same P_{Sig} and t_i for the direct detection scheme, the matched filter analysis estimated both ΔL and v_0 to 2.52 m and -6527 m/s respectively.

The results in this section support the coherent detection scheme provides a better estimate of both the ΔL and v_0 parameters compared to the direct detection scheme for the same received signal power P_{Sig} and analysis integration time t_i.

5.4.2 Precision of the Matched Filter Analysis

Section 5.4.1 showed that the matched filter analysis was able to provide an estimate of both the distance d_0 and velocity v_0 parameters using the amplitude modulated PRN code recovered from the beat note. The results also showed that the coherent system provides a more accurate estimate of the two parameters than the direct detection scheme.

Figure 5.24 illustrates the steps taken to determine the precision of the matched filter analysis in estimating the target velocity v_{SD} for the coherent detection scheme ($v_{SD} = -7000$ m/s).

First, a total of 25 signals at the same received optical power P_{Sig} are acquired from the bench-top experiment, each 0.1 s long. Before the matched filter analysis, every acquired signal is first divided into segments. The time length of each segment depends on the integration time t_i chosen for the matched filter analysis. For example, if a 10 ms integration

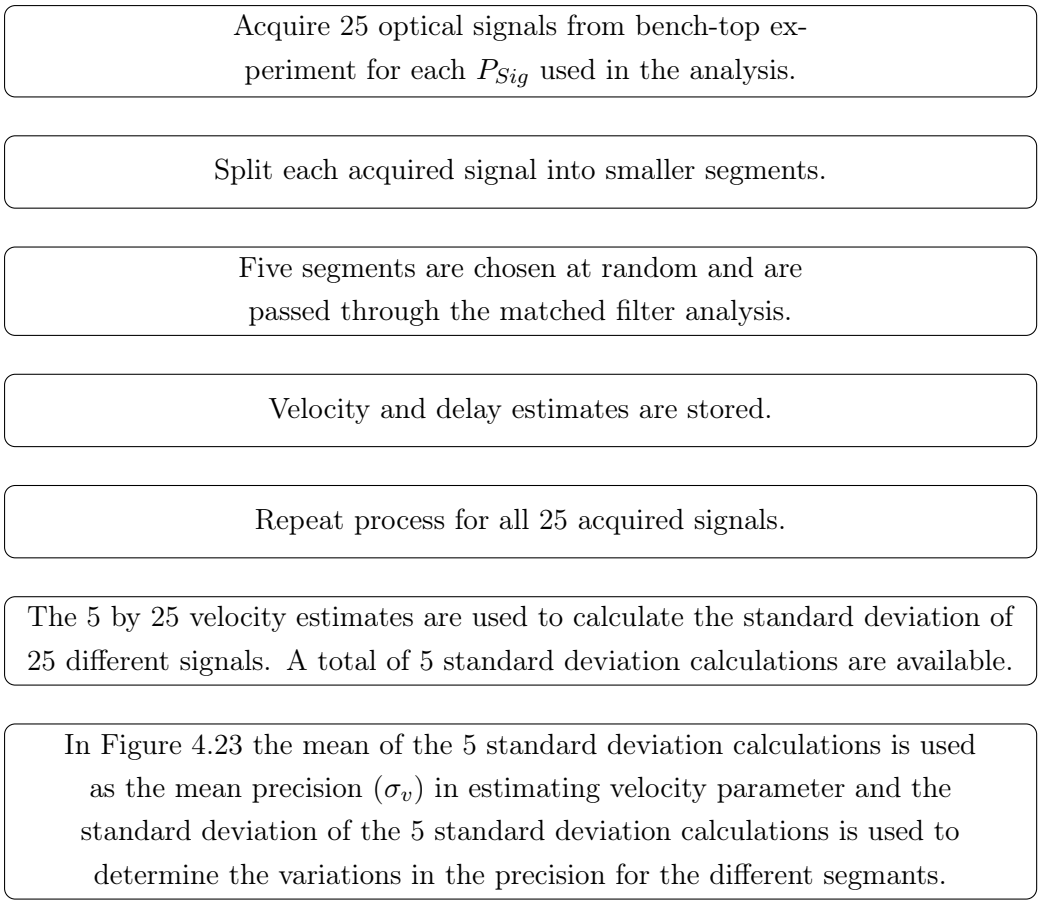

Figure 5.24: Flowchart describing how the precision of the matched filter analysis is determined.

time is chosen, the acquired signal is divided into ten segments, each 10 ms long. Five of these segments are chosen at random and passed through the matched filter analysis. This step was taken to identify the variation in estimating v_0 using different sections of the same acquired signal.

The matched filter analysis provides 5 estimates for each acquired signal and the process is repeated for 25 acquired signals. In total there are 125 estimates of v_0 stored in a 25 by 5 matrix for every P_{Sig} and t_i. The main reason the matched filter analysis is repeated for the same acquired signal is because the initial results for the matched filter analysis showed that different portions of the same acquired signal produced a different estimated value of the target velocity v_{SD}. This highlighted there is a variance in the velocity estimate within the same acquired signal that must be taken into account.

The standard deviation (1σ) of the v_{SD} estimates using the 25 different acquired signals gives the precision of the bench-top experiment in estimating v_{SD} using the matched filter analysis. This step of the analysis is repeated for the 5 different segments resulting in a total of 5 different precision measurements of the target's velocity. The 5 different precision measurements are not the same. Therefore these 5 precision measurements are used to find the mean precision (σ_v) in estimating v_{SD} for the received signal power P_{Sig} and integration time t_i chosen for the analysis. The standard deviation of the 5 different error measurements is used as the variation in the precision measurement for the different segments of the 25 signals. The same steps are repeated for different P_{Sig} and t_i, providing information on how the precision of the matched filter's estimate of v_{SD} varies with the two experimental parameters.

Section 4.3.2 for the direct detection scheme showed that the slope of the correlation influences the mean precision of the matched filter analysis estimate of the velocity parameter. For the direct detection scheme, the mean precision is inversely proportional to received signal power P_{Sig} and is $t_i^{-1.5}$ to the integration time t_i.

For the coherent detection scheme, the same relationship is expected with the integration time, i.e. the mean precision changes by $t_i^{-1.5}$. Increasing the integration time reduces the FWHM and increases the peak value of the signal correlation resulting in t_i^2 improvement in the slope of the correlation. However, increasing the integration time also increases the noise in the correlation by $t_i^{0.5}$. Hence, the mean precision reduces by $t_i^{-1.5}$ with increasing integration time. Section 4.3.2 provides a more detailed explanation of the effect the integration time has on the slope of the signal correlation.

In the coherent detection scheme, the amplitude of the PRN code recovered from the beat note is $\sqrt{P_{Sig}P_{LO}}$ since the signal has interfered with the local oscillator. Assuming P_{LO} is fixed, the relationship between the received signal power and the slope of the signal correlation is $\sqrt{P_{Sig}}$. This means the mean precision would change by $P_{Sig}^{-0.5}$ in estimating the velocity parameter for varying P_{Sig}.

To recap, the mean precision σ_v for the coherent detection scheme is expected to be:

- $P_{Sig}^{-0.5}$ with received signal power P_{Sig}
- $t_i^{-1.5}$ with the integration time t_i

Figure 5.25 presents the precision of the matched filter analysis in estimating v_{SD} as a function of received signal power P_{Sig}. Figure 5.25 also presents the results of the analysis performed for three different integration times using the same acquired signals. The mean precision is represented as a solid dot while the variation (1σ) in both the precision measurement and the received signal power is represented as a shaded region. The variations in the optical signal power P_{Sig} is due to fluctuations in the output intensity of the Fibre Mach-Zehnder.

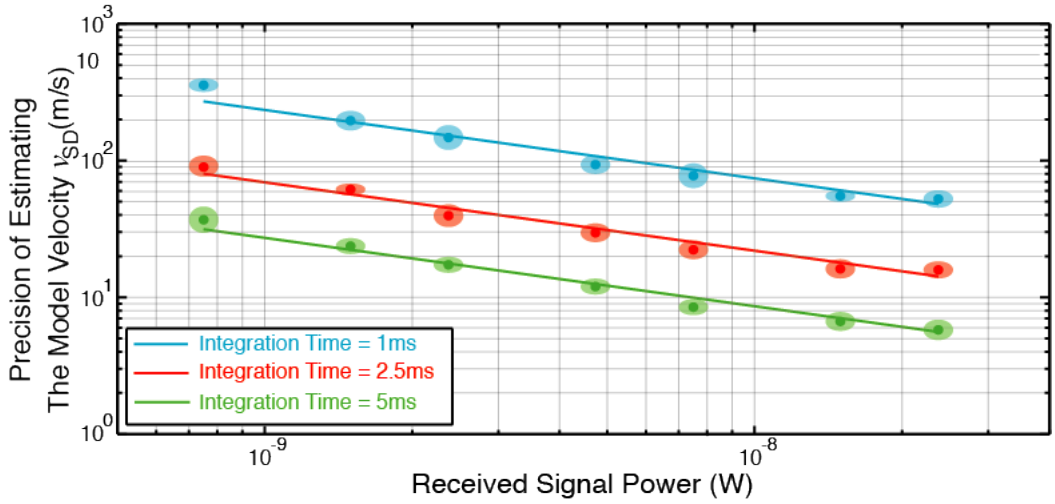

Figure 5.25: Precision of estimating v_{SD} as a function of received signal power. The solid dots represents the mean precision of the velocity measurement while the shaded region around the mean represents the variation in the precision and received signal power. The line is fitted to the mean of the precision and has a slope of -0.5.

Figure 5.25 also shows three straight lines, in the logarithmic scale, fitted to the mean error

for all three integration times. Each line has a slope fixed to -0.5 taking into account the expected relationship of the mean error σ_v with P_{Sig}.

The result in Figure 5.25 shows that the mean precision of the matched filter analysis matches closely, within the variations of the precision, with the expected slope of the line. This result confirms that for different integration times the matched filter analysis has $P_{Sig}^{-0.5}$ relationship with the mean precision in estimating v_{SD} for the coherent detection scheme.

Figure 5.26 presents the the matched filter analysis mean precision in estimating v_{SD} as a function of the integration time t_i. The analysis was repeated for four different received signal powers P_{Sig}. As in Figure 5.25, the precision of the matched filter analysis has variations, and a line is fitted to the mean precision. The slope of the line is -1.5 and the results show that the line passes through, within the variations of the precision. This confirms that the mean precision changes by $t_i^{-1.5}$.

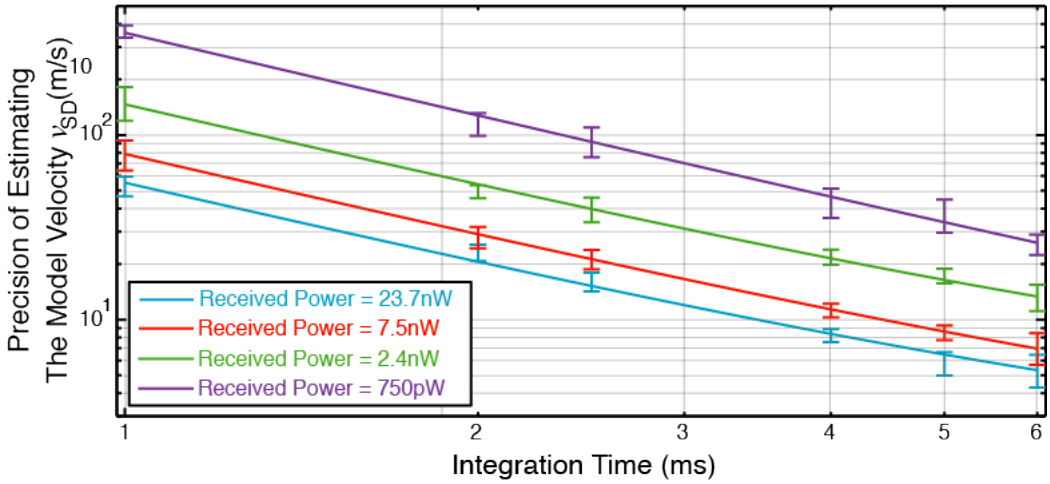

Figure 5.26: Precision of estimating the velocity parameter as a function of integration time. The line is fitted to the mean precision has a slope of -1.5.

The relationship between the precision of the matched filter analysis to the estimated v_{SD} can be represented as an equation using the results from both Figure 5.25 and Figure 5.26 by using the mean precision σ_v from the experimental results for a given received signal power P_{Sig} and integration time t_i. In equation 5.25 the mean precision of 150.59 m/s was chosen for 2.4 nW received signal power and 1 ms integration time.

$$\sigma_v \; m/s = 150.59\,\mathrm{m/s}\left(\sqrt{\frac{2.4\,\mathrm{nW}}{P_{Sig}\;W}}\right)\left(\frac{1\,\mathrm{ms}}{t_i\;s}\right)^{1.5} \tag{5.25}$$

Equation 5.25 is used in Chapter 6 to predict the precision of estimating a target's velocity for varying received signal powers and integration times, as part of the discussion for implementing the coherent detection scheme for space debris ranging applications. This analysis is compared with using the direct detection scheme for a space ranging application. However a quick comparison between equation 5.25 and equation 4.7 shows that for a P_{Sig} equal to 1 nW and t_i equal to 1 s produces a σ_v equal to 7.4 mm/s for the coherent detection scheme and 532 mm/s for the direct detection scheme. The result shows that the coherent detection scheme is better in estimating v_{SD} than the direct detection scheme.

5.4.3 Adding Random Frequency to the Heterodyne Beat Note

Figure 5.27 shows the precision in the matched filter analysis in estimating v_{SD} when a random frequency is added to the laser frequency of the signal path beam as discussed in Section 5.2.4. The random frequency added to the signal path laser beam has an RMS equal to 5 MHz and follows a Gaussian distribution. Figure 5.27 also includes the matched filter analysis results from Figure 5.25, where the random frequency is not added to the heterodyne beat note, for comparison.

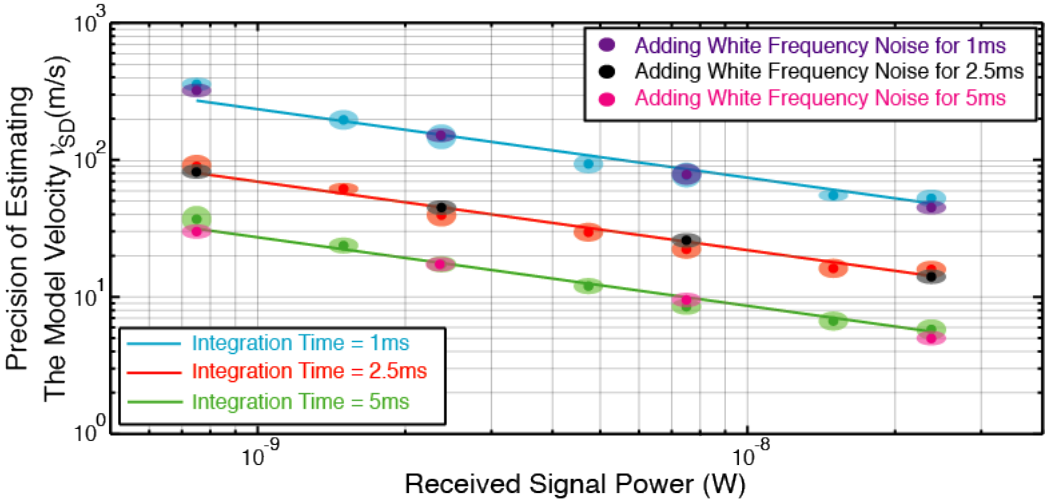

Figure 5.27: Comparing the precision in estimating the velocity parameter using the matched filter analysis when a random frequency with a RMS of 5 MHz is added to the signal path laser with results from Figure 5.25.

The matched filter analysis results with the random frequency overlap with the result from Figure 5.25 for the different received signal power and integration time. The result indicates that even when a random frequency is added to the signal laser, resulting in reduced amplitude of the heterodyne beat in the frequency domain as shown in Figure 5.14, the frequency noise does not affect the matched filter estimate of the target's velocity v_{SD} using the amplitude modulated PRN code recovered from the beat note.

5.4.4 Free-Running Laser with $\frac{1}{f}$ Frequency Noise

Figure 5.28 compares the matched filter analysis precision using the two optical layouts presented in Section 5.2.5. For one of the arrangements, a second laser is used as the local oscillator source. Both laser sources are free-running, with $\frac{1}{f}$ frequency noise, and are neither phase-locked or stabilised. The mean precision results in Figure 5.28 also includes a line with a slope of -0.5 fitted to the mean error for all three integration times.

Comparing the two results in Figure 5.28, both produced a similar mean precision in estimating v_{SD} as the mean precision of both optical layouts overlaps each other. Both results also follow the -0.5 slope trend line applied to the measurement. These results indicate that $\frac{1}{f}$ laser frequency noise does not affect the matched filter analysis in estimating the velocity parameter. The mean precision measurements in Figure 5.28 also closely match the results in Figure 5.25. The slight difference in the result is due to the higher overlap efficiency using fibre to interfere the signal beam with the local oscillator beam as well as using a fibre coupled photodetector.

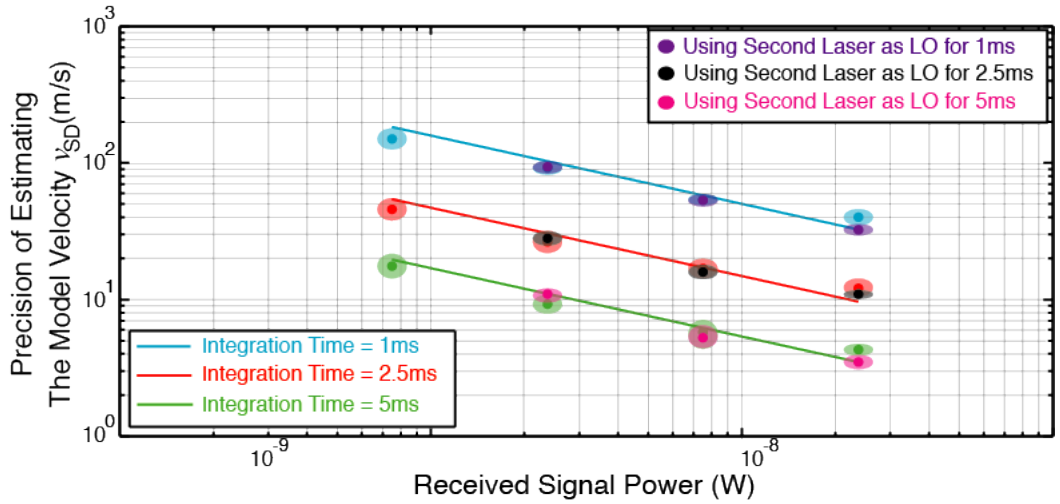

Figure 5.28: Comparing the error in estimating the velocity parameter using the matched filter analysis when the LO is from the same source as the signal with using a second LO laser.

5.5 Chapter summary

The chapter discussed the theory of using a coherent detection scheme to amplify the amplitude modulated PRN code to improve the signal-to-noise ratio. The PRN code is recovered from the resulting beat note using a $I^2 + Q^2$ demodulation method in post-processing. The recovered PRN code is then used as an input to the matched filter analysis to estimate both the distance d_0 and velocity v_0 parameters.

The chapter also presented the optical layout where the PRN code is amplitude modulated onto the signal laser beam using a Fibre Mach-Zehnder interferometer. The chip frequency of the modulating PRN code can be altered to model the Doppler shift of the PRN code by a moving space debris target. The modulated signal laser beam is then interfered with the local oscillator beam to produce a PRN code encoded heterodyne beat note. The PRN code is recovered using the $I^2 + Q^2$ demodulation method. The discussion on the bench-top experimental layout also presented adding a random frequency to the heterodyne beat note and $\frac{1}{f}$ laser frequency noise into the experiment.

The bench-top experimental results showed that the accuracy and precision of the matched filter analysis in estimating ΔL and v_{SD} parameters using a coherent detection scheme outperformed the direct detection scheme for the same received signal power P_{Sig} and integration time t_i. This is because the modulated PRN code is amplified above the dominant photodetector noise source in the direct detection scheme.

The experimental results presented in Section 5.4.2 showed that the mean precision of the matched filter analysis in estimating the target's velocity has the relationship $P_{Sig}^{-0.5}$ and is $t_i^{-1.5}$ to the received signal power and integration time respectively. The experimental results in Section 5.4.3 and Section 5.4.4 also showed that the effect of both random frequency and $\frac{1}{f}$ laser frequency noise do not impact the matched filter analysis performance. This result shows that the coherent detection scheme with matched filter analysis would be suitable for a space debris application.

Experimental Results Discussion

Section 1.3 stated that the aim of the thesis is to present a space debris ranging system compatible with the continuous wave laser that would be used in the future attempt to manoeuvre a low earth orbit (LEO) piece of space debris. The proposed method is amplitude modulating the outgoing continuous wave laser with a pseudo-random noise (PRN) code. Chapter 4 and Chapter 5 presented two different detection schemes, a direct detection scheme and coherent detection scheme respectively. In the direct detection scheme, the intensity of the optical signal is directly measured while in the coherent detection scheme the optical signal is interfered with a second laser beam to amplify the signal and increase the signal-to-noise ratio.

The space debris' motion Doppler shifts the amplitude modulated PRN code's chip frequency amd a matched filter analysis is proposed to estimate the time-varying delay. The Space Environmental Research Centre (SERC) requires a ranging system that is capable of measuring the velocity of a piece of space debris with a 1 mm/s precision (σ_v). This chapter builds on the experimental results for space debris application, investigating the required received signal power P_{Sig} and integration time t_i using the EOS telescope to achieve the desired 1 mm/s σ_v precision.

6.1 Ground-Based Telescope Design

The telescope design is crucial in determining the received signal power P_{Sig}. The size of the telescope affects the beam divergence of the transmitted optical signal and the amount of reflected optical signal collected. Section 2.3 discussed in more detail the factors that impact the received signal power P_{Sig}. Equation 6.1 is used to estimate the upper bound limit of the received signal power P_{Sig}. Table 6.1 presents the values used for the different parameters.

$$P_{Sig} = P_T \frac{(A_T A_{SD})^2}{(R\lambda)^4} \frac{F^2}{\beta} \tag{6.1}$$

The aperture D of the telescope can be used to calculate the effective collecting area of the telescope A_T. A larger telescope A_T would result in the squared improvement in the received signal optical power. However, Section 2.3.4 discussed limitations to the size of a single telescope mirror. The space debris ranging analysis in this thesis uses the characteristics of the EOS telescope on Mount Stromlo. The EOS telescope is a single mirror telescope with a aperture of 1.8 m. The telescope is currently used for pulse laser ranging of space debris in a mono-static arrangement. A_T of the EOS telescope is equal to 2.54 m^2.

Parameters	Chosen Parameter Values
Telescope Aperture D	1.8 m
Telescope area A_T	2.54 m^2
Transmitted Power P_T	10 kW
Laser wavelength λ	1064 nm
Space debris diameter	1 cm to 10 cm
Range R	500 km to 5500 km
Atmospheric loss F^2	Variable
Non-cooperative target signal loss β	Variable

Table 6.1: Table showing the parameters chosen as input to equation 6.1 to calculate the optical signal P_{Sig} collected by the telescope.

The wavelength of the laser λ and transmitted power P_T depends on the transmitting optical laser source and is assumed to be fixed. At the time of writing this thesis, P_T is equal to 10 kW and λ is equal to 1064 nm. This is the transmitted optical power and laser wavelength expected to be used in the SERC space debris manoeuvring demonstration [28].

The target surface area A_{SD} of a piece of space debris can vary depending on the size of the target debris. As discussed in Section 2.3.1, tracking space debris between 1 cm and 10 cm are of most concern to active satellite operators. These space debris are large enough to cause significant damage to an active satellite and contribute to the increase in the number of space debris in orbit. Larger space debris reflects more signal photons in the direction of the telescope and increases the received signal power.

The range R of a space debris target also varies as the telescope tracks the target during the flyover. The main focus of this thesis are space debris in a LEO orbit. The minimum LEO orbit the EOS telescope can track is 500 km and the maximum range of LEO target is 5500 km.

Equation 6.1 also has the terms, β and F^2, to take into account the signal loss from both a non-cooperative target and when the optical signal propagates through the atmosphere. As discussed in Section 2.3, providing approximate values for both parameters can be difficult. The signal loss F is due to atmospheric condition and can vary from day to day. β will vary for different space debris targets as it depends on the size, shape and reflecting surface of a piece of space debris.

6.1.1 Approximating P_{Sig} using $\beta = 10^8$ and $F^2 = 0.9$

The purpose of the section is to approximate the received signal power P_{Sig} that can be expected for a space debris target. This information will help in the discussions for the direct detection and coherent detection scheme in this chapter.

Figure 6.1 presents the calculated received signal power P_{Sig} as a function of the range R for different sizes of space debris between 1 cm and 10 cm. Figure 6.1 was generated using Equation 6.1 and the parameter values presented in Table 6.1. For F^2, a value of 0.9 was chosen to approximate minimal wavefront distortion and some signal loss due

to atmospheric absorption and scattering. β is set to equal 10^8. This value was chosen to approximate the signal loss between a cooperative target with a retro-reflector and a non-cooperative target [46]. However, this value was obtained from a study comparing the impact of retro-reflectors for satellite laser ranging not for space debris targets. Therefore the received signal power could be smaller than that calculated in this section.

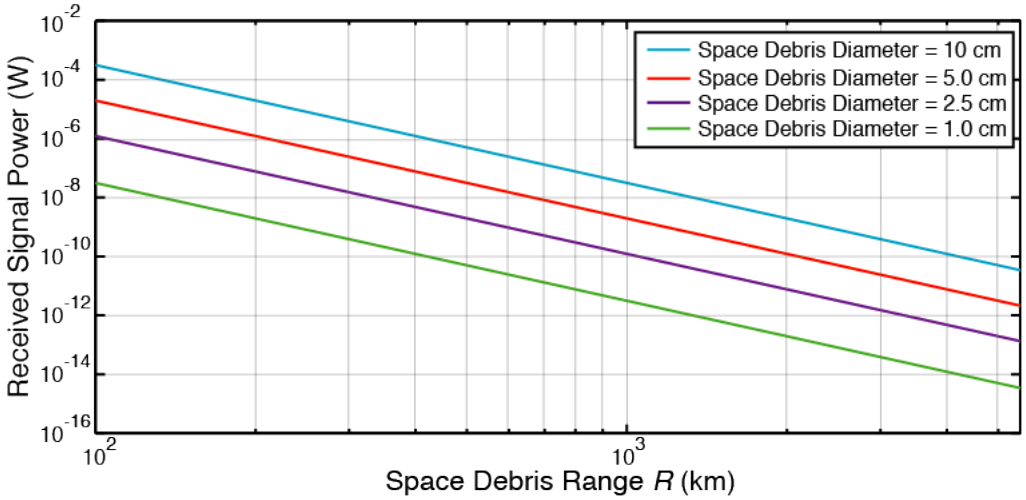

Figure 6.1: The calculated received laser signal power P_{Sig} for varying space debris diameter based on equation 6.1 and the input parameter values from Table 6.1.

Using the results in Figure 6.1, at the maximum range of 5500 km away, the received signal power P_{Sig} from 10 cm space debris target is 35 pW and from 1 cm space debris target is 3.5 fW. Both these power measurements will be used to aid the discussions in Section 6.2 and Section 6.3 to determine the integration times needed to achieve the desired precision in estimating the velocity parameter.

6.2 Conclusion From the Direct Detection Scheme

Chapter 4 presented the bench-top experimental layout and results to evaluate the direct detection scheme. The results showed that the amplitude modulated PRN was able to estimate both d_0 and v_0 parameters of two different path lengths. Both parameter estimations closely matched the path length difference ΔL and the velocity v_{SD} used to Doppler shift the modulating PRN code in the bench-top experiment. The chapter also evaluated the relationship of the precision σ_v of estimating the v_0 parameter with both received signal power P_{Sig} and integration time t_i. The experiment proved that the σ_v relationship is:

- P_{Sig}^{-1} with received signal power P_{Sig}
- $t_i^{-1.5}$ with the integration time t_i

The experimental results were used to produce an equation to calculate σ_v for varying input P_{Sig} and t_i. This is presented as equation 6.2 for the precision of the direct detection scheme σ_{v-DD}.

$$\sigma_{v-DD}\ m/s = 224.35\,\text{m/s}\Big(\frac{75\,\text{nW}}{P_{Sig}\ W}\Big)\Big(\frac{1\,\text{ms}}{t_i\ s}\Big)^{1.5} \tag{6.2}$$

The study, using equation 6.2, of the direct detection scheme for space debris application focuses on the following conditions:

1. The received signal power P_{Sig} required to achieve a velocity estimate of 1 mm/s and 1 m/s precision for 1 s integration time t_i.
2. Increasing the integration time t_i to achieve the same precision at a lower received signal power P_{Sig}.
3. For received signal power P_{Sig} between 35 pW and 3.5 fW.
4. The largest integration time required to achieve 1 mm/s precision for 1 cm diameter space debris at the range of 5500 km.

Figure 6.2 uses equation 6.2 to present the σ_{v-DD} as a function of received signal power for 1 s, 100 s and 1700 s integration times. The dominant noise source in this experiment is from a background photon noise from an incoherent light source with an optical power of approximately 120 μW. From Figure 6.2, as the signal-to-noise ratio increases for higher P_{Sig}, the precision σ_{v-DD} improves.

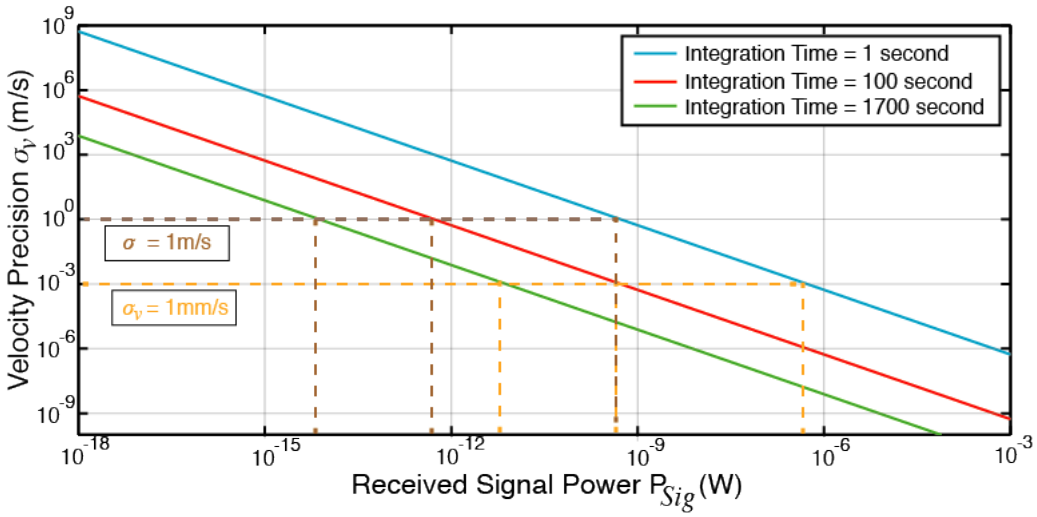

Figure 6.2: Calculating σ_{v-DD} of the direct detection scheme for varying received signal power using equation 6.2 for 1 s, 100 s and 1700 s integration times.

From the result in Figure 6.2, for an integration time of 1 s, the direct detection scheme can achieve 1 mm/s precision if the minimum received signal power is approximately equal to 515 nW. To achieve 1 m/s precision for the same 1 s integration time, the minimum received signal power is approximately equal to 550 pW. Figure 6.2 also shows that by increasing the integration time to either 100 s or 1700 s, the velocity estimate with 1 mm/s or 1 m/s precision can be achieved for lower received signal power.

Figure 6.3 presents the calculated σ_{v-DD} as a function of integration time t_i. The integration time chosen for the analysis can be anything from the time taken to complete a single code length to the maximum time the telescope tracks the space debris during the flyover. This maximum time depends on the space debris orbit and telescope design. The slew rate of the telescope may limit the telescope's capability to continuously track a lower orbit debris' trajectory over the telescope's location.

Using Figure 6.3, if the received signal power is equal to 550 pW, by increasing the integration time to approximately 100 s, the matched filter analysis can improve the precision of the target velocity estimate to 1 mm/s.

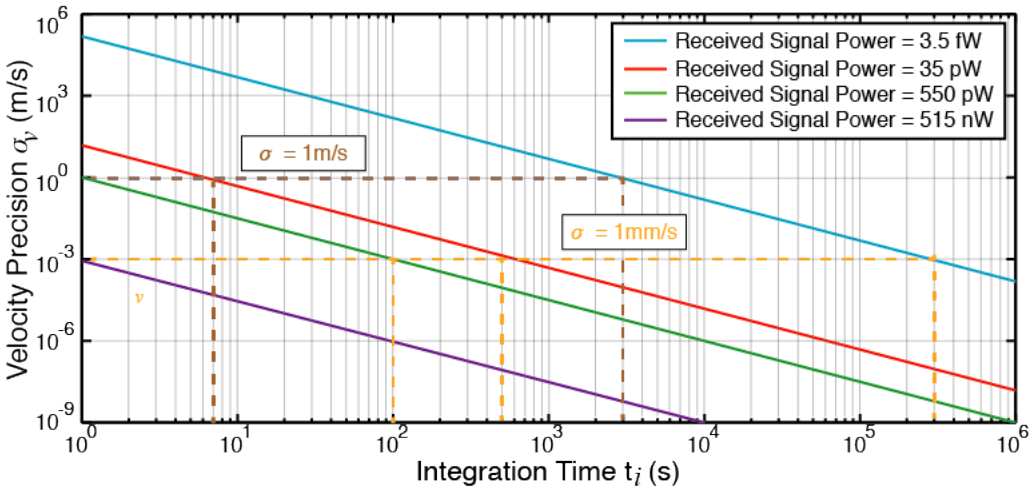

Figure 6.3: Calculating σ_v of the direct detection scheme for varying integration times.

6.2.1 Using $\beta = 10^8$ and $F^2 = 0.9$

In Section 6.1.1, both β and F^2 were approximated to equal 10^8 and 0.9 respectively. Figure 6.1 shows that the calculated received signal power from a 1 cm and 10 cm space debris is equal to 3.5 fW and 35 pW respectively. Both received power are also shown in Figure 6.3.

In the case the received signal power is equal to 35 pW, a 1 s integration time is inadequate to achieve 1 m/s precision. A larger integration time is needed. Increasing the integration time to approximately 6 s would achieve 1 m/s precision and increasing the integration time to approximately 610 s would achieve 1 mm/s precision.

In the case the received signal power is equal to 3.5 fW, increasing the integration time to approximately 2850 s (47.5 min) would achieve 1 m/s precision. For comparison the total orbital period of a LEO space debris in a circular orbit with 500 km altitude is approximately 100 min. To achieve 1 mm/s precision, the integration time has to be increased to approximately 84.5 hours.

Assuming the approximation for both β and F^2 parameters are accurate, the direct detection scheme would be able to estimate the velocity of a 10 cm piece of space debris to 1 mm/s precision. However, this is not possible for 1 cm piece of space debris. The integration time required is larger than the observable time of a single flyover. For 1 cm space debris the direct detection scheme can only achieve 1 mm/s precision up to a range of 800 km. The smallest debris size the direct detection scheme can track up with 1 mm/s at the maximum range of 5500 km is a 5 cm piece of space debris.

This result shows that the direct detection scheme may not be a suitable method to estimate a space debris target velocity with the desired 1 mm/s precision.

6.2.2 Using an Avalanche Photo-Diode

An Avalanche Photo-Diode (APD) is capable of measuring single photons [170] due to the detector's lower noise floor and high quantum efficiency. In the pulsed laser ranging scheme currently used at the EOS telescope, an APD is used to measure the reflected pulse collected by the telescope.

The Newport 1811 photodetector used in the bench-top experiment is an off the shelf

commercial photodetector. A direct comparison using experimental results to confirm an APD would better perform than the Newports 1811 could not be carried out since the APD used at the EOS telescope had a low bandwidth equal to 30 MHz [171]. The low bandwidth of the EOS telescope APD would filter out the 75 MHz chip frequency PRN code, but higher bandwidth APDs are available [172].

The discussion on improved estimation of the parameters is based on the coherent detection scheme results seen in Chapter 5 and discussed in Section 6.3. An APD has a lower noise floor. Therefore the acquired signal would have a higher signal-to-noise ratio. In the coherent detection scheme, by interfering with a bright local oscillator, the acquired signal's signal-to-noise ratio is improved. The results in coherent detection scheme showed improved signal detection and measurement precision and accuracy. Based on these results, this thesis suggests that if a suitable APD is used, the direct detection scheme would perform better than the experimental results in Chapter 4.

In the case an APD is used at the receiver, the dominant noise source for the direct detection scheme is background photon noise which prevents current space debris pulsed-ranging daylight operations [33]. Even though background photon count may vary from day to day, the background noise approximated for the EOS telescope in this thesis is equal to 90 pW, less than the photodetector and background noise source used in the bench-top experiment, which was equal to 120 μW. The bench-top experimental results show that the direct detection scheme can be used for daylight operation.

Assuming the 90 pW background photon noise as the dominant noise source, the precision of the velocity estimate is expected to better than presented in both Figure 6.2 and Figure 6.3. In this scenario, if the integration time is equal to 1700 s and taking into account the assumptions that $\beta = 10^8$ and $F^2 = 0.9$, the direct detection scheme can estimate the time-varying delay of a 1 cm diameter space debris to within 1 mm/s for a range up to approximately 3400 km. This result is a significant improvement from 800 km with the results from the bench-top experiment.

Using the bench-top experiment results, the following assumptions can also be made:

1. When an avalanche photo-diode (APD) with a lower photodetector noise floor than the Newport 1811, a better precision in estimating the parameters can be achieved.
2. Direct detection scheme can be used for daylight operations.

The thesis, however, moves to focus on overcoming the measurement precision limited by background photon and photodetector noise sources by moving to a coherent detection scheme which would outperform the direct detection scheme.

6.3 Conclusion From the Coherent Detection Scheme

Chapter 5 presented the theoretical discussions and the bench-top experimental layout where the signal laser beam is interfered with a bright local oscillator to improve the signal-to-noise ratio above the photodetector noise. The chapter also presented the experimental results to evaluate and compare the coherent detection scheme with the direct detection scheme. The result showed an improved signal detection, measurement accuracy and precision for the same received signal power and analysis integration time used in the direct detection scheme. The results also showed the coherent detection scheme could estimate the d_0 and v_0 parameters for smaller received signal powers.

The chapter evaluated the relationship of the precision σ_v with both received signal power P_{Sig} and integration time t_i. The experiment proved that σ_v relationship is:

- $P_{Sig}^{-0.5}$ with received signal power P_{Sig}
- $t_i^{-1.5}$ with the integration time t_i

The experimental result was used to produce an equation to calculate σ_v for varying input P_{Sig} and t_i. This is presented as equation 6.3 for the precision of the coherent detection scheme σ_{v-CD}.

$$\sigma_{v-CD}\ m/s = 150.59\,\mathrm{m/s}\left(\sqrt{\frac{2.4\,\mathrm{nW}}{P_{Sig}\ W}}\right)\left(\frac{1\,\mathrm{ms}}{t_i\ s}\right)^{1.5} \tag{6.3}$$

The study, using equation 6.3, of the coherent detection scheme for space debris application focuses on the following conditions:

1. The received signal power P_{Sig} required to achieve a velocity estimate of 1 mm/s and 1 m/s precision for 1 s integration time t_i.
2. Increasing the integration time t_i to achieve the same precision at a lower received signal power P_{Sig}.
3. For received signal power P_{Sig} between 35 pW and 3.5 fW.
4. The largest integration time required to achieve 1 mm/s precision for 1 cm diameter space debris at the range of 5500 km.

Figure 6.4 uses equation 6.3 to present the σ_{v-CD} as a function of received signal power for 1 s, 100 s and 1700 s integration times. The dominant noise source in this experiment is shot noise from the local oscillator that has an optical power equal to 115 μW. Figure 6.5 presents the calculated σ_{v-DD} as a function of integration time t_i.

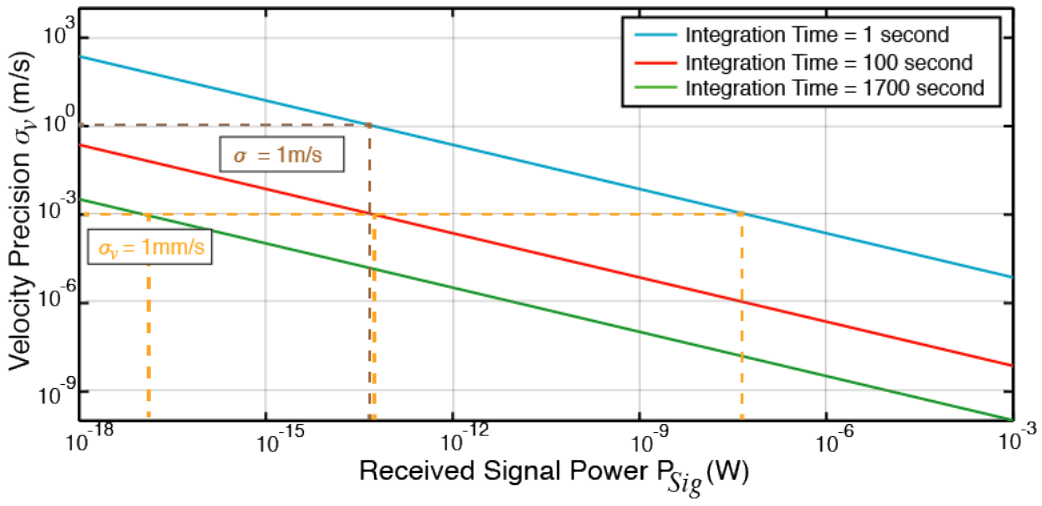

Figure 6.4: Calculating σ_v of the coherent detection scheme for varying received signal power using equation 4.7 for 1 s, 100 s and 1700 s integration times.

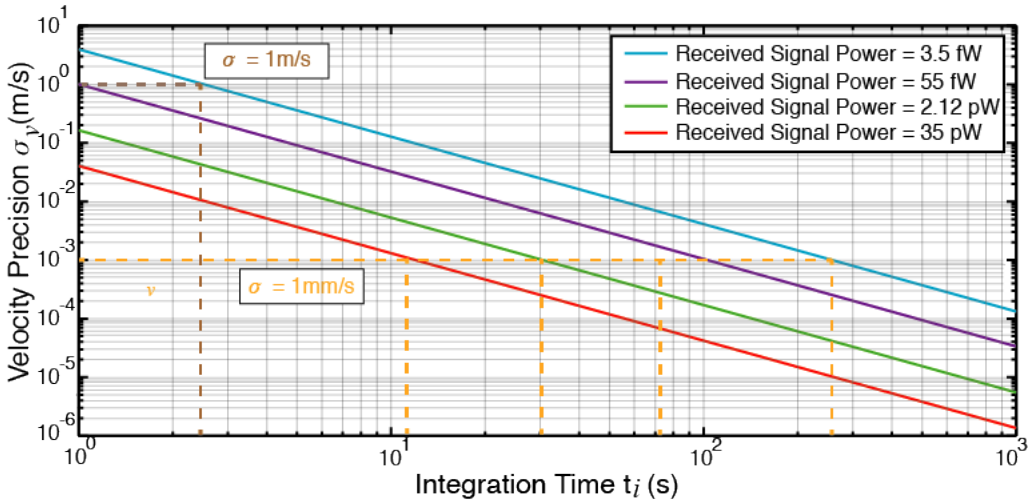

Figure 6.5: Calculating σ_v of the coherent detection scheme for varying integration times.

Using both Figure 6.4 and Figure 6.5, for an integration time of 1 s, the coherent detection scheme can achieve 1 mm/s precision if the minimum received signal power is approximately equal to 55 nW. To achieve 1 m/s precision for the same 1 s integration time, the minimum received signal power is approximately equal to 55 fW. Figure 6.4 also shows that if the received signal power is 55 fW, increasing the integration time from 1 s to 100 s improves the velocity estimate precision to 1 mm/s.

6.3.1 Using $\beta = 10^8$ and $F^2 = 0.9$

From Section 6.1.1, both β and F^2 were approximated to equal 10^8 and 0.9 respectively. Figure 6.1 shows that the calculated received signal power from a 1 cm and 10 cm space debris is equal to 3.5 fW and 35 pW respectively. Both received power are also shown in Figure 6.5.

In the case the received signal power is equal to 35 pW, a minimum integration time of approximately 0.11 s is sufficient to achieve 1 m/s precision. Increasing the integration time to 11.5 s would be sufficient to achieve 1 mm/s precision. In the case the received signal power is equal to 3.5 fW, increasing the integration time to approximately 2.5 s would achieve 1 m/s precision. To achieve 1 mm/s precision, the integration time has to be increased to approximately 250 s.

Using the same assumptions to approximate for both β and F^2 parameters, the coherent detection scheme outperforms the direct detection scheme for the same received signal power, requiring smaller integration times to achieve the desired precision. For 1 cm space debris the coherent detection scheme is able to achieve 1 mm/s precision of the velocity parameter estimate within a single flyover at the maximum range of a LEO space debris.

6.4 Comparison of the Two Detection Schemes

Comparing the results in Section 6.2 and Section 6.3 for the direct detection and coherent detection scheme respectively, the coherent detection scheme has better performance for space debris ranging application for the same integration time by amplifying the signal laser above the background photon noise. If background photon noise increases during daylight

operation, the local oscillator optical power is increased to amplify the signal above the new noise floor further and achieve the same level of ranging performance.

Figure 6.6 compares the velocity measurement precision for both the direct detection and coherent detection schemes with varying received power at 1 s and 100 s integration times. As discussed in Chapter 4 and Chapter 5, the precision in the velocity measurement with the received signal power for the direct and coherent detection scheme is equal to P_{Sig}^{-1} and $P_{Sig}^{-0.5}$ respectively. Due to the different relationships, the two detection methods intersect in Figure 6.6 at 5 μW received signal power.

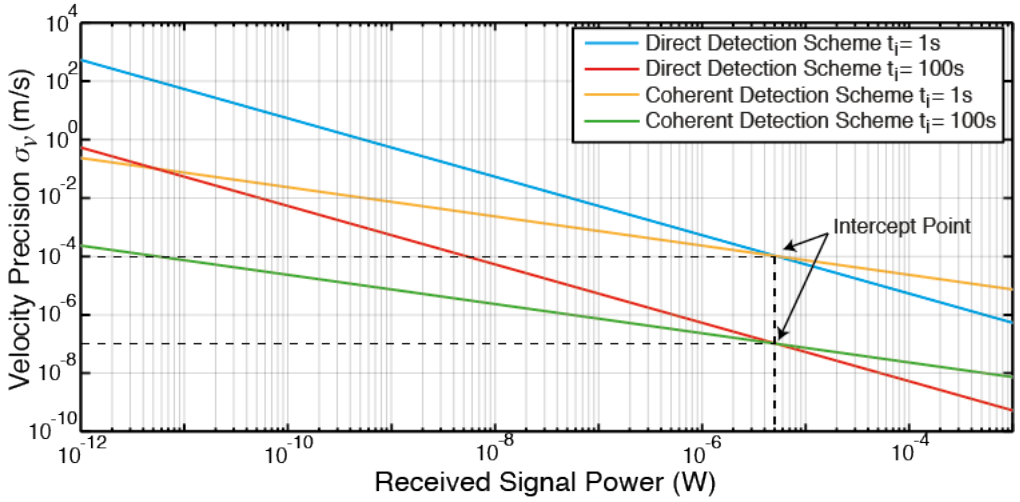

Figure 6.6: Comparing σ_v of the direct detection scheme and coherent detection scheme for 1 s and 100 s integration times. The plot shows for both integration times the two schemes' σ_v calculations intersect at 5 μW.

This intersection point can be explained using equation 6.4, discussed in more detail in Section 5.2.2, which describes the optical signal measured at the photodetector for a coherent detection scheme. The discussion in Chapter 5 ignored the 1st beat note term since at low P_{Sig} power, this term would be much smaller than the 2nd and 3rd beat note terms. However, for increasing received signal power, the 1st beat note term starts affecting the measured beat note waveform observed in the time series. Since this is a region that is not of interest to the space debris application, this is not further investigated.

$$
\begin{aligned}
P_{PD}(t) = \frac{1}{2}\Big[& \underbrace{P_{Mod} + P_{FS} + P_{LO}}_{\text{DC Term}} \\
& + \underbrace{P_{FMZ}(t)}_{\text{1st Beat Note Term}} \\
& + \underbrace{2\sqrt{P_{Mod}P_{LO}}\cos(2\pi f_h t + (\phi_{Mod} + \phi_{Sig} - \phi_{LO}) + \phi_{PRN}(t))}_{\text{2nd Beat Note Term}} \\
& + \underbrace{2\sqrt{P_{FS}P_{LO}}\cos(2\pi f_h t + (\phi_{FS} + \phi_{Sig} - \phi_{LO}))}_{\text{3rd Beat Note Term}}\Big]
\end{aligned}
\tag{6.4}
$$

In conclusion, from Figure 6.6 the coherent detection scheme can perform much better than the direct detection scheme for weaker received signal power P_{Sig}, achieve a more precise time-varying delay measurement from space debris with a diameter between 1 cm and 10 cm for space debris application.

6.5 Chapter Summary

The Space Environmental Research Centre (SERC) aims to develop a space debris ranging system to track and manoeuvre space debris in LEO orbit using ground-based optical lasers. SERC has identified that the ranging method should be capable of measuring the velocity of the space debris to within 1 mm/s for improved orbit prediction and determine the impact of the manoeuvring attempt. SERC also aims to have a technology demonstration at the EOS telescope on Mount Stromlo.

This chapter first provides the telescope design, based on the EOS facility, and how the design impacts the received signal power collected at the telescope. The discussions also provides a brief overview of other factors that impact the received signal power. Using the size and range of the space debris the received signal power can be estimated.

This chapter compared both the direct and coherent detection scheme results presented in Chapter 4 and 5 respectively. Using the calculated received signal power for varying space debris size and range, the discussion showed that the coherent detection scheme outperforms the direct detection scheme in a space debris application. The coherent detection scheme can estimate the velocity parameter of a 1 cm diameter LEO space debris target to within 1 mm/s at a range of 5500 km using 250 s integration time. To achieve the same precision for the same target and range, the direct detection scheme needed a 83 hours integration time which is not feasible.

Conclusion and future work

7.1 Conclusion

This thesis presented an optical bench-top experiment to amplitude modulate a continuous wave laser with pseudo-random noise codes for space debris ranging applications. A matched filter analysis is used to measure the time-varying delay of the received amplitude modulated laser beam. The measured time-varying delay can be used to predict the space debris' orbit to determine possible collisions with other orbiting objects as well as to identify the impact of the manoeuvring attempt with a ground-based laser to change the space debris' orbit.

The thesis aimed to investigate a space debris laser ranging system that is compatible with using a continuous wave laser. As discussed in Chapter 1, using a continuous wave laser at a ground station is one proposed method to mitigate the growth in the number of space debris in Low Earth Orbit (LEO). The Space Environmental Research Centre (SERC) is aiming to develop the technology to range and manoeuvre space debris in LEO using a continuous wave laser with the 1.8 m telescope at Mt Stromlo Canberra. SERC has requested investigating a space debris ranging method that is capable of measuring the time-varying delay of a space debris target with 1 mm/s precision. The additional challenge is that a piece of space debris is a non-cooperative target where the reflected signal is scattered in random directions. Together with the small size of the space debris and large propagating distance, the optical signal power P_{Sig} collected by a telescope could be low. The low signal-to-noise ratio of the received signal results in low ranging accuracy and precision. In addition, current space debris laser ranging method at Mount Stromlo is unable to perform daylight operations because of the high background photon noise.

When the space debris reflects the optical signal with the amplitude modulated PRN code, the debris' time-varying delay causes a Doppler shift of the PRN code chip frequency. The matched filter analysis method with parameter estimation is investigated to recreate the Doppler effect of the acquired signal onto a template code. Using the parameter estimation approach, the parameters of the acquired signal can be estimated and used to determine the time-varying delay of the signal laser. This is accomplished by generating a parameter bank, containing a range of values, for each time-varying delay parameter. Each template code undergoes a cross-correlation with the acquired signal to determine the similarity of the two codes. The parameters of the template code with the most significant cross-correlation are the best estimate of the acquired signal's time-varying delay. The bench-top experiment only applied the distance and velocity parameters. Higher-order terms such as acceleration were not included due to the low integration times used in the analysis. Chapter 3 also showed that both the PRN code chip frequency and integration time impact the time-varying delay measurement.

Chapter 4 presented the bench-top experiment for the direct detection scheme where a photodetector directly measures the intensity of the signal laser. A Fibre Mach-Zehnder interferometer is used to amplitude modulate the PRN code onto the continuous wave laser. The modulating PRN code chip frequency can be altered to model the Doppler effects for a moving space debris target. The matched filter analysis of the direct detection scheme estimated both the distance and velocity parameters accurately. The results also showed the relationship of the precision in estimating the velocity parameter depends on the received signal power P_{Sig} and integration time t_i. The relationships are:

- P_{Sig}^{-1} with received signal power P_{Sig}
- $t_i^{-1.5}$ with the integration time t_i

Chapter 5 discussed using the coherent detection scheme to amplify the amplitude modulated PRN code by interfering the modulated signal laser with a bright local oscillator. This improved the signal-to-noise ratio of the amplitude modulated signal over additive noise sources. The chapter discussed using a $I^2 + Q^2$ demodulation method to recover the amplitude modulated PRN code from the interference pattern. The same matched filter analysis used in the direct detection scheme was also used for the coherent detection scheme to estimate the time-varying delay.

The bench-top experimental results for the coherent detection scheme showed improved signal detection and parameter estimation precision compared to the direct detection scheme at the same received signal power P_{Sig} and integration time t_i. The results also showed how the relationship of the precision of the matched filter analysis in estimating the velocity parameter:

- $P_{Sig}^{-0.5}$ with received signal power P_{Sig}
- $t_i^{-1.5}$ with the integration time t_i

The experimental results for the coherent detection scheme also showed that frequency noise does not impact the matched filter analysis result. This means laser frequency noise potentially would not impact the time-varying delay measurement using the coherent detection scheme.

Chapter 6 compared the two detection schemes for space debris ranging application using the 1.8 m telescope at Mount Stromlo for varying received signal power and integration times. The coherent detection scheme was found to be the better of the two methods thanks to the amplification of the low signal-to-noise ratio received signal. Assuming the received signal power from a piece of space debris is equal to 3.5 fW, the direct detection scheme needs an integration time of 47.5 min and 83 hours to achieve 1 m/s and 1 mm/s precision respectively. For the coherent detection scheme, for the same 3.5 fW received signal power, an integration time of 2.5 s and 250 s to achieve 1 m/s and 1 mm/s precision respectively.

The results in this thesis predict that amplitude modulating the continuous wave laser with PRN codes and using a matched filter analysis with parameter estimation can measure the time-varying delay of space debris to the level of precision required by SERC. The results in this thesis show that the 1 mm/s velocity estimate precision is best achieved using a coherent detection scheme by amplifying the signal laser with a bright local oscillator to overcome the additive amplitude noise sources. The coherent detection scheme also could potentially be less susceptible to background photon noise and allow day time operations.

7.2 Future Work

This section presents the future experimental work beyond the scope of this thesis to further investigate the application of the matched filter analysis for space debris ranging. These future studies are:

1. Polarisation of the reflected signal
2. Reflecting the signal from a diffuse surface
3. Reducing the time taken for the matched filter analysis

Two properties that impact a coherent detection scheme are polarisation and the diffuse reflection. Both these effects would be introduced into the signal when propagating through the atmosphere and when reflected by the space debris target. Future studies will look into applying these effects to the bench-top experiment and investigating the impact on the amplitude modulated optical signal for a coherent detection scheme. Also, the computational resources for the matched filter analysis need to be improved to allow lower processing times and analysis for longer integration times than that carried out in this thesis.

7.2.1 Polarisation

The polarisation of the optical signal [100, 173] could potentially be affected as the beam propagates through the atmosphere and by the reflecting surface of the target. In a coherent detection scheme, the matched polarisation of both the signal and local oscillator beam is essential when coherently combining the two laser beams for power scaling [174]. The polarisation fluctuations of the signal beam can change the amount of signal power interfered with the local oscillator [175], hence causing fluctuations in the resultant beat note amplitude.

Studies presented by Toyoshima et al. [176] have shown that the polarisation of the beam is preserved when propagating through the atmosphere between a satellite and ground station. In the bench-top experiment presented in this thesis, the polarisation of the optical signal beam and local oscillator beam are fixed to produce the maximum optical power of the resulting heterodyne beat note. The polarisation of the optical signal was not altered.

Further studies should be carried out the determine the impact of the heterodyne beat note, and hence the recovered PRN code, if the polarisation of the optical signal beam is altered.

7.2.2 Diffuse Surface

Section 2.3.3 discussed the impact of a diffuse reflecting surface of a piece of space debris. The theoretical discussions and simulated results in this thesis have shown that the diffuse surface would not impact the amplitude modulated PRN code in a coherent detection scheme. However, a future experimental layout should be designed to confirm the simulated results.

Figure 7.1 proposes a bench-top experiment where the continuous wave laser is amplitude modulated with a PRN code and is reflected by a diffuse surface. The diffuse surface is

simulated using a spatial light modulator (SLM) with the aim of introducing a random path length to the reflected optical signal. The reflected signal then interferes with the local oscillator laser. The acquired signal is then passed through the same matched filter analysis used for the coherent detection scheme.

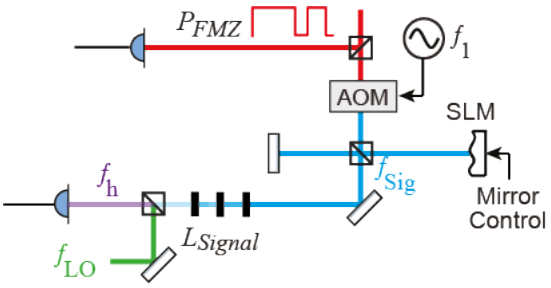

Figure 7.1: Proposed optical layout to test the amplitude modulated PRN coherent detection scheme with a diffuse reflecting surface.

The result from this experiment would confirm if the PRN amplitude modulated coherent detection scheme is suitable for ranging to a piece of space debris with a diffuse surface.

7.2.3 Reducing the computational time of the matched filter analysis

The discussion in this thesis has shown that for a space debris application, higher integration times are needed for both detection schemes than those used in the matched filter analysis for Chapters 4 and 5. The main reasons for not performing the analysis at higher integration times is due to:

1. Limited memory at the data acquisition stage
2. Limited computational resources for matched filter analysis
3. Large analysis time taken when running the analysis for higher integration times

At the acquisition stage, the FPGA memory could only allow collecting a maximum of 0.1 s of the optical signal from the bench-top experiment. The analysis was then performed in post-processing using a desktop computer to run the matched filter analysis on MATLAB. For 1 ms integration time, a single template takes approximately 3 s to complete a correlation with the acquired signal. In a space debris application, hundreds of templates will be used and for an integration time of hundreds of seconds. Therefore the computational resources used in this thesis were not suitable for a space debris application.

One method around the current limitation is improving the processing capability. Many analysis methods in other fields are performed using a graphics processing unit (GPU) that has a parallel architecture and can perform multiple tasks simultaneously. Many different fields are using the computing potential of powerful GPUs to run a complex analysis for scientific research, financial markets and deep learning applications [177, 178].

Reducing the computational load of the matched filter analysis will also improve the computational performance. The analysis used in Chapters 4 and 5 produced a parameter bank for each parameter of interest. The parameter values of each parameter bank are equally spaced. This may not be the most efficient analysis approach. The shape of the signal correlation is known, depending on PRN code properties. A more efficient parameter spacing chosen to estimate the optimal parameter values could reduce the number of templates required for the analysis.

Another consideration is if the analysis is to be performed in real-time or in post-processing. Current space debris ranging methods do offer real-time results of the space debris range and time-varying delay. These results are then used in post-processing to predict the debris orbit and potential collision with active satellites. However, achieving real-time matched filter analysis results would require powerful computational resources. Post-processing methods may be a more suitable approach as the acquired signal can be stored and analysed thoroughly using the matched filter analysis and provide a predicted orbit of the space debris.

Machine learning methods could potentially be another method added as part of the analysis to better predict the orbit of the space debris and potential collisions with other orbiting objects.

References

[1] N. Kiefert, "New interactive chart shows just how many satellites are orbiting earth," Jan 2017. [Online]. Available: http://www.astronomy.com/news/2017/01/interactive-satellite-chart

[2] [Online]. Available: https://orbitaldebris.jsc.nasa.gov/

[3] D. J. Kessler and B. G. Cour-Palais, "Collision frequency of artificial satellites: Creation of a debris belt," *Journal of Geophysical research*, vol. 83, no. A6, pp. 2637 – 2646, June 1978.

[4] H. Riebeek. (2009, September) Catalog of earth satellite orbits. [Online]. Available: http://earthobservatory.nasa.gov/Features/OrbitsCatalog/

[5] B. Weeden. (2009, November) 2009 iridium-cosmos collision fact sheet.

[6] "Orbital debris quarterly news," NASA Orbital Debris Program Office, Tech. Rep. 1 2, May 2019.

[7] E. S. Agency, "Hypervelocity impacts and protecting spacecraft," April 2013. [Online]. Available: http://www.esa.int/Our_Activities/Operations/Space_Debris/Hypervelocity_impacts_and_protecting_spacecraft

[8] A. F. I. of Technology (U.S.), *Critical technologies for national defense*, J. S. Przemieniecki, Ed. AIAA Education Series, 1991.

[9] J. Nicholas, "The collision of iridium 33 and cosmos 2251: The shape of things to come," in *60th International Astronautical Congress*. National Aeronautics and Space Administration, October 2009.

[10] J. Liou, "An active debris removal parametric study for leo environment remediation," *Advances in Space Research*, vol. 47, no. 11, pp. 1865–1876, 2011.

[11] J. Mason, J. Stupl, W. Marshall, and C. Levit, "Orbital debris-debris collision avoidance," *Pergamon*, vol. 48, no. 10, pp. 1643–1655, November 2011.

[12] J. Walker, "Satellite constellations," *British Interplanetary Society, Journal (Space Technology)*, vol. 37, pp. 559 – 572, December 1984.

[13] J. C. Liou and N. L. Johnson, "Risks in space from orbiting debris," *Science*, vol. 311, pp. 340 – 341, Jan 2006.

[14] "Orbital debris quarterly news," NASA Orbital Debris Program Office, Tech. Rep. 3, July 2009.

[15] E. S. Agency, "Esa's annual space environmental report," ESA Space Debris Office, Tech. Rep., July 2019.

[16] K. Takahashi, C. Charles, R. W. Boswell, and A. Ando, "Demonstrating a new technology for space debris removal using a bi-directional plasma thruster," *Scientific Reports*, vol. 8, no. 1, p. 14417, 2018. [Online]. Available: https://doi.org/10.1038/s41598-018-32697-4

[17] C. P. Mark and S. Kamath, "Review of active space debris removal methods," *Space Policy*, vol. 47, pp. 194 – 206, 2019. [Online]. Available: http://www.sciencedirect.com/science/article/pii/S0265964618300110

[18] "Orbital debris mitigation standard pratices," U.S. Government, Tech. Rep., November 2019.

[19] P. C, "Catcher's ,itt as an alternative to laser space debris mitigation," in *AIP Conference*, vol. 1278, 2010.

[20] J. Harrington, "Debris remediation," Orbital Debris Program Office. [Online]. Available: https://orbitaldebris.jsc.nasa.gov/remediation/

[21] J. Amos. (2019, February) Space harpoon skewers 'orbital debris'. [Online]. Available: https://www.bbc.co.uk/news/science-environment-47252304

[22] L. Anselmo and C. Pardini, "Long term dynamical evolution of high area-to-mass ratio debris released into earth orbits," *Acta Astronaut*, vol. 67, pp. 204–216, 2010.

[23] R. L. Garwin, "Solar sailing-a practical method of propulsion within the solar system." Jet Propulsion, Tech. Rep. 52, 1958.

[24] R. L. Forward, "Pluto the gateway to the stars. missiles and rock- ets," *Science Digest*, vol. 10, pp. 26–28, April 1862.

[25] L. Roberts, "Internally sensed optical phased arrays," PhD Thesis, The Australian National University, 2016.

[26] J. Campbell, "roject orion: Orbital debris removal using ground-based sensors and laser." NASA Technical Memorandum, Tech. Rep. 108522, 1996.

[27] C. Phipps, G. Albrecht, H. Friedman, D. Gavel, E. George, J. Murray, C. Ho, W. Priedhorsky, M. Michaelis, and Reilly, "Orion: Clearing near-earth space debris using a 20-kw, 530-nm, earth-based, repetitively pulsed laser," *Laser and Particle Beams*, vol. 14, no. 1, pp. 1–44, 1996.

[28] B. Greene, "Optical techniques for space environment management," in *Advance Maui Optical and Space Surveillance*. Maui, Hawai'i: Space Environment Research Centre, September 2016.

[29] ——, "Laser tracking of space debris," in *13th International Workshop on Laser Ranging Instrumentation*, Washington DC, October 2002.

[30] J. F. McGarry, E. D. Hoffman, J. J. Degnan, J. W. Cheek, C. B. Clarke, I. F. Diegel, H. L. Donovan, J. E. Horvath, M. Marzouk, A. R. Nelson, D. S. Patterson, R. L. Ricklefs, M. D. Shappirio, S. L. Wetzel, and T. W. Zagwodzki, "Nasa's satellite laser ranging systems for the twenty-first century," *Journal of Geodesy*, Sep 2018. [Online]. Available: https://doi.org/10.1007/s00190-018-1191-6

[31] M. Wilkinson, U. Schreiber, I. Procházka, C. Moore, J. Degnan, G. Kirchner, Z. Zhongping, P. Dunn, V. Shargorodskiy, M. Sadovnikov, C. Courde, and H. Kunimori, "The next generation of satellite laser ranging systems," *Journal of Geodesy*, Sep 2018. [Online]. Available: https://doi.org/10.1007/s00190-018-1196-1

[32] G. Kirchner, F. Koidl, F. Friederich, I. Buske, U. Volker, and W. Riede, "Laser measurements to space debris from graz slr station," *Advances in Space Research*, vol. 51, pp. 21–24, September 2012.

[33] "Technical report on space debris," United Nations Publications, Tech. Rep., 1999.

[34] R. Matthey and V. Mitev, "Pseudo-random noise-continuous-wave laser radar for surface and cloud measurements," *Optics and Lasers in Engineering*, vol. 43, no. 3–5, pp. 557 – 571, March 2004.

[35] *Pseudo-Noise (PN) Ranging Systems.* The Consultative Committee for Space Data System, 2014.

[36] *Development of a pseudo-random noise modulation continuous-wave (PRN-cw) total backscatter lidar*, vol. 2505, June 1995.

[37] Y. Emery and C. Flesia, "Use of the a1- and the a2-sequences to modulate continuous-wave pseudorandom noise lidar," *Applied Optics*, vol. 37, no. 12, pp. 2238 – 2241, 1998 1998.

[38] D. M. Norman and C. S. Gardner, "Satellite laser ranging using pseudonoise code modulated laser diodes," *Applied Optics*, vol. 27, no. 17, September 1988.

[39] D. A. Shaddock, "Digitally enhanced heterodyne interferometry," *Optics Letters*, vol. 32, no. 22, pp. 3355–3357, 2007.

[40] L. Roberts and S. Francis, "Continuous-wave laser techniques for space debris ranging and manoeuvring," in *Proceedings of the Advanced Maui Optical and Space Surveillance Technologies Conference*, T. M. E. D. Board, Ed. Wailea, Maui, Hawaii: Advanced Maui Optical and Space Surveillance Technologies, September 2015.

[41] C. B. Chang, "Parameter estimation accuracy for radar targets closely spaced in range," Lincoln Laboratory, Tech. Rep., November 1980.

[42] B. Moision and B. Erkmen, "Achievable precision for optical ranging systems," in *Instrumentation and Photography*, August 2012.

[43] B. Bécsy, P. Raffai, N. J. Cornish, R. Essick, J. Kanner, E. Katsavounidis, T. B. Littenberg, M. Millhouse, and S. Vitale, "Parameter estimation for gravitational-wave bursts with the bayeswave pipeline," *Astrophy J*, vol. 839, no. 1, April 2017.

[44] E. Tretkoff, "British patent for radar system for air defense granted to robert watson-watt," American Physical Society News, April 2006.

[45] M. A. Richards, W. L. Melvin, J. Scheer, J. A. Scheer, and W. A. Holm, *Principles of Modern Radar: Volume 3: Radar Applications.* Institution of Engineering and Technology, 2013.

[46] C. G. Lehr, "Satellite tracking with a laser," *SAO Special Report*, no. 215, 1966.

[47] R. J. Doviak and D. S. Zrnic, *Doppler Radar and Weather Observations*, 2nd ed., ser. Dover Books on Engineering. Dover Publications, May 2006.

[48] J. Murray, C. Blackwell, J. Gaynor, and T. Kennedy, "Haystack ultra-wideband satellite imaging radar measurements of the orbital debris environment: 2014-2017," National Aeronautics and Space Administration (NASA), Tech. Rep., July 2019.

[49] E. S. Agency. (2014, February) Space surveillance and tracking - sst segment. [Online]. Available: http://www.esa.int/Our_Activities/Operations/Space_Situational_Awareness/Space_Surveillance_and_Tracking_-_SST_Segment

[50] R. J. Burkholder, L. J. Gupta, and J. T. Johnson, "Comparison of monostatic and bistatic radar images," *IEEE Antennas and Propagation Magazine*, vol. 45, no. 3, pp. 41–50, June 2003.

[51] S. Saha, *Aperture Synthesis: Methods and Applications to Optical Astronomy*, ser. Astronomy and Astrophysics Library. Springer New York, 2010. [Online]. Available: https://books.google.com.au/books?id=BIHe2Mmv08cC

[52] G. Ruiz, T. Patzelt, L. Leushacke, and O. Loffeld, "Autonomous tracking of space objects with the fgan tracking and imaging radar," *GI Jahrestagung*, January 2006.

[53] D. Mehrholz, L. Leushacke, W. Flury, R. Jehn, H. Klinkard, and M. Landgraf, "Detecting, tracking and imaging space debris," ESA Bulletin, February 2002.

[54] E. S. Agency. (2013, April) Space debris scanning and observing. [Online]. Available: http://www.esa.int/Our_Activities/Operations/Space_Debris/Scanning_observing

[55] J. Ring, "The laser in astronomy," *New Scientist*, pp. 672–673, June 1963.

[56] G. G. Goyer and R. Watson, "The laser and its application to meteorology," *Bulletin America Meterological Society*, vol. 44, September 1963.

[57] J. Hecht, "Lidar for self-driving cars," *Optics and Photonics News*, vol. 29, pp. 26 – 33, 2018.

[58] R. Paschotta, *Lidar*, Wiley-VCH, Ed. Encyclopedia of Laser Physics and Technology, December 2008.

[59] C. Weitkamp, *Lidar: Range-Resolved Optical Remote Sensing of the Atmosphere*. Springer, 2005.

[60] J. Machol, "Comparison of the pseudorandom noise code and pulsed direct-detection lidars for atmospheric probing," *Applied Optics*, vol. 36, no. 24, August 1997.

[61] L. L. Gurdev and T. N. Dreischuh, "On the determination by coherent lidar of doppler-velocity profiles in turbulent atmosphere," *Proceedings of SPIE - The International Society for Optical Engineering*, 2003.

[62] N. Chiodo, K. Djerroud, O. Acef, A. Clairon, and P. Wolf, "Lasers for coherent optical satellite links with large dynamics," *Applied Optics*, vol. 52, no. 30, October 2013.

[63] I. Coddington, W. C. Swann, L. Nenadovic, and N. R. Newbury, "Rapid and precise absolute distance measurements at long range," *Nature Photonics*, vol. 3, pp. 351–356, May 2009.

[64] F. Bennet, C. D'Orgeville, I. Price, F. Rigaut, I. Ritchie, and C. Smith, "Adaptive optics for satellite imaging and space debris ranging," in *Proceedings of the Advanced Maui Optical and Space Surveillance Technologies Conference*, T. M. E. D. Board, Ed. Wailea, Maui, Hawaii: Advanced Maui Optical and Space Surveillance Technologies, September 2015.

[65] M.-C. Amann, T. Bosch, R. Myllyla, and M. Rioux, "Laser ranging: a critical review of usual techniques for distance measurement," *Society of Photo-Optical Instrumentation Engineers*, vol. 40, pp. 10–19, January 2001.

[66] G. Kirchner and F. Koidl, "Graz khz slr system: design, experiences and results," in *14th ILRS Workshop*, 2004, pp. 501–505.

[67] J. McGarry, T. Zagwodzki, J. Degnan, P. Dunn, J. Cheek, D. Patterson, H. Donovan, A. Mann, A. Mallama, and R. Ricklefs, "Early satellite track- ing results from slr2000," in *14th ILRS Workshop*, 2004.

[68] D. Hampf, E. Schafer, F. Sproll, T. Otsubo, P. Wagner, and W. Riede, "Satellite laser ranging at 100 khz pulse repetition rate," *CEAS Space Journal*, vol. 11, pp. 363–370, April 2019.

[69] Z. Zhang, H. Zhang, M. Long, H. Deng, Z. Wu, and W. Meng, "High precision space debris laser ranging with 4.2 w double-pulse picosecond laser at 1 khz in 532nm," *Optik*, vol. 179, pp. 691 – 699, 2019. [Online]. Available: http://www.sciencedirect.com/science/article/pii/S003040261831742X

[70] J. Sang, J. Bennett, and C. Smith, "Experimental results of debris orbit predictions using sparse tracking data from mt. stromlo," *Elsevier*, no. 102, pp. 258 – 268, June 2014.

[71] H. D.Griffiths, "From a different perspective : Principles, practice and potential of bistatic radar," in *2003 Proceedings of the International Conference on Radar.* IEEE, September 2003.

[72] R. Paschotta, *Gaussian Beams.* Encyclopedia of Laser Physics and Technology, December 2008. [Online]. Available: https://www.rp-photonics.com/lasers.html

[73] ——, *Lasers.* Encyclopedia of Laser Physics and Technology, December 2008. [Online]. Available: https://www.rp-photonics.com/lasers.html

[74] ——, *Beam Divergance.* Encyclopedia of Laser Physics and Technology, December 2008. [Online]. Available: https://www.rp-photonics.com/beam_divergence.html

[75] "The threat of orbital debris and protecting nasa space assets from satellite collisions," National Aeronautics and Space Administration (NASA), Tech. Rep., April 2009.

[76] C. R. Phipps, K. I. Baker, and S. B. Libby, "Removing orbital debris with pulsed lasers," *Advances in Space Research*, vol. 49, pp. 1283–1300, 2012.

[77] E. L. Christiansen, J. L. Crews, J. E. Williamsen, J. H. Robinson, and A. M. Nolen, "Enhanced meteoroid and orbital debris shielding," *International Journal of Impact Engineering*, vol. 17, pp. 217–228, 1995.

[78] J. A. Overbeck, "Comparison of coherent to incoherent detection at 2.09 um using a solid state ladar system," Wright Laboratory, Tech. Rep., February 1994.

[79] J. W. Goodman, "Some fundamental properties of speckle∗," *J. Opt. Soc. Am.*, vol. 66, no. 11, pp. 1145–1150, Nov 1976. [Online]. Available: http://www.osapublishing.org/abstract.cfm?URI=josa-66-11-1145

[80] R. Paschotta, *Optical Phase*, ser. ISBN 978-3-527-40828-3, E. of Laser Physics and Technology, Eds. Wiley-VCH, October 2008.

[81] C. Bachman, *Laser Radar Systems and Techniques.* Artech House, Massachusetts, 1979.

[82] A. Sutton, K. McKenzie, B. Ware, and D. Shaddock, "Laser ranging and communications for lisa," *Optical Express*, vol. 18, no. 20, September 2010.

[83] R. Egerman, S. De Smitt, and D. Strafford, "Low-weight, low-cost, low-cycle time, replicated glass mirrors," pp. 77 390G–77 390G–7, 2010. [Online]. Available: http://dx.doi.org/10.1117/12.858299

[84] *Giant Magellan Telescope - Overview*, vol. 8444, no. Ground-based and Airborne Telescopes IV. SPIE, September 2012. [Online]. Available: http://www.gmto.org/resources/

[85] H. Wirnsberger, O. Baur, and G. Kirchner, "Space debris orbit prediction errors using bi-static laser observations. case study: Envisat," *Advances in Space Research*, vol. 55, pp. 2607–2615, February 2015.

[86] H. G. Horak, "The effect of the atmosphere on laser range," *Smithsonian Astrophysical Observatory*, 1966.

[87] D. L. Fried, "Optical resolution through a randomly inhomogeneous medium for very long and very short exposures," *J. Opt. Soc. Am.*, vol. 56, no. 10, pp. 1372–1379, Oct 1966. [Online]. Available: http://www.osapublishing.org/abstract.cfm?URI=josa-56-10-1372

[88] H. Hodara, "Laser wave propagation through the atmosphere," *Proceedings of the IEEE*, vol. 54, no. 3, pp. 368 – 375, March 1966.

[89] J. W. Hardy, *Adaptive optics for astronomical telescopes*, 1st ed. Oxford University Press, December 2010.

[90] *Adaptive optics tracking and pushing system for space debris manoeuvre*, vol. 10703, SPIE Astronomiocal Telescope and Instruments. SPIE, 2018.

[91] R. Davies and M. Kasper, *The Annual Review of Astronomy and Astrophysics*, vol. 50, pp. 305–351, June 2012.

[92] A. L. Buck, "Effects of the atmosphere on laser beam propagation," *Applied Optics*, vol. 6, no. 4, pp. 703 – 708, April 1967.

[93] L. Combrinck, "Satellite laser ranging," in *Science of Geodesy-I.* Springer, 2010, pp. 301 – 338.

[94] D. Arnold, O. Montenbruck, S. Hackel, and K. Sośnica, "Satellite laser ranging to low earth orbiters: orbit and network validation," *Journal of Geodesy*, Apr 2018. [Online]. Available: https://doi.org/10.1007/s00190-018-1140-4

[95] J. Wertz, *Spacecraft Attitude Determination and Control*, ser. Astrophysics and Space Science Library. Springer Netherlands, 2012. [Online]. Available: https://books.google.com.au/books?id=crTwCAAAQBAJ

[96] R. Paschotta, *Retroreflectors*, Wiley-VCH, Ed. Encyclopedia of Laser Physics and Technology, December 2008.

[97] D. Kessler and K. Jarvis, "Obtaining the properly weighted average albedo of orbital debris from optical and radar data," *Advances in Space Research*, vol. 34, no. 5, 2011.

[98] M. C. Rezende[U+10FC00], I. M. Martin[U+10FC00][U+10FC00], and R. Faez, "Radar cross section measurements (8-12 ghz) of magnetic and dielectric microwave absorbing thin sheets," *Rev. Fıs. Apl.Instrum*, vol. 15, no. 1, December 2002.

[99] M. Skolnik, *Introduction to radar systems*, 3rd ed. McGraw-Hill Education, 2002.

[100] B. Saleh and M. Teich, *Fundamentals of Photonics*, ser. Wiley Series in Pure and Applied Optics. Wiley, 2007. [Online]. Available: https://books.google.com.au/books?id=Ve8eAQAAIAAJ

[101] E. N. Gilbert and H. O. Pollak, "Amplitude distribution of shot noise," Bell System, Bell System Technical Journal 39, March 1960.

[102] F. Haight, *Handbook of the Poisson distribution*, ser. Publications in operations research. Wiley, 1967. [Online]. Available: https://books.google.com.au/books?id=l8Y-AAAAIAAJ

[103] R. Paschotta, *Shot noise in the Encyclopedia of Laser Physics and Technology*, Wiley-VCH, Ed. Encyclopedia of Laser Physics and Technology, December 2008. [Online]. Available: https://www.rp-photonics.com/shot_noise.html

[104] M. Iqbal, *An Introduction To Solar Radiation.* Elsevier, 2012.

[105] R. Paschotta, A. Schlatter, S. Zeller, H. Telle, and U. Keller, "Optical phase noise and carrier-envelope offset noise of mode-locked lasers," *Applied Physics B*, vol. 82, no. 2, pp. 265–273, Feb 2006. [Online]. Available: https://doi.org/10.1007/s00340-005-2041-9

[106] R. Paschotta, *frequency noise*, 1st ed., Wiley-VCH, Ed. Encyclopedia of Laser Physics and Technology, December 2008.

[107] K. McKenzie, R. E. Spero, and D. A. Shaddock, "Performance of arm locking in lisa," *Phys. Rev. D*, vol. 90, no. 10, November 2009.

[108] L. Mercer, "1/f frequency noise effects on self-heterodyne linewidth measurements," *Journal of Lightwave Technology*, vol. 9, no. 4, pp. 485 – 493, April 1991.

[109] R. W. P. Drever, J. L. Hall, F. V. Kowalski, J. Hough, G. M. Ford, A. J. Munley, and H. Ward, "Laser phase and frequency stabilization using an optical resonator," *Applied Physics B*, vol. 31, no. 2, pp. 97–105, Jun 1983.

[110] T. Hansch and B. Couillaud, "Laser frequency stabilization by polarization spectroscopy of a reflecting reference cavity," *Optics Communication*, vol. 35, no. 3, 1980.

[111] E. Black, "An introduction to pound–drever–hall laser frequency stabilization," *Am. J. Phys.*, vol. 69, pp. 70 – 87, January 2001.

[112] B. Argence, B. Chanteau, O. Lopez, D. Nicolodi, M. Abgrall, C. Chardonnet, C. Daussy, B. Darquié, Y. Le Coq, and A. Amy-Klein, "Quantum cascade laser frequency stabilization at the sub-hz level," *Nature Photonics*, vol. 9, no. 7, pp. 456–460, July 2015.

[113] W. M. Folkner, G. deVine, W. M. Klipstein, K. McKenzie, D. Shaddock, R. Spero, R. Thompson, D. Wuchenich, N. Yu, M. Stephens, J. Leitch, M. Davis, J. deCino, C. Pace, and R. Pierce, "Laser frequency stabilization for grace-ii."

[114] O. Gerberding, K.-S. Isleif, M. Mehmet, K. Danzmann, and G. Heinzel, "Laser-frequency stabilization via a quasimonolithic mach-zehnder interferometer with arms of unequal length and balanced dc readout," *Phys. Rev.*, vol. 7, October 2016.

[115] P. M. Woodward, *Probability and Information Theory, with Applications to Radar: International Series of Monographs on Electronics and Instrumentation*, D. W. Fry, Ed. Pergamon, January 1953, vol. 3.

[116] G. I. Turin, "A introduction to matched filters," *IEEE Transactions on Information Theory*, vol. 6, no. 3, pp. 311 – 329, June 1960.

[117] J. R. Klauder, A. C. Price, S. Darlington, and W. J. Albersheim, "The theory and design of chirp radars," *The Bell System Technical Journal*, vol. 39, no. 4, pp. 745–808, July 1960.

[118] M. J. Withers, "Matched filter for frequency-modulated continuous wave radar systems," *Proceedings: The Institution of Electronical Engineers*, vol. 113, no. 3, March 1966.

[119] A. Tomescu and F. Tomescu, "Matched filters for system identification," *IEEE Transactions on Automatic Control*, vol. 15, no. 3, pp. 398–399, June 1970.

[120] A. Poole, "On the use of pseudorandom codes for "chirp" radar," *IEEE Transactions on Antennas and Propagation*, vol. 27, no. 4, pp. 480 – 485, July 1979.

[121] B. J. Owen and B. S. Sathyaprakash, "Matched filtering of gravitational waves from inspiraling compact binaries: Computational cost and template placement," *Physical Review D*, vol. 60, no. 2, August 1998.

[122] H. Gabbard, M. Williams, F. Hayes, and C. Messenger, "Matching matched filtering with deep networks for gravitational-wave astronomy," *Phys. Rev. Lett.*, vol. 120, no. 141103, April 2018.

[123] R. Mutagi, "Pseudo noise sequences for engineers," *Electronics Communication Engineering Journal*, vol. 8, no. 2, pp. 79–87, Apr 1996.

[124] T. G. Birdsall and M. P. Ristenablt, "Introduction to linear shift resigter generated sequences," Res. Inst., University of Michigan, Ann Arbor, Tech. Rep. 90, 1958.

[125] R. Mutagi, "Pn sequences provide robust synchronisation and ber monitoring in digital radio systems," *Wireless System Design*, January 1996.

[126] R. Dixon, *Spread spectrum systems*, ser. Wiley-Interscience publication. J. Wiley, 1984. [Online]. Available: https://books.google.com.au/books?id=WO5SAAAAMAAJ

[127] R. Gold, "Optimal binary sequences for spread spectrum multiplexing," *IEEE Transactions on Information Theory*, vol. 13, no. 4, pp. 619–621, October 1967.

[128] M. George, M. Hamid, and A. Miller, "Gold code generators in virtex devices," Xilinx, Tech. Rep., January 2001.

[129] S. Craig, W. Fishbein, and O. Rittenbach, "Continuous wave radar with high range resolution and unambigous velocity determination," *IRE Trans Military Electron*, vol. MIL6, no. 2, pp. 153 – 161, April 1962.

[130] X. Ai, R. Nock, J. G. Rarity, and N. Dahnoun, "High-resolution random-modulation cw lidar," *Appl. Opt.*, vol. 50, no. 22, pp. 4478–4488, Aug 2011. [Online]. Available: http://ao.osa.org/abstract.cfm?URI=ao-50-22-4478

[131] H. Takeuchi, N. Sugimoto, H. Baba, and K. Sakurai, "Random modulation cw lidar," *Applied Optics*, vol. 22, no. 9, pp. 1382–1386, 1983.

[132] S. Hawking, *On the Shoulders of Giants: The Great Works of Physics and Astronomy*. Running Press, 2003.

[133] I. Newton, *Philosophiae Naturalis Principia Mathematica*, 3, Ed., London, 1728.

[134] V. A. Chobotov, *Orbital Mechanics*, 3rd ed. AIAA Education Series, 2002.

[135] J. I. Thorpe, K. Numata, and J. Livas, "Laser frequency stabilization and control through offset sideband locking to optical cavities," *Opt. Express*, vol. 16, no. 20, pp. 15 980–15 990, Sep 2008. [Online]. Available: http://www.opticsexpress.org/abstract.cfm?URI=oe-16-20-15980

[136] R. P. Feynman, R. B. Leighton, and M. Sands, *The Feynman Lectures on Physics*. Addison–Wesley, 2005, vol. 1. [Online]. Available: http://www.feynmanlectures.caltech.edu

[137] C. Shannon, "Communication in the presence of noise," *Proceedings of the IRE*, vol. 37, no. 1, pp. 10–21, January 1949.

[138] *125-MHz Photoreceivers Models 1801 and 1811*, New Focus, 2001.

[139] "Agilent n4970a prbs generator 10gb/s user guide," Agilent Technologies, Tech. Rep., 2012.

[140] R. Paschotta, *Electro-Optic Modulators*. Encyclopedia of Laser Physics and Technology, December 2008. [Online]. Available: https://www.rp-photonics.com/electro_optic_modulators.html

[141] "Nir-mpx-ln series 1000nm band phase modulators," iXblue, 3, Rue Sophie Germain France, Phase Modulators, 2017.

[142] D. A. Skoog and D. M. West, *Principles of Instrumental Analysis*, 6th ed., J. J. Leary, Ed. Thomson Learning, January 1992.

[143] OPTIPHASE, "High-speed fiber stretcher," Tech. Rep., February 2011.

[144] P. Hariharan, *Basics of Interferometry*, 1st ed. Academic Press, 1992.

[145] H. Muller, A. Peters, and C. Braxmaier, "Optical fibers with interferometric path length stability by controlled heating for transmission of optical signals and as components in frequency standards," *Applied Physics*, vol. 84, pp. 401 – 408, November 2006.

[146] M. Hart, S. Jefferies, D. Hope, J. Nagy, and R. Swindle, "A comprehensive approach to high-resolution daylight imaging for ssa," AMOS Conference, Tech. Rep., 2016.

[147] *NI 5771R User Guide and Specifications*, National Instrument, May 2012.

[148] *NI FlexRIO FPGA Module Installation Guide and Specifications*, National Instruments, October 2011.

[149] *Interpolation for 2-D gridded data*, Copyright 1984-2017 The MathWorks, Inc. [Online]. Available: https://www.mathworks.com/help/matlab/ref/interp2.html#btyq8s0-1-method

[150] (2009). [Online]. Available: https://www.mathworks.com/help/signal/ref/decimate.html

[151] J. Scheer, "Coherent radar system performance estimation," *IEEE International Conference on Radar*, May 1990.

[152] R. Paschotta, *optical heterodyne detection.* Encyclopedia of Laser Physics and Technology, December 2008. [Online]. Available: https://www.rp-photonics.com/optical_heterodyne_detection.html?s=ak

[153] T. Udem, J. Reichert, R. Holzwarth, and T. W. Hänsch, "Accurate measurement of large optical frequency differences with a mode-locked laser," *Optics Letters*, vol. 24, no. 13, pp. 881 – 883, 1999.

[154] H. R. Carleton and W. T. Maloney, "A balanced optical heterodyne detector," *Applied Optics*, vol. 7, no. 6, pp. 1241 – 1243, 1968.

[155] R. Stierlin, R. Bättig, P. Henchoz, and H. P. Weber, "Excess-noise suppression in a fibre-optic balanced heterodyne detection system," *Opt. Quantum Electron*, vol. 18, no. 6, pp. 445 – 454, November 1986.

[156] S. P. Francis, T. T.-Y. Lam, K. McKenzie, A. J. Sutton, R. L. Ward, D. E. McClelland, and D. A. Shaddock, "Weak-light phase tracking with a low cycle slip rate," *Optics Letters*, vol. 39, pp. 5251–5254, 2014.

[157] N. Bobroff, "Recent advances in displacement measuring interferometry," *Measurement Science and Technology*, vol. 4, no. 9, pp. 907 – 926, September 1993.

[158] T. Okoshi, "Recent advances in coherent optical fiber communications systems," *Journal of Lightwave Technology*, vol. 5, no. 1, pp. 44 – 52, January 1987.

[159] Y. He and B. J. Orr, "Rapidly swept, continuous-wave cavity ringdown spectroscopy with optical heterodyne detection: single- and multi-wavelength sensing of gases," *Applied Optics*, vol. 75, no. 2-3, pp. 267 – 280, September 2002.

[160] J. H. McElroy, "Infrared heterodyne solar radiometry," *Applied Optics*, vol. 11, no. 7, pp. 1619 – 1622, 1972.

[161] Y. qing Li, D. Guzun, and M. Xiao, "Sub-shot-noise-limited optical heterodyne detection using an amplitude-squeezed local oscillator," *Phys. Rev. Lett.*, vol. 82, no. 26, pp. 5225 – 5228, June 1999.

[162] J. F. Holmes and B. J. Rask, "Optimum optical local-oscillator power levels for coherent detection with photodiodes," *Applied Optics*, vol. 34, no. 6, pp. 927 – 933, 1995.

[163] F. Friederich, G. Schuricht, A. Deninger, F. Lison, G. Spickermann, P. H. Bolívar, and H. G. Roskos, "Phase-locking of the beat signal of two distributed-feedback diode lasers to oscillators working in the mhz to thz range," *Opt. Express*, vol. 18, no. 8, pp. 8621–8629, Apr 2010. [Online]. Available: http://www.opticsexpress.org/abstract.cfm?URI=oe-18-8-8621

[164] M. S. Gast, *802.11 Wireless Networks: The Definitive Guide*, 2nd ed. O'Reilly Media, May 2005.

[165] M. Karimi-Ghartemani, H. Karimi, and M. Iravani, "A magnitude/phase-locked loop system based on estimation of frequency and in-phase/quadrature-phase amplitudes," *IEEE Transactions on Industrial Electronics*, vol. 51, no. 2, pp. 511 – 517, April 2004.

[166] D.-S. Ly-Gagnon, S. Tsukamoto, K. Katoh, and K. Kikuchi, "Coherent detection of optical quadrature phase-shift keying signals with carrier phase estimation," *Journal of Lightwave Technology*, vol. 24, no. 1, pp. 12 – 21, January 2006.

[167] D. McCarron, *A guide to acousto-optic modulators*, December 2007.

[168] Bragg, "The diffraction of short electromagnetic waves by a crystal," *Proceedings of the Cambridge Philosophical Society*, vol. 17, pp. 43 – 57, 1913.

[169] E. A. Donley, T. P. Heavner, F. Levi, M. O. Tataw, and S. R. Jefferts, "Double-pass acousto-optic modulator system," *Review of Scientific Instruments*, vol. 76, July 2005.

[170] S. Cova, M. Ghioni, A. Lacaita, C. Samori, and F. Zappa, "Avalanche photodiodes and quenching circuits for single-photon detection," *Appl. Opt.*, vol. 35, no. 12, pp. 1956 – 1976, April 1996.

[171] *Si-Avalanche Photodiode module*, Licel lidar computing and electronics.

[172] J. Campbell, "Recent advances in telecommunications avalanche photodiodes," *Journal of Lightwave Technology*, vol. 25, no. 1, pp. 109 – 121, January 2007.

[173] M. Born and E. Wolf, *Principles of Optics*, 7th ed. Cambridge Univeristy, 1999.

[174] P. B. Phua and Y. L. Lim, "Coherent polarization locking with near-perfect combining efficiency," *Optics Letters*, vol. 31, no. 14, pp. 2148 – 2150, July 2006.

[175] R. Uberna, A. Bratcher, and B. G. Tiemann, "Coherent polarization beam combination," *IEEE JOURNAL OF QUANTUM ELECTRONICS*, vol. 46, no. 8, pp. 1191 – 1196, August 2010.

[176] M. Toyoshima, H. Takenaka, Y. Shoji, Y. Takayama, Y. Koyama, and H. Kunimori, "Polarization measurements through space-to-ground atmospheric propagation paths by using a highly polarized laser source in space." *Opt. Express*, vol. 17, no. 25, pp. 22 333 – 22 340, December 2009.

[177] D. Steinkraus, I. Buck, and P. Y. Simard, "Using gpus for machine learning algorithms," in *Eighth International Conference on Document Analysis and Recognition*, vol. 2, August 2005, pp. 1115–1120.

[178] A. S. Rekhi, B. Zimmer, N. Nedovic, N. Liu, R. Venkatesan, M. Wang, B. Khailanya, W. J. Dally, and C. T. Gray, "Analog/mixed-signal hardware error modeling for deep learning inference," in *Design Automation Conference (DAC)*, June 2019.

Appendix A

A.1 Matched Filter Analysis to Estimate the Heterodyne Beat Note Frequency

This section discusses using the Delay model, presented in equation A.1 to measure the Doppler shift applied to the heterodyne beat note in the bench-top experiment. The delay model is discussed in more detail in Chapter 3. This method of measuring the time-varying delay is not proposed for space debris ranging due to the diffuse surface effects discussed in Section 2.3.3. This analysis was done to test the matched filter analysis method in measuring the Doppler effect due to the time-varying delay of a target on laser frequency before the amplitude modulation pseudo-random noise (PRN) code method was considered.

$$\begin{aligned} \tau(t) &= \frac{d(t)}{c} \\ &\simeq \frac{1}{c}\Big(d_0 + v_0 t + \frac{a_0 t^2}{2}\Big) \end{aligned} \tag{A.1}$$

Section 3.3.2 discussed that the change in the orbiting target's position in reference to the ground-based telescope causes a Doppler shift of the optical signal's laser frequency. The Doppler shift of the laser frequency can be as large as $\pm 8\,\text{GHz}$, much larger than the Doppler shift of the amplitude modulated PRN code which was $\pm 1750\,\text{Hz}$. Due to the large Doppler shift, measuring the heterodyne beat note of the coherent detection system provides a sensitive time-varying delay measurement for a satellite ranging application [62].

Figure A.1 shows the bench-top experiment setup used to test the matched filter analysis to measure the heterodyne beat note. In the bench-top experiment, both the signal beam and local oscillator beam are sourced from the same laser source to have a stable phase [73]. The signal beam is not amplitude modulated with the PRN code. Both the signal beam and local oscillator beam are passed through an acousto-optic modulator (AOM) to frequency shift each beam to f_{Sig} and f_{LO} respectively. The two frequency-shifted beams then interfered with one output of the beam splitter used to measure the heterodyne beat note using the Newport 1811 photodetector.

Equation A.2 shows the expected heterodyne beat note $A_{PD}(t)$ measured by the photodetector from the bench-top experiment. f_h is the heterodyne beat note frequency ($f_h = f_{Sig} - f_{LO}$) and $\phi_{\Delta L}$ is the phase of the beat note ($\phi_{\Delta L} = \phi_{Sig} - \phi_{LO}$). By changing the signal beam frequency f_{Sig}, the heterodyne beat note frequency f_h is also altered. The phase difference $\phi_{\Delta L}$ is fixed in the bench-top experiment since both ϕ_{Sig} and ϕ_{LO} do not vary.

$$A_{PD}(t) = \frac{\alpha}{2}\Big[\underbrace{P_{Sig} + P_{LO}}_{\text{DC Term}} + \underbrace{2\sqrt{P_{Sig}P_{LO}}\,\cos(2\pi f_h t + \phi_{\Delta L})}_{\text{Beat Note}}\Big] \tag{A.2}$$

In the matched filter analysis, the digitised signal acquired from the photodetector is cor-

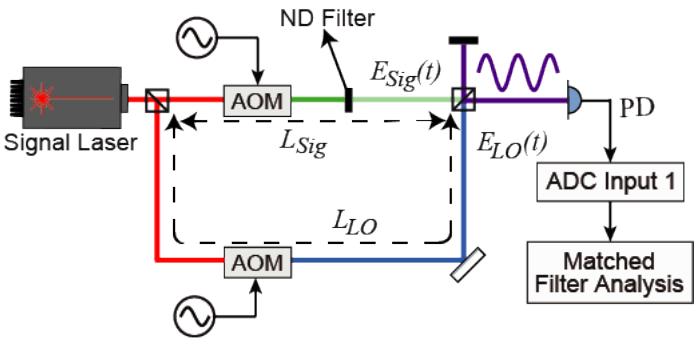

Figure A.1: Coherent detection scheme to test the matched filter analysis method in estimating the frequency change applied to the signal laser beam.

related with a *template signal*. The correlation is used to indicate the similarity of the template to the acquired signal. Changing the input parameter values of the template impacts the correlation output. The input parameter values used to generate a template signal with the most significant correlation output provides the best estimate of the acquired signal properties.

Equation A.3 is used to generate the template signal $h(t)$. The time-varying delay of the target causes a change in the phase of the laser beam. Since the phase is related to the frequency of the laser [80], this causes a Doppler shift of the signal beam. In the template signal, the phase of the laser is changed using the Delay model $d(t)$. The change in the phase would alter the template signal's frequency f_t.

$$\begin{aligned} h(t) &= \cos\left(2\pi f_t - \frac{2\pi f_{Sig}}{c} d(t)\right) \\ &= \cos\left(2\pi f_t - \frac{2\pi f_{Sig}}{c}\left[d_0 + v_0 t + \frac{a_0 t^2}{2}\right]\right) \end{aligned} \tag{A.3}$$

The Delay model $d(t)$ is changed by varying the input parameters d_0, v_0 and a_0. If there is no time-varying delay ($v_0 = 0$ and $a_0 = 0$), then the phase of the template signal depends on d_0, which only cuases a fixed shift in the phase. This results in no frequency change in f_t. Changing the d_0 parameter can only change the phase between 0 radian to 2π radian. This is equivalent to the wavelength of the laser ($\lambda = 1064\,\text{nm}$). Hence, the d_0 parameter cannot be used to measure the absolute range of L_{Sig} which in the bench-top experiment is equal to 2.175 m.

If there is a time-varying delay, the template beat note will have a time-varying phase. If there is only a velocity term ($a_0 = 0$), it causes a fixed frequency shift of f_t. The sign of the velocity term indicates if f_t is increased or reduced. If v_0 is positive, the resulting time-varying phase causes the frequency f_t to reduce while if v_0 is negative, the resulting time-varying phase causes the frequency f_t to increase.

If a_0 is not equal to zero, it causes a linear frequency change similar to a frequency ramp. A positive value of a_0 causes a linear reduction in the frequency f_t as a function of time while a negative value of a_0 causes a linear increase in the frequency f_t as a function of time.

Experimental Analysis

When the signal laser is not Doppler shifted, the heterodyne beat note f_h is equal to 70 MHz. For the analysis shown in Figure A.2 the signal beam laser frequency is increased by 1 MHz to 71 MHz as shown in Figure A.2a. The signal beam power P_{Sig} is equal to 2.4 nW and local oscillator beam power P_{LO} is equal to 115 μW. The expected target velocity v_{SD} to cause a 1 MHz Doppler shift is equal to -1.064 m/s.

Figure A.2b shows cross-correlation using the matched filter analysis as a function of the template velocity parameter v_0. The integration time chosen for the analysis is equal to 1 ms. The maximum signal correlation is generated when v_0 is equal to $-1.063\,95$ m/s, close to the expected target velocity. The result shows that the matched filter analysis can estimate the Doppler shift applied in the bench-top experiment to the signal laser beam frequency.

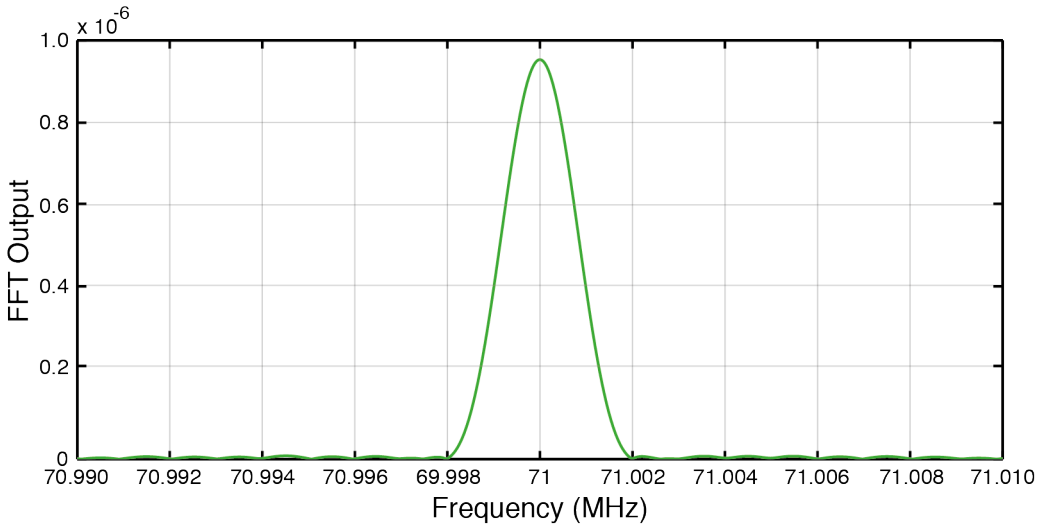

(a) Acquired heterodyne beat note in the frequency domain where f_h is approximately at 71 MHz.

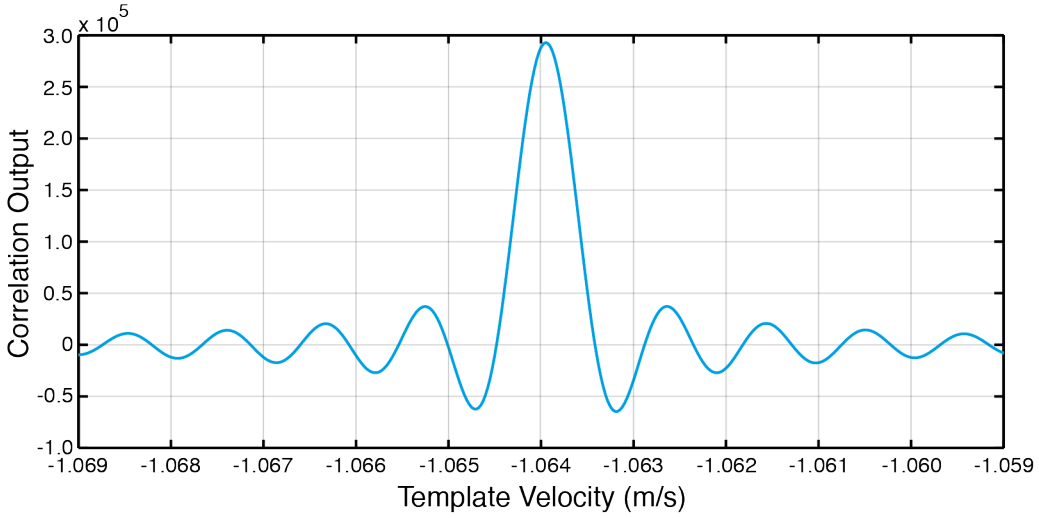

(b) Signal correlation between acquired heterodyne beat note and template beat note using only a velocity parameter bank.

Figure A.2: Comparing a beat note matched filter signal correlation to the heterodyne beat note in the frequency domain.

Figure A.3 compares the frequency spectrum and the signal correlation of the acquired signal when a linear frequency sweep is applied to the signal laser in the bench-top experiment. The linear sweep increases the signal frequency from 70 MHz to 80 MHz within 100 ms. The slope of the sweep is 100 MHz/s and translates to the time-varying delay impact on the heterodyne beat note from a moving target with a constant acceleration equal to 106.4 m/s^2.

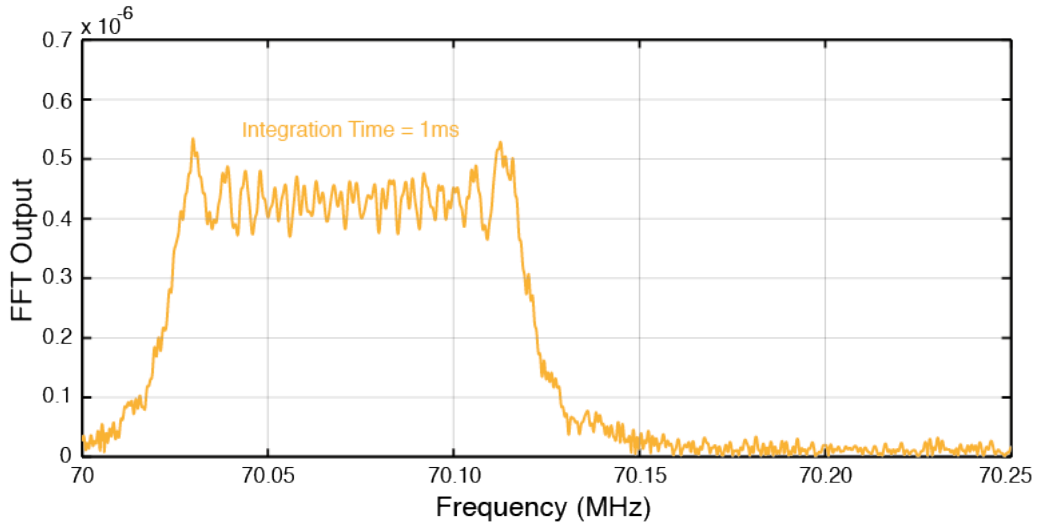

(a) Presenting the impact of the frequency sweep on the heterodyne beat note.

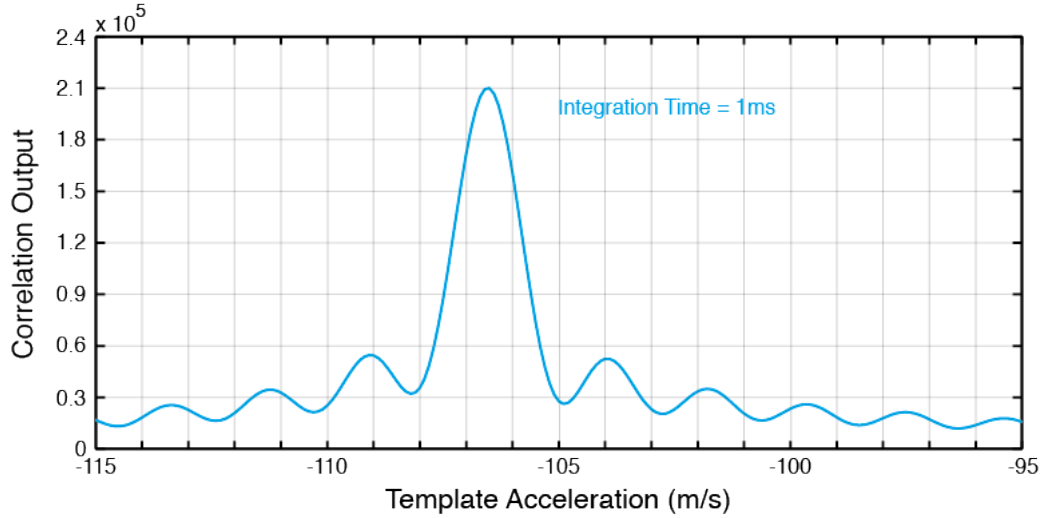

(b) Signal correlation between acquired heterodyne beat note and template beat note for varying acceleration a_0 values.

Figure A.3: Comparing the heterodyne beat note acquired from the bench-top experiment in the frequency domain and the signal correlation with the template beat note when a linear frequency swept of 100 MHz/s is applied to the signal laser to model target acceleration of 106.4 m/s^2.

Figure A.3a shows that the linear sweep term causes the heterodyne beat note frequency to be stretched over a larger frequency range. Figure A.3b shows the heterodyne beat note signal correlation for varying input acceleration a_0 values. The analysis used to produce Figure A.3b used a 1 ms integration time. Using the peak of the signal correlation, the matched filter analysis estimation of the acceleration is equal to 106.5 m/s^2. The result again shows that the matched filter analysis can estimate the acceleration parameter.

No further analysis was performed to measure the Doppler shift applied to the signal laser frequency. The analysis moved to applying the amplitude modulated PRN code to the signal laser and estimate the time-varying delay on the PRN code. This is due to the diffuse surface effects discussed in Section 2.3.3.

In theory, the heterodyne beat is still present but due to the low signal-to-noise ratio, may not be visible in the frequency spectrum. Even though using the matched filter analysis on the heterodyne beat note can provide a more sensitive measurement of the time-varying delay, it is unclear if it would be possible to do so for a diffuse surface. More analysis and experimental results are needed and could be carried out as part of future studies.